IntechOpen

Contact and Fracture Mechanics

Edited by Pranav H. Darji and Veera P. Darji

CONTACT AND FRACTURE MECHANICS

Edited by **Pranav H. Darji** and **Veera P. Darji**

Contact and Fracture Mechanics
http://dx.doi.org/10.5772/intechopen.68756
Edited by Pranav H. Darji and Veera P. Darji

Contributors

Lin Jing, Zhihua Wang, Longmao Zhao, Giuseppe Pintaude, Victor Roda-Casanova, Franscisco Sanchez-Marin, Petr Ogar, Sergey Belokobylsky, Denis Gorokhov, Arnaud Caron, Dengke Yang, Jiangting Wang, Huimin Yang, Peter Hodgson, Jan Dzugan, Pavel Konopik, Martin Rund, Jon Ander Esnaola, Iñigo Llavori, Alaitz Zabala, Xabier Gomez, Miren Larrañaga, Moises Jimenez, Yevgeny Deryugin, Somnath Bhattacharya, Kamal Sharma, Vaibhav Sonkar, Lei Wang, Zesheng Zhang, Zhiping Qiu, Chiara Gastaldi

Notice

First published in London, United Kingdom, 2018 by IntechOpen
eBook (PDF) Published by IntechOpen, 2019
IntechOpen is the global imprint of INTECHOPEN LIMITED, registered in England and Wales, registration number: 11086078, The Shard, 25th floor, 32 London Bridge Street
London, SE19SG – United Kingdom
Printed in Croatia

British Library Cataloguing-in-Publication Data
A catalogue record for this book is available from the British Library

Additional hard and PDF copies can be obtained from orders@intechopen.com

Contact and Fracture Mechanics
Edited by Pranav H. Darji and Veera P. Darji

p. cm.

Print ISBN 978-1-78923-158-8

Online ISBN 978-1-78923-159-5

eBook (PDF) ISBN 978-1-83881-353-6

Meet the editors

Prof. (Dr.) Pranav H. Darji graduated in Mechanical Engineering from the North Gujarat University, Gujarat, India, in 1998. He received his postgraduate degree from the Gujarat University, Gujarat, India, in Mechanical Engineering with a specialization in CAD/CAM in 2001. He received his PhD degree from the S.V. National Institute of Technology, Gujarat, India, in Mechanical Engineering in the specific field of rolling element bearing in 2015. He has 20 years of academic and administrative experience. He is working as a professor at the Department of Mechanical Engineering, C.U. Shah College of Engineering and Technology, C.U. Shah University, Wadhwan City, Gujarat, India, since 2010 and a principal in the same college and university since 2017. He has worked as an Assistant Professor from 2004 to 2010 in the same organization. He has previously worked as a lecturer at N.M. Gopani Polytechnic, Gujarat, India, from 1998 to 2002 and the Head of the Department of Mechanical Engineering from 2002 to 2004. Since 2015, he is also working as the director of P.G. Studies and Research at the Research, Development, and Innovation Center of C.U. Shah University as an additional responsibility and associated with various research activities. His research interest focuses on the areas of bearing technology, tribology, CAD, FEA, and advanced machine design. On the same area, he has published more than 68 research papers in various reputed national and international journals and conferences. He has edited international books *Advances in Tribology* in 2016 and *Bearing Technology* in 2017. He has organized many conferences and workshops for the benefit of the researchers, academicians, and industrialist. He has guided more than 22 dissertations of postgraduate students and 8 PhD scholars. He has given more than 12 invited presentations.

He is also associated actively with the industries to undertake the projects for the mutual benefits. He serves as an editorial board member of reputed international journals. He is a life member of professional bodies such as Institution of Engineers (India), Tribology Society of India, and Indian Society for Technical Education. He is a registered chartered engineer (Mechanical Engineering).

Prof. (Dr.) Veera P. Darji graduated in Mechanical Engineering from the Bhavnagar University, Gujarat, India, in 2000. She received her postgraduate degree from the Maharaja Sayajirao University, Gujarat, India, in Metallurgy Engineering with a specialization in Materials Technology in 2002. She received her PhD degree from the S.V. National Institute of Technology, Gujarat, India, in Mechanical Engineering in the specific field of multiple criteria decision making for manufacturing and industrial environment in 2016. She has 16 years of academic and administrative experience. She is working as a professor at the Department of Mechanical Engineering since 2010 and the Head of the Department of

Mechanical Engineering since 2018 at the C.U. Shah College of Engineering and Technology, C.U. Shah University, Wadhwan City, Gujarat, India. She has worked as a lecturer from 2004 to 2008 and as an Assistant Professor from 2008 to 2010 in the same organization. She has previously worked as a lecturer at N.M. Gopani Polytechnic, Gujarat, India, from 2002 to 2004 and the Head of the Department of Metallurgy Engineering from 2003 to 2004. Since 2008, she is holding the position of chairperson in various women staff and student committees of C.U. Shah College of Engineering and Technology and C.U. Shah University as an additional responsibility. Her research interest focuses on areas of optimization of various situations for manufacturing and industrial engineering issues. On the same area, she has published more than 35 research papers in various reputed national and international journals and conferences. She has coordinated a good number of conferences and workshops for the benefit of the researchers, academicians and industrialist. She has guided 13 dissertations of postgraduate students and 8 PhD scholars. She is also associated actively with the industries to undertake the projects for the mutual benefits. She is a life member of professional bodies such as Institution of Engineers (India), Society of MCDM, and Indian Society for Technical Education. She is a registered chartered engineer (Mechanical Engineering).

Contents

Preface XI

Section 1 Contact Mechanics 1

Chapter 1 **Contact Mechanics of Rough Surfaces in Hermetic Sealing Studies 3**
Peter Ogar, Sergey Belokobylsky and Denis Gorokhov

Chapter 2 **Experimental Studies of Nanometer-Scaled Single-Asperity Contacts with Metal Surfaces 27**
Arnaud Caron

Chapter 3 **Deformation Regimes for Sphere-Plane Contact: Revisiting Tabor's Criteria for Differential Hardness 45**
Giuseppe Pintaude

Chapter 4 **Adaptive Mesh Refinement Strategy for the Semi-Analytical Solution of Frictionless Elastic Contact Problems 59**
Victor Roda-Casanova and Francisco Sanchez-Marin

Chapter 5 **Improving Contact Load-Bearing Resistance of Ultrafine-Grained Materials Through Multilayering and Grading 79**
Dengke Yang, Jiangting Wang, Huimin Yang and Peter Hodgson

Chapter 6 **Modeling Friction for Turbomachinery Applications: Tuning Techniques and Adequacy Assessment of Heuristic Contact Models 97**
Chiara Gastaldi

Chapter 7 **Single-Curvature Sandwich Panels with Aluminum Foam Cores under Impulsive Loading 119**
Lin Jing, Zhihua Wang and Longmao Zhao

Section 2 Fracture Mechanics 141

Chapter 8 **Fracture Toughness Determination with the Use of Miniaturized Specimens 143**
Jan Dzugan, Pavel Konopik and Martin Rund

Chapter 9 **Fatigue Fracture of Functionally Graded Materials Under Elastic-Plastic Loading Conditions Using Extended Finite Element Method 169**
Somnath Bhattacharya, Kamal Sharma and Vaibhav Sonkar

Chapter 10 **Fretting: Review on the Numerical Simulation and Modeling of Wear, Fatigue and Fracture 195**
Iñigo Llavori, Jon Ander Esnaola, Alaitz Zabala, Miren Larrañaga and Xabier Gomez

Chapter 11 **Determination of Fracture Toughness Characteristics of Small-Size Chevron-Notched Specimens 215**
Yevgeny Deryugin

Chapter 12 **Numerical Analysis Methods of Structural Fatigue and Fracture Problems 235**
Qiu Zhiping, Zhang Zesheng and Wang Lei

Chapter 13 **Accelerated Fatigue Test in Mechanical Components 253**
Moises Jimenez

Preface

During recent years, the contact mechanics and fracture mechanics have found a considerable application in the solution of engineering problems to increase the life of the component. Contact mechanics studies the stress and strain states of bodies in contact; it is a contact that leads to friction interaction and wear. In recent years, computational contact mechanics has been a topic of intense research. The aim of this research is to devise robust solution schemes and new discretization techniques for the description of contact phenomena, which can then be applied to a much broader range of engineering analysis areas than is currently the case. The focus will be on a detailed treatment of the theoretical formulation of contact problems with regard to mechanics and mathematics. Fracture is understood to be the separation of a body of material into two or more pieces, whereby the load carrying is reduced to zero. The process of fracture can be considered to be made up of two components, crack initiation and crack propagation. Fracture mechanics has developed into a useful tool in the design of crack-tolerant structures and in fracture control; it also has a place in failure analysis. Fracture mechanics makes it possible to determine whether a crack of a given length in a material of known fracture toughness is dangerous because it will propagate to fracture at a given stress level. If the cause of crack extension may not be controlled, the only thing left to designer is to calculate the critical length in advance.

The different contributions of this book will cover the various advanced topics of research. It provides some needed background with respect to contact mechanics, fracture mechanics, and the use of finite element methods in both. All the covered chapters of this book are of a theoretical and applied nature, suitable for the researchers of engineering, physics, applied mathematics and mechanics with an interest in computer simulation of contact and fracture problems.

This book contains two sections as its name; Chapters 1–7 deal with contact mechanics, and Chapters 8–13 deal with fracture mechanics. Hermetic sealing studies are carried out in Chapter 1. Sealing capacity depends on the contact characteristics—the relative contact area and the gap density in the joint. In this chapter, the contact of a single asperity is considered taking into account the influence of the remaining contacting asperities. The response of a nanometer-scaled single asperity onto flat surfaces is experimentally accessible using atomic force microscopy, which is studied in Chapter 2. The author describes three experimental methods based on atomic force microscopy and corresponding methods for statistical data analysis. Chapter 3 presents an update of theories involving the differential hardness problem, starting from the hypothesis made by Tabor for the contact between a sphere and a

plane. In this way, the reader interested in problems that directly affect these formulations, such as contact area and contact fatigue, can take part in a fundamental theoretical basis to perform investigations in this field. In Chapter 4, a new approach is presented by the authors, whose main purpose is to improve the efficiency of the semianalytical methods that are used to solve frictionless elastic contact problems. To do so, an adaptive refinement of the pressure element mesh is implemented. This strategy allows for a reduction of the computational cost of the method, while its accuracy remains unaffected. In Chapter 5, the contact load-bearing response and surface damage resistance of multilayered hierarchical structured (MHSed) Ti were evaluated by experimental indentation on the overall loading response in conjunction with detailed computational simulations of local stresses and strain distribution. The purpose of Chapter 6 is to illustrate the experimental/numerical tools and methods developed to fill this gap on a common family of friction dampers, called "underplatform dampers" with a curved-flat cross section. Both cylinder-on-flat and flat-on-flat interfaces are addressed. The study contained in Chapter 7 presents a comprehensive report on the dynamic response and shock resistance of singly curved sandwich panels, comprising two aluminium alloy face sheets and an aluminium foam core, subjected to air-blast loading, in terms of the experimental investigation and numerical simulation. The results are significant to guide the engineering applications of sandwich structures with metallic foam cores subjected to air-blast loading.

Fracture toughness determination with the use of miniaturized specimens is discussed in Chapter 8. This chapter provides an overview of the reported values of the results obtained with the use of miniaturized specimens with hints of how can small-size-based results be related to the standard-sized specimen results. In Chapter 9, extended finite element method (XFEM) has been used to simulate the fatigue crack growth problems in functionally graded material (FGM) in the presence of hole, inclusion and minor crack under elastic and plastic conditions. Chapter 10 has introduced the state of the art of the currently available modeling and simulation methods to analyse the fretting phenomenon. Finally, a numerical architecture of coupled wear, fatigue, and fracture methodology has been introduced, which allows to analyse the fretting phenomena as a whole. Chapter 11 presents a new method for determining the fracture toughness of materials according to the test data of nonstandard small-size chevron-notched specimens. There are no empirical constants and phenomenological dependencies in the calculations. Chapter 12 reviews the most common empirical models and numerical methods of structural fatigue lifetime prediction. FEM (extended finite element method and fractal finite element method) is introduced as an important method to obtain the stress intensity factor or crack growth route. Chapter 13 deals with the review of accelerated fatigue tests, as it can be used to evaluate the component fatigue strength but is necessary to perform the statistical analysis during the test to monitor the test development, or this analysis is used to evaluate the test results, through the slope and its standard deviation.

Our intention for this book is to make current research on contact mechanics and fracture mechanics accessible to the researchers and scientists working in this field. It is also intended to bring together solutions of special problems, which may be of practical importance, and to describe theoretical and experimental methods of the solution of associated fields' problems. The work presented in this book will be useful, effective, and beneficial to mechanical engineers, automobile engineers, civil engineers, and material scientists from industry, research, and education and will stimulate new research in these fields.

We feel amazing pleasure to edit this book. We are deeply gratified by the enthusiastic response given by all the authors and their outstanding research contribution in the form of book chapters. We take this opportunity to thank the IntechOpen editorial staff, in particular, Ms. Maja Bozicevic and Mr. Slobodan Momcilovic, Publishing Process Manager, for obligatory technical assistance and continuous follow-up during book preparation and publishing. And of course , my special thanks to our parents and family members for the support they always gave to us.

Prof. (Dr.) Pranav H. Darji
Professor and Principal
C. U. Shah College of Engineering and Technology
Director
P. G. Studies and Research
Research, Development and Innovation Centre
C. U. Shah University
Wadhwan City, Gujarat (India)

Prof. (Dr.) Veera P. Darji
Professor and Head
Department of Mechanical Engineering
C. U. Shah College of Engineering and Technology
C. U. Shah University
Wadhwan City, Gujarat (India)

Section 1

Contact Mechanics

Chapter 1

Contact Mechanics of Rough Surfaces in Hermetic Sealing Studies

Peter Ogar, Sergey Belokobylsky and
Denis Gorokhov

Additional information is available at the end of the chapter

http://dx.doi.org/10.5772/intechopen.72196

Abstract

It is indicated that the sealing capacity depends on the contact characteristics—the relative contact area and the gap density in the joint. To determine the contact characteristics, a discrete roughness model is used in the form of a set of spherical segments, the distribution of which in height is related to the bearing curve described by the regularized beta function. The contact of a single asperity is considered with taking into account the influence of the remaining contacting asperities. The equations for determining the relative contact area and gap density in the joint depending on the dimensionless force parameters for elastic and elastic-plastic contacts are provided.

Keywords: contact mechanics, hermetic sealing studies, rough surface, spherical asperity, discrete model, elastic contact, elastic-plastic contact, hardening power law, relative contact area, gaps density, sealing joint, tightness

1. Introduction

Tightness is the property of the joints to provide an acceptable leakage value, determined from the conditions of normal operation of various systems and equipment, human safety, and environmental protection. To quantify the tightness, the leakage rate is used, that is, the mass or volume of the medium per unit time per unit length along the SJ's perimeter. By 'sealing joint' (SJ), we mean a set of details that form a structure to ensure tightness.

The SJ's tightness is provided by loading with a compressive load (the contact sealing pressures), which is largely determined by the stress-strain state in the contact area and depends on the contact interaction of the rough surfaces. The main contact characteristics ensuring SJ's tightness are the approaching of rough surfaces, the relative contact area, the density of gaps in the joint, and the degree of fusion of contact spots of single asperities. Depending on the

materials' properties and microgeometry parameters, there are elastic, viscoelastic, elastic-plastic, and rigid-plastic contacts.

At present, to solve the tribology problems, we need to use the roughness models and the rough surfaces contacting theory developed by the authors [1, 2] and their followers. However, the use of such models to solve the problems in hermetic sealing studies leads to significant errors, which is explained by the following:

1. the contact pressures of the sealing are approximately 1–2 orders of magnitude higher than for friction and at that, it is necessary to be taken into account the mutual influence of the contacting asperities;
2. in the sealing joint, all the asperities's contacting is possible, which requires the description of the whole bearing profile curve but not only its initial part, as in [2];
3. when determining the gaps volume (or density), the displacements of the points of the asperities surfaces have not been taken into account; and
4. the extrusion of the material into the intercontact space under elastic-plastic contact has not been taken into account.

Therefore, to describe the SJ, a rough surface model is required that adequately describes the real surface and corresponds to the whole bearing curve, and not just its initial part. In addition, in order to improve the accuracy of the calculation of the contact characteristics, the discrete model of a rough surface must be taken into account, the real distribution of dimensions of microasperities and the mutual influence. The criterion of plasticity must take into account the general stress-strain state when contacting of a rough surface and not just of a single asperity. In most cases, the contact of metallic rough surfaces is elastic-plastic, therefore, to determine the contact characteristics, it is necessary to take into account the parameters of material hardening.

To estimate the SJ's sealing property, in [3, 4], the nondimensional permeability functional is used

$$C_u = \frac{\Lambda^3 \upsilon_k}{4(1-\eta)^2}, \tag{1}$$

where Λ is the gaps density in the joint; η is the relative contact area; υ_k is the probability of a medium flowing, which depends on the single contact spots fusion.

All the parameters that appear in Eq. (1) depend on the parameters of microgeometry and dimensionless force parameters f_q or $\overline{q}_\sigma$, the determination of which is given in the following sections.

The purpose of the given research is to develop methods for calculating the contact characteristics that ensure the given tightness of the immobile joints with taking into account the complex of functional parameters of the sealing surfaces and mutual influence of asperities.

http://dx.doi.org/10.5772/intechopen.72196

2. Discrete model of the rough surface

We consider that the initial data for the model representation of a rough surface are parameters of roughness according to ISO 4287–1997, ISO 4287/1–1997: maximum roughness depth R_{max}, arithmetic mean deviation of the profile R_a, root-mean-square deviation of the profile R_q, mean height of the profile elements R_p, mean width of the profile elements S_m, bearing profile curve t_p, and bearing profile curve on the midline t_m. Thus, the standard parameters of the roughness for the developed model must coincide with the corresponding parameters of the real surface.

To describe the entire rough surface, it is required to know one of two functions:

$$\eta_u(\varepsilon) = \frac{A_u}{A_c} \text{ or } \varphi_n(u) = \frac{n_u}{n_c}, \tag{2}$$

where A_u is the material cross-sectional area at a relative level $\varepsilon = h/R_{max}$; A_c is the contour area; n_u is the number of asperities whose peaks are located above the level u; $n_c = A_c/A_{ci}$ is the total number of asperities; and A_{ci} is the area due to a single asperity.

According to ISO 4287–1997, parameters of roughness are determined from profilograms and the functions describing the distribution for the profile t_p and the surface $\eta_u(\varepsilon)$, but it is not fulfilled for the peaks and valleys asperities distribution functions of the profile $\varphi_{nl}(u_l)$ and the surface $\varphi_n(u)$, then the model is based on the bearing profile curve.

Let us assume that the function $\eta_u(\varepsilon)$ is monotonic and twice differentiable. A rough surface (**Figure 1**) is a set of asperities in the form of spherical segments of radius r and height ωR_{max}, and base radius $a_c = \sqrt{A_{ci}/\pi}$. It is necessary to find such a function $\varphi_n(u)$ for which the distribution of the material in the rough layer corresponds to the bearing surface curve.

The cross-section of the i-th asperity at the level ε is

$$A_{ri} = 2\pi r R_{max}(\varepsilon - u), \tag{3}$$

where u is the relative distance from the peaks level to the peak of the i-th asperity.

The number of peaks in the layer du and at a distance u is equal to

$$dn_r = n_c \varphi_n'(u) du. \tag{4}$$

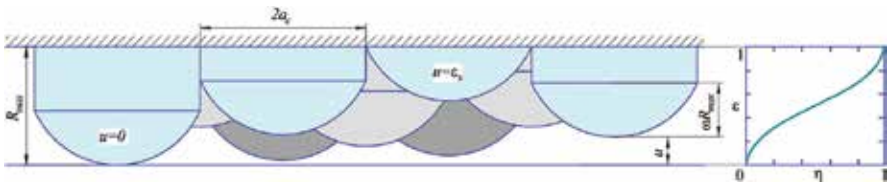

Figure 1. The scheme and the bearing curve of a rough surface.

Then, $A_u = A_r = 2\pi r R_{\max} n_c \int_0^{\varepsilon} \varphi_n'(u)(\varepsilon - u)du$;

$$\eta_u(\varepsilon) = \frac{A_r(\varepsilon)}{A_c} = C\int_0^{\varepsilon}(\varepsilon - u)\varphi_n'(u)du, C = \frac{2\pi r R_{\max} n_c}{A_c}. \tag{5}$$

Further, we have

$$\eta(\varepsilon) = C\left(\varepsilon\int_0^{\varepsilon}\varphi_n'(u)du - \int_0^{\varepsilon}u\varphi_n'(u)du\right) = C\left(\varepsilon\varphi_n(\varepsilon) - u\varphi_n(u)\Big|_0^{\varepsilon} + \int_0^{\varepsilon}\varphi_n(u)du\right),$$

$$\eta(\varepsilon) = C\int_0^{\varepsilon}\varphi_n(u)du. \tag{6}$$

Twice differentiating the left and right sides of ε, we have

$$\eta'(\varepsilon) = C\varphi_n(\varepsilon), \quad \eta''(\varepsilon) = C\varphi_n'(\varepsilon); \tag{7}$$

$$\varphi_n(\varepsilon) = \frac{\eta'(\varepsilon)}{C}, \quad \varphi_n'(\varepsilon) = \frac{\eta''(\varepsilon)}{C}. \tag{8}$$

To describe the bearing surface curve, we use the regularized beta function:

$$t_p(\varepsilon) = \eta(\varepsilon) = I_\varepsilon(p,q) = \frac{\mathrm{B}_\varepsilon(p,q)}{\mathrm{B}(p,q)}, \tag{9}$$

where

$$p = \left(\frac{R_p}{R_q}\right)^2\left(\frac{R_{\max} - R_p}{R_{\max}}\right) - \frac{R_p}{R_{\max}},\ q = p\left(\frac{R_{\max}}{R_p} - 1\right). \tag{10}$$

$\mathrm{B}_\varepsilon(\alpha,\beta)$ и $\mathrm{B}(\alpha,\beta)$ are the incomplete and complete beta-functions.

Double differentiating Eq. (9), from Eq. (8), for the function and the distribution density of the asperities, we have

$$\varphi_n(u) = \frac{\eta_u'(u)}{C} = \frac{u^{p-1}(1-u)^{q-1}}{\varepsilon_s{}^{p-1}(1-\varepsilon_s)^{q-1}}; \tag{11}$$

$$\varphi_n'(u) = \frac{\eta''_u(u)}{C} = \frac{u^{p-2}(1-u)^{q-2}[(p-1)(1-u) - (q-1)u]}{\varepsilon_s^{p-1}(1-\varepsilon_s)^{q-1}}. \tag{12}$$

The relative height of the spherical asperity is $\omega = 1 - \varepsilon_s$ and the radius of spherical asperity is $r = a_c^2/(2\omega R_{\max})$.

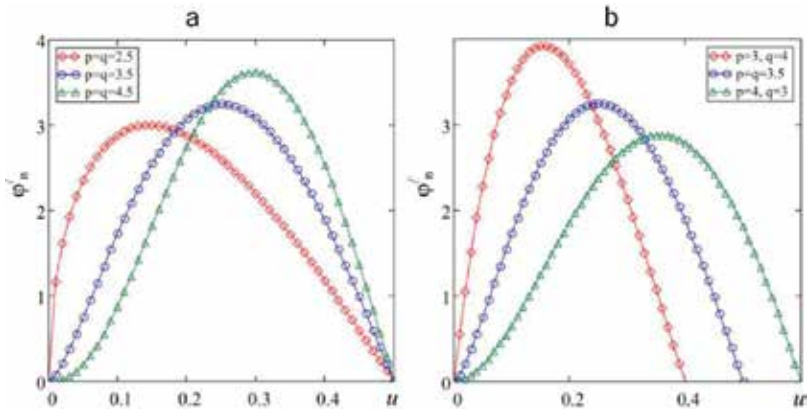

Figure 2. The distribution densities of asperities for different values of p and q.

This section describes a model of a rough surface in the form of a set of spherical asperities with constant radii and heights. More complex models with asperities with variable radii and heights are given in work [3, 4].

The contact of two rough surfaces $z_i(x, y)$ can be represented as a contact of an equivalent rough surface $z(x, y) = \sum_{i=1}^{2} z_i(x, y)$ and a flat surface. The parameters of the microgeometry of an equivalent surface are given in [3, 4].

3. Description of contact of a single asperity

3.1. Contact of a spherical asperity and the low-modulus half-space

Elastic contact occurs when low-modulus materials are used, which are used widely in sealing technology in the form of coatings or individual details [3, 5]. According to the strength criteria, the construction materials belong to the low-modulus materials if the values of the elastic moduli $E < 10^3$ MPa [6]. When contacting metallic rough surfaces, elastic contact is possible for high surface cleanliness classes and large values of the yield strength of the material.

As shown by experiments [7, p. 179] with polymeric interlayers (a coating on one of the conjugate details), loaded by [1] compressive stresses, the real touching area tends to be a constant value, depending on the physico-mechanical properties of the interlayer material.

During elastic contact, the mutual influence of discretely loaded sections leads to the growth retardation of the contact area [3]. It is reflected in the Bartenev-Lavrentyev's formula [7]

$$\eta = 1 - \exp\left(-b\frac{q}{E}\right), \tag{13}$$

where b is the coefficient depending on the surface quality, q_c is the contour contact pressure, and E is the elastic modulus. As it follows from Eq. (13), $\eta \to 1$ for $q \to \infty$.

The question of the influence of neighboring asperities in the case of elastic contact was considered in [8, 9], where the mutual influence is replaced by the action of equal concentrated forces located at the nodes of the hexagonal lattice.

According to the Saint-Venant's principle, at a point sufficiently distant from the region of application of the load, the stresses and deformations do not depend on the nature of the load distribution in its application area, in [10, 11]. Using the principle, the influence of the other contacting asperities is replaced by the action of a uniformly distributed load in some circular area. It allows considering the problem posed as an axisymmetric problem.

Let us consider the contact of a single absolutely rigid spherical asperity of radius r, whose peak is located at a distance uR_{max} from the peaks line of a rough surface with an elastic half-space in the system of cylindrical coordinates z, ρ, and φ with origin at the point O (**Figure 3**).

From an analysis of the numerous solutions of contact problems in the theory of elasticity and plasticity, it follows that a change of the distribution of external loads near the contact area

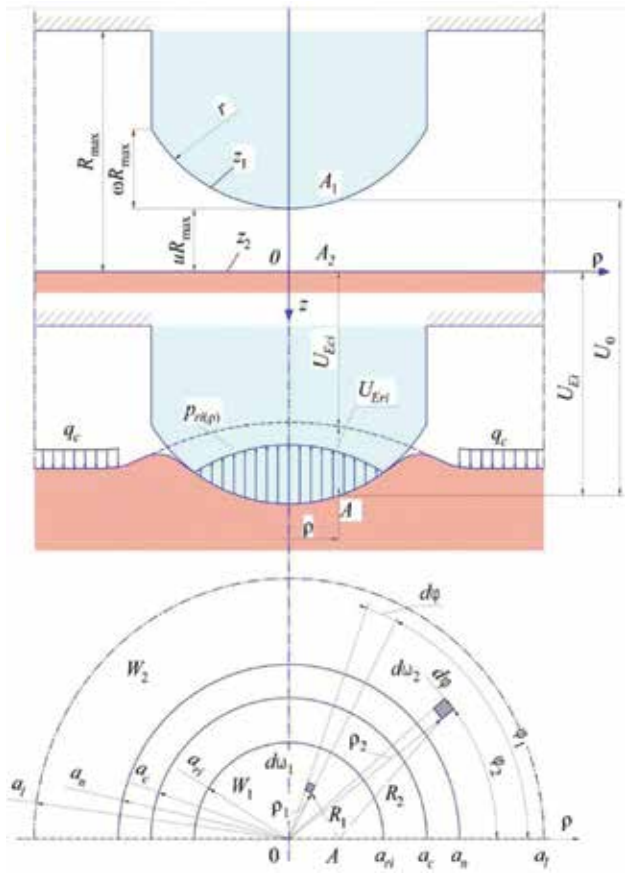

Figure 3. Scheme of contact of a single asperity.

under constancy of its average intensity leads to insignificant changes only near the boundary of the contact area.

Then, taking into account, the nature of the mutual location of the individual contact spots, the influence on the contact characteristics of an individual asperity within the circular contact area $W_1(\rho = \overline{0, a_{ri}})$ and the circular unloaded area $W(\rho = \overline{a_{ri}, a_n})$ on the remaining contact spots will be equivalent to the effect of the uniformly distributed load q_{cn} acting in the circular area $W_2(\rho = \overline{a_n, a_l})$, and the assigned problem may be regarded as an axisymmetric (**Figure 3**). The size of the unloaded area a_n depends on the number of contacting asperities and with increasing applied load, it decreases from a_l to a_c.

The solution of this problem is given in Ref. [11]. Studies on the effect of the parameter $k_a = a_n/a_c$ on the relative contact area show only 4% increase of last one; therefore, with a margin to tightness ensure, we will give a solution for $k_a = 1$ or $a_n = a_c$ below.

Let A_1 and A_2 be two points on the surface of the circular contact area W_1. The A_1 and A_2 coming into contact after application of the compressive load. Since the total normal displacement U_0 of the point A_1 is constant for any point in area W_1, we have

$$U_0 = U_E + z_1 = U_{Eri} + U_{Eci} + z_1, \tag{14}$$

where U_{Eri} is the normal contact displacement under the pressure p_{ri} acting in the region W_1; U_{Eci} is the normal displacement under the pressure q_{cn}; and z_1 is the equation of the surface of a spherical asperity in an unloaded state.

As for the real surfaces, $r >> R_{\max}$, then

$$z_1 = -uR_{\max} - \frac{\rho^2}{2r}. \tag{15}$$

Elementary displacements dU_{Eri} and dU_{Eci} under pressures q_{ri} and q_c acting on elementary areas dw_1 and dw_2, respectively, are determined by [12]:

$$dU_{Eri} = \frac{\theta q_{ri}(\rho_1)}{\pi R_1} dw_1,\ dU_{Eci} = \frac{\theta q_{cn}}{\pi R_2} dw_2; \tag{16}$$

where $R_j^2 = \rho^2 + \rho_j^2 - 2\rho\rho_j \cos\varphi_j$, $j = 1, 2$; $\rho \equiv \rho_i$; $\theta = (1 - \nu^2)/E$, ν is Poisson's ratio; $dw_1 = \rho_1 d\rho d\varphi$; and $dw_2 = \rho_2 d\rho d\varphi$.

After integrating Eq. (16), we have

$$U_{Eri} = \frac{\theta}{\pi} \int_{W_1} \frac{p_{ri}(\rho) dw_1}{R_1}, \tag{17}$$

$$U_{Eci} = \frac{4}{\pi} \theta q_c \left[a_l \mathrm{E}\left(\frac{\rho_i}{a_l}\right) - a_c \mathrm{E}\left(\frac{\rho_i}{a_c}\right) \right], \tag{18}$$

where $E(x)$ is the complete elliptic integral of the second kind.

From Eq. (15), taking into account Eqs. (16)–(18), we have

$$\int_{W_1} \frac{p_{ri}(\rho)dw_1}{R_1} = f(\rho_i), \tag{19}$$

$$f(\rho_i) = \frac{\pi}{\theta}\left(U_0 - uR_{\max} - \frac{\omega R_{\max}\rho_i^2}{a_c^2}\right) - 2\pi q_c\left[a_l - \frac{2}{\pi}E\left(\frac{\rho_i}{a_c}\right)\right]. \tag{20}$$

The Eq. (19) is the basic equation of an axisymmetric contact problem. The common decision of Eq. (19) is [13].

$$p_{ri}(\rho_i) = -\frac{1}{2\pi}\int_{\rho_i}^{a_{ri}} \frac{F(s)ds}{\sqrt{s^2-\rho_i^2}},\ P_i = -\frac{2}{\pi}\int_0^{a_{ri}} \frac{f'(\sigma)\sigma^2 d\sigma}{\sqrt{a_r^2-\sigma^2}}, F(s) = \frac{2}{\pi}\left[f(0) + s\int_0^s \frac{f'(\sigma)d\sigma}{\sqrt{s^2-\sigma^2}}\right]. \tag{21}$$

As a result from (21), we have

$$p_{ri}(\rho_i) = \frac{4\omega R_{\max}}{\pi\theta a_c^2}\sqrt{a_{ri}^2-\rho_i^2} + \frac{q_c}{\pi}\arcsin\sqrt{\frac{a_{ri}^2-\rho_i^2}{a_c^2-\rho_i^2}}, \tag{22}$$

$$P_i = \frac{8\omega R_{\max}a_{ri}^3}{3\theta a_c^2} + 2q_c a_c^2\left[\arcsin\frac{a_{ri}}{a_c} - \sqrt{\frac{a_{ri}^2}{a_c^2}\left(1-\frac{a_{ri}^2}{a_c^2}\right)}\right]. \tag{23}$$

Taking into account that $\eta_i = a_{ri}^2/a_{ci}^2$, $q_{ci} = P_i/(\pi a_{ci}^2)$, from Eqs. (22) and (23), we have

$$p_{ri}(\rho_i) = \frac{4\eta_i^{0.5}\omega R_{\max}}{\pi\theta a_c^2}\sqrt{1-\frac{\rho_i^2}{a_{ri}^2}} + \frac{q_c}{\pi}\arcsin\sqrt{\frac{a_{ri}^2-\rho_i^2}{a_c^2-\rho_i^2}}, \tag{24}$$

$$q_{ci} = \frac{8\omega R_{\max}\eta_i^{1.5}}{3\pi\theta a_c} + \frac{2}{\pi}q_c\left[\arcsin\eta_i^{0.5} - \sqrt{\eta_i(1-\eta_i)}\right]. \tag{25}$$

The mean p_{mi} and the maximum $p_{ri}(0)$ stresses at the contact spot are described by equations

$$p_{mi} = \frac{N_i}{A_{ri}} = \frac{q_{ci}}{\eta_i} = \frac{8\eta_i^{0,5}\omega R_{\max}}{3\pi\theta a_c} + \frac{2q_c}{\pi\eta_i}\left[\arcsin\eta_i^{0.5} - \sqrt{\eta_i(1-\eta_i)}\right], \tag{26}$$

$$p_{ri}(0) = \frac{4\eta_i^{0,5}\omega R_{\max}}{\pi\theta a_c} + \frac{q_c}{\pi}\arcsin\eta_i^{0..5}. \tag{27}$$

With sufficient accuracy (with an error of less than 1%), Eq. (24) can be written as.

$$p_r(\eta_i,\rho_i) = p_{r0}(\eta_i,0)\left(1-\rho_i^2/a_r^2\right)^{\beta},\ \beta = p_{r0}(\eta_i,0)/p_m(\eta_i,0) - 1. \tag{28}$$

3.2. The contact of a spherical asperity and the hardenable elastic-plastic half-space

Problems of a spherical asperity elastic-plastic indentation are not studied sufficiently and some suggested solutions are needed for clarification and improvement. One of the important problems is material hardening. The authors' approach to solve this problem is given in Ref. [14].

In several works [15, 16], the empirical Meyer law linking the spherical indentation load and an indenter diameter was used to allow for material hardening in solving the tribomechanic problems. Let us consider this approach at length.

In describing elastic-plastic characteristics of the hardenable material, the Hollomon's power law is widely used. According to it, the relation between the true stress S and the true strain ε under uniaxial tension or compression is described by equations

$$S = \begin{cases} \varepsilon E, & \varepsilon \le \varepsilon_y; \\ K\varepsilon^n, & \varepsilon \ge \varepsilon_y; \end{cases} \tag{29}$$

where E is the elastic modulus and n is the strain-hardening exponent.

The constant K is determined from the equality condition for σ at ε_y. Then the second equation in Eq. (29) can be written as.

$$\frac{S}{\sigma_y} = \left(\frac{E\varepsilon}{\sigma_y}\right)^n = \left(\frac{\varepsilon}{\varepsilon_y}\right)^n, \varepsilon \ge \varepsilon_y. \tag{30}$$

where $\sigma_y \approx S_y$, σ_y is the yield strength, and $\varepsilon_y = \sigma_y/E$.

Taking into accord that the limiting uniform strain $\varepsilon_u = n$, the exponential deformation hardening can be determined according to Ref. [17] from the following equation:

$$n\ln n - n\left(1 + \ln \varepsilon_y\right) - \ln\frac{\sigma u}{\sigma_y} = 0, \tag{31}$$

where σ_u is the tensile strength.

Meyer was the first who described a material behavior in the elastic-plastic domain. He related the load P to the indentation diameter d as

$$P = Ad^m. \tag{32}$$

The empirical Meyer law is often written as:

$$\frac{4P}{\pi d^2} = HM = A^*\left(\frac{d}{D}\right)^{m-2}. \tag{33}$$

where m, A, and A^* are constants. A^* has a dimension of strength.

The equation on the left side is a mean contact area pressure referred to as the Meyer hardness

$$\frac{4P}{\pi d^2} = \frac{P}{\pi a^2} = p_m = HM, \tag{34}$$

where a is the radius of the contact area.

Using [16], we have

$$\frac{P}{E^* R^2} = \frac{2}{k_\sigma \cdot k_n} \left(\frac{n}{e}\right)^n \varepsilon_y^{1-n} \left(\frac{a}{R}\right)^{2+1.041n}. \tag{35}$$

where E^* is reduced elastic modulus, $k_\sigma = 0.333$ for carbon and pearlitic steel, for other materials, the values of k_σ are given in Ref. [18].

$$k_n = \frac{(2 + 1.041n)^{1+0.5205n}}{(1 + 1.041n)^{1+1.041n}} (1.041n)^{0.5205n}. \tag{36}$$

The limits of using of Eq. (35) are given in Ref. [16].

As it was indicated in Ref. [16], the obtained results are in good agreement with the experimental data given in Ref. [19], and with the data of FE analysis [20].

Thus, the proposed approach suggests an alternative to a more complex method for describing elastic-plastic penetration of a sphere on the basis of the kinetic indentation diagram [14], which was used in solving problems of elastic-plastic contacting of rough surfaces.

4. Contacting rough surfaces

4.1. Elastic contact of rough surfaces

4.1.1. Relative contact area

Consider the contact of a rough surface with an elastic-plastic half-space using a roughness model for which the function and the density of the distribution of the asperities are described by Eqs. (15) and (16). The displacement of a rough surface in the general case is determined from Eq. (21) under the condition $F(a_{ri}) = 0$:

$$U_0 = uR_{\max} + 2\Theta q_c (a_l - a_c) + 2\omega R_{\max} \frac{a_{ri}^2}{a_c^2} + +2\theta q_c a_c \left(1 - \sqrt{1 - \frac{a_{ri}^2}{a_c^2}}\right). \tag{37}$$

For an asperity contacting at a point, that is, for $a_{ri} = 0$, we have

$$U_0 = \varepsilon R_{\max} + 2\theta q_c (a_l - a_c). \tag{38}$$

Since the value of U_0 is constant for all points of the contact regions, it follows from Eqs. (56) and (38) that

$$\eta_i + \frac{\theta q_c a_c}{\omega R_{\max}} \left(1 - \sqrt{1 - \eta_i}\right) - \frac{\varepsilon - u}{2\omega} = 0. \tag{39}$$

This equation has a solution

$$\eta_i = \frac{\varepsilon - u}{2\omega} - f_q\left(1 + \frac{f_q}{2} - \sqrt{\left(1 + \frac{f_q}{2}\right)^2 - \frac{\varepsilon - u}{2\omega}}\right), \tag{40}$$

where $f_q = \frac{\theta q_c a_c}{\omega R_{\max}}$.

Contour pressure in the joint of a rough surface with a half-space and the relative area are described by equations.

$$q_c = \frac{N}{A_c} = \frac{1}{A_c}\sum_{i=1}^{n_r} q_{ci}A_{ci};\ \eta = \frac{A_r}{A_c} = \frac{1}{A_c}\sum_{i=1}^{n_r} A_{ci}\eta_i. \tag{41}$$

Considering that for this roughness model $A_{ci} = \text{const}$, $A_c = A_{ci}n_c$, and $dn_r = n_c\varphi_n'(u)\,du$, we represent Eq. (41) in the form.

$$q_c(\varepsilon) = \int_0^{\min(\varepsilon,\varepsilon_s)} q_{ci}\varphi_n'(u)du,\ \eta(\varepsilon) = \int_0^{\min(\varepsilon,\varepsilon_s)} \eta_i\varphi_n'(u)du. \tag{42}$$

Taking into account Eq. (25), we have.

$$f_q(\varepsilon) = \frac{\theta q_c(\varepsilon)a_c}{\omega R_{\max}} = \frac{\frac{8}{3\pi}\int_0^{\min(\varepsilon,\varepsilon_s)} \eta_i^{1,5}\varphi_n'(u)du}{1 - \int_0^{\min(\varepsilon,\varepsilon_s)} \Psi_\eta(\eta_i)\varphi_n'(u)du},\ \Psi_\eta(\eta_i) = \frac{2}{\pi}\left[\arcsin\eta_i^{0.5} - \sqrt{\eta_i(1-\eta_i)}\right]. \tag{43}$$

Figure 4 shows the dependences of the relative contact area on the force elastic-geometric parameter f_q.

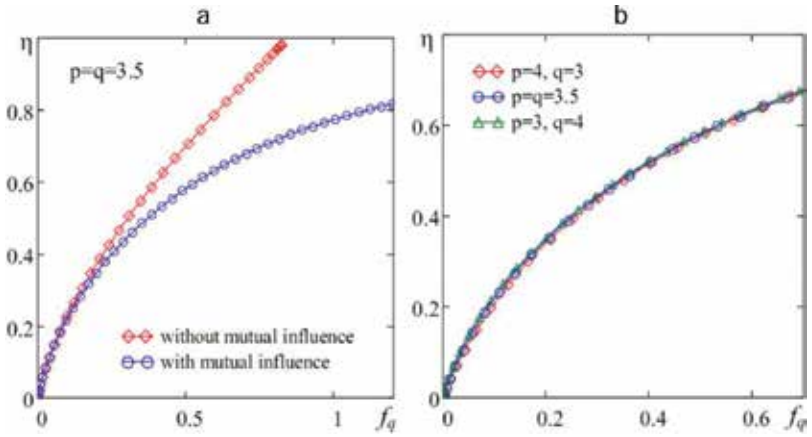

Figure 4. The relative contact area with/without taking into account the mutual influence of asperities (a) and for different values of p and q (b).

4.1.2. Gaps density of the joint

To determine the volume of the intercontact space, it is necessary to determine the volumes of gaps attributable to single contacting and noncontacting asperities [10],

$$V_i = \begin{cases} V_{ri} = 2\pi \int\limits_{a_{ri}}^{a_c} [z_{20}(\rho) - z_{10}(\rho)]\rho d\rho; \\ \\ V_{0i} = 2\pi \int\limits_{0}^{a_{ci}} [z_{2r}(\rho) - z_{1r}(\rho)]\rho d\rho, \end{cases} \tag{44}$$

where z_{10}, z_{20} and z_{1r}, z_{2r} are the equations describing the surfaces of noncontacting and contacting asperities and half-spaces, respectively.

Then, the total volume of the intercontact space at the joint is described by the equation

$$V_c = \sum_{i=1}^{n_r} V_{ri} + \sum_{i=1}^{n_c - n_r} V_{0i}, \tag{45}$$

And the corresponding gap density is equal to

$$\Lambda(\varepsilon) = \frac{V_c}{A_c R_{\max}} = \frac{1}{A_{ci} R_{\max}} \left[\int\limits_{0}^{\min(\varepsilon, \varepsilon_S)} V_{ri} \varphi_n'(u) du + \int\limits_{\min(\varepsilon, \varepsilon_S)}^{\varepsilon_S} V_{0i} \varphi_n'(u) du \right]. \tag{46}$$

Taking into account that $\Lambda_{ri} = V_{ri}/(A_{ci} R_{\max})$ и $\Lambda_{0i} = V_{0i}/(A_{ci} R_{\max})$, it can be represented in the form

$$\Lambda(\varepsilon) = \int\limits_{0}^{\min(\varepsilon, \varepsilon_S)} \Lambda_{ri} \varphi_n'(u) du + \int\limits_{\min(\varepsilon, \varepsilon_S)}^{\varepsilon_S} \Lambda_{0i} \varphi_n'(u) du. \tag{47}$$

We provide the equations of surfaces of the asperities and the half-space that enter into Eq. (44):

$$z_{10} = \omega R_{\max} \left[\frac{\varepsilon - u}{\omega} - x^2 + 2 f_q (k - 1) \right], \tag{48}$$

where $x = \frac{\rho}{a_c}; k = \frac{a_l}{a_c}$,

$$z_{20} = 2\omega R_{\max} f_q \left[k \cdot {}_2F_1\left(-\frac{1}{2}, \frac{1}{2}; 1; \frac{x^2}{k^2} \right) - {}_2F_1\left(-\frac{1}{2}, \frac{1}{2}; 1; x^2 \right) \right], \tag{49}$$

where ${}_2F_1$ is the Gaussian hypergeometric function,

for contacting asperity $z_{1r} = z_{10}$;

$$z_{2r} = \begin{cases} z_{1r}, & 0 \le x < \eta_i^{0,5} \\ \\ U_{Eri} + U_{Eci}, & \eta_i^{0,5} \le x \le 1; \end{cases} \tag{50}$$

$$U_{Eci} = z_{20},\ U_{Eri} = \omega R_{\max} \frac{f_{qi}}{x} {}_2F_1\left(\frac{1}{2}, \frac{1}{2}; \beta + 2; \frac{\eta_i}{x^2}\right),\ f_{qi} = \frac{8\eta_i^{1,5}}{3\pi} + \Psi(\eta_i) \cdot f_{q'} \tag{51}$$

where $\beta = p_{ri}(0)/p_m - 1$.

Figure 5 shows the different positions of the single asperity in the process of contacting with the rough surface: case *a* corresponds to original position; case *b* corresponds to the touching at a point; and cases *c* and *d* correspond to the contact under the different loads.

Taking into account that $x^2 = t$, we have

$$V_{0i} = \pi a_c^2 \int_0^1 \Delta z_0(t)dt,\ V_{ri} = \pi a_c^2 \int_{\eta_i}^1 \Delta z_r(t)dt. \tag{52}$$

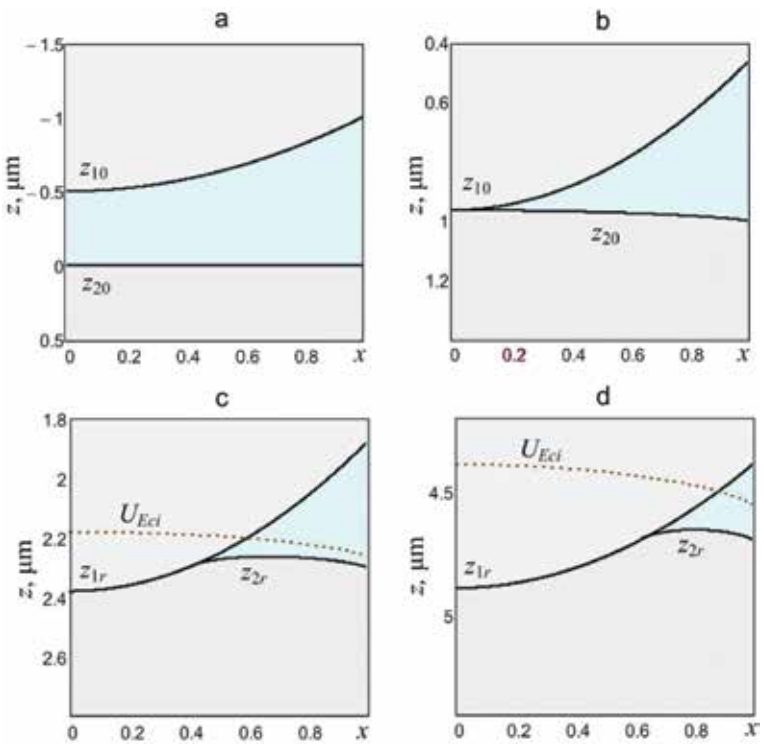

Figure 5. The scheme for contacting a single asperity located at level $u = 0.5$.

where $\Delta z_0 = z_{20} - z_{10}$ and $\Delta z_r = z_{2r} - z_{1r}$.

Since $\Lambda_i = \frac{V_i}{\pi a_c R_{\max}}$, after integrating (52), we have

$$\Lambda_{oi} = \omega\left\{\frac{1}{2} - \frac{\varepsilon - u}{\omega} - 2f_q\left[(k-1) - k\cdot{}_2F_1\left(-\frac{1}{2},\frac{1}{2};2;\frac{1}{k^2}\right) + {}_2F_1\left(-\frac{1}{2},\frac{1}{2};2;1\right)\right]\right\}. \tag{53}$$

$$\begin{aligned}\Lambda_{ri} =& \omega\left\{(1-\eta_i)\left[\frac{1+\eta_i}{2} - \frac{\varepsilon - u}{\omega} - 2f_q(k-1)\right] + 2f_q k\left[{}_2F_1\left(-\frac{1}{2},\frac{1}{2};2;\frac{1}{k^2}\right) - \right.\right.\\ &- \eta_i\,{}_2F_1\left(-\frac{1}{2},\frac{1}{2};2;\frac{\eta_i}{k^2}\right)\Big] - 2f_q\left[{}_2F_1\left(-\frac{1}{2},\frac{1}{2};2;1\right) - \eta_i\,{}_2F_1\left(-\frac{1}{2},\frac{1}{2};2;\eta_i\right)\right] + \\ &\left.\left. + 2f_{qi}\left[{}_2F_1\left(-\frac{1}{2},\frac{1}{2};\beta+2;\eta_i\right) - \eta_i^{0,5}\,{}_2F_1\left(-\frac{1}{2},\frac{1}{2};\beta+2;1\right)\right]\right\}.\end{aligned} \tag{54}$$

Substituting the equations obtained in Eq. (47), we determine the joint density $\Lambda(\varepsilon)$. To determine the dependence $\Lambda\left(f_q\right)$, it is necessary to exclude the parameter ε from the dependences $f_q(\varepsilon)$ and $\Lambda(\varepsilon)$.

Figure 6 shows the dependence of the gap density on the complex parameter f_q when two rough surfaces come into contact. **Figure 2** shows that the contact density does not depend on the parameters p and q, since the dependences for the different values of p and q.

4.1.3. The criteria for the appearance of plastic deformations

To determine the limits of using the above equations for metal surfaces, it is necessary to have a reliable criterion of plasticity. The closest coincidence with the experimental data on the indentation into elastic-plastic media was shown by the energy Mises' theory of shear strain and the theory of the maximum tangential stresses of Tresca. The difference between the two

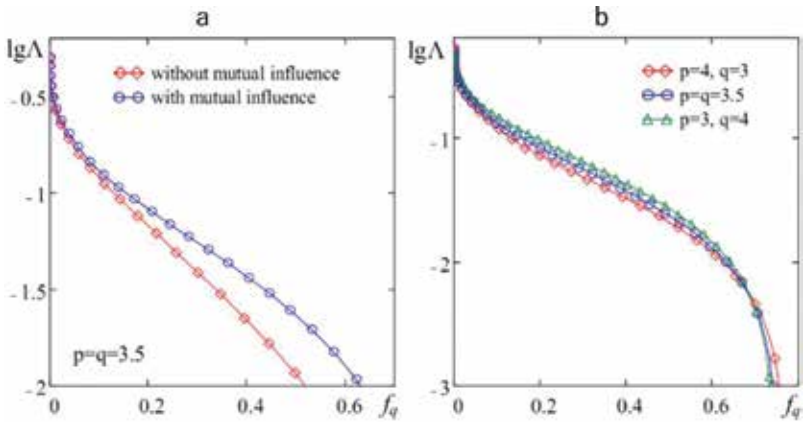

Figure 6. The gap density with/without taking into account the mutual influence of asperities (a) and for different values of p and q (b).

criteria is small; therefore, it is advisable to use the Tresca criterion because of its algebraic simplicity. The problem of determining the plasticity criterion for the considered loading scheme for a single asperity (**Figure 3**) was considered in [21]. In this case, the data of the effect of an axisymmetric load of the form Eq. (28) on the stress-strain state were taken into account. An important conclusion of [21] is the statement of stability of the values of the relative contact area η_{ip} for distributed at different heights asperities, at which plastic deformation begins. Thus, the value of η_{ip} for any asperity loaded according to **Figure 3** can be determined for the highest asperity at $u = 0$, $q_c = 0$, and $\beta = 0,5$.

By the Tresca criterion of the maximum tangential stresses, the plastic deformation on the z axis corresponds to the equivalent stress [22].

$$\sigma_{eq} = 2\tau_{1\max} = 0,62p_0 = \sigma_y. \tag{55}$$

The maximum contact pressure is defined as $p_0 = K_y\sigma_y$, where $K_y = 1,613$. The mean contact pressure is $p_m = K_y\sigma_y/(1+\beta)$.

Using Hertz's expressions for the radius of the contact area.

$$a_{ri} = \left(\frac{3P_i r}{4E^*}\right)^{\frac{1}{3}}, \tag{56}$$

and taking into account that.

$$P_i = \pi a_{ri}^2 p_m,\ r = \frac{a_c^2}{2\omega R_{\max}},\ \frac{a_{ri}^2}{a_c^2} = \eta_i,\ \frac{\sigma_y}{E^*} = \varepsilon_y, \tag{57}$$

We obtain the value of the criterion for the appearance of plastic strains in the near-surface layer

$$\eta_p^* = \left(\frac{3\pi K_y}{8(\beta+1)} f_y\right)^2, \tag{58}$$

where $f_y = \frac{\sigma_y a_c}{E^*\omega R_{\max}}$.

For the highest asperity $\eta_p^* = 1,605 f_y^2$. Thus, the proposed criterion of plasticity does not depend on loading conditions and this is its advantage.

Similarly, we define the criterion of occurrence of plastic deformation at the contact area. According to [23], the equivalent stresses at the center of the area are

$$\frac{\sigma_{eq}(0)}{p_m} = 0,2(1+\beta). \tag{59}$$

The highest value of the equivalent stress $\sigma_{eq}(1)$ is on the contour of the contact area, where it slightly exceeds $\sigma_{eq}(0)$ in the center of the loading area. It is convenient to represent

$\sigma_{eq}(1) = K_\sigma \cdot \sigma_{eq}(0)$, where for $\beta = 0,5$ according to the energy theory of shear strains $K_\sigma = 1,16$, according to the theory of maximal tangential stresses $K_\sigma = 1,33$.

At the moment of appearance of plastic deformation along the contour of the contact area $\sigma_{eq}(1) = \sigma_y$, and the average contact pressure.

$$p_m = \frac{5\sigma_y}{K_\sigma(1+\beta)}. \tag{60}$$

Then, similarly to the above reasoning, the criterion of the appearance of plastic deformations in the contact area is

$$\eta_p^{**} = \left(\frac{15\pi}{8K_\sigma(\beta+1)} f_y\right)^2. \tag{61}$$

For the highest asperity $\eta_p^{**} = 15,42K_\sigma^{-2} f_y^2$. According to the theory of maximum tangential stresses $\eta_p^{**} = 5,405\eta_p^*$, according to the energy theory of shear deformations $\eta_p^{**} = 7,105\eta_p^*$.

4.2. Elastic-plastic contact of rough surfaces

Contact characteristics for elastic-plastic contact will be considered taking into account the mutual influence of the contacting asperities. By analogy with the elastic contact, we assume that the mutual influence of the asperities is equivalent to the action of the additional load q_c (**Figure 3**). We use a discrete roughness model, described by Eqs. (15) and (16).

4.2.1. Relative contact area

According to Eq. (33), the load applied to a single asperity

$$\frac{P_i}{E^* R^2} = \frac{2}{k_\sigma \cdot k_n} \left(\frac{n}{e}\right)^n \varepsilon_y^{1-n} \left(\frac{a_{ri}}{R}\right)^{2+1.041n}. \tag{62}$$

Considering that for the roughness model used $R = a_c^2/(2\omega R_{\max})$ and $\eta_i = a_{ri}^2/a_c^2$, from Eq. (62) we have

$$\frac{q_{ci}}{E^*} = \frac{P_i}{E^* \cdot \pi a_c^2} = \frac{2}{k_\sigma \cdot k_n} \cdot \left(\frac{2\omega R_{\max}}{a_c}\right)^{1.041n} \left(\frac{n}{e}\right)^n \varepsilon_y^{1-n} \eta_i^{1+0.52n}. \tag{63}$$

For elastic-plastic contact, it is convenient to use the parameter $\overline{q}_\sigma = q_c/\sigma_y$, then from Eq. (63) we have

$$\overline{q}_{\sigma i} = \frac{q_{ci}}{\sigma_y} = C_a \cdot \eta_i^{1+0.52n}, \tag{64}$$

where

$$C_a = C_a(\varepsilon_y, n) = \frac{2}{k_\sigma \cdot k_n} \cdot \left(\frac{2\omega R_{\max}}{a_c}\right)^{1.041n} \left(\frac{n}{e \cdot \varepsilon_y}\right)^n. \tag{65}$$

By analogy with Eq. (25), taking into account Eq. (64), for an elastic-plastic contact, we have

$$\overline{q}_{\sigma i} = C_a \cdot \eta_i^{1+0.52n} + \overline{q}_\sigma \cdot \Psi_\eta(\eta_i). \tag{66}$$

In order to preserve the acceptability of the equations for elastic and elastic-plastic contacts, we use the relations.

$$f_q = \frac{q_c a_c}{E^* \omega R_{\max}} = \frac{q_c}{\sigma_y} \cdot \frac{\sigma_y}{E^*} \cdot \frac{a_c}{\omega R_{max}} = \overline{q}_\sigma \cdot f_y; f_y = \frac{\varepsilon_y a_c}{\omega R_{\max}}; f_{qi} = \overline{q}_{\sigma i} \cdot f_y. \tag{67}$$

Then Eq. (66) can be represented in the form

$$f_{qi} = C_a \cdot \eta_i^{1+0.52n} + f_q \cdot \Psi_\eta(\eta_i), \tag{68}$$

where $C_f = C_a \cdot f_y$, η_i is determined by Eq. (40).

Summing up f_{qi} over all asperities, we have

$$f_q(\varepsilon) = \frac{C_f \int_0^{\min(\varepsilon,\varepsilon_s)} \eta_i^{1+0.52n} \varphi_n'(u) du}{1 - \int_0^{\min(\varepsilon,\varepsilon_s)} \Psi_\eta(\eta_i) \varphi_n'(u) du}. \tag{69}$$

For a given value ε, we solve the system of transcendental Eqs. (40), (69) and obtain the dependence $f_q(\varepsilon)$.

Similarly, using Eq. (40) and $f_q(\varepsilon)$, we have

$$\eta(\varepsilon) = \int_0^{\min(\varepsilon,\varepsilon_s)} \eta_i\left(\varepsilon, f_q\right) \varphi_n'(u) du. \tag{70}$$

Excluding the parameter ε from Eqs. (69) and (70), we obtain the dependence $\eta\left(f_q\right)$ or $\eta(\overline{q}_\sigma)$.

Figures 7 and **8** present the dependencies of the relative contact area on the relative force parameter $\overline{q}_\sigma$.

4.2.2. Gaps density of the joint

The scheme of the action of the loads p_r and q_c is similar to the scheme for elastic contact (**Figure 3**).

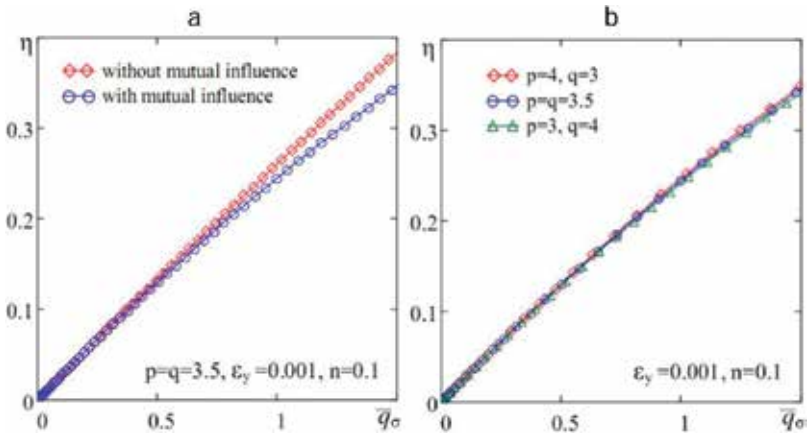

Figure 7. The relative contact area with/without taking into account the mutual influence of asperities (a) and for different values of p and q (b).

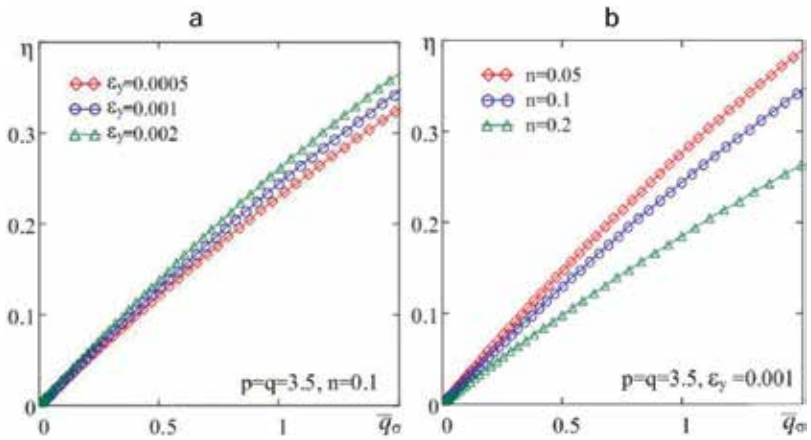

Figure 8. The relative contact area for different values of ε_y and n.

For an elastic-plastic contact

$$\overline{P}_i = \frac{P_i}{E^* R^2} \propto \left(\frac{h_i}{R}\right)^{0,5205n+1}, \tag{71}$$

therefore, the pressure distribution in the contact area described by [4]

$$p(r) = p_0\left(1 - \frac{r^2}{a^2}\right)^{\beta}, \tag{72}$$

where $p_0 = p_m(1+\beta)$ is pressure at $r = 0$, p_m is the mean pressure on contact area and $\beta = 0,5205n$.

Total density of gaps with elastic-plastic contact

$$\Lambda = \Lambda_e - \Lambda_p = \Lambda_{e0} + \Lambda_{er} - \Lambda_p, \tag{73}$$

where Λ_e is the density of gaps due to the elastic punching of the half-space, which accounted for single contacting and noncontacting asperities; Λ_p is reduction of the gap density due to the plastic displacement of the material into the interfacial space.

The value of Λ_e is determined, similarly to the elastic contact, by Eq. (47). In this case, f_{qi} is determined by Eq. (68) and the parameter β is used in Eq. (72).

Let us determine the volume of the displaced material for a single contacting asperity (**Figure 9**).

Let us assume that the unloaded crater has a constant radius R_{fi} and the unloaded depth from the level of the initial surface h_{fi}. The volume of plastically displaced material falling on a single crater is equal to the volume of a spherical segment of height h_f and radius R_{fi}:

$$V_{pi} = \pi h_{fi}^2 \left(R_{fi} - \frac{h_{fi}}{3} \right). \tag{74}$$

The total volume of the displaced material

$$V_p = n_c \int_0^{\min(\varepsilon,\varepsilon_s)} V_{pi} \varphi_n'(u) du. \tag{75}$$

Since $\Lambda_p = V_p/(A_c R_{\max})$, we have

$$\Lambda_p = \omega \int_0^{\min(\varepsilon,\varepsilon_s)} \left(\frac{\eta_i}{c^2} - \eta_i^{-0,5} f_{qi} K_{\beta 0} \right)^2 \left\{ 0,5 \left[1 - \eta_i^{-1,5} f_{qi} (K_{\beta 0} - K_{\beta c}) \right]^{-1} - \frac{(\omega R_{\max})^2}{3 a_c^2} \times \right.$$
$$\left. \times \left(\frac{\eta_i}{c^2} - \eta_i^{-0,5} f_{qi} K_{\beta 0} \right) \right\} \varphi_n'(u) du. \tag{76}$$

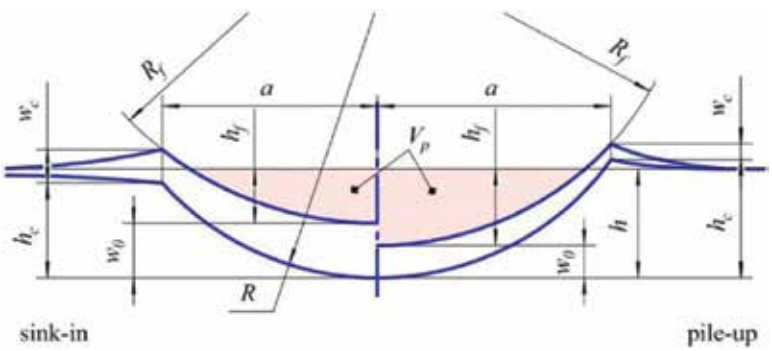

Figure 9. Scheme of the unloaded crater.

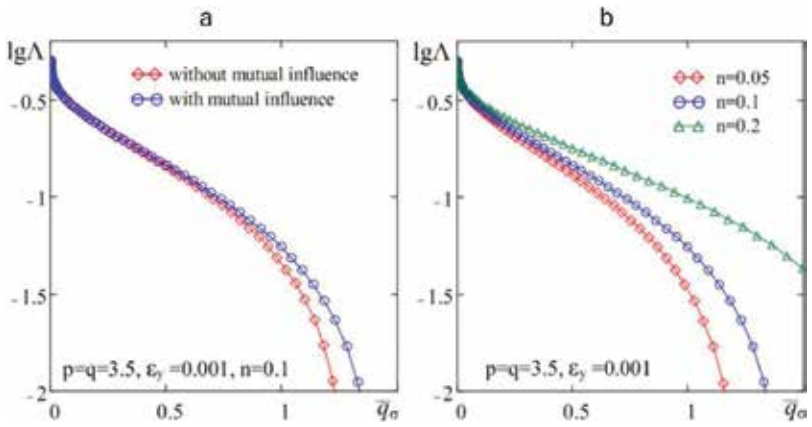

Figure 10. The gap density with/without taking into account the mutual influence of asperities (a) and for different values of p and q (b).

Substituting Eq. (76) into Eq. (73), we find the total gap density for elastic-plastic contact.

Figure 10 presents the dependencies of the gap density on the relative force parameter $\overline{q}_\sigma$.

5. Ensuring specified tightness

Ensuring specified tightness or leakage rate is related to the determination of the force parameters f_q or $\overline{q}_\sigma$. The sealing capacity of the SJ is evaluated by the permeability functional by Eq. (1). The contact characteristics—the relative contact area η and the gap density Λ, included in Eq. (1), are defined in the previous section. Included in Eq. (1), the probability v_k of the medium flowing through the SJ is determined by the fusion of contact spots and is given in Ref. [3]. Two adjacent asperities will merge if $\eta_i > 0.5$for each asperity.

Figure 11 shows the dependences for the elastic and elastic-plastic contacts.

The required permeability functional is determined by [3]

$$C_u^* = \frac{2l\mu G_l^*}{R_{\max}^3 \rho \Delta p}, \tag{77}$$

where G_l^* is the specified tightness; ρ is the density of the sealed medium; p_1 and p_2 are the inlet and outlet pressures; μ is the dynamic viscosity; $\Delta p = p_1 - p_2$; and l is the compacting band width.

The force parameters f_q or $\overline{q}_\sigma$, that providing a given level C_u^* are determined from the $C_u\left(f_q\right)$ or $C_u\left(\overline{q}_\sigma\right)$ (**Figure 11**).

http://dx.doi.org/10.5772/intechopen.72196

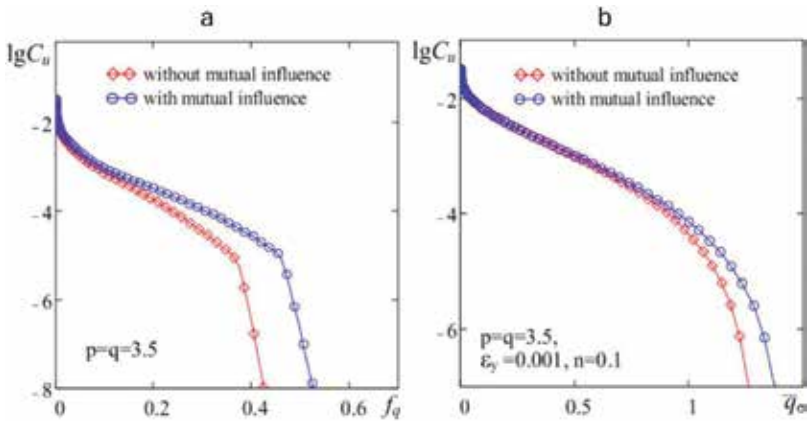

Figure 11. The dependences of the permeability functional for the elastic (a) and elastic-plastic (b) contacts.

6. Conclusion

Using the proposed model of roughness as a result of the studies, methods for determining the contact characteristics and the conditions for ensuring a specified tightness of the joints were developed and established:

1. Contact characteristics and the permeability functional are determined depending on the introduced dimensionless power parameters f_q for the elastic and $\overline{q}_\sigma$ for elastic-plastic contacts.
2. The relative contact area and the gap density for elastic contact do not depend on the values of the parameters of the bearing curve p and q. To a large extent, the mutual influence of asperities affects, and at $f_q > 0.47$, the determining factor affecting the permeability functional is the probability v_k of the medium flowing (**Figure 11**).
3. To describe the elastic-plastic contact, Mayer's law and the relation between the hardening exponent n and the Mayer index m were used.
4. In the case of elastic-plastic contact, the exponent of hardening n has a greater effect on the contact characteristics and to a lesser extent, the parameter ε_y and the mutual influence of the asperities. For the considered range of the parameter $\overline{q}_\sigma$, the fusion of the contact spots is insignificant.

Author details

Peter Ogar*, Sergey Belokobylsky and Denis Gorokhov

*Address all correspondence to: ogar@brstu.ru

Bratsk State University, Bratsk, Russia

References

[1] Greenwood JA, Williamson JBR. Contact of nominally flat sufaces. Proceedings of the Royal Society. 1966;**A295**:301-313

[2] Demkin NB. Contact of Rough Surfaces. Moscow: Nauka; 1970. p. 227

[3] Ogar PM, Sheremeta RN, Lkhanag D. The Tightness of the Metal-Polymeric Joints of Rough Surfaces. Bratsk: BrSU; 2006. p. 159

[4] Ogar PM, Gorokhov DB, Turchenko AV. Contact Mechanics of Rough Surfaces. Brstu: Bratsk; 2016. p. 282

[5] Golubev AI, Kondakov LA, editors. Handbook of Seals and Sealing Equipment. 2nd ed. Moscow: Mechanical Engineering; 1994. p. 448

[6] Goldade VA, Neverov AS, Pinchuk LS. Low-Modulus Composites Based on Thermoplastics. Minsk: Science and Technology; 1984. p. 231

[7] Bartenev GM, Lavrentiev VV. Friction and Wear of Polymers. Moscow: Chemistry; 1972. p. 240

[8] Goryacheva IG, Dobychin NM. Contact Problems in Tribology. Mechanical Engineering: Moscow; 1988. p. 256

[9] Goryacheva IG. Mechanics of Frictional Contact. Moscow: Nauka; 2001. p. 478

[10] Dolotov AM, Ogar PM, Chegodaev DE. Fundamentals of the Theory and Design of Seals Pneumohydraulic Valves of Flying Machines. Moscow: MAI; 2000. p. 296

[11] Ogar PM, Gorokhov DB, Elsukov VK. Elastic contact of a rigid rough surface with the low-modulus half-space. Systems. Methods. Technologies. 2017;**34**:7-12. DOI: 10.18324/2077-5415-2017-2-7-12

[12] Timoshenko SP, Goodyer J. Theory of Elasticity. Moscow: Nauka; 1979. p. 560

[13] Shtaerman IY. Contact Problem of the Theory of Elasticity. Moscow-Leningrad: Gostekhizdat; 1949. p. 270

[14] Ogar PM, Tarasov VA. Kinetic indentation application to determine contact characteristics of sphere and elastic-plastic half-space. Advances in Materials Research. 2013;**664**: 625-631

[15] Ogar PM, Gorokhov DB. Meyer law application for solving problems of surface plastic deformation by spherical indentation. Applied Mechanics and Materials. 2015;**788**:199-204

[16] Ogar P, Gorokhov D. Meyer law application to account of material hardening under rigid spherical indentation. In: Proceeding of 22nd international conference (MECHANIKA 2017). Kaunas: KUT; 19 May 2017. p. 287-290

[17] Ogar PM, Gorokhov DB. Parameters for elastic-plastic body to calculate contact characteristics under the sphere indentation, Systems. Methods. Technologies. 2016;**1**(29):28-32. DOI: 10.18324/2077-5415-2016-1-28-32

[18] Gaško M, Rosenberg G. Correlation between hardness and tensile properties in ultra-high strength dual phase steels – Short communication. Materials engineering - Materiálové inžinierstvo. 2011;**18**:155-159

[19] Kucharski S, Mroz Z. Indentation of plastic hardening parameters of metals from spherical indentation tests. Materials Science and Engineering. 2001;**A318**:65-76

[20] Hernot X, Bartier O, Bekouche Y, El Abdi R, Mauvoisin G. Influence of penetration depth and mechanical properties on contact radius determination for spherical indentation. International Journal of Solids and Structures. 2006;**43**:4136-4153

[21] Ogar PM, Tarasov VA, Turchenko AV. The criterion plasticity for individual asperity when contacting rigid rough surfaces with the half-space. Systems. Methods. Technologies. 2013; **2**(18):29-34

[22] Johnson KL. Contact Mechanics. Cambridge University Press; 1981. p. 452

[23] Ogar PM, Tarasov VA. Influence of the shape of an axisymmetric load on a stress-strain elastically plastic half-space. Systems. Methods. Technologies. 2010;**5**:14-20

Chapter 2

Experimental Studies of Nanometer-Scaled Single-Asperity Contacts with Metal Surfaces

Arnaud Caron

Additional information is available at the end of the chapter

http://dx.doi.org/10.5772/intechopen.72990

Abstract

The contact between two surfaces initiates at surface asperities whose properties determine the mechanical behavior of the contact. The response of a nanometer-scaled single asperity onto flat surfaces is experimentally accessible using atomic force microscopy (AFM). The high spatial and force resolution of atomic force microscopy and spectroscopy enables to determine the mechanisms governing plastic deformation, friction, and wear down to the atomic scale. In this chapter, we describe three experimental methods based on atomic force microscopy and corresponding methods for statistical data analysis to determine: the hardness and the deformation mechanisms of metallic surfaces during indentation with an AFM tip and the mechanisms governing wear and friction of metallic surfaces.

Keywords: friction, wear, nanotribology, hardness, metals, atomic force microscopy

1. Introduction

Contact mechanical testing methods are the oldest techniques to characterize the mechanical response of materials [1]. The hardness of a material describes its resistance to the penetration of a harder indenter and correlates to its strength. Similarly, scratch hardness testing has long been used to describe the response of a material to the relative motion of a harder indenter sliding at the velocity v and under the action of a load F_n, thus enabling the study of friction and wear. According to Bowden and Tabor, friction and wear of metals are mediated either by the formation and shearing of junctions between surface asperities leading to their de-bonding or the plowing of a surface by a harder asperity leading to debris formation (see, e.g., Ref. [2]).

With the development of atomic force microscopy (AFM), the investigation of friction and wear between a smooth surface and a single asperity has become possible. This has allowed bridging the gap between macroscale experiments and the underlying tribological mechanisms that typically take place at the nm scale. At low load, single-asperity sliding friction of

metals has been observed to be governed by the dragging of nanoscale metallic junction giving rise to atomic stick-slip [3, 4]. The effects of surface-assembled monolayer (SAM) and oxidation on the nanotribology of Au(111) have been investigated and compared to the sliding friction behavior of an Au(111) surface [5]. It was shown that the formation of an Au neck at the Au (111)/tip interface determines the nanotribology of gold. Further, the authors have shown how the formation of such a neck can be suppressed by SAM and how the friction response of a gold surface can be switched by applying an electrochemical potential. In Refs. [6, 7], friction between Au islands and graphite was studied. $AF_n^{2/3}$ dependence of the friction force on gold islands measured in ambient conditions was observed, where F_n is the normal force [6]. These contrasts with results in Refs. [3, 4], where almost no frictional energy dissipation was measured. In this load regime also, the authors recently showed how the shear strength of such junctions can be tuned by changing the metallurgical affinity between the contact materials [7]. Also, nanoscale wear experiments by AFM demonstrated the determinant role of plastic deformation mechanisms [8, 9]. AFM indentation has proven to be a capable experimental method to resolve the atomistic mechanisms of plastic deformation [10–14]. For example, this method has been applied to study single dislocation activation in KBr(100) single crystals [10], Cu(100) [11], and Au(111) [12–14]. There, atomistic plasticity events were observed in the shape of pop-ins, with lengths in the range of 1 Å. More recently, AFM indentation has been combined with noncontact AFM to quantitatively determine the hardness and the fundamental mechanisms of plastic deformation of Au(111) [14], and Pt(111), and Pt-based metallic glass surfaces [15].

In this chapter, we describe three experimental methods based on atomic force microscopy and corresponding methods for statistical data analysis to determine the hardness and the mechanisms governing wear and friction of metallic surfaces.

2. Experimental setups and materials

The contact mechanical methods described in this chapter all rely on atomic force microscopy. The results presented below were obtained with two different instruments operated in different environments, i.e., ambient air and ultrahigh vacuum. Measurements in ambient air were performed using an XE-100 AFM manufactured by Park Systems, Republic of Korea. Measurements in ultrahigh vacuum were performed with a VT-AFM manufactured by Omicron NanoTechnology GmbH, Germany. **Figure 1** shows the respective schematics for each experimental setup. In both cases, a microfabricated cantilever with a sharp tip at its end is used to probe interaction forces with a sample surface. Depending on the physical properties of the tip and of the sample surface, various interaction forces can be probed: van der Waals, electrostatic, magnetic, and short-range forces [16]. In both experimental setups, such forces are measured using an optical beam deflection system. Thereby, a laser beam is reflected at the end of the cantilever onto a photodiode that yields an output voltage in proportion to the cantilever deflection. Typically, a four-segment photodiode is used. This enables to measure both normal and lateral forces according to.

$$F_n = C_n S V_{AB} \text{ and } F_l = \frac{3}{2} C_l \frac{h}{L} S V_{CD} \tag{1}$$

where S is the sensitivity of the photodiode, which we assume to be isotropic; V_{AB} and V_{CD} are the sum voltages for the photodiode segments indicated in the subscripts; C_n and C_l are, respectively, the bending and torsion stiffnesses of the cantilever; h is the tip height; and L is the cantilever length.

The setups illustrated in **Figure 1** mostly differ in the arrangement of their piezoelectric scanners. For the measurements in UHV, a sample tube xyz-scanner was used to both scan the sample surface and control the height of the cantilever or the interaction force between tip and sample. In the setup used for measurements in ambient conditions, a linear xy nanopositioning stage was used to scan the sample surface, while a separate linear z-scanner was used to control the height of the cantilever or the interaction forces between tip and sample.

In this work, the cantilever stiffnesses were determined either according to the geometrical beam theory [17] or following the thermal noise analysis [18]. According to the geometrical beam theory, $C_n = \frac{Ewt^3}{4L^3}$ and $C_l = \frac{Gwt^3}{3h^2L}$, where E is Young's modulus, G is the shear modulus, w is the width of the cantilever, and t its thickness. The length and the width of the cantilever can be measured by means of optical or electron microscopy. The thickness is usually determined from the first bending resonance frequency of the cantilever f_0, with $t = \frac{2\sqrt{12}\pi}{1.875^2}\sqrt{\frac{\rho}{Ef0}}L^2$, where ρ is the mass density. Alternatively, the normal stiffness can be determined from the mean square

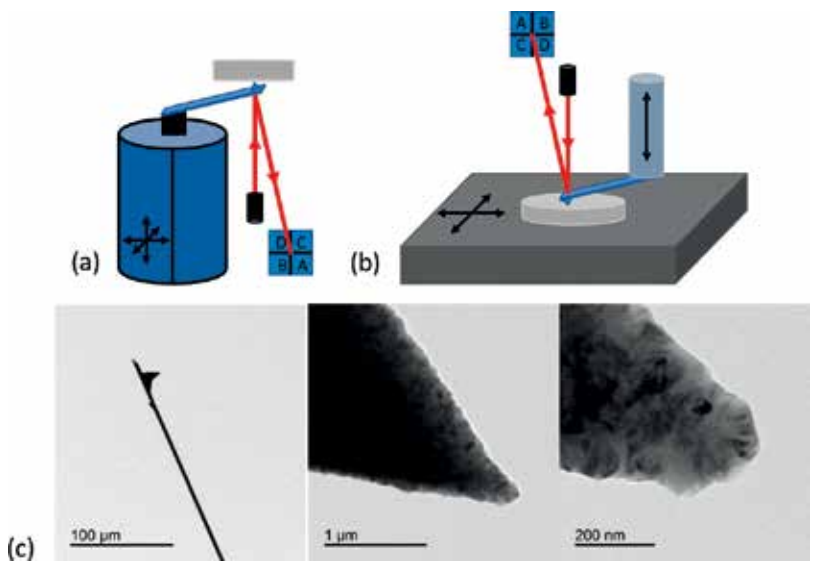

Figure 1. Experimental setups: instrumental setup used in (a) UHV and (b) ambient conditions; (c) TEM images of a typical diamond-coated Si single-crystalline AFM cantilever and its tip.

average of the thermal noise amplitude $\left\langle \overline{z^2} \right\rangle$ according to $C_n = \frac{k_B T}{\left\langle \overline{z^2} \right\rangle}$, where k_B is the Boltzmann constant and T the absolute temperature. The thermal noise vibrations of a cantilever beams can be recorded with the same optical beam deflection system as illustrated in **Figure 1**. The recorded signal consists in the superposition of all vibrational bending modes. It is important to note that the modes are not phase coherent. The identification of each mode is usually determined by fast Fourier transformation (FFT) of the time signal into a frequency spectrum (see **Figure 2**). In the case of the results shown in **Figure 2**, the power spectral density (PSD) function of the thermal noise amplitude was calculated by using the *pburg* function of the MATLAB software. The area below the spectra then corresponds to the mean square of the thermal noise.

Experimental records of the thermal noise are, however, limited by the bandwidth of the photoelectric detector. In our experimental setups, the bandwidth of the detector is 2 MHz. The detection of the thermal noise is, however, further limited by the electrical noise level of the photoelectric detector. This becomes critical for higher frequent modes and stiffer structure in which case the vibration amplitude may be below the noise level of the detector. In this project, the electrical noise background of the photodetector was measured independently by reflecting the laser beam onto the photoelectric detector from a smooth surface of a bulk sample of the same material as used to manufacture the measured microstructures. As shown in **Figure 2(c)**, only the first two vibration modes of the cantilever can be identified. To account for the difficulty of analysis of higher vibration modes, the thermal noise analysis is usually restricted to the first mode. In this case, Eq. (1) can be multiplied by a weight factor:

$$\frac{3}{16}\alpha_1^2\left(\frac{\sin\alpha_i + \sinh\alpha_i}{\sin\alpha_i \sinh\alpha_i}\right)^2 C_n \left\langle \overline{z_1^{*2}} \right\rangle = k_B T \tag{2}$$

where α_1 = 1.875 is the dimensionless wavenumber of the first bending vibration mode (see Ref. [18] for more details).

To determine the stiffness of the cantilever, it is thus of utmost importance to accurately calculate the mean square amplitude of the thermal noise vibrations. The fast Fourier transformation (FFT) methods, such as implemented in the *pburg* function, are usually applied to estimate the PSD function. Integrating the PSD function and using Eq. (2) to determine the cantilever stiffness from

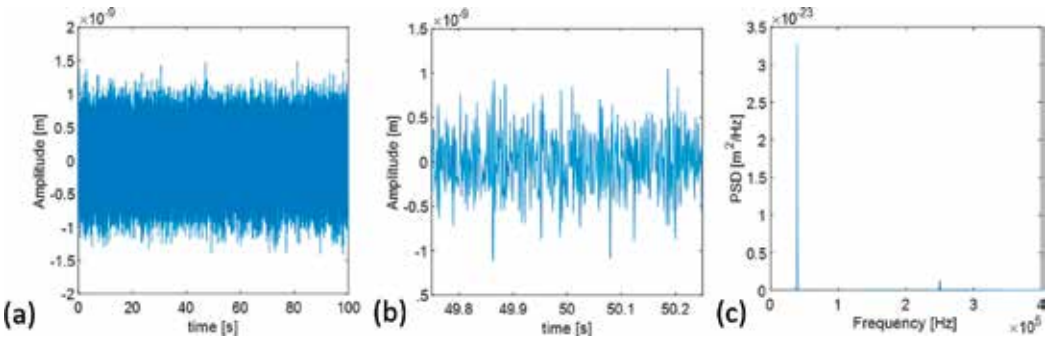

Figure 2. (a and b) Recorded time-dependent amplitude signals, (c) power spectral density (PSD) function of the signal shown in (a and b) and after background electrical noise removal.

the signals shown in **Figure 2** yield $\left\langle \overline{z_1^{*2}} \right\rangle = 4.32 \times 10^{-21}$ m^2 at $T = 293.15$ K and $C_n = 0.764$ N/m. Similarly, the first peak of the PSD function can be fitted with the response function for a simple harmonic oscillator (SHO):

$$R(f) = \frac{A_1 f_1^4}{\left(f^2 - f_1^2\right)^2 + \left(\frac{f f_1}{Q_1}\right)^2} \tag{3}$$

where f_1 and Q_1 are the resonance frequency and the quality factor of the first peak and A_1 gives the zero-frequency amplitude of the SHO response [19]. Integration of the SHO response function over all frequencies provides an estimate of the cantilever stiffness if one only considers the lowest resonance mode:

$$\int_0^\infty R(f)\mathrm{d}f = \frac{\pi A_1 f_1 Q_1}{2} = \left\langle \overline{z_1^{*2}} \right\rangle = \frac{16 k_B T}{3\alpha_1^2 C_n} \left(\frac{\sin\alpha_i \sinh\alpha_i}{\sin\alpha_i + \sinh\alpha_i} \right)^2 \tag{4}$$

Figure 3 shows the first peak of the PSD function and corresponds to fitting curve using Eq. (4) for the same measurement data plotted in **Figure 2**; we obtain $C_n = 0.814$ N/m.

Atomic force microscopy imaging can either be performed in intermittent contact (tapping) or noncontact modes [20]. A detailed description of AFM operation in intermittent and noncontact modes is given elsewhere (see, e.g., Ref. [20]). In noncontact AFM an AFM cantilever is excited to its resonance frequency. The distance between tip and surface is kept in the range of a few

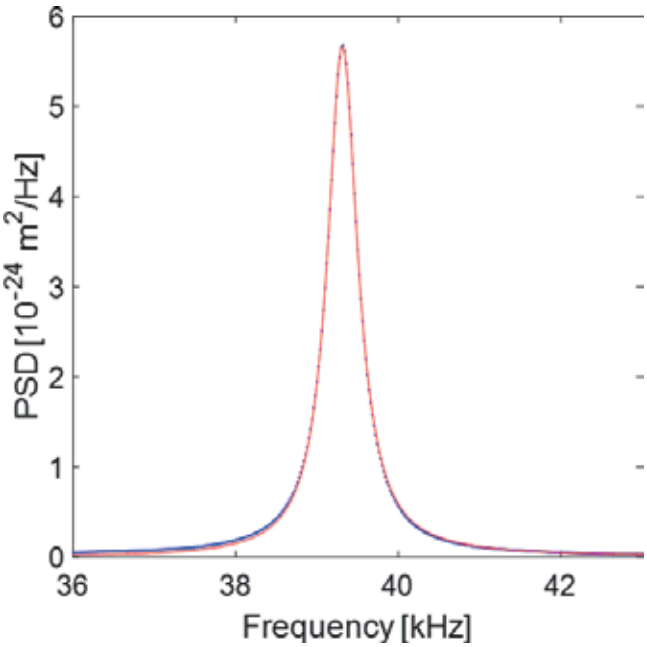

Figure 3. First peak of the PSD function shown in **Figure 2** and fitted with the response function for a simple harmonic oscillator.

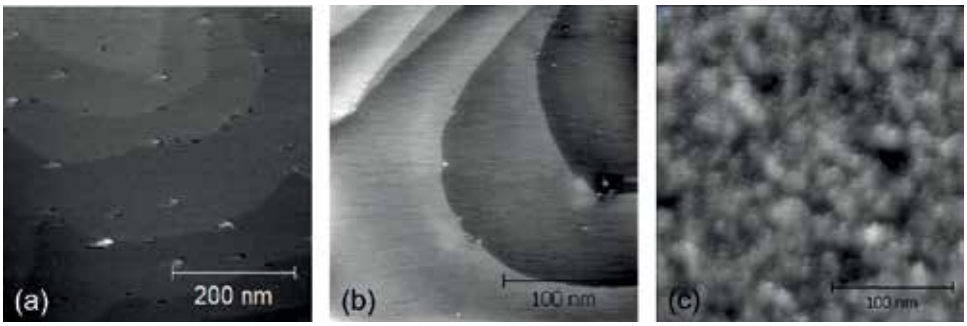

Figure 4. Topography images recorded by nc AFM on (a) Au(111), (b) Pt(111), and (c) $Pt_{57.5}Cu_{14.7}Ni_{5.3}P_{22.5}$ metallic glass surfaces.

nanometers. During scanning over a surface, changes in tip-sample distance due to sample topography result in changes in the amplitude and in a frequency shift of the cantilever resonance. To measure topography amplitude and/or frequency shift can be tracked by a feedback loop to keep the cantilever oscillation in resonance. Contact mode imaging relies on short-range interaction forces between the tip of a cantilever and the sample surface, the nature of which can be adhesive (attractive forces) or elastic (repulsive forces). During scanning, local changes in topography yield changes in the contact force between sample and surface. In this case, topography can be measured by tracking the normal contact force with a feedback loop to keep the contact force constant.

In this chapter, we present results obtained on single-crystalline metal and on metallic glass surfaces. An Au(111) polycrystalline thin film deposited on mica by physical vapor deposition was purchased by Phasis GmbH, Switzerland, and measured in ambient conditions (see Chapters III–V). Also, a Pt(111) surface and the surface of a $Pt_{57.5}Cu_{14.7}Ni_{5.3}P_{22.5}$ metallic glass were prepared for measurements in ultrahigh vacuum. The (111) surface of a platinum single crystal, purchased by MaTeck, Germany, was prepared by several cycles of Ar sputtering and annealing at 1000°C. This resulted in the formation of 50–100 nm wide atomically flat terraces. A $Pt_{57.5}Cu_{14.7}Ni_{5.3}P_{22.5}$ metallic glass master alloy was prepared according to [21] and subsequently melt-spun. The amorphousness of the as-prepared metallic glass ribbons was confirmed by X-ray diffraction (XRD) with Cu Kα radiation and differential scanning calorimetry (DSC). To remove its native oxide layer, the surface of an as-prepared metallic glass ribbon was prepared by gentle Ar sputtering for 5 min with an energy of 1 keV.

All three sample surfaces were imaged by noncontact (nc) AFM to determine their respective RMS roughness R_q (see **Figure 4**). For atomically flat Au(111) and Pt(111), we found $R_q = 0.407$ nm and 0.372 nm, respectively, caused by atomic steps between terraces and adsorbates in the case of Au(111). For the Ar-sputtered $Pt_{57.5}Cu_{14.7}Ni_{5.3}P_{22.5}$ metallic glass, we found $R_q = 0.375$ nm.

3. AFM indentation for quantitative hardness measurements

The nanometer-scaled plastic deformation of Au(111), Pt(111), and $Pt_{57.5}Cu_{14.7}Ni_{5.3}P_{22.5}$ metallic glass was investigated by AFM indentation and subsequent nc AFM imaging. For indentation and

imaging, diamond-coated silicon single-crystalline cantilevers were used (type CDT-NCLR, manufactured by NanoSensors, Switzerland). For the cantilever used on Au(111), the bending stiffness was found to be C_n = 55 N/m. For AFM indentation of Pt(111) and $Pt_{57.5}Cu_{14.7}Ni_{5.3}P_{22.5}$ metallic glass, a single cantilever of the same type as on Au(111) was used, whose normal stiffness was found to be C_n = 46 N/m.

Prior to the measurements on Au(111), the sensitivity S of the photodiode was calibrated by recording a force-distance curve on nanocrystalline diamond, consisting in an initial retraction of the z-scanner by 50 nm away from the sample surface and a subsequent series of approach and retraction by the same distance at a velocity of 0.3 μm/s. These parameters were set to avoid tip damages during contact between the diamond-coated tip and the nanocrystalline diamond sample. The sensitivity of the photodiode was then determined by fitting the repulsive part of the force-distance curve with a linear function. In contrast, before AFM indentation on Pt(111) and $Pt_{57.5}Cu_{14.7}Ni_{5.3}P_{22.5}$ metallic glass, the sensitivity of the photodiode is calibrated in the noncontact mode of AFM, according to Ref. [22]. Thereby, we considered a conversion factor for the vibration energy of the cantilever determined from the optically measured deflection [17].

AFM indentation measurements consisted in recording the cantilever deflection upon extension of the z-scanner of the AFM. Owing to the tilt angle of the cantilever about the sample surface, a tilt correction was applied by moving the lateral scanner by $Z \times \tan \varphi$ during a vertical scanner extension Z, where $\varphi = 13°$ is the tilt angle [23]. In this work the extension length Z of the z-scanner was varied from 10 to 160 nm in the case of Pt(111) and $Pt_{57.5}Cu_{14.7}Ni_{5.3}P_{22.5}$ metallic glass and was set to Z = 150 nm for Au(111).

The plastic deformation of the three samples was analyzed based on nc AFM topographical images of the remaining indents and on the force-penetration curves. Typical topographical images of indented surfaces are shown for Au(111), Pt(111), and $Pt_{57.5}Cu_{14.7}Ni_{5.3}P_{22.5}$ metallic glass in **Figure 5**. For each indent, the projected area was determined by masking the area with threshold height values. This analysis was performed with the indentation analysis function of the software package Gwyddion [24]. It is, however, important to note that due to convolution effects with the shape of the tip, the size of indents imaged by nc AFM is underestimated (this effect is more pronounced for smaller indents). Also, in the case of $Pt_{57.5}Cu_{14.7}Ni_{5.3}P_{22.5}$ metallic glass, the prominence of the pileups makes an accurate determination of the projected area more difficult and less accurate.

The force-penetration ($F_n - \delta$) curves were calculated from the recorded force-distance ($F_n - Z$) curves (see **Figure 6**). The principle of AFM indentation relies on the fact that the surface to be indented is softer than the AFM tip. In this case, an extension of the z-scanner leads, besides a deflection D of the cantilever, to a penetration of the AFM tip into the sample surface by the penetration depth $\delta = Z - D$.

Figure 6 shows a series of nc AFM images of Au(111), Pt(111), and $Pt_{57.5}Cu_{14.7}Ni_{5.3}P_{22.5}$ metallic glass surfaces after AFM indentation. In the case of Au(111), all indentations were performed with the same maximal load F_n = 7 μN and a same loading rate dF_n/dt = 16 μN/s. For Pt(111) and $Pt_{57.5}Cu_{14.7}Ni_{5.3}P_{22.5}$ metallic glass surfaces, indentation is shown that was performed with varying maximum normal force values between F_n = 0.8 μN and F_n = 6 μN.

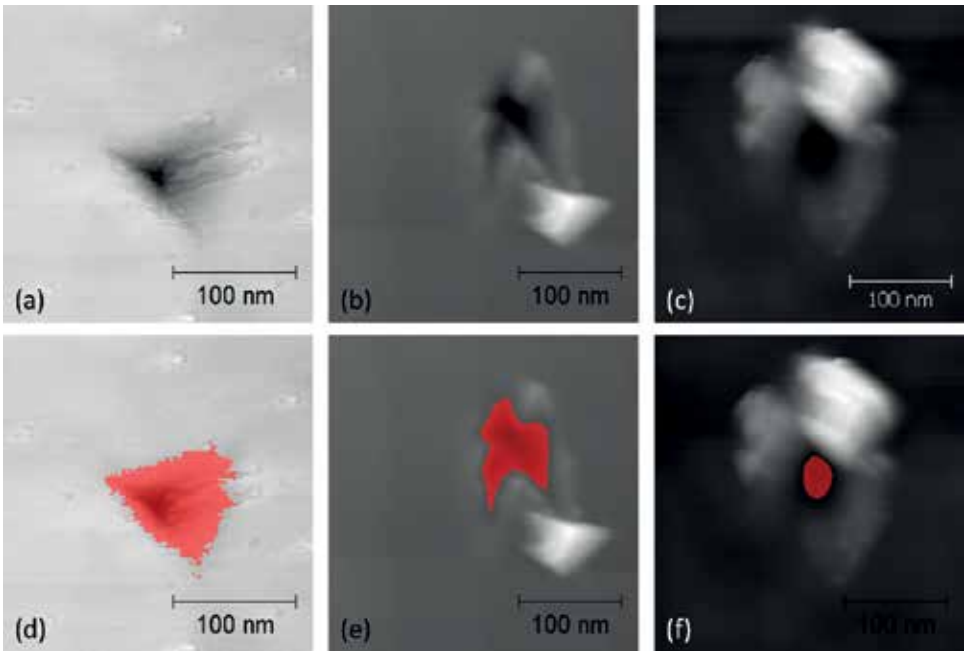

Figure 5. Nc AFM topography images of (a and d) Au(111), (b and e) Pt(111), and (c and f) $Pt_{57.5}Cu_{14.7}Ni_{5.3}P_{22.5}$ metallic glass surfaces after AFM indentation; in (d–f) the projected area was masked and calculated to determine the hardness values of each material.

For Au(111) two series of indentation measurements with the same maximum load values F_n = 7.2 μN but with different tips are shown. Within both series, the shape and size of the remaining indents are very similar. For Pt(111) and $Pt_{57.5}Cu_{14.7}Ni_{5.3}P_{22.5}$ metallic glass, remaining indents were only observed for maximum load values F_n > 0.8 μN. For these two materials, the projected area of the indents is observed to increase with the maximal load.

In the case of Au(111), almost no pileup can be observed. In this case, clear dislocation can be identified around indents. In the case of Pt(111), small pileups can be observed. More importantly, above an indentation load F_n = 3 μN, the indent exhibits a chevron-like shape that was never observed on the two other samples and which attribute to anisotropic elastic relaxation of Pt(111). The pileups around indents on $Pt_{57.5}Cu_{14.7}Ni_{5.3}P_{22.5}$ metallic glass are much more prominent than on Au(111) or Pt(111). This indicates that the plastic deformation of Au(111) and Pt(111) was accommodated over much longer distances than in the case of the metallic glass. This view is also supported by the observation of dislocation lines on Au(111) that extends hundreds of nanometers away from the indents. In the case of the $Pt_{57.5}Cu_{14.7}Ni_{5.3}P_{22.5}$ metallic glass, plastic flow appears to be closely confined around the indenting tip.

Figure 7 shows indentation curves recorded on Au(111), Pt(111), and $Pt_{57.5}Cu_{14.7}Ni_{5.3}P_{22.5}$ metallic glass. In the case of Au(111) and Pt(111), the force-penetration curves overlap with each other, demonstrating the good reproducibility of the method. For those two materials, also the indentation curves show clear pop-ins that are attributed to the activation of dislocations. For $Pt_{57.5}Cu_{14.7}Ni_{5.3}P_{22.5}$ metallic glass, the force-penetration curves do not show any of pop-in. In this case, the deformation appears to be continuous.

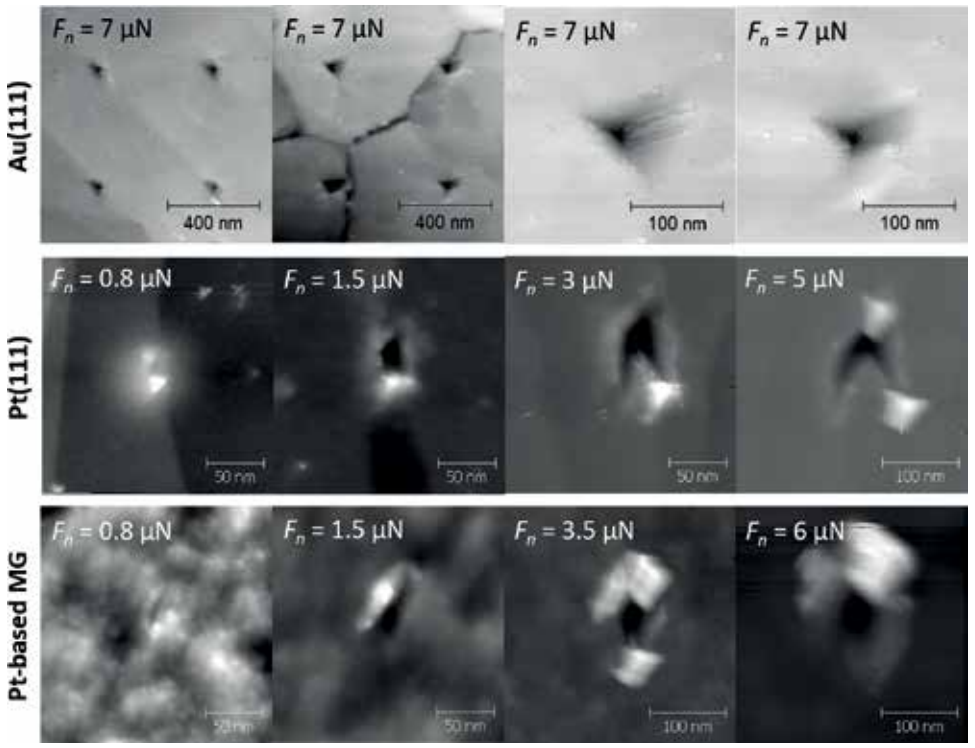

Figure 6. Nc AFM topography images after AFM indentation measurements with the indicated normal force on Au(111), Pt(111), and $Pt_{57.5}Cu_{14.7}Ni_{5.3}P_{22.5}$ metallic glass.

Figure 8 shows the load dependence of the projected area A_p for Pt(111) and $Pt_{57.5}Cu_{14.7}Ni_{5.3}P_{22.5}$ metallic glass. The projected area A_p of indents is found to be much smaller for $Pt_{57.5}Cu_{14.7}Ni_{5.3}P_{22.5}$ metallic glass than for Pt(111). Further, we used the load dependence of A_p to calculate the hardness of Pt(111) and $Pt_{57.5}Cu_{14.7}Ni_{5.3}P_{22.5}$ metallic glass, according to $dA_p/dF_n = 1/H$. For Pt(111), we obtained $H = 1.14 \pm 0.09$ GPa. For $Pt_{57.5}Cu_{14.7}Ni_{5.3}P_{22.5}$ metallic glass, we obtained $H = 7.3 \pm 2.4$ GPa. These values are larger than the measured ones by nanoindentation with a Berkovich diamond tip (see Ref. [15] for more details). This can be explained by tip convolution during nc AFM imaging that results in an underestimation of the projected area.

In the case of the indentation on Au(111), shown in **Figure 5**, we found $A_p = 4703.52$ nm^2, corresponding to $F_n = 7.2$ μN. Using the classical expression for the determination of hardness, we obtained $H = \frac{F_n}{A_p} = 1.53$ GPa. Alternatively, the shape of the AFM tip used to indent Au(111) was estimated from the noncontact AFM images shown in **Figure 6** with the free SPM data analysis software *Gwyddion* (**Figure 9**). The half-opening angle of the as-reconstructed indenter was determined to be $\alpha = 67.21°$. The hardness was then calculated according to $H = \frac{F_n}{3\sqrt{3}\tan^2\alpha(\delta_{max}-\delta_{el})^2} = 1.46$ GPa [25], where δ_{max} is the maximal penetration depth in **Figure 7(a)**, and δ_{el} was taken as the penetration depth at the first pop-in event in **Figure 7(c)**. Both hardness calculations deliver virtually the same value: $H_{Au(111)} = 1.5$ GPa.

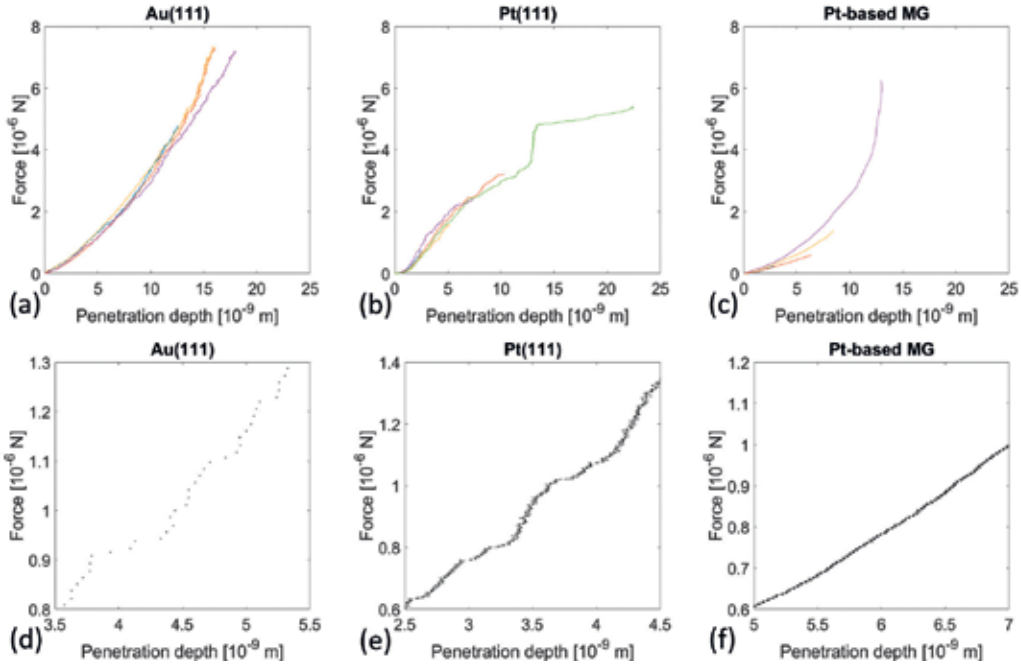

Figure 7. (a–c) Indentation curves and (d–e) magnification in the low load regime recorded on (a and d) Au(111), (b and e) Pt(111), and (c and f) $Pt_{57.5}Cu_{14.7}Ni_{5.3}P_{22.5}$ metallic glass.

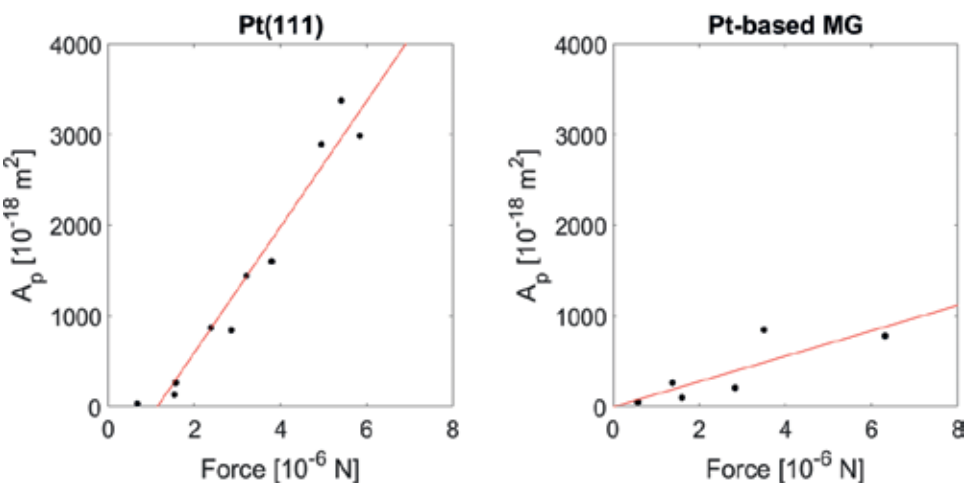

Figure 8. Indentation load dependence of the projected area A_p for (left) Pt(111) and (right) $Pt_{57.5}Cu_{14.7}Ni_{5.3}P_{22.5}$ metallic glass.

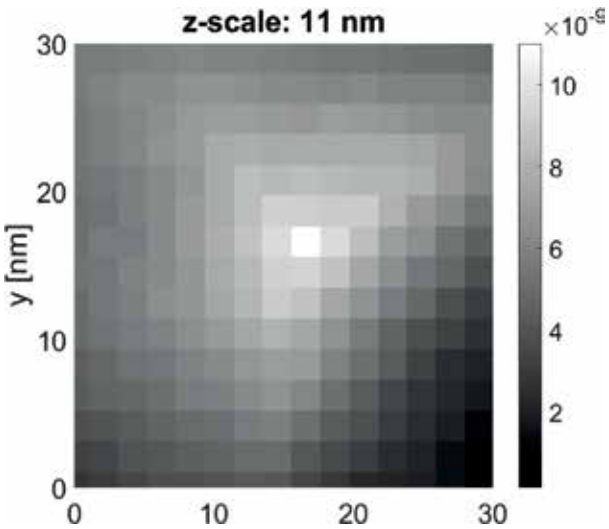

Figure 9. Estimated tip shape of the indenter used on Au(111).

4. AFM scratch test for friction and wear measurements

Wear and friction experiments were performed on Au(111) at room temperature and in ambient conditions (T = 293 K, RH = 40%) by friction force microscopy (FFM) [26] with diamond-coated silicon cantilever (CDT-NCLR, manufactured by NanoSensors, Switzerland). The normal and lateral stiffnesses of the cantilevers, C_n and C_l, were determined from the geometrical beam theory; for the cantilever used on Au(111), we found C_n = 50 N/m and C_l = 6954 N/m. The sensitivity of the photodiode S was obtained by recording a force-distance curve on a non-compliant surface and fitting its repulsive part with a linear function. The normal and lateral forces were calculated from the vertical and lateral voltages of the photodiode, V_n and V_l, according to $F_n = C_n S V_n$ and $F_l = \frac{3}{2} C_l \frac{h}{L} S V_l$.

Wear and friction measurements consisted in reciprocal sliding over the same area A_s = 2.5 × 2.5 μm^2 successively scanned over a load range F_n = 20–4600 nN. The topography and the lateral force were recorded during the forward and backward cantilever motion along the fast-scan direction (v = 10 μm/s). Amplitude-modulated noncontact AFM topography images of the area subjected to tribological testing were recorded before and after measurements and compared to extract the wear volume by integration. Topographical changes during tribological testing were analyzed by correlating successively recorded topography images with the initial topography image recorded at the lowest load (F_n = 20 nN). Thereby, we used the *corrcoeff* function of the MATLAB software package to extract a correlation factor R. The slopes of the $R(F_n)$-plot were further used to identify the transitions between wear mechanisms. Friction force images were calculated from the lateral force signals recorded in the forward and backward direction

according to $F_f = \frac{F_{l,fwd} - F_{l,bwd}}{2}$. In the case of Au(111), the probability distributions were calculated fitted with a Gaussian curve to provide the mean value and the standard deviation (see **Figure 10**). For the same ranges of normal force values as identified from the $R(F_n)$-plots, coefficients of friction (COF) were determined from the linear slopes $COF = \frac{dF_f}{dF_n}$.

Figure 11 shows topography and friction force images simultaneously recorded on Au(111). Plastic deformation was observed to start at a load value F_n = 129 nN as indicated by the occurrence of dislocation lines in the corresponding topography image. Increasing the load to F_n = 259 nN resulted in an increased number of dislocation. In this load range, surface

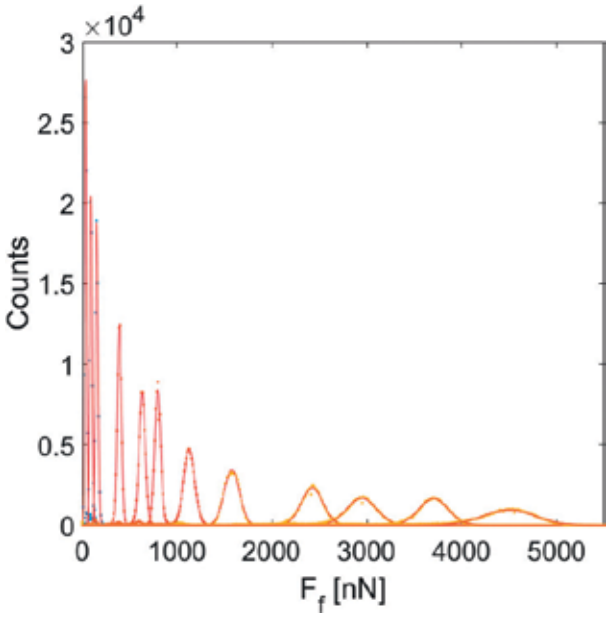

Figure 10. Probability distributions of friction force values measured at different normal force values. Each probability density distribution was fitted with a Gaussian function (red lines) to extract the mean friction force values and the corresponding standard deviation values.

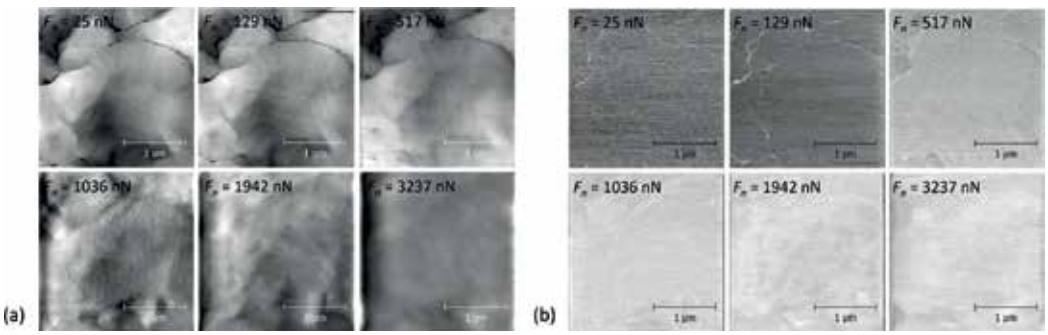

Figure 11. (a) Topography and (b) friction force images successively recorded on the same area of an Au(111) surface at the indicated loads.

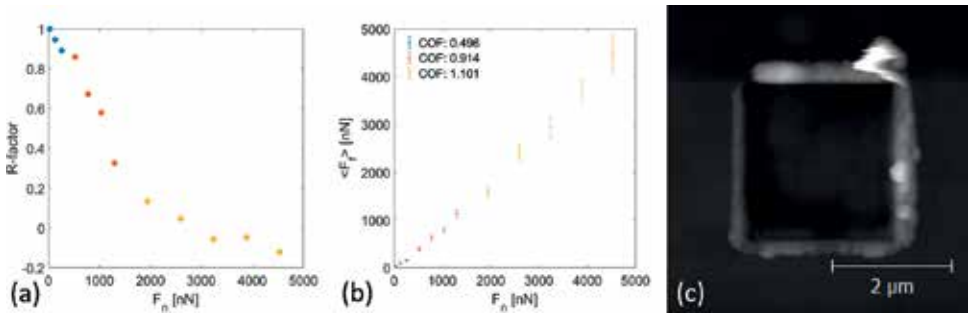

Figure 12. (a) Cross correlation factor R between the initial topography image in **Figure 11(a)** and the successive topography images recorded at the indicated load, (b) load dependence of friction, and (c) topography images of the area subjected to tribological tests (see **Figure 2(a)**).

topography features such as atomic steps remained clearly visible. This indicates in this load range that the sliding contact was rather governed by shearing and not plowing. In the load range F_n = 517–1295 nN, atomic steps were no longer observable, and a ripple structure was developed. In this load range, the mechanisms governing the sliding contact are considered to have a transition from shearing to plowing. In the range of the highest load values, F_n = 1942–4531 nN, pileups at the left and right side of the topography images became clearly observable. In this case, the governing mechanism was plowing. The three load ranges indicated above are illustrated in the $R(F_n)$-plot, each of them being characterized by a different slope of decrease with increasing normal load $\mathrm{P} = \frac{dR}{dF_n}$ (see **Figure 12(a)**).

Figure 11 also shows the friction force images corresponding to the topography measurements shown in the same figure. These images were further analyzed to determine the average friction force and its standard deviation (see above). **Figure 12(b)** shows the friction force F_f plotted against the normal force F_n. In the same figure, the error bars correspond to the standard deviation of the measurements. In agreement with the different load regimes determined in **Figure 12(a)**, the $F_f(F_n)$-plot can be divided into different load ranges which corresponds a coefficient of friction $COF = \frac{dF_f}{dF_n}$. **Figure 12(c)** shows a noncontact AFM topography image of the area tested by contact AFM shown in **Figure 11**. The scratched surface exhibits pileups at the edges of the area scanned in contact. The corresponding wear volume was determined by integration of the height signal using the MATLAB software package. We calculated a wear volume V_w = 0.0811 μm^3 corresponding to an average wear depth of δ_w = 13 nm.

5. Atomic-scale sliding friction measurements

Sliding friction experiments on Au(111) were performed in ambient conditions (T = 293 K, RH = 40%) by FFM with a soft gold-coated AFM cantilevers of the type CONTSC-Au (manufactured by NanoSensors, Switzerland).

Prior to friction experiments, the sensitivity of the AFM photodiode S was determined following the same methods as above. The bending and torsion stiffnesses C_n and C_l of the cantilever were determined by thermal noise analysis. The cantilever stiffnesses are listed in **Table 1**.

Cantilever type	C_n [N/m]	C_l [N/m]	L^* [mm]	R^{**} [nm]
CONTSC-Au	0.685	136.24	225	25

*Manufacturer's data.
**Estimated data from SEM measurements.

Table 1. Cantilever properties.

The friction experiments consisted in recording the lateral deflection signal of the AFM cantilever in both forward and backward directions of the x-scanner. The experiments consisted in scanning an area of 10×10 nm^2 with a normal load in the range F_n = 0–10 nN (**Figure 13**).

For each measurement, the friction force was calculated according to $F_f = \frac{F_{l,fwd} - F_{l,bwd}}{2}$, where $F_{l,fwd}$ and $F_{l,bwd}$ are the forward and backward images of the lateral force, respectively. Subsequently, the calculated friction force image was averaged line by line, and a corresponding error was calculated as the standard deviation from the mean value using the MATLAB software package. Moreover, the shear strength τ and the adhesion force F_{ad} were calculated by fitting the $F_f(F_n)$-plot with the function $F_f = \tau A_c(F_n)$, where we consider τ to be constant and $A_c(F_n)$ is the normal force-dependent real area of contact between surface and tip (see Ref. [27]). Based on the Johnson-Kendall-Roberts (JKR) theory, the real area of an adhesive contact between a spherical elastic body and the flat surface of an elastic body can be expressed as $A_c = \pi\left(\frac{R}{E^*}\right)^{2/3}\left[(F_n - F_{ad}) + 2F_{ad} + \sqrt{4F_{ad}(F_n - F_{ad}) + (2F_{ad})^2}\right]^{2/3}$, where F_{ad} is the adhesion force between the two elastic bodies [28], R is the radius of the spherical body, $E^* = \left[\frac{1-\nu_1^2}{E_1} + \frac{1-\nu_2^2}{E_2}\right]^{-1}$ is the reduced modulus of elasticity, and E_i and ν_i are Young's moduli and Poisson's ratios of the two elastic bodies involved in the contact [29]. The resulting $F_n^{2/3}$ dependence of the friction force has been experimentally verified in Refs. [6, 27]. The following values were used for Young's modulus and Poisson's ratio: E_{Au} = 75 GPa and ν_{Au} = 0.44.

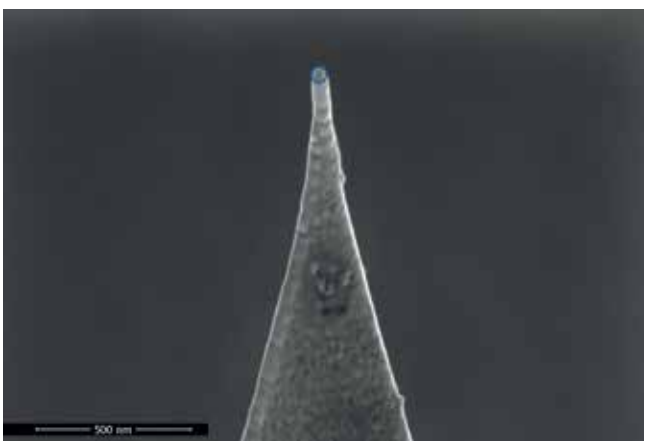

Figure 13. SEM image of the gold-coated AFM tip used friction measurements on Au(111).

In this work, the radius of curvature R of the AFM tip was determined by scanning electron microscopy (SEM) after the friction experiments (see **Figure 2** and **Table 1**) using a Helios 600i DualBeam FIB-SEM manufactured by FEI, Netherlands. A value $R \approx 25$ nm was found and used to fit the experimental $F_f(F_n)$-plots. In **Figure 2**, a circle with a radius of 25 nm is overlaid to demonstrate the validity of this value.

Atomic-scale stick-slip was observed and statistically analyzed. The analysis consisted in line-by-line calculation of the power spectral density (PSD) function of each recorded $F_{l,fwd}$ images using the *pburg* function of the MATLAB software package. The calculated PSD functions corresponding to each line were averaged to provide a single PSD function out of one $F_{l,fwd}$ image. This statistical analysis transforms a signal in real space into a one-dimensional reciprocal space (k-space) signal, from which characteristic wavelengths $\lambda = 2\pi/k$ can be identified.

Figure 14 shows the load dependence of friction on Au(111) with an Au-coated tip. For this tribological couple, a shear strength value $\tau = 24.21$ MPa and an adhesion force value $F_{ad} = 25.8$ nN were calculated. Also, **Figure 3** shows a typical FFM image and corresponding forward and backward traces that exhibit periodic atomic scale stick-slip. In the following, the averaged power spectrum density (PSD) functions of the friction signals recorded at different loads were evaluated (see **Figure 15**). The PSD function corresponding to a typical friction measurement on Au(111) with an Au-coated tip shows a peak at a wavenumber $k = 21.36$ rad/nm. Neither the position nor the amplitude of this peak was found to change upon increasing load, except for $F_n = 10$ nN, in which case two slightly less prominent peaks were observed at $k = 20.11$ rad/nm and $k = 22.62$ rad/nm (see **Figure 15**).

Correspondingly, a characteristic wavelength $\lambda_2 = 0.294$ nm was calculated that well matches with the interatomic distance of Au in the [110] direction ($a_{[110]} = 288$ pm). The small discrepancy arises from the numerical approximation of the PSD function. The peak in the PSD functions was also found to split into two equidistant peaks at $F_n = 10$ nN, with corresponding wavelength values $\lambda_3 = 0.277$ nm and $\lambda_1 = 0.312$ nm, respectively. These peaks may correspond to the herringbone reconstruction of the Au(111) surface and the resulting different tilt angles of the fcc and hcp domains with respect to the unreconstructed surface [30].

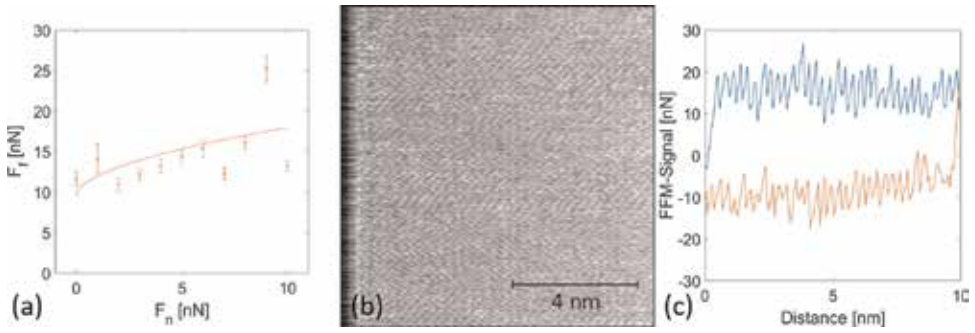

Figure 14. (a) Load dependence of friction and corresponding fit with a function of the type $F_f = \tau A_c(F_n)$, where τ is the shear strength and the real contact area A_c is expressed according to the JKR model [29]; (b) typical FFM image and (c) corresponding forward and backward traces exhibiting atomic scale stick-slip.

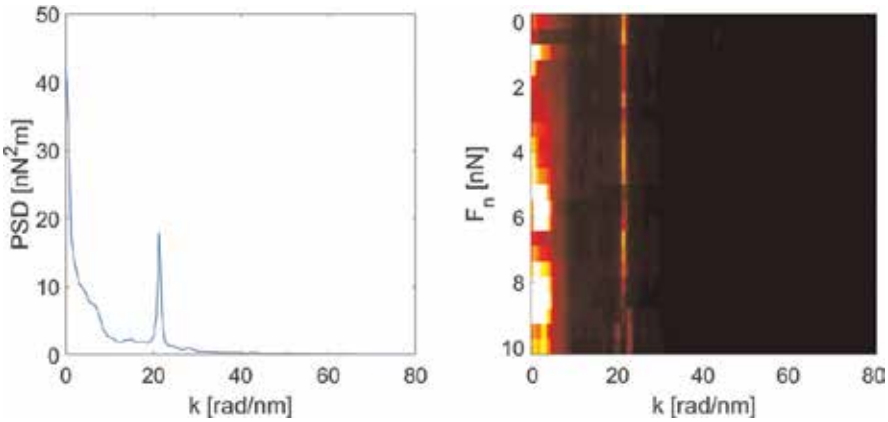

Figure 15. (Left) Typical power spectral density function calculated from FFM measurements on Au(111) with an Au-coated tip and (right) load dependence of the power density function as a function of the normal force F_n.

6. Conclusions

Experimental procedures based on atomic force microscopy to measure hardness, friction and wear, and the shear strength of metallic surfaces at the nanometer scale have been presented. AFM indentation was used to quantitatively and reproducibly determine the hardness and deformation mechanisms of Au(111), Pt(111), and a $Pt_{57.5}Cu_{14.7}Ni_{5.3}P_{22.5}$ metallic glass with unprecedented resolution in imaging and force curves. At the nanometer scale, the plastic deformation of single-crystalline metal surfaces is accommodated over large distances and mediated by dislocations. For $Pt_{57.5}Cu_{14.7}Ni_{5.3}P_{22.5}$ metallic glass, the nanometer-scaled plastic deformation is continuous and localized around the indenter; this contrasts with the observation of serrated flow at the μm scale.

AFM scratch testing was used to demonstrate the transitions between different wear regimes on Au(111) during single-asperity sliding contact. The coefficient of friction is found to increase with the severity of wear (from adhesive to abrasive). In the low load regime, wear is governed by adhesive effects, although in this regime the first dislocation lines could be observed. In the transitional regime, the formation of surface ripples was observed with the spacing between ripples increasing with the load. This regime corresponds to a transition from adhesive to abrasive wear, in which case materials start to be displaced ahead of the AFM tip. At larger loads, plowing is the governing mechanism. In this regime, the topography images are featureless, with exception of pileups at the side of the scanned area.

Atomic stick-slip images recorded on an Au(111) surface with a gold-coated tip were used to determine the shear strength of a metallic junction. By statistical analysis, we determined the periodicity of atomic stick-slip. Expectedly, it is found to correspond to the interatomic distance of gold.

Acknowledgements

The author is grateful to KOREATECH, Korea University of Technology and Education for the financial support. The author thanks Dr. M. Koch from Leibniz Institute for New Materials, Germany, for his help in providing TEM images of cantilevers.

Author details

Arnaud Caron

Address all correspondence to: arnaud.caron@koreatech.ac.kr

KoreaTech—Korea University of Technology and Education, Republic of Korea

References

[1] Tabor D. The Hardness of Metals. Oxford, UK: Oxford University Press; 1951

[2] Bowden FP, Tabor D. The Friction and Lubrication of Solids. Oxford, UK: Oxford University Press; 1950

[3] Gosvami NN, Filleter T, Egberts P, Bennewitz R. Microscopic friction studies on metal surfaces. Tribology Letters. 2010;**39**:19-24

[4] Gosvami NN, Feldmann M, Peguiron J, Moseler M, Schirmeisen A, Bennewitz R. Ageing of a microscopic sliding gold contact at low temperatures. Physical Review Letters. 2011; **107**:144303-1-144303-5

[5] Bennewitz R, Hausen F, Gosvami NN. Nanotribology of clean and modified gold surfaces. Journal of Materials Research. 2013;**28**:1279-1288

[6] Cihan E, Özogul A, Baykara MZ. Structure and nanotribology of thermally deposited gold nanoparticles on graphite. Applied Surface Science. 2015;**354**:429-436

[7] Ko HE, Kwan SG, Park HW, Caron A. Chemical effects on the sliding friction of Ag and Au(111). Friction. 2017. https://doi.org/10.1007/s40544-017-0167-5

[8] Caron A, Louzguine-Luzgin DV, Bennewitz R. Structure vs. chemistry: Friction and wear of Pt-based metallic surfaces. ACS Applied Materials & Interfaces. 2013;**5**:11341-11347

[9] Ko HE, Park HW, Jiang JZ, Caron A. Nanoscopic wear behavior of face centered cubic metals. (Submitted to Acta Materialia)

[10] Egberts P, Bennewitz R. Atomic scale nanoindentation: Detection and identification of single glide events in three dimensions by force microscopy. Nanotechnology. 2011; **22**(42):425703-1-425703-9

[11] Filleter T, Bennewitz R. Nanometer scale plasticity of Cu(100). Nanotechnology. 2007;**18**(4): 044004-1-044004-4

[12] Asenjo A, Jaafar M, Carrasco E, Rojo JM. Dislocation mechanisms in the first stage of plasticity of nanoindented Au(111) surfaces. Physical Review B. 2006;**73**(7):075431

[13] Paul W, Oliver D, Miyahara Y, Gruetter P. Minimum threshold for incipient plasticity in the atomic-scale nanoindentation of Au(111). Physical Review Letters. 2013;**110**(13): 135506

[14] Caron A. Quantitative hardness measurement by instrumented AFM-indentation. Journal of Visualized Experiments. 2016;**117**:e54706

[15] Caron A, Bennewitz R. Lower nanometer-scale size limit for the deformation of a metallic glass by shear transformations revealed by quantitative AFM indentation. Beilstein Journal of Nanotechnology. 2015;**6**:1721-1732

[16] Meyer E, Hug HJ, Bennewitz R. Scanning Probe Microscopy: The Lab on a Tip. Berlin, Heidelberg, Germany: Springer; 2004

[17] Nonnenmacher M, Greschner J, Wolter O, Kassing R. Journal of Vacuum Science and Technology B. 1991;**9**:1358

[18] Butt H-J, Jaschke M. Calculation of thermal noise in atomic force microscopy. Nanotechnology. 1995;**6**:1-7

[19] Cook SM, Schaeffer TE, Chynoweth KM, Wigton M, Simmonds RW, Lang KM. Practical implementation of dynamics methods for measuring atomic force microscope cantilever spring constants. Nanotechnology. 2006;**17**:2135-2145

[20] Voihtlaender B. Scanning Probe Microscopy: Atomic Force Microscopy and Scanning Tunneling Microscopy. Berlin, Heidelberg, Germany: Springer; 2015

[21] Schroers J, Johnson WL. Ductile bulk metallic glass. Physical Review Letters. 2004;**93**: 255506

[22] Giessibl FA. Direct method to calculate tip-sample forces from frequency shifts in frequency-modulation atomic force microscopy. J. Applied Physics Letters. 2001;**78**:123

[23] Cannara RJ, Brukman MJ, Carpick RW. Cantilever tilt compensation for variable-load atomic force microscopy. The Review of Scientific Instruments. 2005;**76**:053706

[24] http://www.gwyddion.net

[25] Fischer-Cripps A, Nanoindentation C. 2nd ed. Springer: New York; 2004

[26] Bennewitz R. Friction force microscopy. In: Gnecco E, Meyer E, editors. Fundamentals of Friction and Wear. Berlin, Heidelberg, Germany: Springer; 2007

[27] Meyer E, Luethi R, Howald R, Bammerlin M, Guggisberg M, Guentherodt H-J. Site-specific friction force spectroscopy. Journal of Vacuum Science and Technology B. 1996; **14**:1285-1288

[28] Johnson KL, Kendall K, Roberts AD. Proceedings of the Royal Society of London. Series A. 1971;**324**:301-313

[29] Johnson KL. Contact Mechanics. Cambridge, UK: Cambridge University Press; 1985

[30] Li Q, Dong Y, Martini A, Carpick RW. Atomic friction modulation on the reconstructed Au(111) surface. Tribology Letters. 2011;**43**:369-378

Chapter 3

Deformation Regimes for Sphere-Plane Contact: Revisiting Tabor's Criteria for Differential Hardness

Giuseppe Pintaude

Additional information is available at the end of the chapter

http://dx.doi.org/10.5772/intechopen.72642

Abstract

This chapter presents an update of theories involving the differential hardness problem, starting from the hypothesis made by Tabor for the contact between a sphere and a plane. In this way, the reader interested in problems affected directly by these formulations, such as contact area and contact fatigue, can take part of a fundamental theoretical basis to perform investigations in this field.

Keywords: differential hardness, sphere-plane contact, deformation regimes

1. Introduction

The contact mechanics, a branch of structural mechanics developed by the German physicist Heinrich Rudolf Hertz, describes the stresses and strains associated with a surface. His 1882 work, "Ueber die Berührung elastischer fester Körper" ("On the Contact Elastic Solid") is considered the starting point of this branch of science [1].

The solutions presented by Hertz do not involve friction; therefore, the bodies do not experience adhesion, and they are associated with purely elastic deformation field. The advancing in contact mechanics for modeling different deformation regimes depended on the development of computational simulation tools, especially the finite element method (FEM). In this sense, Mackerle [2] presented a summary on the use of FEM for indentation problems, a specificity of contact mechanics. In a period of 4 years, this author reported 187 references using FEM for a better understanding of indentation phenomena.

An immediate finding of this list of articles is that the contact stress distribution depends on the geometry of the bodies and the contact between a sphere and a plane is always the first approach for that, given the amount of engineering systems that can be associated with this kind of system. One of them is the hardness testing, wherein different scales are composed of this geometry, such as Brinell [3] and Rockwell B [4].

A very important aspect of the reliability of the hardness testing is to ensure that the plastic deformation occurs in the tested body, while only small deformations are allowed on the sphere. This warranty is given by the difference in hardness between the sphere and the tested body, which can be called differential hardness. Tabor [5] described an analytical estimate of what would be necessary for differential hardness. For that purpose, Tabor made use of some nontrivial simplifications, deserving to be detailed.

In this context, this book chapter intends to present an update of the theories involving the problem of differential hardness from the presentation of the assumptions made by Tabor to the initial problem, involving concepts of elasticity and plasticity. Thus, the tribology student interested in issues directly affected by these formulations, such as contact area calculation and contact fatigue, can find a fundamental theoretical basis for conducting investigations in this field of knowledge.

2. Differential hardness: Tabor's model

As the force applied during a hardness test is increased, the tested material passes to experience different regimes of deformation. Initially, Tabor [5] identified three regimes: elastic, elastic-plastic, and fully plastic. **Figure 1** shows these regimes schematically.

By measuring the hardness of a material, one should ensure that it is subject to full plasticity. Therefore, load values should be sufficient for the ratio between the mean contact pressure (which may be equivalent to the hardness (H)) and the material yield stress (Y) which exceeds a typical value. The relationship between the mean pressure and the yield stress is defined as the constraint factor (C (= H/Y)).

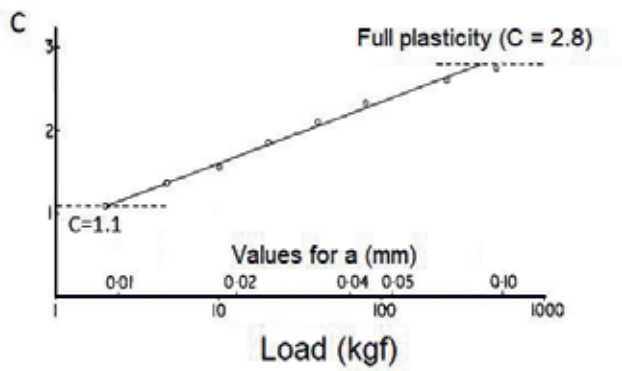

Figure 1. Deformation regimes under sphere-plane contact (Adapted from [5]).

http://dx.doi.org/10.5772/intechopen.72642

On the other hand, if the sphere cannot experience plasticity, the deformation seen by the ratio of the mean contact pressure and yield stress must be restricted to a certain value. Thus, using the values for C shown in **Figure 1**, Tabor [5] calculated the differential hardness required for a sphere as follows:

$$p_m \approx 2.8 Y_M \geq 1.1 Y_B . \therefore Y_M \geq 0.4 Y_B \quad (1)$$

where Y_M is the yield stress of metal and Y_B is the yield stress of sphere.

If the material hardness has equivalency to the yield stress, the sphere must be 2.5 times harder than the tested body. As an example, Tabor describes a sphere of quenched and tempered steel, with typically 900 HV; for this case, it could be used to test materials with a 400 HV maximum.

The next items will be devoted for detailing the values used by Tabor for each regime—beginning of elastic-plastic regime and full plasticity—and further advances in the literature, provided by the numerical simulation techniques.

3. Yielding inception

The imminence of plastic yielding shall be described with the use of a suitable criterion. The criteria commonly used for metals are Tresca and von Mises, which are equivalent only in few specific conditions. Regardless of these conditions, the result of applying both criteria indicates that a metal yields by the action of shear forces, which makes the maximum shear stress significant to know. In a sphere-plane contact, the resulting shear stress can be described considering a normalized distance (z/a), where "z" is the depth below the surface and "a" is the contact radius established by Hertzian analytical solution.

The analytical equations necessary for calculating the maximum shear stress in the sphere-plane contact will not be presented here, but it is known that these are dependent upon Poisson's ratio of the material (ν) [6]. To describe a single curve as shown in **Figure 2**, it is necessary to set a value for this property, in which Tabor used 0.3 as a convenient value for most metals.

The curve in **Figure 2** with ν = 0.3 has the maximum value for the ratio τ_{max}/p_m of 0.468, which is normalized to a defined depth. In applying Tresca's criterion, one obtains [7]

$$p_m = \frac{\tau_{max}}{\left(\tau_{max}/p_m\right)} = \frac{Y}{2.(0.468)} = 1.07Y \quad (2)$$

Therefore, a relationship between the mean pressure and the yield stress of 1.07 is obtained, and this value was rounded to 1.1, as presented by Tabor for the formulation of the differential hardness, according to Eq. (1). For a material not yielding in a sphere-plane contact, the value of the applied load must correspond to a mean pressure not exceeding this value (see **Figure 1**).

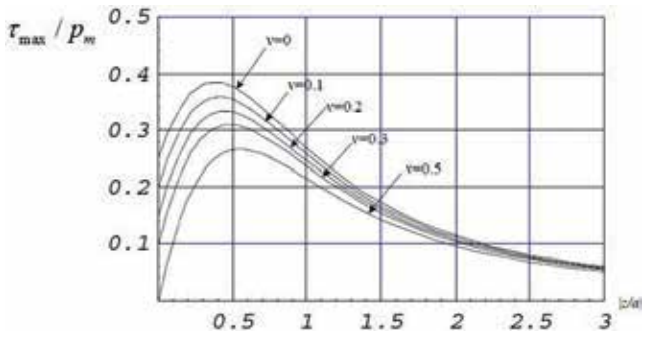

Figure 2. Distribution of normalized shear stress along normalized depth (z/a) under sphere-plane contact considering different values of Poisson's ratio (Adapted from [8]).

Changes in Poisson's ratio are sufficient to change both the magnitude of ratio τ_{max}/p_m and the location of this maximum value, as shown in **Figure 2**.

It is logical to expect that the relationship of Eq. (2) presents variations with ν. A series of equations have been proposed in the literature for that, having been summarized by Pintaude [9]. The author showed that five equations of the literature did not show great differences and that they can be divided into just two groups, in which some difference begins to be considered significant. This difference is associated with the given equivalence between the yield stress and the hardness, i.e., the constraint factor previously defined, which will be treated with utmost importance in the next section.

4. Full plasticity

The full plasticity regime associated with the contact between a sphere and a plane as defined by Tabor [5] presents no variations in the mean contact pressure; once this regime has been reached, this pressure has a defined value in relation to the yield stress of material. Tabor empirically found that the relationship between the hardness and the yield stress during a Brinell hardness test is 2.8; the value used by him to calculate the differential hardness ensures the plasticity of the material tested.

The use of a constant value to the constraint factor independent of system properties is a simplification in many ways, since a set of mechanical properties of materials dictates the behavior during the mechanical loading. Therefore, it is necessary to understand in a section, which occurs during this loading process, until the full plasticity is established for relatively large deformations/depths.

Figure 3 shows the definition of a plastic zone developed along an indentation process.

The contour of the plastic zone (c/a), shown in **Figure 3**, was modeled by Bishop et al. [11], which defines the limits of elastic-plastic deformation, being the same proportional to the ratio

http://dx.doi.org/10.5772/intechopen.72642

between the elastic modulus and the yield stress (E/Y). Thus, the same authors indicated that, by similarity, the constraint factor is also proportional to this ratio.

Since then, many models have been proposed to express the dependence of the factor C to the E/Y, and two currents are shown in **Figure 4** for a perfectly plastic material. One of them is due to Song and Komvopoulos (SK model) [12], in which Poisson's ratio is implicit into the value of E (one can consider ν as fixed), while Megalingam and Mayuram (model MM) [13] made this coefficient in its equation explicit. **Figure 4** compares the models for a fixed Poisson's ratio of 0.3.

It is found that SK and MM models differ more significantly for materials with relatively low values of E/Y and them approaching to 2.8 (used by Tabor) as E/Y increases.

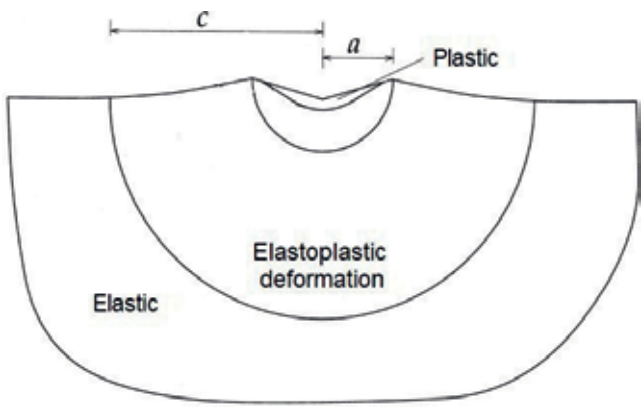

Figure 3. Plastic zone definition during an indentation process. Contours indicate the limits for deformation regimes (Adapted from [10]). Caption: a = contact radius and c = radius of plastically affected zone.

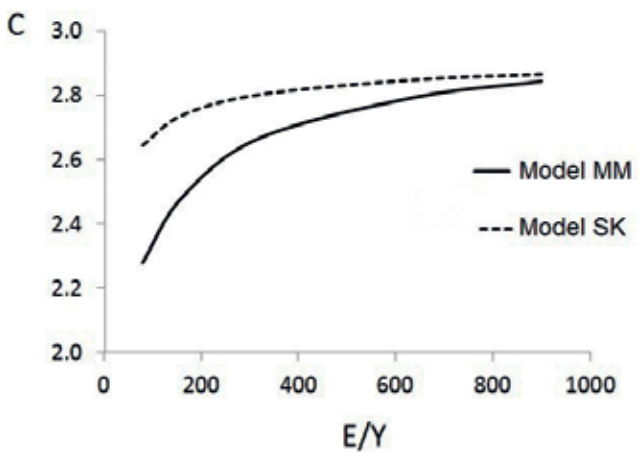

Figure 4. Variation of constraint factor with ratio E/Y following models SK [12] and MM [13], for a material with Poisson's ratio of 0.3.

The work-hardening effects could be added to the results of **Figure 4**, but before checking it is important to discuss the failure of **Figure 1** for describing the behavior of a material at high loads, which produce consequently large contact radii.

A pioneer investigation for comprehension of the full plasticity is due to Mesarovic and Fleck [14]. These authors defined two regimes for the full plasticity, finite deformation, and plastic similarity. The transition among them depends on the ratio E/Y, as previously demonstrated in **Figure 4**. A more detailed description can be seen in the work done by Alcalá and Esqué-de los Ojos [15]. For the current purpose, only a general description will be presented (**Figure 5**), for a perfectly plastic material ($n \rightarrow 0$) with specific properties.

In **Figure 5** it is possible to clearly observe the existence of three regions. Firstly, the C factor increases as the contact radius increases. This will happen up to a characteristic value, which depends on the ratio E/Y. The second region is one in which there is a drop in the C values, typical to simulate perfectly plastic materials, in which one would expect in fact a constant value. In [15] one can see that the plasticity theory applied to the simulation (deformation theory vs. flow plasticity theory) affects the description of this region (topic beyond the scope of this chapter). Finally, there is a third regime, in which the constraint factor backs to increase with increasing loading. This regime will be explained in detail further.

An effect that helps explain the fall in C factor with the a/D was demonstrated by Mesarovic and Fleck [14], verifying that there is lack of uniformity of the vertical speed at which the material experiences as the contact radius increases. In other words, this means that the friction between the sphere and the plane should be considered to provide a more realistic simulation.

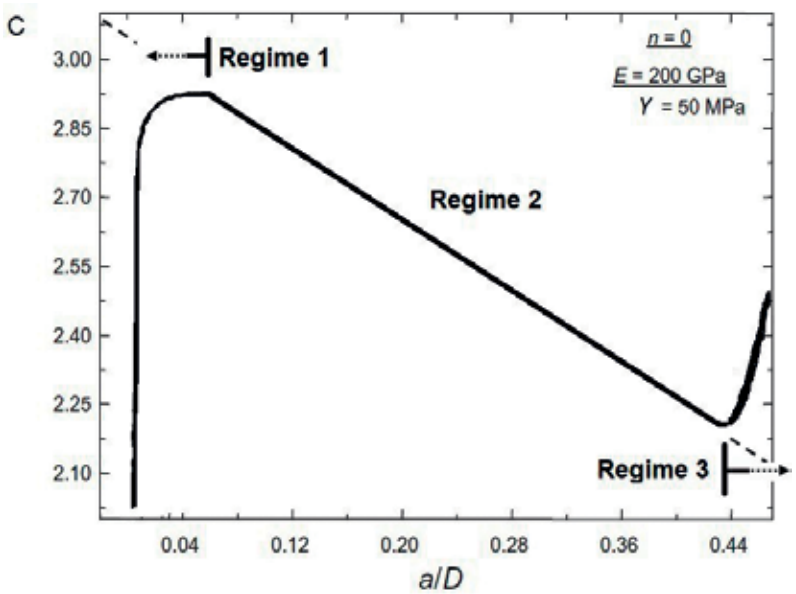

Figure 5. Variation of constraint factor with ratio a/D (Adapted from [15]).

http://dx.doi.org/10.5772/intechopen.72642

Alcalá and Esqué-de los Ojos [15] consider a friction coefficient value of 0.07 as ideal for property extraction from a spherical indentation test. The effect of friction described in [14] can be seen in **Figure 6**.

Moreover, Alcalá and Esqué-de los Ojos [15] commented on the difficulty of any experimental support existence to prove the decay in C. According to these authors, the reasons for this are related to the strain hardening, being:

i. Metals with low work-hardening exponent generally have sufficiently high yield stress, such that the increase occurring in C takes place within a broad range, which limits the occurrence of hardness drop with high values of a/R

ii. The frictional effects are significant enough to lower work-hardening exponent values, such that an increase in hardness occurs, while the decay is not observed.

While this experimental evidence is not presented, the simulation results generated a series of equations for region 2 of **Figure 5** (the decay). **Figure 7** shows a comparison among some of these equations, for the variation of C with a/R.

The last regime inserted into the full plasticity of a perfectly plastic material can be defined as a physical limit for the mechanical contact existence. This phenomenon can be treated as a "decoupling" of the contact. **Figure 8** helps to explain better the phenomenon.

Figure 8A shows the geometry of the sphere-plane contact, indicating a depth δ that varies in conjunction with the contact radius for a same radius R or diameter D. It is possible to relate the variation of the a/D ratio with δ/A by means of simple geometry, and this variation is shown in **Figure 8B** for a ball diameter with D = 3 mm. One can see that δ/a ≈ a/D for a certain

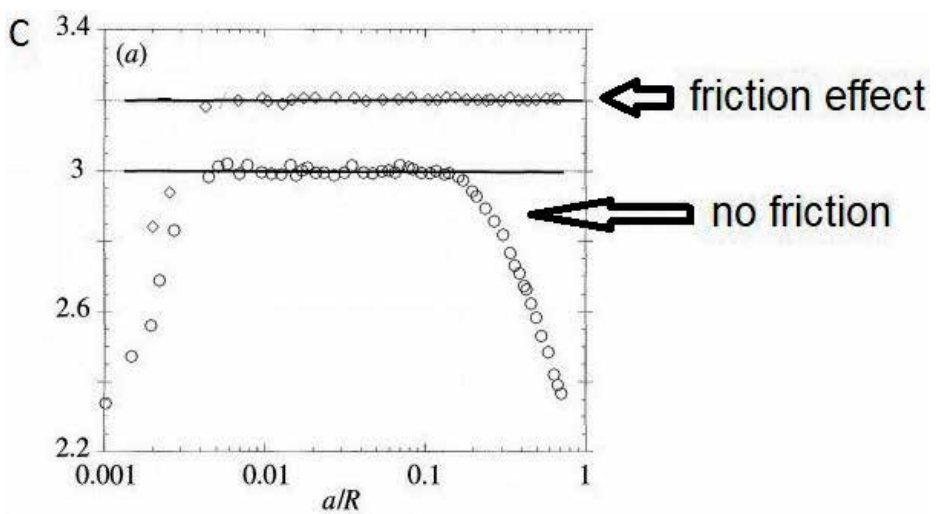

Figure 6. Variation of constraint factor with ratio a/R for a material with E/Y = 10,000 and Poisson's ratio of 0.3, with and without friction (Adapted from [14]).

value, there is a small deviation thereafter. Thus, increments above a certain value mean a geometric inconsistency, in which the ball cannot make a suitable contact with the plane in the axial direction of loading, representing a "decoupling" of the contact, which would entail artificially greater contact pressures (proportionally smaller radius values) as shown in **Figure 5**.

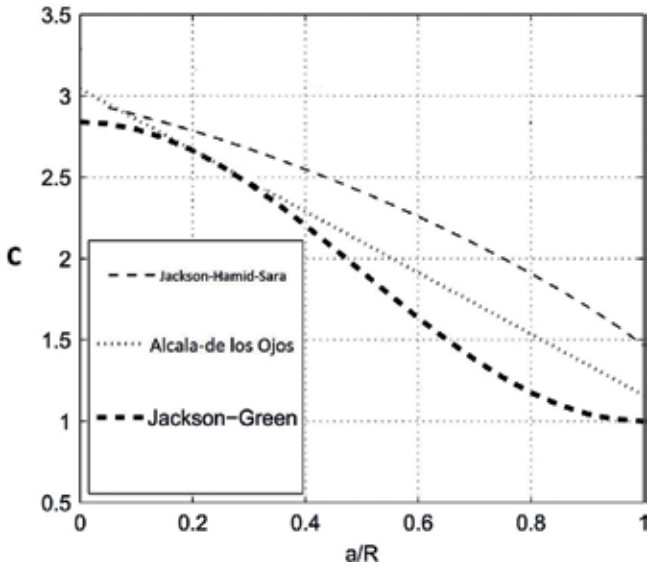

Figure 7. Equations to describe the finite deformation regime for a perfectly plastic material: Jackson-Green [16], Alcalá et al. [17], and Jackson et al. [18] (Adapted from [19]).

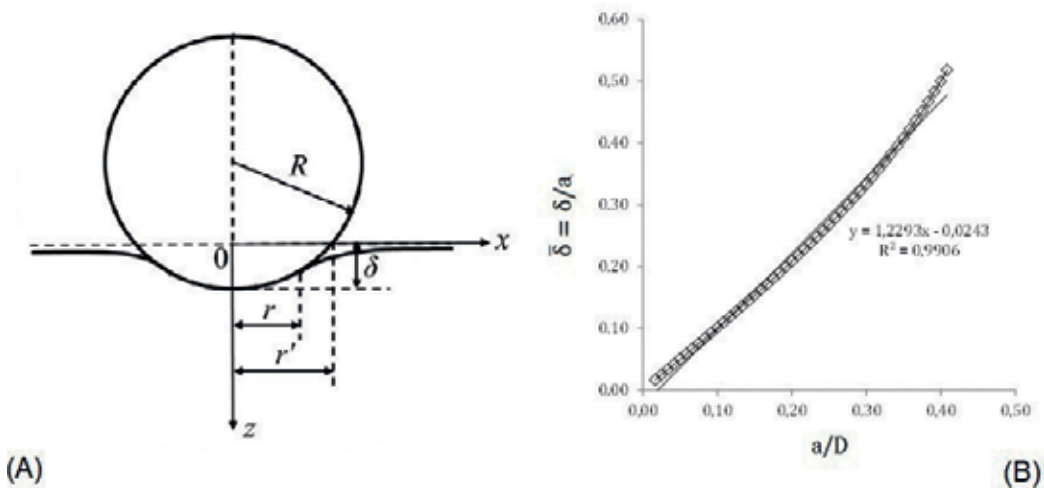

Figure 8. (A) Detailed geometry of sphere-plane contact and (B) variation of normalized depth with the normalized contact radius (Adapted from [12]).

http://dx.doi.org/10.5772/intechopen.72642

5. Hardening effects

The hardening of metals was incorporated into Tabor's concept, through work-hardening exponent (n). To the full plasticity regime, empirical equations can be derived to compute the effect of this property in the constraint factor. This type of relationship was shown, for example, by Matthews [20] and subsequently reviewed by Sundararajan and Tirupataiah [21], who demonstrated it for a wider range of experimental points.

Although these formulations may be useful from a practical point of view, here it is relevant to present in what deformation regime during the mechanical contact the work-hardening can alter the behavior. The example presented by Komvopoulos and Song [12] for a material with E/Y = 11 (**Figure 9**) makes it interesting for that.

It is noticed that the work-hardening exponent changes with great intensity of the C values in the full plasticity regime. Thus, the differential hardness value will be affected by the work hardening, as will be discussed in the next section.

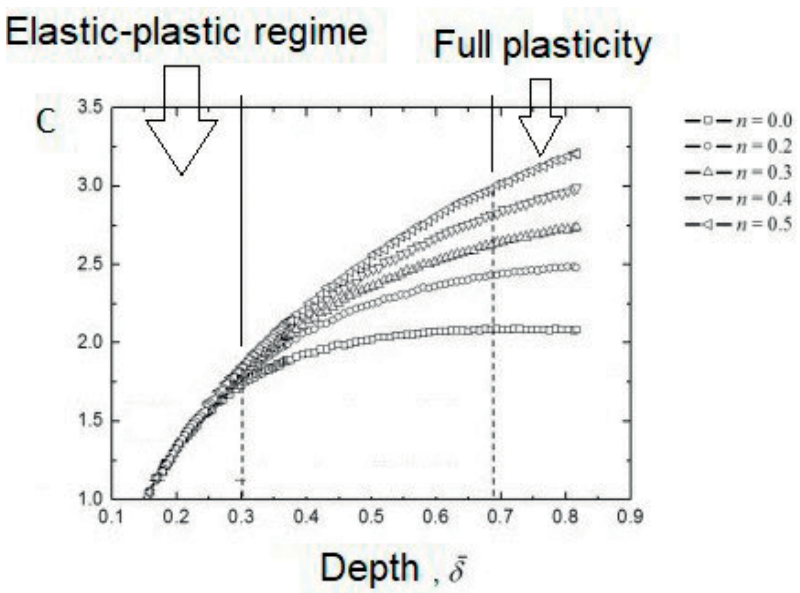

Figure 9. Variation of constraint factor with normalized depth for a material with E/Y = 11, for different work-hardening exponents (Adapted from [12]).

6. Experimental evaluation of differential hardness and trends in numerical simulation

An experiment to certify the existence of the differential hardness as predicted by Tabor is not a simple task. Jamari and Schipper [22] made an important attempt for that. These researchers used SiC as rigid plane, in which copper or aluminum balls were pressed against it.

Whereas deformation profiles plotted after the test, it was shown that the hardness difference for the case of Cu would be 1.33 and 1.39 for the case of Al, much lower than that established by Tabor (2.5).

Perhaps, for this reason, the results were the scenes of further discussion. Jackson and Green [23] criticized especially the method of measuring the deformation by profilometry after removal of the load and the effect of hardening. Jamari and Schipper [24] argued explaining the measuring method for the profile of spheres before the test and the approximation of the profile thereof after deformation. About hardening, they provided values showing the increasing of sphere hardness, which was relatively insignificant.

The experimental demonstrations for differential hardness remain scarce, especially for the boundary conditions given by Alcalá and Esqué-de los Ojos [15] in the abovementioned. These can be considered as inherent challenges to the contact mechanics in its present state of the art.

In this line, the work presented by Ghaednia et al. [19] sheds light to the theories discussed here, with a new numerical limit for the occurrence of differential hardness in the sphere-plane contact.

The first important question raised by these authors, also discussed by Jamari and Schipper [22], is the effect to consider if the load is being applied either on the plan or on the sphere. For that, Ghaednia et al. [19] make it clear what equation to adopt for each case, being adopted the Jackson-Green expression [16] for plane hardness and the Jackson et al. one [18] for the ball hardness.

From this, each equation is then used to calculate a stress ratio (Y*), equivalent to the differential hardness:

$$Y^* = {}^{Y_B}/_{Y_M} \tag{3}$$

By selecting different combinations of properties for sphere and plane, these authors got simulated for what value the constraint factor presents with no further changes, within the full plasticity regime for the plane. The found value for the differential hardness is equivalent to 1.7, 32% lower than that predicted by Tabor.

7. Conclusions and final remarks

The main contributions in the field of contact mechanics were demonstrated along this chapter applied for an important specific system, sphere-plane contact, in which several hardness tests are performed.

Clearly, there is a lack in the experimental demonstration of theories presented. This is an interesting challenge, as the numerical simulation increases at much higher speed than the experimental results.

An updated value obtained through numerical simulation for the differential hardness is 1.7, different from that predicted by Tabor (2.5). Certainly, an experimental demonstration could be elucidating this difference.

In addition, the hardening and friction effects on the sphere-plane system can be more explored through both numerical simulations and experimental arrangements.

Acknowledgements

The author thanks CNPq, through Project 312385/2014-5.

Nomenclature

a	Contact radius
c	Radius of plastically affected zone
C	Constraint factor
D	Sphere diameter
E	Elastic modulus
H	Hardness
n	Work-hardening exponent
p_M	Mean contact pressure
R	Sphere radius
Y	Yield stress
Y*	Ratio between yield stress of sphere and plane
Y_B	Yield stress of sphere
Y_M	Yield stress of metal
z	Depth from the surface
δ	Deflected depth
τ_{max}	Maximum shear stress
ν	Poisson's ratio

Author details

Giuseppe Pintaude

Address all correspondence to: giuseppepintaude@gmail.com

UTFPR – Federal University of Technology, Paraná, Brazil

References

[1] Hertz H. On the contact of elastic solids. Journal für die reine und angewandte Mathematik. 1881;**92**(156-171):110

[2] Mackerle J. Finite element and boundary element simulations of indentation problems: A bibliography (1997-2000). Finite Elements in Analysis and Design. 2001;**37**(10):811-819

[3] ASTM E10-15. Standard Test Method for Brinell Hardness of Metallic Materials. In: ASTM International. editor. West Conshohocken, PA: ASTM; 2015

[4] Song J, Ma L, Low SR. Finite-element modeling and experimental comparisons of the effects of deformable ball indenters on Rockwell B hardness tests. Journal of Testing and Evaluation. 2003;**31**(6):1-10

[5] Tabor D. The hardness of solids. Review of Physics in Technology. 1970;**1**(3):145-179

[6] Johnson KL, editor. Contact Mechanics. Cambridge: Cambridge University; 1985

[7] Shaw MC, de Salvo GJ. On the plastic flow beneath a blunt axisymmetric indenter. Journal of Manufacturing Science and Engineering. 1970;**92**(2):480-492

[8] Green I. Poisson ratio effects and critical values in spherical and cylindrical Hertzian contacts. International Journal of Applied Mechanics and Engineering. 2005;**10**(3):451-462

[9] Pintaude G. Analysis of spherical contact models for differential hardness as a function of Poisson's ratio. Journal of Tribology. 2015;**137**(4):044502

[10] Giannakopoulos AE, Suresh S. Determination of elastoplasctic properties by instrumented sharp indentation. Scripta Materialia. 1999;**40**(10):1191-1198

[11] Bishop RF, Hill R, Mott NF. The theory of indentation and hardness tests. The Proceedings of the Physical Society. 1945;**57**(3):147-159

[12] Song Z, Komvopoulos K. Elastic–plastic spherical indentation: Deformation regimes, evolution of plasticity, and hardening effect. Mechanics of Materials. 2013;**61**:91-100

[13] Megalingam A, Mayuram MM. A comprehensive elastic-plastic single-asperity contact model. Tribology Transactions. 2014;**57**(2):324-335

[14] Mesarovic SD, Fleck NA. Spherical indentation of elastic–plastic solids. Proceedings of the Royal Society of London. Series A. 1999;**455**:2707-2728

[15] Alcalá J, Esqué-de Los Ojos D. Reassessing spherical indentation: Contact regimes and mechanical property extractions. International Journal of Solids and Structures. 2010; **47**(20):2714-2732

[16] Jackson RL, Green I. A finite element study of elasto-plastic hemispherical contact against a rigid flat. Journal of Tribology. 2005;**127**(2):343-354

[17] Alcalá J, Barone AC, Anglada M. The influence of plastic hardening on surface deformation modes around Vickers and spherical indents. Acta Materialia. 2000;**48**(13):3451-3464

[18] Jackson RL, Ghaednia H, Pope S. A solution of rigid–perfectly plastic deep spherical indentation based on slip-line theory. Tribology Letters. 2015;**58**(3):1-7

[19] Ghaednia H, Pope S, Jackson RL. A comprehensive study of the elasto-plastic contact of a sphere and a flat. Tribology International. 2016;**93**:78-90

[20] Matthews JR. Indentation hardness and hot pressing. Acta Metallurgica. 1980;**28**(3):311-318

[21] Sundararajan G, Tirupataiah Y. The hardness-flow stress correlation in metallic materials. Bulletin of Materials Science. 1994;**17**(6):747-770

[22] Jamari J, Schipper DJ. Experimental investigation of fully plastic contact of a sphere against a hard flat. Journal of Tribology. 2006;**128**(2):230-235

[23] Jackson RL, Green I. Discussion: Experimental Investigation of Fully Plastic Contact of a Sphere Against a Hard Flat (Jamari J, Schipper DJ, 2006, ASME J Tribol, 128, pp. 230–235). Journal of Tribology. 2007;**129**(3):700

[24] Jamari J, Schipper DJ. Closure to Discussion of Experimental Investigation of Fully Plastic Contact of a Sphere Against a Hard Flat (2007, ASME J Tribol, 129, p. 700). Journal of Tribology. 2007;**129**(3):701

Chapter 4

Adaptive Mesh Refinement Strategy for the Semi-Analytical Solution of Frictionless Elastic Contact Problems

Victor Roda-Casanova and Francisco Sanchez-Marin

Additional information is available at the end of the chapter

http://dx.doi.org/10.5772/intechopen.72422

Abstract

Semi-analytical methods are commonly used to solve contact problems. These methods require the discretization of the domain into a mesh of pressure elements. In general, it can be said that their accuracy increases as the pressure element mesh is refined. However, the refinement of the pressure element mesh also implies an increase in their computational cost. So, in the great majority of the cases, a commitment between accuracy and computational cost must be achieved. In this work, a new approach is presented, whose main purpose is to improve the efficiency of the semi-analytical methods that are used to solve contact problems. To do so, an adaptive refinement of the pressure element mesh is implemented. This strategy allows for a reduction of the computational cost of the method, while its accuracy remains unaffected.

Keywords: contact analysis, semi-analytical methods, adaptive refinement

1. Introduction

The contact stress analysis plays an important role during the design process of several mechanical elements like bearings, gears, etc. In order to accomplish a contact analysis, the so-called contact problem must be solved to obtain the following relevant information:

i. The contact area, which involves the determination of the size, shape, and location of the true contact area in each one of the contacting bodies.

ii. The contact stresses, which involve the determination of the contact pressure distribution on the surface of the bodies and the stress distribution underneath the surfaces.

iii. The deformation of the bodies produced by the contact pressure.

Different approaches have been used to solve contact problems, which can be classified into three groups: numerical, analytical, and semi-analytical methods. Compared to the numerical methods, it can be said that the analytical methods are more efficient in terms of computational cost, but they have severe applicability limitations imposed by the hypotheses of the underlying theory. On the other hand, the numerical methods can overcome these limitations, but at a much higher computational cost.

The semi-analytical methods (SAMs) can be considered as an intermediate approach: they are potentially faster than the numerical methods, while they allow overcoming some of the limitations of the analytical methods. SAMs are usually based on the discretization of the potential contact area into a mesh of n pressure elements, with a uniform pressure distribution assumed to be acting over each one of them. Influence coefficients are used to relate the pressure applied over each pressure element with the displacements that this pressure produces at the centroid of the other elements of the mesh. Using these influence coefficients, the solution to the contact problem can be numerically found in terms of the contact pressure distribution that satisfies the contact conditions.

As usual, in numerical methods based on the discretization of the domain, the election of the number of pressure elements in which the domain is divided involves a commitment between accuracy and computational cost. Kalker [1] stated that the computational cost of these semi-analytical methods can be defined by the number of influence coefficients that need to be calculated to solve the contact problem (that, in general, is proportional to n^2). He also argued that the accuracy of the solution to the contact problem, in terms of contact area and contact pressure distribution, depends on the refinement of the pressure element mesh, especially in those regions close to the border of the contact area. Consequently, an improvement of the accuracy of the results necessarily implies an increment of the computational cost.

When both shape and location of the true contact area are known in advance, the efficiency of the method can be maximized by discretizing an area similar to the true contact area. But when the true contact area is unknown, it is difficult to optimize the efficiency of the method, since the whole potential contact area must be discretized to consider any possible shape and location of the true contact area. In those cases, it is common to use a uniform pressure element mesh for the whole domain, being more or less dense depending on the desired accuracy and on the capabilities of the computer used to solve the contact problem. In consequence, there could be many pressure elements in the discretization out of the true contact area, what causes a loss in the efficiency of the method.

These difficulties could be partially overcome using adaptive mesh refinement strategies. These techniques have been previously used to improve the efficiency of numerical methods based in the discretization of the domain, especially in FEM procedures [2]. However, no previous use of adaptive refinement has been found in the literature for the solution of contact problems using semi-analytical methods.

In this work, an approach to solve frictionless elastic contact problems is presented, whose main purpose is to improve the efficiency of the semi-analytical methods that are used to solve contact problems. To do so, an adaptive refinement of the pressure element mesh is implemented, which

http://dx.doi.org/10.5772/intechopen.72422

is based on the discrete rate of change of any magnitude that is related with the solution of the contact problem. This strategy allows for a reduction of the computational cost of the method, while its accuracy remains unaffected. The theoretical background and the computational implementation of the method are described, and its performance is illustrated with numerical examples.

2. Theoretical background

This section describes the theoretical background under which the proposed approach to solve frictionless elastic contact problems is developed. The concept of pressure element is described, as well as those considerations required to solve contact problems between bodies of finite dimensions. Finally, the quadtree decomposition of the domain is introduced, which is a useful strategy to perform adaptive mesh refinement.

2.1. Pressure elements and surface normal deflection in an elastic half-space

Consider a body that, because of its main features, can be approached to an elastic half-space, as the one shown in **Figure 1a**. A Cartesian coordinate system is defined over the surface of this body, which X and Y axes define a plane that is coincident with its surface, and the Z axis points inward him. A normal pressure distribution (p) is applied over the surface of the body, acting over an area that is denoted by S.

Now consider a generic point C within the area S, whose position is defined by the vector $\boldsymbol{r}'(x, y, z)$, being $z = 0$. Consider another point H in the surface of the body, whose position is defined by the vector $\boldsymbol{r}(x, y, z)$, being $z = 0$. The normal elastic deflection produced at a point H due to a normal pressure distribution applied over the area S can be determined by the superposition of the Boussinesq relation [3]:

$$\omega(\boldsymbol{r}) = \frac{1-\nu}{2\pi G}\int_S \frac{p(\boldsymbol{r}')}{|\boldsymbol{r}-\boldsymbol{r}'|}dS \tag{1}$$

where ν is the Poisson coefficient and G is the shear modulus of the material of the considered body.

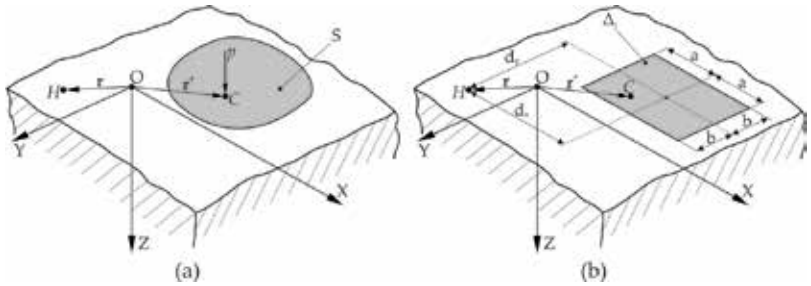

Figure 1. Pressure distributions applied over an elastic half-space.

Obtaining a generic closed-form solution for Eq. (1) is not possible, since it depends on the shape of the area S and on the considered pressure distribution. However, several closed-form solutions can be found in the literature for certain pressure distributions applied over areas with a specific shape (such as triangles, rectangles, hexagons, etc.).

Let's focus on the closed-form solution for Eq. (1) that Love [4] obtained for uniform pressure distributions acting over areas with rectangular shape, as the one shown in **Figure 1b**. From now on, this combination of shape and pressure distribution will be called pressure element, and will be denoted by Δ_j. The area of the pressure element shown in **Figure 1b** is $A_j = 2a \times 2b$, and the uniform pressure distribution that acts over this area is $p(\boldsymbol{r}') = p_j$. Under these conditions, the closed-form solution for Eq. (1) is

$$\omega(\boldsymbol{r}) = f_j(\boldsymbol{r}) \cdot p_j \tag{2}$$

where $f_j(\boldsymbol{r})$ is the influence coefficient of pressure element Δ_j over the point H, which can be analytically determined as

$$f_j(\boldsymbol{r}) = \frac{1-\nu}{2\pi G}\left\{ C \cdot ln\left[\frac{A+\sqrt{A^2+C^2}}{B+\sqrt{B^2+D^2}}\right] + A \cdot ln\left[\frac{C+\sqrt{A^2+C^2}}{D+\sqrt{A^2+D^2}}\right] + D \cdot ln\left[\frac{B+\sqrt{B^2+D^2}}{A+\sqrt{A^2+D^2}}\right] + B \cdot ln\left[\frac{D+\sqrt{B^2+D^2}}{C+\sqrt{B^2+C^2}}\right]\right\} \tag{3}$$

where coefficients A, B, C, and D are calculated as

$$A = d_y + b \quad C = d_x + a$$
$$B = d_y - b \quad D = d_x - a$$

These pressure elements can be useful to determine the normal displacement produced at the surface of a body due to a non-uniform pressure distribution applied over a complex area. To illustrate this methodology, consider a complex area S, as the one shown in **Figure 2a**, over which an arbitrary pressure distribution is acting. To determine the displacement field produced by this pressure distribution, the area S is discretized into a mesh of n rectangular pressure elements Δ_j, as shown in **Figure 2b**. Then, the arbitrary pressure distribution is approached by assigning a uniform pressure value p_j to each pressure element, as shown in **Figure 1c**.

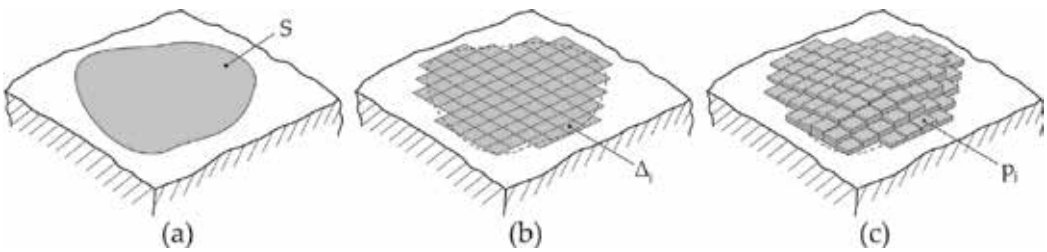

Figure 2. Normal deflection produced by a complex pressure distribution.

http://dx.doi.org/10.5772/intechopen.72422

Finally, the displacement at any point of the surface of the body can be determined by superposition of the displacements produced at this point by uniform pressures acting over each pressure element of the mesh as

$$\omega(\boldsymbol{r}) = \sum_{j=1}^{n} \left[p_j \cdot f_j(\boldsymbol{r}) \right] \tag{4}$$

This methodology can be applied with different types of pressure elements, having different shapes and pressure distributions acting over them. However, using rectangular pressure elements has some advantages, which are discussed in [5].

2.2. Semi-analytical method to solve frictionless elastic contact problems

The solutions exposed in the previous section can be used to obtain the pressure distribution that is produced when two bodies are pressed together in the absence of friction. For such a purpose, it is necessary that the two bodies can be approached to elastic half-spaces in the vicinity of the area in which the contact between them is produced.

Consider two bodies 1 and 2 in its undeformed contact position, contacting at the initial point of contact O_L (**Figure 3a**). At this point, a common tangent plane Π is defined, which is assumed to be so close to the surface of the bodies in the vicinity of the contact area that the deformation of the surfaces of both bodies can be referred to it in the linear small strain theory of elasticity.

A Cartesian coordinate system is defined with origin at point O_L, being the local axis Z_L normal to the plane Π and pointing inward the body 2. Consider a generic point Q in the plane Π, whose position is defined by the vector $\boldsymbol{r}(x_L, y_L, z_L)$, being $z_L = 0$. The gap between the two bodies, measured along Z_L axis, is denoted by the function $\mathrm{B}(\boldsymbol{r})$, which in the first instance is assumed to be smooth and continuous.

The two bodies are pressed together in the absence of friction by the effect of the force F_T (**Figure 3b**), causing a normal approach between them that is denoted by δ. Since penetration is physically inadmissible, a contact pressure distribution $p(\boldsymbol{r})$ is generated in the true contact area S that deforms the contacting bodies. In this way, elastic normal deflections are produced

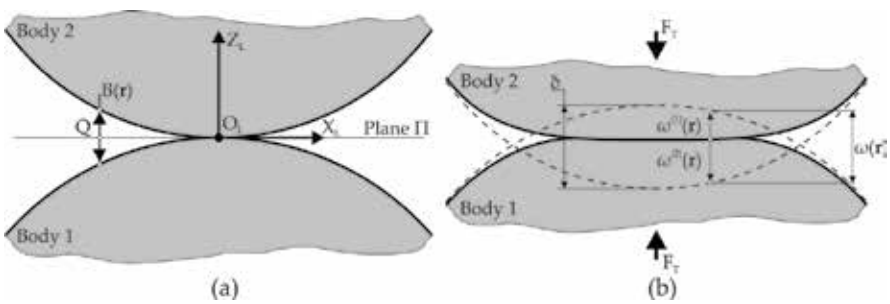

Figure 3. Contact between two bodies: (a) undeformed position and (b) deformed position.

in the surfaces of the bodies 1 and 2, which are denoted by $\omega^{(1)}(\boldsymbol{r})$ and $\omega^{(2)}(\boldsymbol{r})$, respectively. The total normal deflection is denoted by $\omega(\boldsymbol{r})$ and can be calculated as

$$\omega(\boldsymbol{r}) = \omega^{(1)}(\boldsymbol{r}) + \omega^{(2)}(\boldsymbol{r}) \tag{5}$$

The essence of the resulting contact problem is to determine the pressure distribution that fulfills the contact conditions, both inside and outside the contact area, whose geometry and size are unknown

$$\begin{array}{llll} p(\boldsymbol{r}) > 0 & \text{and} & B(\boldsymbol{r}) + \omega(\boldsymbol{r}) - \delta = 0 & \text{inside} \quad S \\ p(\boldsymbol{r}) = 0 & \text{and} & B(\boldsymbol{r}) + \omega(\boldsymbol{r}) - \delta > 0 & \text{outside} \quad S \end{array} \tag{6}$$

Kalker [5] demonstrated that the solution to this contact problem can be found minimizing the total complementary energy (V^*) under the condition that the contact pressure is equal or greater than zero in all the domain of the problem. The total complementary energy is defined as the sum of the internal complementary energy of the stressed bodies and the external complementary energy as

$$V^* = \frac{1}{2}\int_S p(\boldsymbol{r})\cdot\omega(\boldsymbol{r})\cdot dS + \int_S p(\boldsymbol{r})\cdot[B(\boldsymbol{r}) - \delta]\cdot dS \tag{7}$$

To enable the numerical solution, the potential contact area is discretized into a set of n pressure elements Δ_j (described in Section 2.1), with a uniform pressure distribution assumed to be acting over each one of them, as shown in **Figure 4**. The position of the centroid of each pressure element Δ_j is denoted by vector $\boldsymbol{r_j}$.

Under a discretized domain, the total complementary energy may be expressed as

$$V^* = \frac{1}{2}\sum_{i=1}^{n}\left[p_i\int_{A_i}\omega(\boldsymbol{r})\cdot dA_i\right] + \sum_{i=1}^{n}\left[p_i\int_{A_i}[B(\boldsymbol{r}) - \delta]\cdot dA_i\right] \tag{8}$$

Taking into account Eq. (4), Eq. (5) may be rewritten as

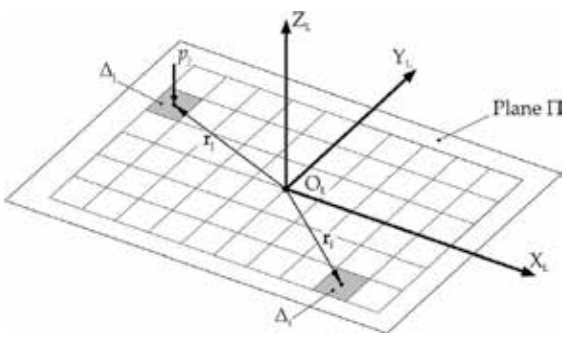

Figure 4. Discretization of the potential contact area into a pressure element mesh.

$$\omega(\boldsymbol{r}) = \sum_{j=1}^{n} \left[p_j \cdot f_j^{(1)}(\boldsymbol{r}) \right] + \sum_{j=1}^{n} \left[p_j \cdot f_j^{(2)}(\boldsymbol{r}) \right] = \sum_{j=1}^{n} \left[p_j \cdot t_j(\boldsymbol{r}) \right] \tag{9}$$

where $t_j(\boldsymbol{r})$ is defined as the cumulated influence coefficient of pressure element Δ_j over point Q

$$t_j(\boldsymbol{r}) = f_j^{(1)}(\boldsymbol{r}) + f_j^{(2)}(\boldsymbol{r}) \tag{10}$$

Considering Eq. (9), Eq. (8) can be rewritten as:

$$V^* = \frac{1}{2} \sum_{i=1}^{n} \left[p_i \cdot \sum_{j=1}^{n} p_j \int_{A_i} t_j(\boldsymbol{r}) \cdot dA_i \right] + \sum_{i=1}^{n} \left[p_i \int_{A_i} [B(\boldsymbol{r}) - \delta] \cdot dA_i \right] \tag{11}$$

To reduce the computational cost of the calculations, two assumptions are made:

i. The distance between the surfaces of the bodies $B(\boldsymbol{r})$ is assumed to be constant in all the pressure element Δ_i, and equal to the distance between the surface of the two bodies at its centroid, in such a way that $B(\boldsymbol{r}) = B(\boldsymbol{r}_i) = B_i$.

ii. The cumulated influence coefficient $t_j(\boldsymbol{r})$ is assumed to be constant over all the pressure element Δ_i, and equal to the value in its centroid, in such a way that $t_j(\boldsymbol{r}) = t_j(\boldsymbol{r}_i) = t_{j,i}$. The coefficient $t_{j,i}$ can be defined as the cumulated influence coefficient of element Δ_j over the centroid of element Δ_i, and it may be expressed as:

$$t_{j,i} = f_{j,i}^{(1)} + f_{j,i}^{(2)}$$

where $f_{j,i}^{(1)}$ and $f_{j,i}^{(2)}$ are the influence coefficients of element Δ_j over the centroid of element Δ_i, which can be determined for each contacting body using Eq. (3).

Under these assumptions, the total complementary energy can be expressed as

$$V^* = \frac{1}{2} \sum_{i=1}^{n} \sum_{j=1}^{n} p_i \cdot p_j \cdot t_{j,i} \cdot A_i + \sum_{i=1}^{n} p_i \cdot [B_i - \delta] \cdot A_i \tag{12}$$

The solution to the contact problem, in terms of contact pressure distribution, can be found by minimizing Eq. (12) under the following restrictions:

$$\begin{aligned} \frac{\partial V^*}{\partial p_i} &= \sum_{j=1}^{n} p_j \cdot t_{j,i} \cdot A_i + [B_i - \delta] \cdot A_i = 0 \quad \text{if} \quad p_i > 0 \\ \frac{\partial V^*}{\partial p_i} &= \sum_{j=1}^{n} p_j \cdot t_{j,i} \cdot A_i + [B_i - \delta] \cdot A_i \geq 0 \quad \text{if} \quad p_i = 0 \end{aligned} \tag{13}$$

The true contact area is then defined, within the precision of the mesh size, by the boundary between the elements with zero and non-zero pressures. The total contact load (F_T) can be calculated as

$$F_T = \sum_{i=1}^{n} p_i \cdot A_i \tag{14}$$

2.3. Contact between bodies of finite dimensions

The method described in the previous section is based on the utilization of influence coefficients that relate the contact pressures with the surface displacements. These influence coefficients can be determined in several ways, but in the great majority of the cases, they are calculated using the superposition of the Boussinesq relation (described in Section 2.1).

Because of the hypotheses under which this relation is established, influence coefficients determined using the Boussinesq relation should only be used to solve contact problems between contact bodies that can be approached to half-spaces. Otherwise, the application of the described method can lead to erroneous solutions of the contact problem.

However, the influence coefficients determined using the Boussinesq relation can be corrected, so they can be used to solve contact problems between bodies that *a priori* cannot be approached to elastic half-spaces. Among the correction methods that can be found in the literature, a correction method to consider contact bodies of finite dimensions is described in this section.

In this correction method, the finiteness of the contacting bodies is characterized by stress-free surfaces that are perpendicular to the length direction of the bodies, as illustrated in **Figure 5**. To leave those areas of the half-space that coincide with these surfaces free of normal and shear stresses, the correction method proposed by de Mul [6] is used, which consist in modifying the calculation of the influence coefficients $f_{j,i}$ for each body with finite dimensions in the following way:

$$f_{j,i} = f_{jo,i} + \overbrace{\left[1.29 - \frac{1}{1-\nu} \cdot (0.08 - 0.5 \cdot \nu)\right]}^{\Psi} \cdot \sum_{m=1}^{n} f_{jm,i} \tag{15}$$

where $f_{j0,i}$ is the influence coefficient of the original pressure element Δ_{jo}, Ψ is a correction factor proposed by Guilbault [7], and $f_{jm,i}$ are the influence coefficients of the pressure elements Δ_{jm}, that are mirrored instances of the element Δ_{jo} respect to the planes that coincide with the n free-stress surfaces of the body.

This method involves the calculation of additional influence coefficients of the mirrored pressure elements, and hence the computational cost of the method is multiplied by $(n+1)$, being n the number of finite dimensions taken into account in the problem.

2.4. Quadtree decomposition of the domain

According to Samet [8], the basic concept of the quadtree is to enclose the domain of the problem (Γ) into a containing cell, usually a square, which is denoted as the root of the quadtree, as shown in **Figure 6a**. This cell is then subdivided into four sons of the same size (**Figure 6b**), one in each direction: North-West (NW), Nord-East (NE), South-West (SW), and South-East (SE).

http://dx.doi.org/10.5772/intechopen.72422

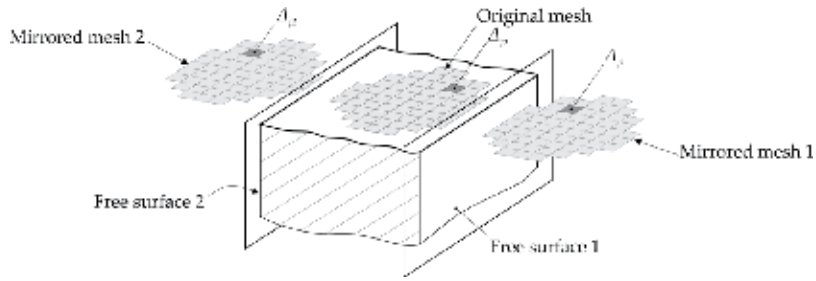

Figure 5. Contact between bodies of finite dimensions.

Each one of these cells is subdivided recursively until a stopping criterion is reached, which may be based upon the local geometry of the domain or in user-defined parameters (**Figure 6c** and **d**).

The information related to the quadtree decomposition of the domain is stored in a hierarchical tree structure, as shown in **Figure 6e**. For every cell, references to its ancestor and sons are stored. This kind of structure eases the performance of several operations, such as the neighbor finding in a defined direction, which will play an important role in the proposed method.

Each corner of a cell is called vertex. The level of a cell j in the structure is denoted by L_j, and represents the number of divisions performed from the root of the quadtree. According to this definition, L_j is also related to the relative size of the cell inside the quadtree structure and the degree of mesh refinement that this size represents. Given the size of the root cell of the quadtree, the size of any cell can be determined if its degree of refinement L_j is known. The root cell of the quadtree is usually denoted by level 0. Any cell that is not subdivided anymore is a leaf cell (displayed in gray in **Figure 6e**), while subdivided cells are referred to as non-leaf cells.

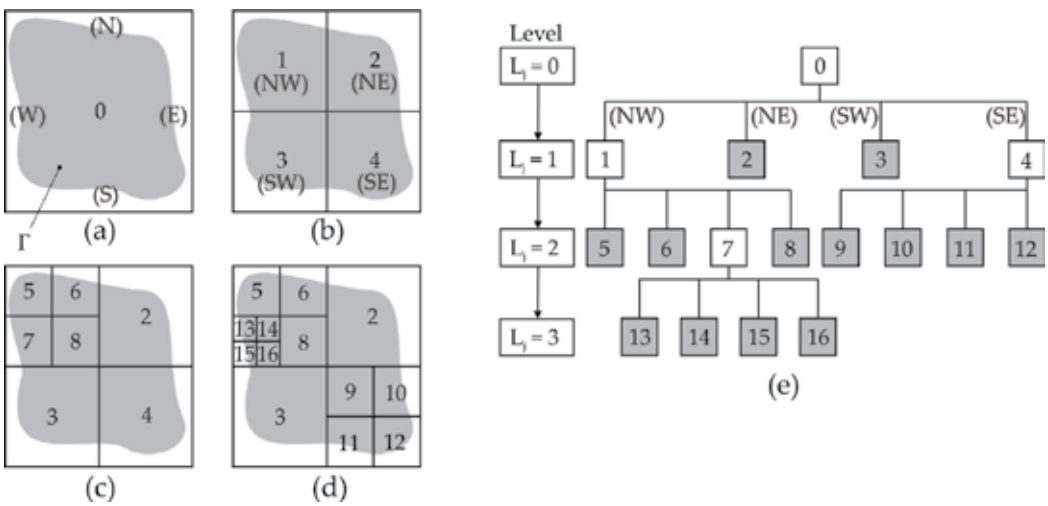

Figure 6. Example of a quadtree decomposition of the domain.

3. Computational approach to solve frictionless elastic contact problems using adaptive mesh refinement

In this section, the major topics of the computational implementation of the semi-analytical method to solve frictionless elastic contact problems described in Section 2.2 are discussed. As it has been said before, this method is based on the discretization of the potential contact area (Γ) into a mesh of pressure elements. The potential contact area is defined as the Boolean intersection of the projection of the bodies on the plane Π, as shown in **Figure 7**.

In the classical approach, the potential contact area is discretized using a uniform mesh of pressure elements. In contrast, to improve the efficiency of the method, adaptive mesh refinement is implemented in this approach. To do so, a quadtree decomposition (described in Section 2.4) of the potential contact area is performed, where all the leaf cells of the quadtree are considered pressure elements. The use of a quadtree offers two interesting features to this implementation. In first place, the recursive division of the cells provides a robust local mesh refinement strategy. In second place, transverse operations such as neighbor finding algorithms are computationally efficient and easy to implement.

The main algorithm of the approach to solve contact problems using adaptive mesh refinement is shown in **Figure 8**. The following inputs are required by the algorithm:

i. The geometry and position of the contact surfaces in undeformed contact position.

ii. The initial point of contact (O_L) and a vector defining the contact normal.

iii. The magnitude of the contact force (F_T).

iv. The initial level of uniform mesh density (L_{uni}), which is a parameter that describes the size of the elements of the initial uniform pressure element mesh.

The algorithm starts determining the common tangent plane Π, where a local Cartesian coordinate system is defined, being the Z_L axis normal to the plane Π (step **A1**). The

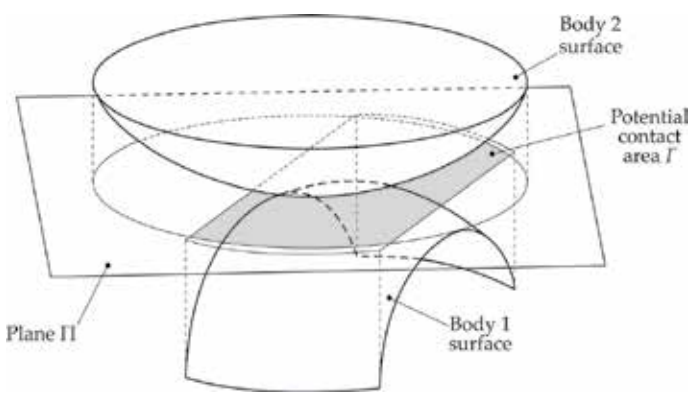

Figure 7. Definition of the potential contact area Γ.

http://dx.doi.org/10.5772/intechopen.72422

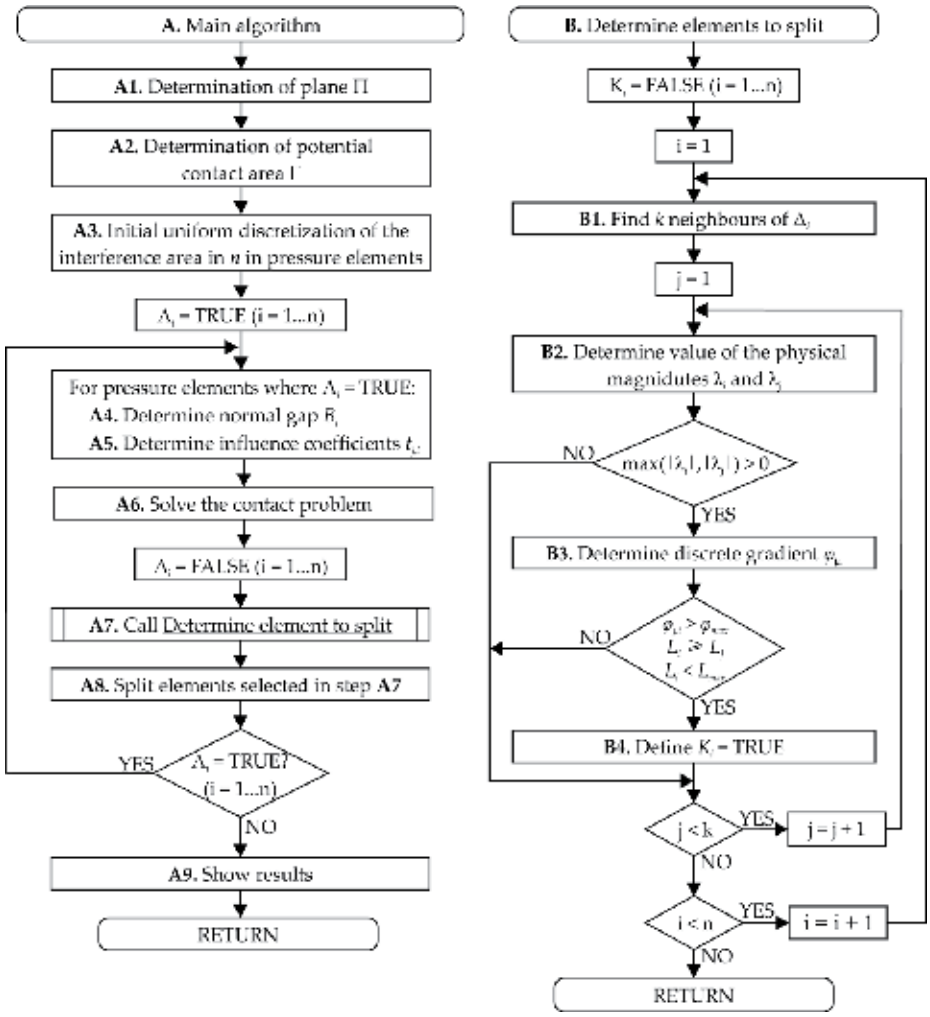

Figure 8. Main algorithm of the proposed approach and algorithm to determine elements to split.

boundaries of the contacting bodies are normally projected onto the plane Π to determine the potential contact area Γ (step **A2**).

The potential contact area is enclosed by the root cell of a quadtree, which is recursively subdivided until the desired initial level of uniform mesh density L_{uni} is reached for all the cells of the quadtree (step **A3**). All leaf cells of the quadtree are considered pressure elements Δ_i for the initial iteration of the algorithm, which is performed using a uniform pressure element mesh. All the elements are marked with the flag $\Lambda_i = TRUE$, indicating that their properties (associated area A_i, normal gap B_i, contact pressure p_i, and cumulated influence coefficients $t_{j,i}$) are not computed yet.

To maximize the efficiency of the proposed approach, it is important to minimize the number of pressure elements located outside of the potential contact area. This can be achieved by

ensuring that the potential contact area is enclosed by a root cell of the quadtree coincident with the minimum bounding rectangle (MBR), defined as the minimum rectangle that contains every point in the region [9].

Then, an iterative process starts whose first step is the determination of the normal gap B_i for all the pressure elements (step **A4**) where $\Lambda_i = TRUE$. The cumulated influence coefficients $t_{j,i}$ of those elements are also determined (step **A5**), using Eq. (3). Finally, the contact problem is solved using Eq. (13) (step **A6**), in the way indicated in [5], obtaining a contact pressure value p_i for each element Δ_i of the discretization.

The flag Λ_i is defined as *FALSE* for all the elements present in the discretization, indicating that the properties of these elements have already been computed.

At this point, the adaptive mesh refinement is performed. For such a purpose, the algorithm that determines the elements that must be split (that is described in section 3.1) is called (step **A7**), which returns an array with the indexes of these elements. Then, the selected elements are split (step **A8**) and the quadtree data structure is updated with the information of the new elements, which are marked with the flag $\Lambda_i = TRUE$, indicating that their properties are not computed yet. If no new elements are created, the iterative process finishes and the contact results are displayed (step **A9**). In contrast, if new elements are created, the iterative process starts again (step **A4**), and it is repeated until no new elements are created.

The main advantage of this implementation is that only the normal gap and the influence coefficients related to the new elements are computed for each iteration, decreasing the global computational cost of the method. The number of influence coefficients calculated in the proposed approach (N_f) can be determined afterwards using the following equation:

$$N_f = \sum_{i=1}^{t} \left[2 \cdot n_{(i)} \cdot n_{new(i)} - n_{new(i)}^2 \right] \tag{16}$$

where t is the number of iterations performed by the algorithm, $n_{(i)}$ is the number of elements in iteration i, and $n_{new(i)}$ is the number of new elements in iteration i.

3.1. Algorithm to determine elements to split

An adaptive mesh refinement may be based upon several criteria. In this work, the rate of change of a given physical magnitude (denoted by λ) related with the solution of the contact problem is used to perform adaptive refinement of the pressure element mesh. Since the proposed approach works under a discretized domain, each pressure element Δ_i will have an associated value λ_i of the observed physical magnitude, and in consequence, a discrete rate of change $\varphi_{j,i}$ of λ can be established between an element Δ_i and any of its neighbors Δ_j as

$$\varphi_{j,i} = \frac{|\lambda_j - \lambda_i|}{max(|\lambda_j|, |\lambda_i|)} \tag{17}$$

If the discrete rate of change $\varphi_{j,i}$ between a pressure element Δ_i and any of its neighbors Δ_j is higher than an arbitrarily defined value φ_{max} (representing the maximum allowed rate of

http://dx.doi.org/10.5772/intechopen.72422

change of the observed physical magnitude), then the pressure element Δ_i is marked as a candidate to be split.

However, in some situations, the rate of change of λ is so high that the condition $\varphi_{j,i} < \varphi_{max}$ cannot be reached, and the refinement strategy based on the rate of change of λ would refine the pressure element mesh endlessly. In order to limit the number of iterations performed by the algorithm, an additional stopping criterion based on the minimum size allowed for a pressure element needs to be included. As mentioned before, the level L_j that a pressure element occupies in the quadtree structure is related to its size, so limiting the former will also limit the latter. This limit is defined by an user-defined parameter L_{max}, referred to as the maximum degree of mesh refinement.

It is important to point out that φ_{max} is a target value and may not be always reached. If the maximum degree of mesh refinement L_{max} is reached for all pressure elements before the target value for φ_{max} is achieved, the mesh refinement will finish.

The main routine of the algorithm to determine elements to split is shown in **Figure 8b**. The following input information is required by the algorithm:

i. The properties associated with the pressure elements (area A_i, normal gap B_i, contact pressure p_i, and cumulated influence coefficients $t_{j,i}$).

ii. The quadtree data structure.

iii. The maximum degree of mesh refinement (L_{max}).

iv. The maximum allowed rate of change of the observed physical magnitude (φ_{max}).

The algorithm starts defining the flag K_i as *FALSE* for all the elements present in the current discretization. The flag K_i indicates when a pressure element must be split, so in principle, it is assumed that none of the elements will be divided.

Then, the iterative process starts searching the k neighbors of every pressure element Δ_i in the domain (step **B1**). For this purpose, the algorithm proposed by Samet [8] is used, which is based in the quadtree data structure. As a result, this algorithm provides an array that contains the indexes of the k neighbors of a given pressure element.

For each pair of neighboring pressure elements Δ_i and Δ_j, the algorithm determines the associated physical magnitudes λ_i and λ_j (step **B2**). These magnitudes can be already given by the main algorithm (as in the case of the contact pressures), or they can be specifically determined from these values by performing additional calculations.

Then, the discrete rate of change $\varphi_{j,i}$ of the observed magnitude between pressure element Δ_i and his neighbor Δ_j is obtained using Eq. (17) (step **B3**). If $\varphi_{j,i}$ is lower than the user-defined value φ_{max}, the next neighbor pressure element Δ_{j+1} is evaluated. In contrast, if the discrete rate of change of the observed magnitude between both elements is greater than φ_{max}, then element Δ_i is considered as a candidate to be split. Two additional conditions must be fulfilled so Δ_i can be marked to be split:

i. On one hand, L_i must be lower than L_{max}, to avoid that the algorithm refines the mesh indefinitely in those cases where φ_{max} cannot be reached.

ii. On the other hand, L_i must be less than or equal to L_j, to ensure that the level difference between two adjacent elements does not differ more than one level in the quadtree structure, avoiding unbalanced meshes.

If these conditions are met, the pressure element Δ_i is marked to be split by defining $K_i = TRUE$. The algorithm finishes when all the pressure elements have been evaluated, returning an array that contains the indices of those elements where $K_i = TRUE$.

3.2. Final remarks

In contact problems, there are different physical magnitudes that can be observed to perform the adaptive mesh refinement, having each one its advantages and disadvantages. In this work, the observed magnitude to perform the adaptive mesh refinement is the contact pressure ($\lambda_i = p_i$), and the mesh refinement is performed based on the discrete gradient of the contact pressures. The main advantages of choosing the gradient of the contact pressure as refinement criterion instead of any other derived magnitude are:

i. On one hand, in this approach, the solution of the contact problem is found in terms of the contact pressure distribution. From the calculated contact pressure distribution, derived results are obtained. Since the accuracy of the derived results is dependent from the accuracy in which contact pressure distribution is calculated, it is important to obtain an accurate description of the contact pressure distribution.

ii. On the other hand, using the contact pressure distribution, instead of the derived results, as refinement criteria helps reducing the computational cost of the proposed approach, because obtaining derived results implies additional calculations.

However, it must be taken into account that the contact pressure distribution function is not differentiable in the border of the contact area. In consequence, according to Eq. (17), the discrete rate of change of the contact pressure between an element Δ_i that is within the contact area ($p_i > 0$) and of an adjacent element Δ_j that is outside of the contact area ($p_j = 0$) is always $\varphi_{j,i} = 1$. Therefore, if a value lower than 1 is specified for φ_{max}, the refinement strategy will refine the mesh at the boundary of the contact area until the maximum degree of mesh refinement will be reached at the border of the true contact area.

The topology of the resulting pressure element mesh, inside and outside the true contact area, depends on the configuration of the proposed approach, which is defined by a unique combination of the three input parameters:

i. The initial level of uniform mesh density, L_{uni}.

ii. The maximum degree of mesh refinement, L_{max}.

iii. The maximum allowed rate of change of the physical magnitude, φ_{max}.

The possible configurations of the approach, and their effect on the resulting pressure element mesh, are categorized intro three different settings:

i. **Setting 1** ($L_{uni} \geq L_{max}$, φ_{max} not relevant): using this setting, the contact problem is solved using a uniform mesh, whose mesh density is defined by L_{uni}.

ii. **Setting 2** ($L_{uni} < L_{max}$, $\varphi_{max} = 0$): using this setting, the contact problem is solved using adaptive mesh refinement outside the true contact area. Inside the true contact area, a uniform mesh is used, whose mesh density is defined by L_{max}.

iii. **Setting 3** ($L_{uni} < L_{max}$, $\varphi_{max} > 0$): using this setting, the contact problem is solved using adaptive mesh refinement both inside and outside the true contact area.

From the nine steps of the main algorithm, step **A5** is the most time consuming. For this reason, the computational cost of the approach can be defined by the number of influence coefficients that are calculated to solve the contact problem, which can be determined using Eq. (16).

4. Numerical examples

The performance of the proposed approach is illustrated in this section, considering its accuracy and computational cost. For such a purpose, two cases of study are considered:

- Case of study I (CoSI) corresponds to a punctual contact between a plane and a spherical indenter, whose dimensions are shown in **Figure 9a**. Punctual contacts are common in mechanical components such as ball bearings, gears and rail-wheel systems.
- Case of study II (CoSII) corresponds to a line contact between a plane and a cylindrical indenter, whose dimensions are shown in **Figure 9b**. Line contacts are common in mechanical , such as roller bearings or standard spur and helical gears.

The material of both indenters (CoSI and CoSII) and the plane is assumed to have a Young modulus of 70 GPa and a Poisson coefficient of 0.35. A total contact load $F_T = 60$ kN is considered.

In both cases, the root cell of the quadtree results in a 20×20 mm square. The spherical indenter has been considered as an elastic half-space. In contrast, two finite dimensions have been considered for the longitudinal direction of the cylindrical indenter, using the correction method described in Section 2.3.

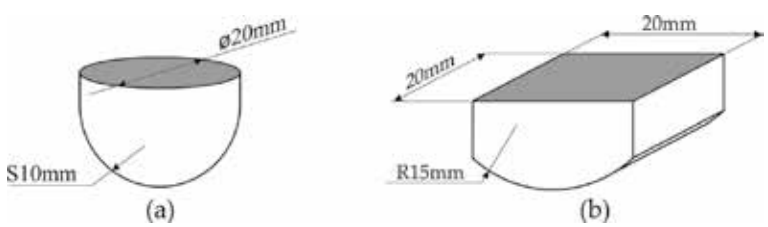

Figure 9. Definition of the indenters for (a) case of study I and (b) case of study II.

The cases of study I and II are solved under several configurations of the proposed approach, selected from the three settings described in Section 3.2, and the performance of each configuration is discussed in Sections 4.1 (for configurations within setting 1), 4.2 (for configurations within setting 2), and 4.3 (for configurations within setting 3).

For each configuration, the computational cost of the approach to solve the contact problem is evaluated using Eq. (16). The accuracy of the approach is evaluated by comparing the obtained contact pressure distributions with reference solutions. For case of study I, the reference solution is determined using the analytical solution provided by the Hertz contact theory [10]. In contrast, since Hertz theory is no longer applicable for case of study II, reference results are obtained for this case using a validated finite element model.

4.1. Performance of the approach when a uniform mesh is used for the whole domain of the contact problem

The performance of the approach when a uniform pressure element mesh is used for the whole potential contact area is illustrated in this section. To do so, the contact problems defined by cases of study I and II are solved under several configurations of the approach, in which L_{uni} has been varied, keeping $L_{uni} = L_{max}$ and $\varphi_{max} = 0$ (setting 1 in Section 3.1). **Figure 10a–c** show examples of the resulting contact area and pressure element mesh that have been obtained for

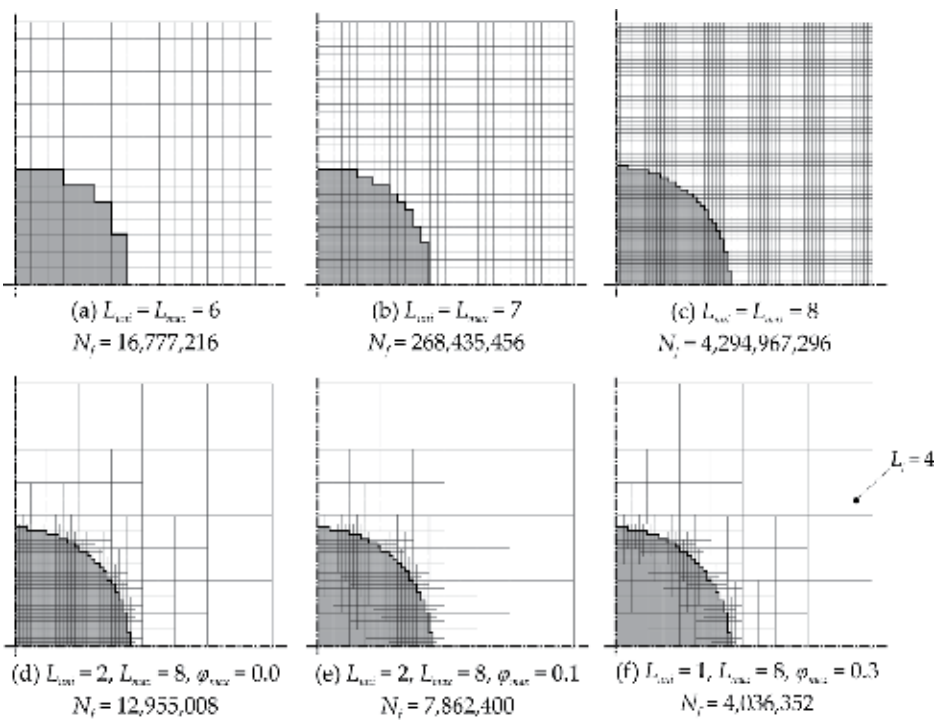

Figure 10. Axisymmetric representation of the resulting contact area and pressure element mesh obtained for CoSI under several configurations of the approach.

http://dx.doi.org/10.5772/intechopen.72422

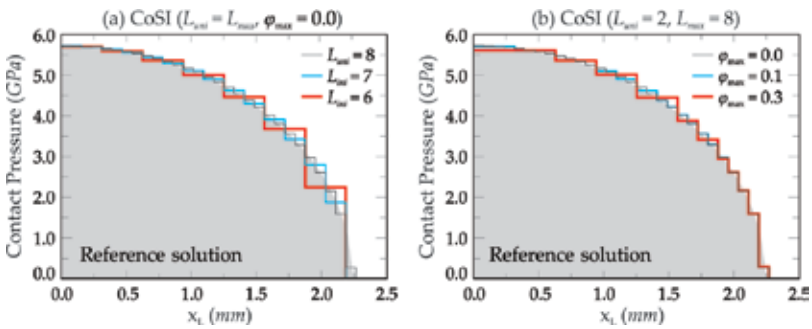

Figure 11. Contact pressure distribution for CoSI under several configurations of the approach.

case of study I under this setting of the approach. The computational cost of the proposed approach to solve the case of study I is also shown for each configuration.

The contact pressure distributions along the principal axes of the contact area of the solutions shown in **Figure 10a–c** are shown in **Figure 11a**. As expected, it can be observed that as the pressure element mesh is refined (by increasing the value selected for L_{uni}), the results obtained by the proposed approach converge toward the reference solution.

Using this configuration of the approach, a mesh containing $4^{L_{uni}}$ pressure elements is used, regardless of the nature of the contact problem to be solved. Under these circumstances, the computational cost is proportional to $4^{2 \cdot L_{uni}}$, and the factor of proportionality is the number of finite dimensions taken into account in the contact problem (as explained in Section 2.3). In consequence, for any value of L_{uni}, the computational cost of the algorithm to solve case of study II will always be greater than the computational cost to solve case of study I.

4.2. Performance of the approach when adaptive mesh refinement is performed outside the true contact area

In this section, the performance of the proposed approach when adaptive refinement is performed outside the true contact area is illustrated. To do so, the contact problems defined by cases of study I and II are solved under several configurations of the approach, in which L_{uni} and L_{max} have been varied, keeping $L_{uni} < L_{max}$ and $\varphi_{max} = 0$ (setting 2 in Section 3.1). **Figures 10d** and **12a** show examples of the resulting contact area and pressure element mesh that have been obtained for cases of study I and II under this setting of the approach.

The results obtained in these cases show that the accuracy in which the contact problem is solved is independent of the value selected for L_{uni}. For any given value of L_{max}, the same contact pressure distributions as the ones obtained with a uniform pressure element mesh for the whole domain have been obtained (shown in **Figure 11a**), regardless of the value selected for L_{uni}. This implies that the variation of the pressure element mesh outside the true contact area does not have any impact on the solution of the contact problem.

On the other hand, comparing the computational cost of the solutions shown in **Figure 10c** (uniform mesh) and **10d** (adaptive refinement outside the true contact area), it can be observed

that an important reduction of the computational cost is achieved by increasing the difference between L_{max} and L_{uni}. Similar tendencies are observed for case of study II, where the reductions of computational cost are even more remarkable due to the presence of finite dimensions.

4.3. Performance of the approach when adaptive mesh refinement is performed both inside and outside the true contact area

In this section, the performance of the proposed approach when adaptive refinement is also performed inside the true contact area is illustrated. To do so, the contact problems defined by cases of study I and II are solved under several configurations of the approach, in which φ_{max} has been varied, keeping $L_{uni} < L_{max}$ (setting 3 in Section 3.1). **Figures 10e**, **f** and **12b** show examples of the resulting contact area and pressure element mesh that have been obtained for cases of study I and II under this setting of the approach.

The contact pressure distributions along the principal axes of the contact area of the solutions shown in **Figure 10d-f** are shown in **Figure 11b**. The contact pressure distributions along the principal axes of the contact area of the solutions shown in **Figure 12a**, **b** are shown in **Figure 13**. It both cases, it can be observed that increasing the value selected for φ_{max} implies that a coarser mesh is used in those regions of the true contact area where the contact pressure

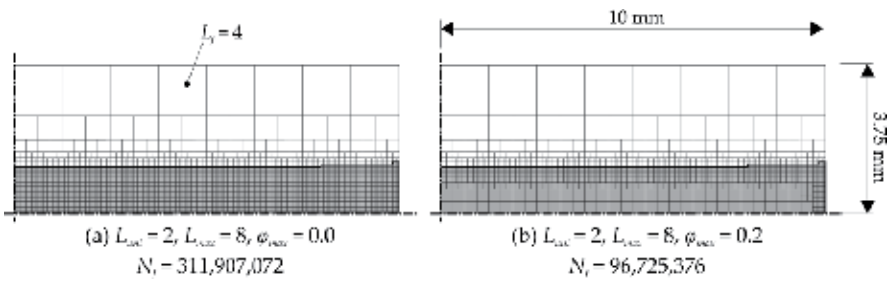

Figure 12. Axisymmetric representation of the resulting contact area and pressure element mesh obtained for CoSII under two different configurations of the approach.

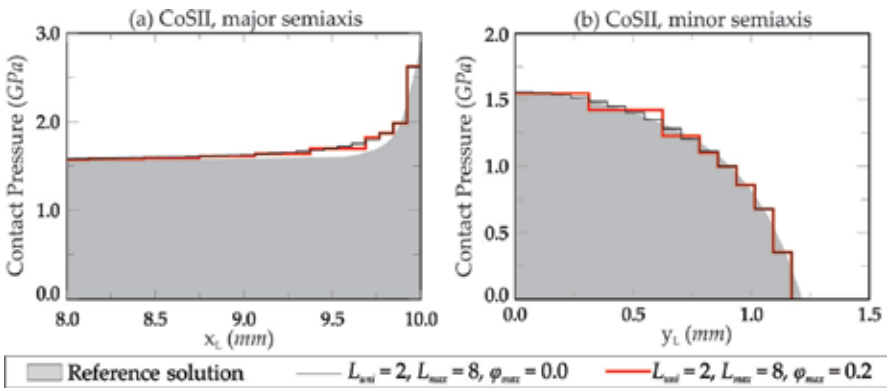

Figure 13. Contact pressure distribution for CoSII under several configurations of the approach.

gradient is small, without a significant loss of accuracy when describing the contact pressure distribution.

The obtained results show that the accuracy of the approach to predict the size of the true contact area does not depend on the value selected for φ_{max}, since the same values are obtained regardless of the value selected for this parameter. This is because when $\varphi_{max} < 1$, the accuracy in which the border of the contact area is computed depends only on the value selected for L_{max}, as stated in Section 3.2.

Finally, comparing the computational cost of the solutions shown in **Figure 10d** and **e** (and **Figure 12a** and **b**), it can be observed that a further reduction of the computational cost can be achieved by specifying values of $\varphi_{max} > 0$. Although this reduction is not as important as the one achieved by maximizing $L_{max} - L_{uni}$ (discussed in Section 4.2), it still can help to reduce the computational cost of the approach.

5. Conclusions

A new semi-analytical approach has been developed to solve frictionless elastic contact problems using adaptive mesh refinement. Starting from a coarse initial uniform mesh (whose density is defined by the parameter L_{uni}), a mesh refinement is performed based on two different criteria: (i) the maximum allowed rate of change of a physical magnitude (the contact pressure), defined by the parameter φ_{max} and (ii) the maximum degree of mesh refinement, defined by the parameter L_{max}.

The configuration of the approach is defined by a unique combination of values for L_{uni}, L_{max}, and φ_{max}. The performance of the proposed approach has been illustrated with several cases of study solved under different configurations of the approach, and the obtained results enable us to draw the following conclusions:

i. When $L_{uni} = L_{max}$, a uniform mesh is used to solve the contact problem, regardless of the value selected for φ_{max}. Under this configuration, it can be observed that the obtained results converge toward the reference solution as L_{uni} is increased. However, an exponential growth of the computational cost is produced as the pressure element mesh is refined.

ii. When $L_{uni} < L_{max}$ and $\varphi_{max} = 0$, adaptive mesh refinement is performed outside the true contact area. Under these circumstances, it can be observed that the computational cost of the approach is reduced by maximizing $L_{max} - L_{ini}$, while the accuracy of the solution remains unaffected.

iii. In last place, when $L_{uni} < L_{max}$ and $\varphi_{max} > 0$, adaptive mesh refinement is performed both inside and outside the true contact area. Under these circumstances, it can be observed that a further reduction of the computational cost can be achieved. However, a loss of accuracy can be expected in the prediction of the contact pressure distribution as φ_{max} is increased.

A further discussion on this topic can be found in Ref. [11].

Acknowledgements

Parts of this chapter are reproduced from authors' previous publication (Ref. [11]).

Author details

Victor Roda-Casanova* and Francisco Sanchez-Marin

*Address all correspondence to: vroda@uji.es

Department of Mechanical Engineering and Construction, Jaume I University, Spain

References

[1] Kalker JJ, Van Randen Y. A minimum principle for frictionless elastic contact with application to non-Hertzian half-space contact problems. Journal of Engineering Mathematics. 1972;**6**(2):193-206

[2] Wriggers P. Computational Contact Mechanics. 2nd ed. Berlin/Heidelberg: Springer-Verlag; 2006. p. 518

[3] Boussinesq J. Application des potentiels à l'étude de l'équilibre et du mouvement des solides élastiques. Paris: Gauthier-Villars; 1885

[4] Love AEH. A Treatise on the Mathematical Theory of Elasticity. Cambridge: Cambridge University Press; 1906

[5] Kalker JJ. Three-Dimensional Elastic Bodies in Rolling Contact. 1st ed. Netherlands: Springer; 1990. p. 314

[6] de Mul JM, Kalker JJ, Fredriksson B. The contact between arbitrarily curved bodies of finite dimensions. Journal of Tribology. 1986;**108**(1):140-148

[7] Guilbault R. A fast correction for elastic quarter-space applied to 3D modeling of edge contact problems. Journal of Tribology. 2011;**133**(3):031402

[8] Samet H. Neighbor finding techniques for images represented by quadtrees. Computer Graphics and Image Processing. 1982;**18**:37-57

[9] Chaudhuri D, Samal A. A simple method for fitting of bounding rectangle to closed regions. Pattern Recognition. 2007;**40**(7):1981-1989

[10] Johnson KL. Contact Mechanics. Cambridge/New York: Cambridge University Press; 1985

[11] Roda-Casanova V, Sanchez-Marin F. Meccanica. 2017. https://doi.org/10.1007/s11012-017-0806-y

Chapter 5

Improving Contact Load-Bearing Resistance of Ultrafine-Grained Materials Through Multilayering and Grading

Dengke Yang, Jiangting Wang, Huimin Yang and Peter Hodgson

Additional information is available at the end of the chapter

http://dx.doi.org/10.5772/intechopen.72197

Abstract

Structural multilayering and grading has been designed to improve the contact load-bearing resistance of ultrafine-grained materials. The contact load-bearing response and surface damage resistance of multilayered hierarchical structured (MHSed) Ti were evaluated by experimental indentation on the overall loading response in conjunction with detailed computational simulations of local stresses and strain distribution. The combination of a hard outer layer, a gradual transition layer and a compliant core results in reduced indentation depth, but a deeper and more diffuse sub-surface plastic deformation zone, compared to the monolithic nanostructured Ti. The macroscopic indentation resistance of MHSed Ti is controlled by the underlying micromechanics of the multilayered hierarchical structure. The finite element analysis (FEA) revealed the multilayered hierarchical structure offers the effective macroscopic mechanical contact loading resistance, where the indenter increasingly "senses" the more compliant core to bear the deformation as the load increases. The structural multilayering modifies the stress and strain redistribution and effectively reduces the maximum stress concentration within the material. The structural grading provide a transitional junction for stress and plastic deformation redistribution and achieve more gradual stress distributions between component layers which mitigates the interface failure, increases the interfacial toughness, thus providing strong resistance to loading damage.

Keywords: ultrafine-grained materials, multilayered hierarchical structure, multilayering, grading, contact load-bearing resistance, finite element modeling

1. Introduction

Materials with high contact damage resistance are extensively required in aerospace and aircraft, vehicle industry, microelectro-mechanical systems and devices, cutting tools and bulletproof vests [1, 2]. An approach for improved resistance to surface contact damage is to design surface gradations in composition, microstructure and elastic and/or plastic properties [2–4]. Such design provide effective means to enhance materials contact damage resistance through redistribution of thermal and/or mechanical stresses, elimination of interface-induced stress concentrations and reduction in the local crack driving force [5–8]. Nature is a master in the design of sophisticated hierarchical structured materials which provide excellent damage resistance [9]. A typical example is the material structural design principle found in a fish armor [10]. In response to predatory threats, fish are protected by armor scales consisting of four distinct reinforcing layers of organic/inorganic nanocomposites with hardness and modulus decreasing gradually from the outer to the inner layers. The juxtaposition of multiple reinforcing composite layers and the gradations, both in microstructure and mechanical properties within and between material layers, provides a more compliant protective mechanism than the monolithic counterpart [10].

Inspired from the material structural design principle discovered in natural/biological systems, materials scientists have generated enormous interest in replicating natural/biological structures with excellent damage resistance than their conventional counterparts. Over the past 2 decades, significant progress has been made in synthesis and fabrication of materials with graded properties over multiple length scales. Elastically graded materials (EGMs), where the materials have gradient in elastic modulus as a function of depth beneath the surface, were synthesized by controlled infiltration of aluminosilicate or oxynitride glass into polycrystalline ceramic matrix, which offered superior resistance to contact damage than either constituent ceramic matrix or glass [11–13]. Plastically graded materials (PGMs) were produced by increasing or decreasing the grain size within the nanocrystalline or microcrystalline range to create a linear gradation of yield strength as a function of depth below the material surface according to classical Hall–Petch effect [3]. The benefit of the gradient effect on the stress–strain and deformation response under normal indentation have been demonstrated by analytical [14], computational [15–17] and experimental studies [18, 19].

In our recent work [20], we extended the EGM/PGM concept to design a multilayered hierarchical structure (MHS) on Ti. By the application of Surface Mechanical Attrition Treatment (SMAT) [21] to cryorolled Ti, a three-layered structure formed consisting of an outer amorphous/nanocrystallite (A/NC) layer, an inner nanograined (NG) layer and ultrafine-grained (UFG) core [20]. Nanoindentation through the cross-section of the multilayered hierarchical structured (MHSed) Ti revealed a gradual decrease in hardness and modulus within and between each successive structural layer [20]. These properties correlate with the microstructure characteristics and the design principle found in natural systems, such as fish armor [10]. The work hardening of the MHSed Ti was improved largely by such structural design [20]. Moreover, the gradations in structure and properties, pore and crack-free nature and the inherently damage tolerant top A/NC layer of MHSed Ti are expected to benefit the contact deformation and damage resistance of MHSed Ti.

Studies of the effects of microstructural, compositional, and property gradients on the overall elastic–plastic response under contact loading are an area of great interest, and much progress has been achieved in the fundamental understanding of graded surface damage resistance [2]. However, systematic investigations of the multilayered hierarchical structure on indentation response, contact damage resistance and contact surface failure of graded ultrafine-grained (UFG) metal, in particular with regards to the structural multilayering and grading, have not been investigated by multiscale experimental and computational approaches and the mechanism of the contact load-bearing response in these situations is also largely unknown.

In this Chapter, we focus on the contact load-bearing response and surface damage resistance of MHSed Ti relative to monolithic nanostructured Ti. Through experimental investigations and computational simulations of local stress and strain distributions, the mechanism of the contact load-bearing response of MHSed Ti is explored. These results provide clear evidence of improved contact load-bearing capacities through structural multilayering and grading. Such information is of practical value for the design of UFG materials with excellent contact load-bearing capacities for engineering applications.

2. Experimental procedures

The MHSed Ti was produced by the following experimental procedures. A commercial Ti plate (Grade 2) with 36 mm in thickness was cryogenically rolled to 5 mm with per reduction of ~2 mm. The detailed microstructure characterizations of the cryorolled Ti have been given elsewhere [22]. The cryorolled workpiece then was cut parallel to the rolling direction (RD) to a rectangular bar with dimensions of $5 \times 5 \times 90$ mm^3. Subsequently, one lateral surface of the rectangular bar was subjected to SMAT. The SMAT process was performed in a low vacuum condition using hardened stainless steel balls (8 mm in diameter) at a vibration frequency of 50 Hz for 60 min. The detailed MHS process can be found in [20]. The production of monolithic NG Ti has been given in [22].

Figure 1a shows a schematic illustration of the nanoindentation and contact load-bearing testing. Nanoindentation experiments were carried out at ambient temperature using an UMIS indentation system with a Berkovich diamond tip at a strain rate of 5×10^{-2} s^{-1} and a maximum load of 20 mN. Before testing, the cross-sectional surface was polished to 0.5 μm diamond suspension finish. The values of the nanoindentation hardness and modulus quoted here were the average of 10 measurements on the cross-sectional surface. Before Vickers microhardness and load-bearing testing, artifacts on the surface caused by MHS process were carefully removed by polishing to 0.5 μm diamond suspension finish (removal thickness < 2 μm). Vickers microhardness testing was conducted using a microhardness tester (FM 700) under a load of 0.5, 1, 3, 5, 10 N on the MHSed surface at more than 10 points and the average values were reported here. Load-bearing testing was conducted with a spherical tungsten carbide (WC) indenter with diameter of 1.5 mm in ambient conditions. The WC indenter had an elastic modulus of 640 GPa and a Poisson's ratio of 0.26. The indenter came into contact with the specimen surface and was loaded to a maximum load of 1000 N at a loading rate of 1000 N/s.

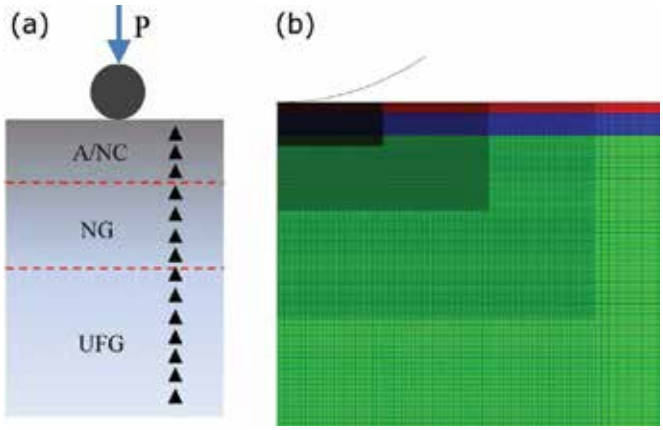

Figure 1. (a) Schematic illustration of the surface load-bearing and cross-sectional nanoindentation testing. The black ball represents the load-bearing testing indenter and the black triangle represents the indent of nanoindentation testing. (b) Finite element mesh of the ball indentation model.

Microstructural and damage observations were conducted using a field-emission gun scanning electron microscope (SEM) Zeiss Supra 55VP operated at 10 kV and a transmission electron microscope (TEM) Jeol JEM 2100 operated at 200 kV.

A two-dimensional axisymmetric model was developed to simulate the ball indentation using Abaqus v6.10. The specimens were modeled as isotropic, elastic–perfectly plastic following the large-deformation theory. The finite element mesh contained 42,163 four-node bilinear axisymmetric quadrilateral elements (CAX4R), with a refined mesh in the indentation region (**Figure 1b**). Mesh convergence was verified by comparing load–depth curves and stress contours using models with element number ranging from 11,183 to 42,163. A user subroutine UMAT was developed to take into account the gradation of material properties, in which the discrete and gradient model parameters were assigned to elements based on their distance from the surface (see later for further details). The ball indenter was modeled as a rigid body, and the contact between the indenter and specimen was assumed frictionless. A maximum load of 1000 N was applied to indent the samples at a loading rate of 1000 N/s. The finite element analysis (FEA) of the microindentation adopted a similar methodology to the axisymmetric nanoindentation simulations. The Vickers indenter was modeled to be a conical rigid indenter with an apex angle of 70.3° and tip radius of 3.4 μm, which approximates a Vickers indenter tip.

3. Results

3.1. Microstructure

A SEM cross-sectional view of the MHSed Ti surface shows three-layered structure without sharp interfaces between the successive layers (**Figure 2a**). TEM analysis revealed that the ~30 μm thick top layer was composed of a bright phase matrix and a discrete darker nanostructure (**Figure 2b**).

The upper right inset taken from the bright matrix region exhibited a broad diffuse halo in a selected-area diffraction pattern (SAD), which is typical of a fully amorphous phase. The SAD pattern in the lower left inset taken from the interface between the bright and dark phases clearly demonstrates the presence of a nanocrystalline phase together with the amorphous phase. The NG layer (~60 μm thick), situated beneath the A/NC layer, consisted of nanograins (**Figure 2c**). The corresponding SAD pattern shows a ring pattern, demonstrating the nanostructure has random crystallographic orientations. The size of the nanograins was in the range from 5 to 80 nm with an average size of ~40 nm (**Figure 2e**). The UFG core is composed of ultrafine equiaxed grains with a grain size distribution of 50–250 nm (**Figure 2d** and **f**).

3.2. Mechanical gradations

Nanoindentation was used to measure the elastic and plastic mechanical properties spatially through the cross-section of the MHSed Ti. The elastic mismatch and delamination, commonly existed in other multilayered systems produced by deposition or coating, are two critical factors controlling crack confinement [23]. In contrast, due to the gradients in both the strain and strain rate induced by the cryorolling and SMAT process from the top surface to the inner core, the reported MHSed Ti is free from elastic mismatch and delamination between layers.

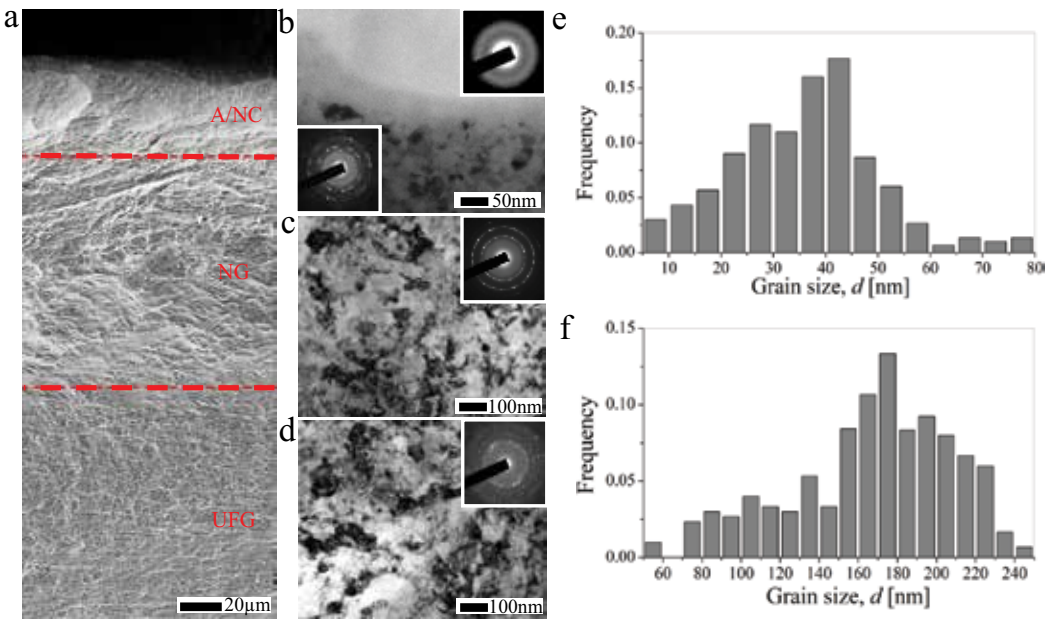

Figure 2. Microstructural characteristic of the MHSed Ti: (a) SEM cross-sectional image. (b) TEM bright-field (BF) image of the microstructure situated 20 μm below the top surface. The upper right and lower left insets are the selected-area diffraction (SAD) patterns of the bright region the dark region, respectively; (c) TEM BF image of the microstructure located 60 μm below the top surface. The inset shows the corresponding SAD pattern; (d) TEM BF image of the innermost core. The inset shows the corresponding SAD pattern; (e and f) histogram of the grain size distribution in the NG layer (e) and UFG core (f). The grain size D was defined by $D = \sqrt{d_T \times d_L}$, d_T is the transverse length of the grain and d_L is the longitudinal length. 300 grains were statistical measured from several TEM dark-field (DF) images.

Moreover the MHSed Ti possesses mechanical gradations within and between each successive layer. The Oliver–Pharr [24] indentation hardness H_{O-P} (ranging from ~5.3 to ~3.2 GPa) and modulus E_{O-P} (ranging from ~137 to ~113 GPa) gradually decreased with the distance from the top surface to the core (**Figure 3a** and **b**). The highest average indentation hardness (~5.2 GPa) of the top A/NC layer is consistent with its microstructure which is composed of amorphous and nanocrystalline phases. The NG layer has nanograins compared with the A/NC layer, but reduced grain size relative to the UFG core, consistent with the mechanical trend observed in **Figure 3a** and **b**. The UFG core, consists of ultrafine equiaxed grains with average grain size of ~180 nm, thus has the lowest average indentation hardness (~3.2 GPa). **Figure 3c** shows the SEM image of the residual indents after indentation unloading. The absence of radial or circumferential cracks confirms the plastic nature of the material layers. The mechanical gradations were calculated as the slope of datasets presented in **Figure 3a**. With the distance from the outer surface to inner core, approximately negative linear gradations in both E_{O-P} and H_{O-P} were obtained within the top A/NC and the NG layers beneath. The UFG core, however, show no detectable gradation. **Table 1** summarizes the gradations of E_{O-P} and H_{O-P} in each layer.

3.3. Contact load-bearing response

The experimental contact load-bearing response of the MHSed Ti and the monolithic NG Ti is shown in **Figure 4**. For the same contact load (1000 N), a relatively small contact impression

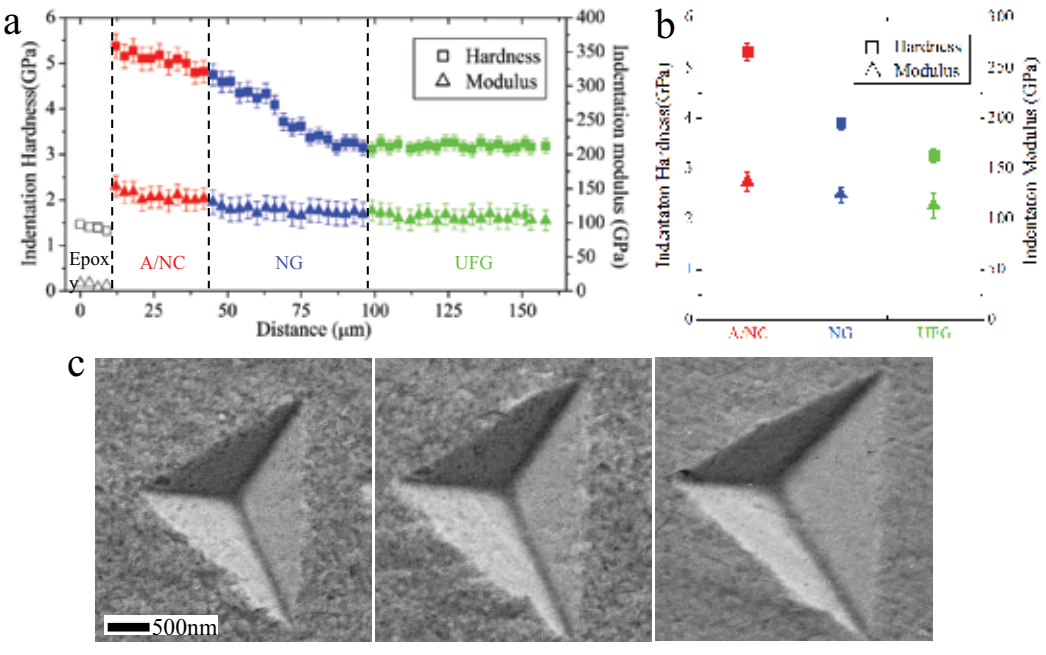

Figure 3. Mechanical gradations of the MHSed Ti. (a) Hardness and modulus through the cross-section of MHSed Ti using a 20 mN maximum load; (b) average indentation hardness and modulus for each of the layers; and (c) SEM images of the residual indents on the cross-section of each layer. From left to right: A/NC, NG, and UFG.

Components (layer)	Gradation E_{O-P} (GPaμm^{-1})	Gradation H_{O-P} (GPaμm^{-1})
A/NC	−0.57	−0.013
NG	−0.25	−0.014
UFG	0	0

Table 1. Mechanical gradations in each component layer.

for the MHSed Ti is expected due to the high hardness and strength of the top A/NC layer. The residual impression radius for the MHSed Ti and the monolithic NG were measured to be 424 and 488 μm (**Figure 4a** and **b**), respectively. A complete suppression of cracks in the MHSed material was clearly substantiated by SEM observations (**Figure 4c**). In contrast, cracks (marked by white arrows) appeared to initiate at the contact edge of the indentation and propagate through the region in the monolithic NG Ti, most likely due to local stress concentrations (**Figure 4d**).

Most of the plastic deformations of the tested materials occur within a semi-circular area as revealed by optical microscopy observation on the cross sections (**Figure 4e–h**). The semi-circle represents an elastic–plastic deformation border and the semi-circular area can be considered as the plastic strain zone. The overall through-thickness impact impression of the MHSed Ti is comparatively much lower (**Figure 4c**) than the monolithic NG Ti (**Figure 4d**), however, the MHSed Ti yields a significant compliance and the elastic–plastic deformation border occurs at a greater depth compared with the monolithic NG material (**Figure 4e** and **f**). The radius of the plastic strain zone for the MHSed Ti and monolithic NG Ti was established to be ~530 μm and ~460 μm, respectively. High magnification observations on the elastic–plastic strain boundary revealed that the MHSed Ti achieves more gradual strain redistribution than the monolithic NG Ti in which intense shear localization were found (**Figure 4g** and **h**). The smooth transitional region for elastic–plastic deformation in the MHSed materials is the direct result of the multilayered structure accommodating the imposed load. These results suggest that the multilayered structure and the associated mechanical gradations in the material offer an advantageous mechanism for contact damage resistance.

3.4. Computational simulations

To better understand how the structural multilayering and grading influences the contact load-bearing behavior of the MHSed materials, an elastic–perfectly plastic finite element analysis (FEA) computational model was developed. Here the three-dimensional indenter geometry represented as two dimensional, axisymmetric and rigid has been simulated to fit the experimental nanoindentation loading-depth data for each layer. The extensive study showed that incorporating the post yield strain hardening (linear isotropic, linear kinematic and Ramberg–Osgood isotropic hardening) into the models had a minimal effect on improving the prediction of the simulated data and the estimated yield strength [10]. Consequently, we assume zero hardening for plastic behavior and that the material deformation is elastic–perfectly plastic. This is a simple and effective approach to describe the mechanical behavior of the material.

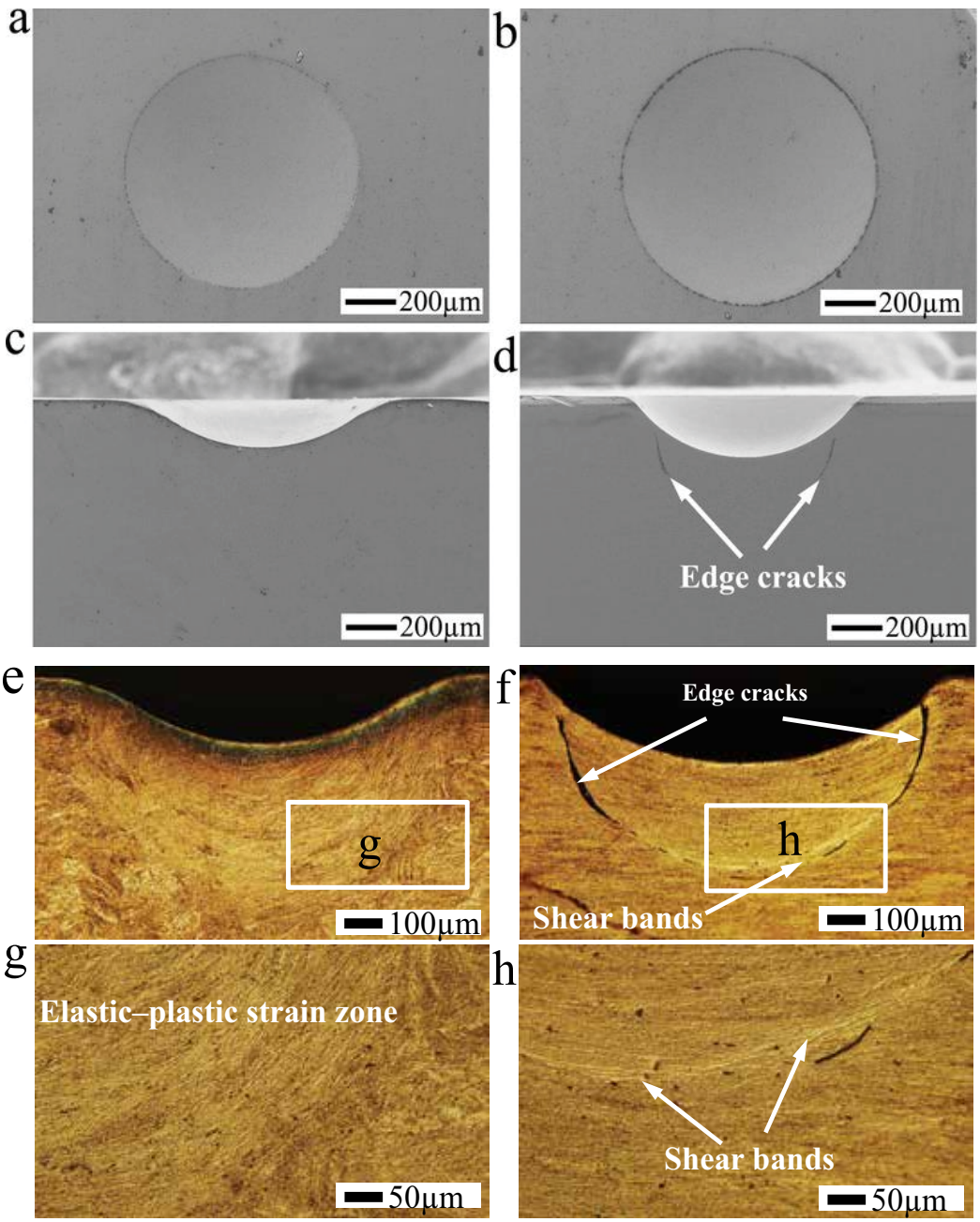

Figure 4. SEM and OM images of indentation testing results of the MHSed Ti and monolithic NG Ti. (a and b) Top surface SEM views of the MHSed Ti and monolithic NG Ti, respectively. (c and d) Cross-sectional view of the MHSed Ti and monolithic NG Ti, respectively. (e and f) OM cross-sectional views of the plastic deformed area in the MHSed Ti and monolithic NG Ti, respectively. (g and h) HR OM images of the boundary of elastic–plastic strain zone for the MHSed Ti and monolithic NG Ti, respectively.

In these simulations, the FEA-predicted unloading slope was selected to match the experimentally calculated average E_{O-P} for each layer (**Figure 3b**). Various material yield strengths (σ_Y) were chosen to determine the optimal value at which the FEA-predicted load and unload–depth curve best fits the experimental load and unload–depth curve. The averaged experimental load–depth curves (solid line in **Figure 5**) were selected from the experimental nanoindentation load–depth curve dataset, whose unloading slope represents the average indentation modulus for each layer presented in **Figure 3b**. In the initial simulations, the yield strength of each layer was based on results from our earlier work using micro-compression testing [20]. Using such yield strength, the simulated load–depth curve (dash line in **Figure 5**) was obtained and compared to the averaged experimental curve. By adjusting the yield strength value and iteratively repeating the simulations until the simulated and experimental curves correlated (**Figure 5**), the yield strength for each layer was determined. **Figure 5** shows the FEA simulations best fit the averaged experimental load–depth curve for each component layer. All the component layers exhibit mechanical hysteresis and energy dissipation (calculated as the area of the average experimental load–depth curves), which increased with the distance from the outer layer. The good agreement between the experimental data and the computational simulations gives the material yield strength σ_Y values of 1.76, 1.38 and 1.15 GPa for the A/NC layer, the NG layer and the UFG core, respectively.

In our FEA simulations, the effects of the structural multilayering and grading on the large-length-scale mechanical indentation of the MHSed Ti were explored by constructing two axisymmetric two-dimensional FEA models. The first "discrete" model consisted of a MHS of three

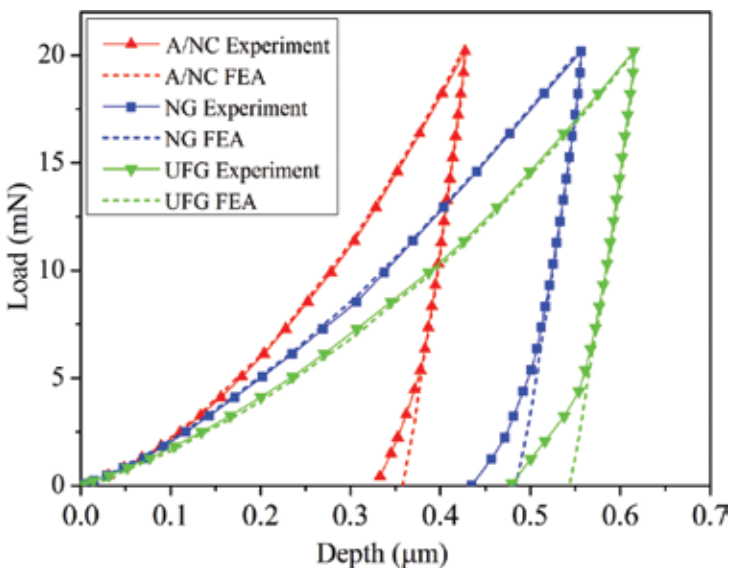

Figure 5. Experimental and FEA simulated average nanoindentation load–depth curves for the A/NC, NG layers and the UFG core.

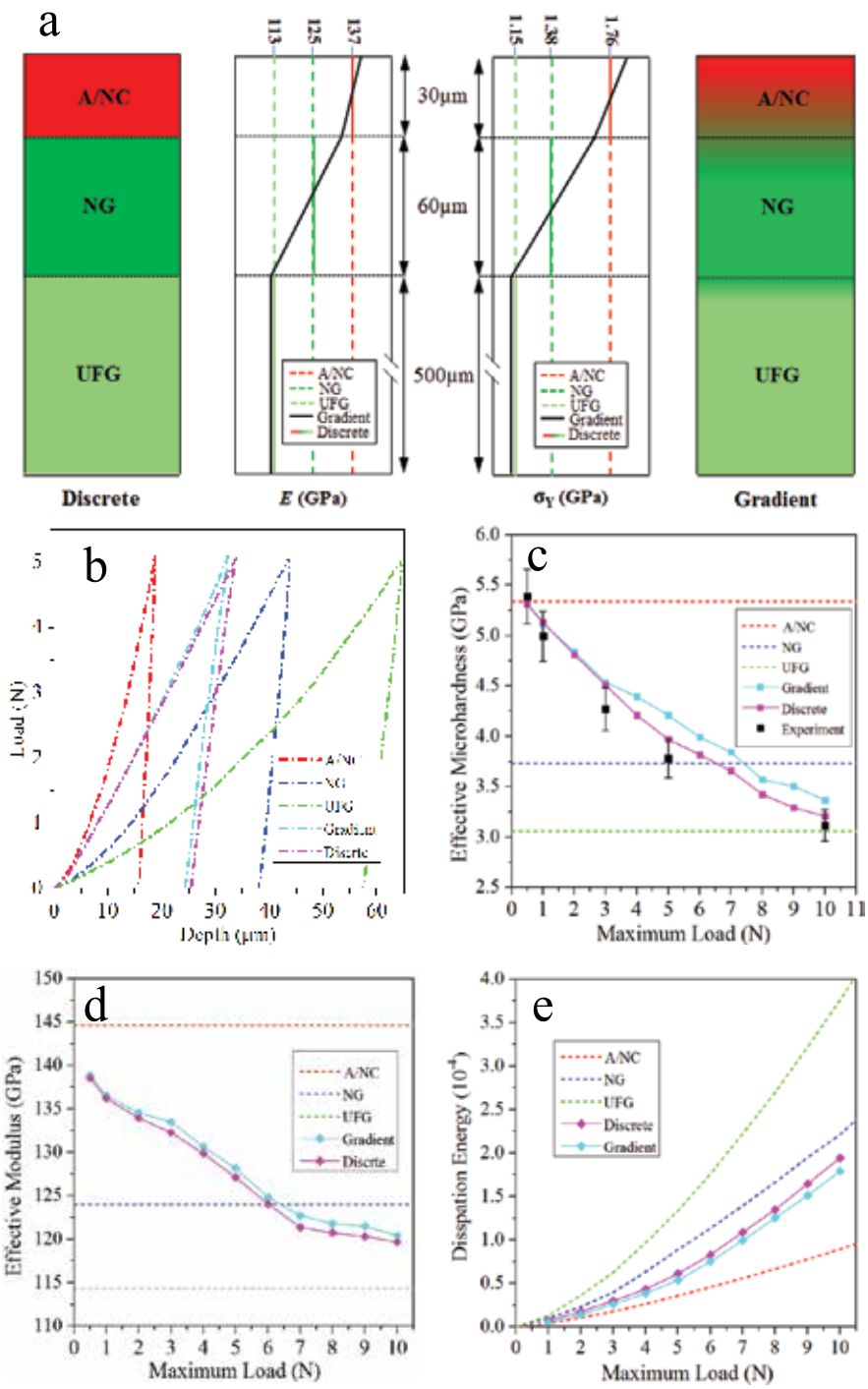

Figure 6. (a) FEA simulated models of discrete (left) and gradient (right) multilayered structure, the corresponding elastic modulus and yield strength distributions are presented in the center. (b) FEA simulated microindentation load–depth curves for different component layer and two models (discrete and gradient), (c) simulated effective microhardness and experimentally measured values, (d) simulated effective indentation modulus, and (e) simulated effective energy dissipation.

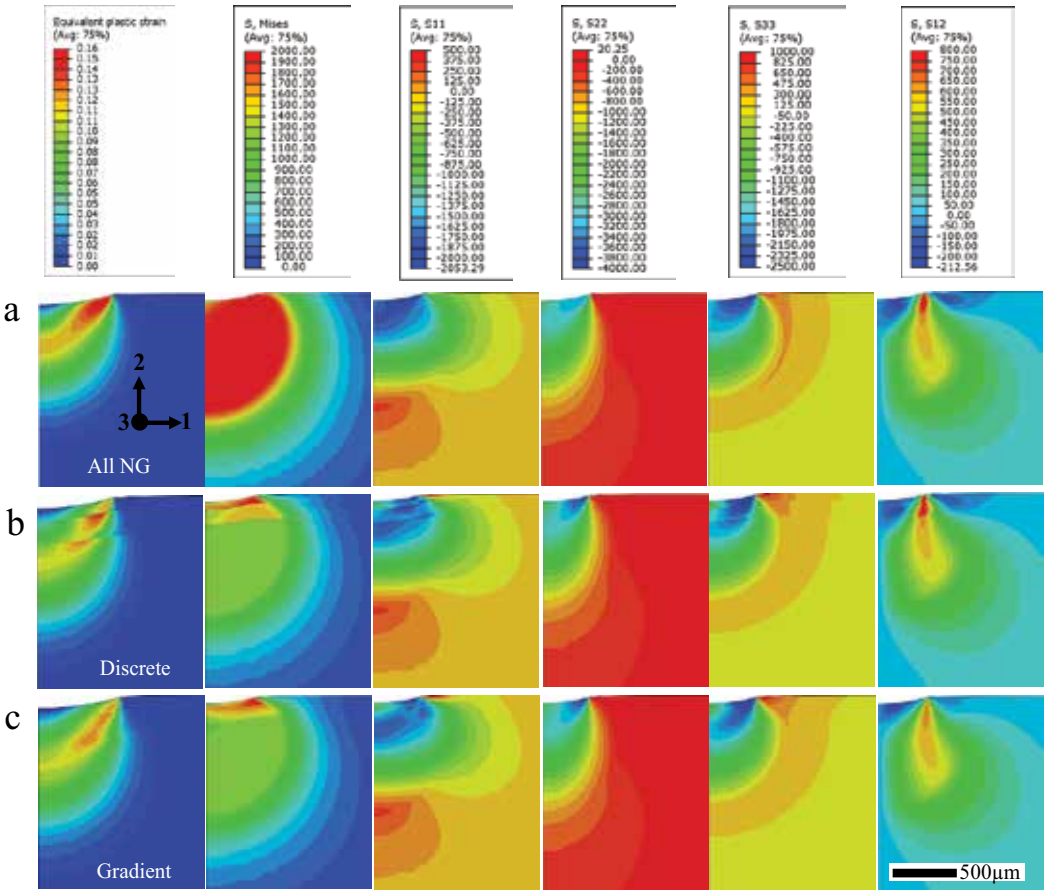

Figure 7. The simulated strain and stress contours for 1000 N maximum load indentation. (a) Monolithic NG, (b) discrete model, and (c) gradient model. S_{ii} (i = 1–3) represents the normal stress along i axis, and S_{12} is the shear stress that is in the plane perpendicular to the 1 axis and acts along the 2 axis.

layers with thicknesses matching their experimentally measured values (**Figure 6a**, left). In the discrete model, each layer was assumed to possess isotropic, elastic–perfectly plastic constitutive behavior with E and σ_Y taken as those calculated from FEA simulations of the averaged loading-depth data in **Figure 5**. The second "gradient" model is also composed of the three component layers with thickness corresponding to their experimental values and assumed isotropic elastic–perfectly plastic material property, but incorporates linear gradations (**Table 1**) in E (scaled by the measured $E_{O–P}$ gradation) and σ_Y (scaled by the measured $H_{O–P}$ gradation) within the material layers (**Figure 6a**, right). **Figure 6b** shows the FEA simulation results of these two models compared with three simulations of the single homogeneous component layer of the A/NC, NG layers and the UFG core. The predications of these two multilayered models show similar load–depth behavior and both fell in between the simulation of the A/NC and the NG layers.

Based on the FEA simulations, the mechanical behavior of the MHS material was explored by deducing each load–depth performance to an effective O–P modulus, effective microhardness and energy dissipation. The effective modulus and hardness predicted for the two models

(discrete and gradient systems) showed a loading-dependency, which is not the case for the single homogeneous systems (**Figure 6c** and **d**). The effective modulus and hardness for discrete and gradient systems decreased nonlinearly between that of the A/NC layer at small loads and the values corresponding to UFG core at maximum load of 10 N. Good agreement in the magnitude and the load dependency was achieved between the effective hardness and the experimentally measured microhardness (**Figure 6d**). The effective energy dissipation of these two models was found to increase with increasing load and all fell in between the A/NC layer and the UFG core (**Figure 6e**).

3.5. Strain and stress simulation

The contact load-bearing behavior of the MHSed Ti was further assessed using FEA to simulate the stress and strain distributions within the materials. **Figure 7** shows the stresses and corresponding equivalent plastic strain contours after unloading (maximum load of 1000 N) for the simulated multilayered systems (discrete and gradient) as compared with that of the monolithic NG material. As presented by the color contours, both the stresses and the equivalent strains exhibit graded distributions within the gradient model, as opposed to the abrupt changes observed in the discrete model. The maximum magnitude of equivalent plastic strain in the monolithic NG material (0.17) is greater than those in both the discrete and gradient multilayers (0.14 and 0.13, respectively). However, the multilayered models (discrete and gradient) achieve deeper and a broader plastic deformation field than that of the monolithic NG material. These simulations further suggest that the structural multilayering and grading modified the stress and strain distribution and reduce the overall plastic strain level throughout the material under indentation conditions.

4. Discussion

4.1. Structural multilayering

The present experimental studies show the plastic deformed area for the MHSed material was markedly greater than that for monolithic NG (**Figure 4**) and this is consistent with the results obtained from FEA microindentation simulations, where the indenter increasingly induces the more compliant UFG core as the load increases (**Figure 6c** and **d**). Further FEA simulations showed that the degree of energy dissipation (occurring by the inelastic deformation) of multilayered cases (discrete and gradient) increased with increasing load (**Figure 6e**). These results indicate that the macroscopic indentation behavior was directly governed by the underlying micromechanics of the multilayered structure. The load–depth FEA simulations (**Figure 6**) revealed that there was negligible difference in the load–depth response for the discrete and gradient models, suggesting that it is the overall structural multilayering that provides the effective macroscopic mechanical loading resistance rather than the grading.

Recent experimental nanoindentation studies, supported by cross-sectional electron microscopy observations, revealed that the multilayered structures provide a higher resistance to deformation than monolithic counterparts [25–27]. FEA simulations indicated that the structural layering

modified the stress distribution and reduced the overall strain values, suppressing crack formation [28]. In our present study, the multilayered models (discrete and gradient) showed a considerable redistribution of the overall equivalent plastic strain field and a significant reduction in the maximum strain levels (**Figure 7**). The plastic equivalent strain contours revealed an increased depth and strain area of plastic deformation for the multilayered systems compared with the monolithic NG material. This is a direct result of transferring the plastic strain to the underlying UFG core with a lower σ_Y than the NG layer, thereby diffusing the total plastic deformation energy. The FEA results coincide with the experimental results presented in **Figure 4** where the MHSed Ti diffuses plastic deformation over a greater region relative to the monolithic NG Ti.

4.2. Mechanical grading

The discrete and gradient models were shown to achieve similar macroscopic effective indentation modulus and microhardness (**Figure 6**). However, FEA simulations revealed differences in the stress and plastic equivalent strain distributions between gradient and discrete models after unloading (**Figure 7**). The magnitude of the equivalent plastic deformation in the top A/NC and NG layers in the gradient system is lower than that experienced in the discrete system. Further, the magnitude and area of plastic deformation in the UFG core are greater in the gradient system compared with the discrete system. This result reveals that the reduction in the stresses and plastic deformation in the top layers is a direct consequence of the increased deformation and energy dissipation accommodated by the softer inner UFG core. Moreover, the mechanical gradations in the successive layers and junctions are observed to give rise to more gradual stress redistribution between component layers, as opposed to the abrupt stress changes observed in the discrete model (**Figure 8**). Such graded stress distribution is believed to lessen the interface failure and increase the interfacial toughness, thus providing strong resistance to loading-damage [10, 29].

The different transition patterns between elastic and plastic deformation shown in **Figure 6** are consistent with the FEA simulation results. The smooth transitional region in the MHSed Ti is attributed to its graded stress distribution achieved by microstructural grading. The absence of any interfacial failure, such as delamination or fracture, observed between the layers in the

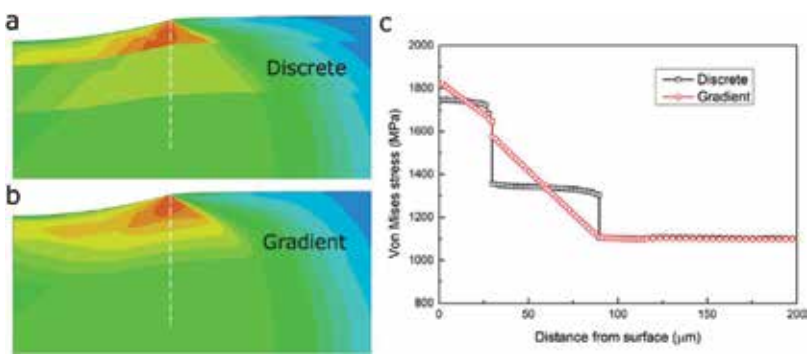

Figure 8. Distribution of Von Mises stress under the indentation regions in (a) discrete and (b) gradient models, while (c) shows the Von Mises stresses across the interfaces along the white dotted lines.

MHSed Ti under indentation further confirms that mechanical gradations provide resistance to interfacial failures. The smaller magnitude of the stresses and plastic deformation within the "stiffer" top layers and the greater plastic deformation in "softer" inner UFG core for the gradient system diffuse the total plastic deformation energy and offer a suppression to strain localization which occurred in the monolithic NG Ti (**Figure 4h**).

4.3. Cracks and stress concentrations

Identifying the linkage between stress and strain concentration and the initiation of cracks experimentally observed is one of the most important issues in FEA analysis. There are three types of cracks in hard materials under indentation conditions: edge, radial and lateral shear cracks (also known as delamination) [26, 28]. Edge cracks begin at the contact edge of the indentation and extend into the material, and are associated with the local tensile and shear stresses [28]. Lateral shear cracks are the result of shear strain localization arising from the high shear stress during indentation testing [30]. Radial cracks generally initiate directly under the indentation and propagates in a direction parallel to the indentation at excessive radial stresses [28]. The cracks observed in the present study (**Figure 4d** and **f**) agree well with the stress concentrations predicted by FEA simulations (**Figure 7**). The location of the edge cracks observed experimentally in monolithic NG Ti are consistent with the tensile stress (S11) and shear stress (S12) locations where the maximum tensile stress and shear stress appear immediately below the indenter (**Figure 7**). However, within the MHSed Ti, the stress (S11 and S12) variation is more gradual, with the shear stress reduced by 38% (0.21–0.13 GPa) at the maximum stress location. Such stress distribution and stress magnitude reduction explains the experimental observation that edge cracks were absent from the MHSed Ti but clearly occurred in monolithic NG Ti. The shear stresses in monolithic NG Ti are distributed over the plastic deformation region and coincide with the sites where shear bands were experimentally observed. With regards to the MHSed Ti, the multilayering and grading reduce the magnitude of maximum shear stress (**Figure 7**), therefore, the shear localized deformation was absent in the MHSed Ti (**Figure 4g**). These analyses reveal that multilayering and grading can significantly modify the stress field and effectively reduced the maximum stress concentration within the materials, thereby reduce the probability of cracks and shear localization which was commonly experienced in monolithic materials under indentation condition.

4.4. Other aspects contribute to the contact load-bearing

Our previous study [31] using micropillar compression testing has shown the deformation-induced precipitation of nanocrystals in the outer A/NC layer. The interaction of microcracks and shear bands with these nanocrystals allowed high ductility in this layer. This plasticity was evident in the present study by the indentation-induced deformation in the A/NC layer (**Figure 4a** and **e**). Previous studies demonstrated that the inelastic deformation occurring in the graded ceramics can contribute toward the cone-crack suppression [11, 12]. The susceptibleness of the A/NC layer to deform plastically reduces the propensity for cracking under indentation condition.

Residual stress may also be contributing to crack suppression in the deformed MHSed Ti structure. Residual surface compressive stress can be induced by various techniques to improve the contact damage resistance and strength of many brittle materials [32]. Further, multilayering and mechanical grading of a surface is known produce complex residual stresses [33, 34]. The residual stress–depth profile analysis [20] revealed that the MHSed Ti has residual compressive stresses through the layers and a tensile stress at the NG layer/UFG core interface. The residual compressive stress in A/NC and NG layers act to arrest crack development and increase damage resistance, however the residual tensile stress at NG/UFG junction theoretically increases the propensity for crack initiation under contact loading. Given the absence of cracking at the NG/UFG interface, it appears the reduction of maximum stress and the attendant of redistribution of the stresses arising from multilayering and mechanical grading more than compensate for the residual tensile stress.

5. Summary and conclusions

In summary, we report on both the contact load-bearing response and underlying deformation mechanism for MHSed Ti using indentation testing in combination with detailed computational simulations of local stresses and plastic deformation strain distributions. The results provide evidence for enhanced contact load-bearing resistance and energy dissipation by introducing multilayers and mechanical gradations into the surface region of the UFG material. This material design strategy is expected to applicable to a broad class of metallic materials. The following conclusions can be drawn from this study:

(1) The MHSed Ti exhibited enhanced resistance to contact loading damage compared to the monolithic NG Ti. The multilayering and grading of UFG materials suppressed the formation of cracks and increased the loading damage resistance.

(2) The macroscopic indentation resistance of the MHSed Ti arises from the underlying micromechanics of the multilayered structure. The overall multilayered structure offers the effective macroscopic mechanical loading resistance, where the loading increasingly induces the more compliant structure to bear the deformation as the load increases.

(3) The mechanical gradation provides a transitional junction for stress redistribution and achieves a more gradual stress distribution between component layers. Such a graded stress distribution mitigates the interface failure and increases the interfacial toughness, thus providing strong resistance to loading damage.

(4) The microstructural multilayering and grading of UFG metal can significantly modify the stress field and effectively reduce the maximum stress concentration within the material, thereby reduce the probability of cracks and shear localization which are commonly experienced in monolithic materials under indentation conditions.

Author details

Dengke Yang[1,2]*, Jiangting Wang[2], Huimin Yang[3] and Peter Hodgson[2]

*Address all correspondence to: dkyang@issp.ac.cn

1 School of Materials Science and Engineering, Anhui University of Technology, Anhui, China

2 Institute for Frontier Materials, Deakin University, Victoria, Australia

3 China National Bamboo Research Center, Zhejiang, China

References

[1] Miyamoto Y, Kaysser WA, Rabin BH, Kawasaki A, Ford RG, editors. Functionally Graded Materials: Design, Processing and Applications. 1st ed. Boston: Springer US; 1999. 330 p. DOI: 10.1007/978-1-4615-5301-4

[2] Suresh S. Graded materials for resistance to contact deformation and damage. Science. 2001;**292**(5526):2447-2451. DOI: 10.1126/science.1059716

[3] Prasada A, Dao M, Suresh S. Steady-state frictional sliding contact on surfaces of plastically graded materials. Acta Materialia. 2009;**57**(2):511-524. DOI: 10.1016/j.actamat.2008.09.036

[4] Kieback B, Neubrand A, Riedel H. Processing techniques for functionally graded materials. Materials Science and Engineering: A. 2003;**362**(1-2):81-106. DOI: 10.1016/S0921-5093(03)00578-1

[5] Kesler O, Matejicek J, Sampath S, Suresh S, Gnaeupel-Herold T, Brand PC, Praskc HJ. Measurement of residual stress in plasma-sprayed metallic, ceramic and composite coatings. Materials Science and Engineering: A. 1998;**257**(2):215-224. DOI: 10.1016/S0921-5093(98)00860-0

[6] Giannakopoulos A, Suresh S. Indentation of solids with gradients in elastic properties: Part I. Point force. International Journal of Solids and Structures. 1997;**34**(19):2357-2392. DOI: 10.1016/S0020-7683(96)00171-0

[7] Suresh S, Giannakopoulos A, Olsson M. Elastoplastic analysis of thermal cycling: Layered materials with sharp interfaces. Journal of the Mechanics and Physics of Solids. 1994; **42**(6):979-1018. DOI: 10.1016/0022-5096(94)90081-7

[8] Chen AY, Li YK, Zhang JB, Pan D, Lu J. The influence of interface structure on nanocrystalline deformation of a layered and nanostructured steel. Materials & Design. 2013;**47**:316-322. DOI: 10.1016/j.matdes.2012.11.050

[9] Munch E, Launey ME, Alsem DH, Saiz E, Tomsia AP, Ritchie RO. Tough, bio-inspired hybrid materials. Science. 2008;**322**(5907):1516-1520. DOI: 10.1126/science.1164865

[10] Bruet BJ, Song J, Boyce MC, Ortiz C. Materials design principles of ancient fish armour. Nature Materials. 2008;**7**:748-756. DOI: 10.1038/nmat2231

[11] Jitcharoen J, Padture NP, Giannakopoulos AE, Suresh S. Hertzian-crack suppression in ceramics with elastic-modulus-graded surfaces. Journal of the American Ceramic Society. 1998;**81**(9):2301-2308. DOI: 10.1111/j.1151-2916.1998.tb02625.x

[12] Pender D, Padture N, Giannakopoulos A, Suresh S. Gradients in elastic modulus for improved contact-damage resistance. Part I: The silicon nitride–oxynitride glass system. Acta Materialia. 2001;**49**(16):3255-3262. DOI: 10.1016/S1359-6454(01)00200-2

[13] Pender D, Thompson S, Padture N, Giannakopoulos A, Suresh S. Gradients in elastic modulus for improved contact-damage resistance. Part II: The silicon nitride–silicon carbide system. Acta Materialia. 2001;**49**(16):3263-3268. DOI: 10.1016/S1359-6454(01)00201-4

[14] Giannakopoulos A. Indentation of plastically graded substrates by sharp indenters. International Journal of Solids and Structures. 2002;**39**(9):2495-2515. DOI: 10.1016/S0020-7683(02)00110-5

[15] Choi I, Dao M, Suresh S. Mechanics of indentation of plastically graded materials—I: Analysis. Journal of the Mechanics and Physics of Solids. 2008;**56**(1):157-171. DOI: 10.1016/j.jmps.2007.07.007

[16] Ruan H, Chen A, Lu J. Characterization of plastically graded nanostructured material: Part I. The theories and the inverse algorithm of nanoindentation. Mechanics of Materials. 2010;**42**(5):559-569. DOI: 10.1016/j.mechmat.2010.02.005

[17] Kot M, Rakowski W, Lackner JM, Major L. Analysis of spherical indentations of coating-substrate systems: Experiments and finite element modelling. Materials & Design. 2013;**43**:99-111. DOI: 10.1016/j.matdes.2012.06.040

[18] Choi I, Detor A, Schwaiger R, Dao M, Schuh C, Suresh S. Mechanics of indentation of plastically graded materials—II: Experiments on nanocrystalline alloys with grain size gradients. Journal of the Mechanics and Physics of Solids. 2008;**56**(1):172-183. DOI: 10.1016/j.jmps.2007.07.006

[19] Ruan H, Chen A, Chan H, Lu J. Characterization of plastically graded nanostructured material: Part II. The experimental validation in surface nanostructured material. Mechanics of Materials. 2010;**42**(7):698-708. DOI: 10.1016/j.mechmat.2010.04.007

[20] Yang DK, Cizek P, Fabijanic D, Wang JT, Hodgson P. Work hardening in ultrafine-grained titanium: Multilayering and grading. Acta Materialia. 2013;**61**(8):2840-2852. DOI: 10.1016/j.actamat.2013.01.018

[21] Lu K, Jian L. Surface nanocrystallization (SNC) of metallic materials-presentation of the concept behind a new approach. Journal of Materials Science & Technology. 1999;**15**(3):193-197

[22] Yang D, Hodgson P, Wen C. Simultaneously enhanced strength and ductility of titanium via multimodal grain structure. Scripta Materialia. 2010;**63**(9):941-944. DOI: 10.1016/j.scriptamat.2010.07.010

[23] Fang T, Li W, Tao N, Lu K. Revealing extraordinary intrinsic tensile plasticity in gradient nano-grained copper. Science. 2011;**331**(6024):1587-1590. DOI: 10.1126/science.1200177

[24] Oliver WC, Pharr GM. An improved technique for determining hardness and elastic modulus using load and displacement sensing indentation experiments. Journal of Materials Research. 1992;**7**(6):1564-1583. DOI: 10.1557/JMR.1992.1564

[25] Kot M, Rakowski W, Major L, Lackner J. Load-bearing capacity of coating–substrate systems obtained from spherical indentation tests. Materials & Design. 2013;**46**:751-757. DOI: 10.1016/j.matdes.2012.11.026

[26] Xie Z, Hoffman M, Munroe P, Bendavid A, Martin P. Deformation mechanisms of TiN multilayer coatings alternated by ductile or stiff interlayers. Acta Materialia. 2008;**56**(4):852-861. DOI: 10.1016/j.actamat.2007.10.047

[27] Wo PC, Munroe PR, Zhou Z, Li KY, Xie ZH. Effects of TiN sublayers on the response of TiSiN nanocomposite coatings to nanoidentation and scratching contacts. Materials Science and Engineering: A. 2010;**527**(16-17):4447-4457. DOI: 10.1016/j.msea.2010.03.100

[28] Zhao X, Xie Z, Munroe P. Nanoindentation of hard multilayer coatings: Finite element modelling. Materials Science and Engineering: A. 2011;**528**(3):1111-1116. DOI: 10.1016/j.msea.2010.09.073

[29] An B, Wang R, Arola D, Zhang D. The role of property gradients on the mechanical behavior of human enamel. Journal of the Mechanical Behavior of Biomedical Materials. 2012;**9**:63-72. DOI: 10.1016/j.jmbbm.2012.01.009

[30] Abdul-Baqi A, Van der Giessen E. Indentation-induced interface delamination of a strong film on a ductile substrate. Thin Solid Films. 2001;**381**(1):143-154. DOI: 10.1016/S0040-6090(00)01344-4

[31] Yang DK, Wang JT, Fabijanic D, Cizek P, Li BS, Lu JZ. Ti-based amorphous/nanocrystal composite with high ductility and strain-hardening. Materials Science and Engineering: A. 2013;**560**(10):339-342. DOI: 10.1016/j.msea.2012.09.076

[32] Green D, Tandon R, Sglavo V. Crack arrest and multiple cracking in glass through the use of designed residual stress profiles. Science. 1999;**283**(5406):1295-1297. DOI: 10.1126/science.283.5406.1295

[33] Lu K, Lu J. Nanostructured surface layer on metallic materials induced by surface mechanical attrition treatment. Materials Science and Engineering: A. 2004;**375-377**:38-45. DOI: 10.1016/j.msea.2003.10.261

[34] Lee S, Saito Y, Tsuji N, Utsunomiya H, Sakai T. Role of shear strain in ultragrain refinement by accumulative roll-bonding (ARB) process. Scripta Materialia. 2002;**46**(4):281-285. DOI: 10.1016/S1359-6462(01)01239-8

Chapter 6

Modeling Friction for Turbomachinery Applications: Tuning Techniques and Adequacy Assessment of Heuristic Contact Models

Chiara Gastaldi

Additional information is available at the end of the chapter

http://dx.doi.org/10.5772/intechopen.72676

Abstract

Friction dampers are commonly included into turbine designs to limit the turbine blades resonant vibrations and thus avoid high cycle fatigue failures. In order to effectively predict the effect of friction dampers on the turbine dynamics, friction is included into the simulation through specific mesoscale contact models. These models require knowledge of contact parameters to offer meaningful predictions. Standard single-contact test arrangements may fail to capture the true contact conditions and kinematics of friction dampers, especially for complex multi-interface contacts interested by variable normal loads. Several methodologies have been proposed in the literature: the lack of a "shared" approach in the field pinpoints a true "gap" in the research. Overcoming this difficulty is of primary importance, as it is the one feature that separates a state-of-the-art numerical code from a true design tool. Purpose of this chapter is to illustrate the experimental/numerical tools and methods developed to fill this gap for a common family of friction dampers, called "underplatform dampers" with a curved-flat cross section. Both cylinder-on-flat and flat-on-flat interfaces are addressed. The adequacy of the state-of-the-art contact model is discussed on the basis of a large data set obtained performing an extended experimental campaign on multiple damper samples.

Keywords: contact modelling, contact parameters estimation, case studies, underplatform damper, friction damping

1. Introduction

High cycle fatigue failure is a primary concern among operators and suppliers of turbo engines because of their suddenness [1].

They are caused by the large response levels at resonance. Since turbine blades do not benefit significantly from material hysteresis and aerodynamic damping, the only option is to add external sources of damping, for example, in the form of dry friction devices [2, 3] such as the underplatform damper. Underplatform dampers, available in several shapes (cylindrical, curved-flat and wedge-like), are small metallic objects placed on the underside of two adjacent blades. As shown in **Figure 1a**, the centrifugal force (CF) provides the necessary precompression and the resonant-induced blade vibration triggers the damper-platform relative motion and therefore friction dissipation. Dampers are extensively used in turbine designs because they are easy to manufacture, install and substitute, while relatively inexpensive.

Whenever a damper is added to the bladed system, its dynamic response is modified into two fundamental ways:

- the blades' resonant frequencies increase since the damper acts as an additional constraint (with a given stiffness) between the platforms and
- the blades' response diminishes for the combined effect of the stiffness introduced by the damper (which acts as a constraint) and of friction damping.

An additional complication is posed by the nonlinearity introduced by friction: it is well known that the non-linear dynamic response of bladed systems (both in frequency and maximum amplitude) is tightly coupled to the motion of the damper and its contact states (stick-slip-separation).

Accounting for the presence of friction is not an easy task. The presence of friction-induced nonlinearities makes solving the equilibrium equations a challenging task, therefore standard FE codes are not suited to the purpose: a complex hierarchy of techniques has been developed, a thorough review can be found in [4]. Furthermore, modeling friction entails:

1. finding a reliable model for the force-displacement relation at the contact interface and
2. a proper way to estimate its parameters.

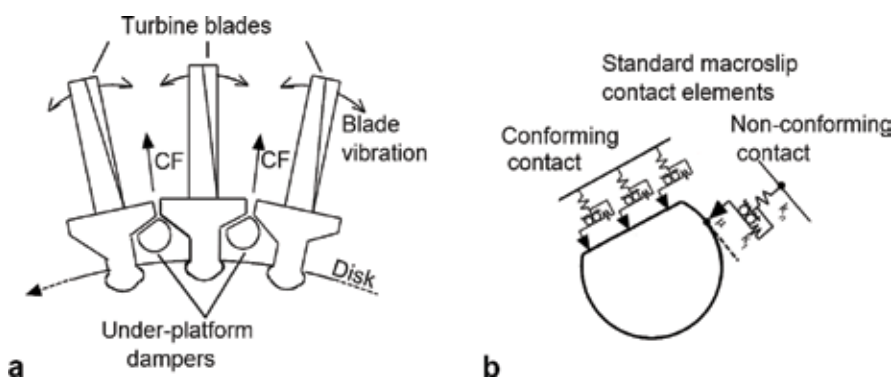

Figure 1. (a) Sketch representing curved-flat underplatform dampers mounted on a turbine disk. (b) Example of standard macroslip contact element used to represent conforming and nonconforming contacts.

1.1. A quick critical review of contact modeling in the turbomachinery field

In the technical literature, the problem of modeling periodical contact forces at friction contacts is still ongoing [5] and has been addressed by several authors, leading to different contact models and techniques. Some authors adopt a Dynamic Lagrangian method to solve on the contact patch [6, 7], that is, the contact constraints are taken into account in their non-regularized form without additional compliance. Other authors, for example, [4, 8] apply a contact element to each meshed node belonging to the contact area, introducing normal and tangential stiffnesses and a Coulomb friction law. This last method is preferred here, as its calibration parameters (k_n, k_t and μ), however difficult to determine, represent a physical measurable property.[1]

The contact elements typically used in turbomachinery belong to the "spring-slider" family, a class of displacement-dependent contact models which neglect features like viscous forces along the normal direction and friction's velocity-dependence. These features, while relevant in other fields, are not typically considered in turbomachinery applications. These models belong to the larger family of heuristic models, as opposed to microscale "realistic" models where asperities and surface roughness are modeled using stochastic distributions [9].

These interactions can be geometrically divided in the normal and the tangential directions. A unilateral contact law is often considered in the normal direction (with or without normal contact stiffness) and frictional law for the tangential contact. The spring-slider elements have undergone an evolution, starting from 1D tangential motion without normal compliance [2] up to a fully coupled 3D motion [10], passing through a 1D element with normal compliance (2D motion) [11]. This last element has been adopted by many authors because of its simplicity and versatility. In fact, it can be applied to represent 1D in-plane relative motion (a quite common occurrence if the first bending modes of the blades are considered), or, with a simple upgrade [12], to give a simplified representation of 2D in-plane motion.[2]

Modeling conforming (i.e. flat-on-flat) or nonconforming (e.g. cylinder-on-flat) surfaces requires a different strategy. Nevertheless, the same standard macroslip contact element presented in [11] can be applied (as it is done in this Chapter, see also **Figure 1b**).

Conforming contact surfaces are typically discretized into contact points (or nodes in FE terms) and each one is assigned a standard macroslip element, either with uncoupled 2D in-plane motion [8, 13, 14] or with a coupled one [15]. This choice allows to account for the presence of "microslip", first theorized by Cattaneo in 1938 [16], and later explored by Mindlin [17]. Modeling microslip is particularly relevant in those cases where high normal loads prevent actual slipping of the complete interface: in that case the gradual loss of stiffness that forecomes gross slip and the consequent dissipation does have an impact on the system response, while it becomes negligible if the gross slip regime is reached [18].

Nonconforming contacts are, in most cases, represented using one of the standard macroslip contact elements described above. Recently, a novel contact element, fit to take into account microslip as well as the nonlinearity in the normal direction typical of nonconforming contacts, has been proposed [18].

---

[1]Furthermore, Herzog et al. [7] have shown that Dynamic Lagrangians may incur in convergence problems for penalty parameters lower than 107 N/m, thus highlighting a possible limitation of their use in case of "softer" contact interfaces.
[2]Where the 2D tangential motion is albeit considered as the combination of two uncoupled 1D motions.

Other ad-hoc elements built to take into account microslip exist [19–24], however they are typically applied to conforming surfaces, which is somewhat limiting, as the kinematics of the contact, which play a significant role in the non-linear dynamic behavior, are not well represented.

1.2. A quick critical review of contact parameter estimation

All contact models require knowledge or information of contact-friction parameters to provide meaningful predictions.

Realistic models, based on the integration over the whole contact surface of mechanical principles applied at the asperity level, for example [9], are the only kind which allow for a predictive contact parameter estimation. In other words, these models can be calibrated using information concerning the geometry, roughness distribution, material properties, etc. Unfortunately, at least in many applications such as the turbomachinery field, this level of refinement has not yet been achieved and heuristic models are preferred.

Heuristic models are instead based on phenomenological friction laws (e.g. Coulomb's friction law), and their calibration is based on fitting to empirical observations.

Taking a state-of-the-art macroslip contact model with normal compliance described in Section 1.1, the parameters to be determined are normal and tangential contact stiffness k_n and k_t and friction coefficient μ.

The first, and perhaps, most obvious choice, is the use of single-contact test arrangements capable of providing the hysteresis cycle at a given (constant) normal load. Friction coefficients can be easily determined taking the ratio of the limit value of the tangential friction force during slip and the corresponding normal load [5, 25]. Tangential contact stiffness k_t [2, 25–27] can be estimated by taking the slope of the hysteresis curve in stick condition. This methodology is effective, as it can explore different temperatures, mean normal loads and frequencies. However, as will be shown in the following sections, it may fail to capture the true contact conditions and kinematics, especially for complex multi-interface contacts such as underplatform dampers.

Other methods are available, especially for the determination of contact stiffness values.

1. A complete analytical solution (k_n and k_t) is available only for circular or elliptical contact areas (i.e. Hertz theory), thus of limited interest in turbomachinery applications, while the normal compliance (k_n) is available for cylinder-on-flat contacts [28].
2. Another possibility is to mimic the single-contact tests using non-linear FE analysis [29]: two contacting bodies are modeled using a very fine FE mesh and each node is assigned a Coulomb-like slip criterion. Stiffness values are evaluated from computed force-deformation curves. Results were found to be 6–11% higher with respect to measured counterparts, possibly because of *"the neglected surface roughness as well as adhesive contact and viscous-elastic solid behavior"* [30].
3. In 2002, the "residual stiffness" method was proposed [31]. It is based on the observation that typical reduction techniques (e.g. CB-CMS [4]), used to reduce the size of FE models, may neglect the small local deformations. A "correction factor" is introduced to take into

account this effect. Unfortunately, a study performed in [32] suggests that this method gives a poor estimation of the contact stiffnesses.

4. In 2009, Allara [33] proposed a model to determine k_n and k_t of a 3D flat indenter with rounded edges pressed against an infinite half-plane. However, its results were found to be overestimating observed compliances [34].

5. The last (and perhaps the most popular) method is based on tuning against experimental [35] or numerically obtained [36] Frequency Response Functions (FRFs). Contact stiffness values are tuned until the experimental (or full FE model) evidence and that obtained from the reduced model with contact elements match. This operation is performed using evidence in full stick condition, so that all contact stiffness are "active" and accounted for.

One common point to approaches 2, 3 and 5 is that they use, as a benchmark, the solution offered by the full model in the FE software environment. This implies relying predictions performed with the Penalty or the Augmented Lagrangian Method to enforce the impenetrability condition and neglecting the possible influence of surface roughness.

Using, as a benchmark, numerical evidence is certainly quite convenient, as it does not require experiments and it is generally quite "complete" (the user can interrogate the software and retrieve displacements, stresses at any point of the mesh). However, it is based on the strong assumption that sees the full FE model as representative of the true contact conditions.

Approach 5 is usually regarded as the fastest and most effective, as it guarantees that the simulated target evidence matches the reference one. However, this local adjustment of parameters does not truly add knowledge to the field. In fact, it has a strong ad-hoc character, and must be repeated for every new system the designer comes across.

Another possible "drawback" of approach 5 is the possible under-determinacy of the contact parameter problem. As shown in [37], there exist multiple combinations of contact parameters capable of satisfying a given FRF. Therefore, if the number of contact parameters to be determined is larger than the (observed or computed) target features to be matched during tuning (or the influence of contact parameters is weak on the available target features), multiple solutions are possible. Two sets of contact parameters which produce equivalent responses at a given excitation level, may give rise to radically different solutions if the excitation level changes (see **Figure 1**, for example, with a curved-flat damper between a set of blades). This may not be a critical issue if a large number of target evidence can be produced (e.g. if the reference evidence is obtained numerically) and/or if the contact parameters to be determined are limited. However, it becomes a strong limitation if curved-flat underplatform dampers, characterized by a complex kinematics and multiple contact interfaces, are considered.

For all these reasons, it is here believed that the contact parameter estimation problem should be tackled using dedicated experimental evidence which focuses on the damper-blade interface. An increased attention to the damper kinematics has been demonstrated by other notable researchers in the field: in detail in [8] laser measurements have been employed to record damper rotation, while in [38] Digital Image Correlation has been used to investigate contact displacements.

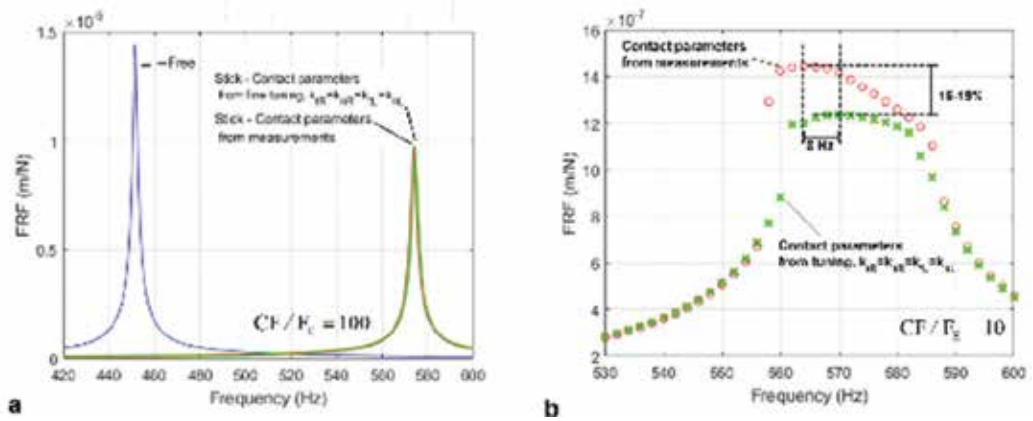

Figure 2. (a) Example of tuning of contact parameters in the full stick regime: two sets of contact parameters (one from Section 3 and one with a simplified assumption) leading to the "same" FRF. (b) Resulting FRFs (excitation level out of the tuning range) produced by the two sets of contact parameters from **Figure 1a**. CF: centrifugal force on the damper, F_E: external excitation on blades.

1.3. Goals of the chapter

The main purpose of this chapter is to present the latest advances made by the AERMEC lab to improve the fidelity of damper modeling and to rigorously assess processes needed for reliable predictions/estimation of contact parameters (see **Figure 2**).

In detail, Section 2 briefly describes the Piezo Damper Rig (see **Figure 3a**), first presented in [39], and recounts its latest improvements.

Section 3 with reference to Section 1.1, defines a numerical damper model (also represented in **Figure 3b**) and justifies all modeling choices.

Section 3.2 uses the experimental evidence gathered on the above-mentioned rig to estimate all contact parameters necessary to represent a curved-flat damper between a set of platforms (conforming and nonconforming surfaces both).

In Section 4, the adequacy of the chosen contact model is discussed on the basis of an experimental campaign on numerous damper samples. Furthermore, the role of rotation of nonconforming contacts, a topic which has never been addressed in this context to the author's knowledge, will be explored.

The chapter conclusion (Section 5) includes a series of warning and recommendation for the damper designer/tester.

2. Experimental evidence

The majority of the rigs developed to test underplatform dampers see a bladed system (equipped with dampers) excited at resonance [8, 35]. Often, the FRF of the system is used as

the sole indicator of the damper performance. The FRF is certainly an important design indicator, however by itself, it is not capable of offering enough information on the damper working conditions. Furthermore, if FRFs are the only experimental evidence available it is likely that, as pointed out in Section 1.2, the contact parameter problem will remain underdetermined.

2.1. The Piezo Damper Rig

For all these reasons, in 2009, the AERMEC lab proposed a novel kind of test rig (see **Figure 3a**) which focuses directly on the underplatform damper. No blades are present (i.e. it is not a resonant rig). On the other hand, two dummy platforms are used to connect the system to the input motion generation and to the force measuring mechanism.

- The left platform is connected to two piezoelectric actuators inserted into a purposely designed mechanical structure. This system allows imposing any user-defined in-plane displacements simulating the so-called In-Phase (IP, vertical) and Out-of-Phase (OOP, horizontal) relative motion between the blades platforms or combinations of the two.
- The right platform is connected to two uniaxial force sensors by means of a tripod structure to the purpose of measuring the forces transmitted between the two platforms through the damper.

The damper is pulled by a deadweight simulating the centrifugal force, CF. The main purpose of the rig is to relate contact forces to the displacements that produce them (see also **Figure 3c**). For this reason, a differential laser head is employed to measure the platforms relative displacement (a necessary precaution owing to the lack of closed loop control of the piezoelectric actuators), the damper radial displacement and rotation angle and the damper-platform relative displacement at the contact. A scheme representing the laser positioning to obtain the tangential relative motion at the contacts and the damper rotation is shown in **Figure 3d**.

2.2. The test rig evolution

The key features of the test rig described above remain unchanged since its first version [39], however several subsequent improvements have been performed (see **Figure 4** for a graphical representation). In detail, the tripod and the structure hosting the force sensors have been redesigned to increase the overall stiffness of the rig [18]. This had a positive impact over the frequency operating range which increased from [≈5–80] Hz to [≈5–160 Hz]. In [40] each platform has been redesigned into two parts: a "fixed" part connected to the rest of the test rig (the left platform to the actuators, the right one to the force sensors) and a second part, termed here "insert" in contact with the damper. This configuration has several advantages: (i) the "insert" can be substituted to test different platform angles, (ii) the contact is localized along the damper axis by means of 4 mm wide protrusions present on both platform inserts which ensure high contact pressures even with moderate deadweights on the damper.

Lastly, the new platform inserts and dampers have been machined with cube-like protrusions oriented with one of the faces perpendicular to the contact line. Each contact line (left and right) is equipped with two cubes (one on the damper and one on the corresponding platform).

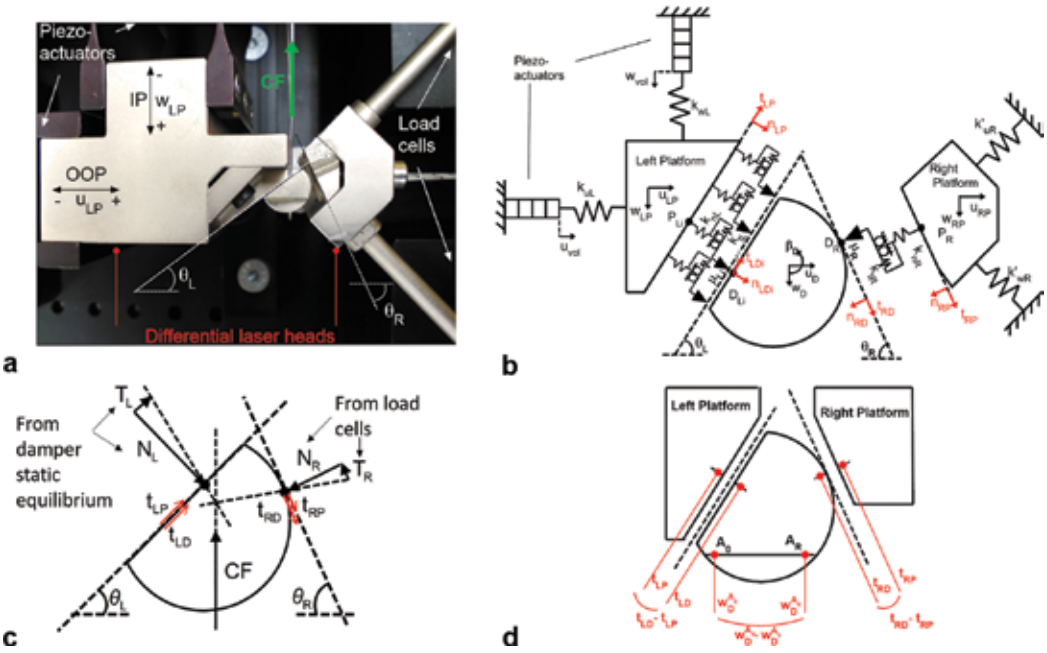

Figure 3. (a) Piezo Damper Rig scheme and relevant quantities. (b) Piezo Damper Rig numerical model. (c) Measured and derived contact forces. (d) Laser positioning to obtain relevant kinematical quantities.

Diagram	Goal	Quantities	Measurement technique	Uncertainty
T/N force ratios (**Figure 5a**)	Estimate friction coefficient	T_R/N_R	Derived	3–5%
	Identify contact states	T_L/N_L	Derived	6–10%
Hysteresis at nonconforming contact	Estimate tangential contact stiffness	t_{RD}-t_{RP}	Laser vibrometer	0.08 μm (~0.2%)
		T_R	Load cells	2%
Hysteresis at conforming contact (**Figure 5b**)	Estimate tangential contact stiffness	t_{LD}-t_{LP}	Laser vibrometer	0.08 μm (~0.2%)
		T_L	Derived	2.5%
Moment vs. Rotation diagram (**Figure 5c**)	Estimate normal contact stiffness (conf. contact)	β_D	Derived[1]	5%
		$M = N_L * x$	Derived	5–7%
Platform-to-platform hysteresis cycle (**Figure 5d**)[2]	Validation	w_{LP}-w_{RP}	Laser vibrometer	0.08 μm (~0.2%)
		V_R	Load cells	2%
Contact forces diagram (**Figure 6a**)	Validation, check position of left contact force	T_R, N_R		2%
		T_L, N_L, application point		2.5%, <1 mm

[1]Damper rotation is here obtained as described in, that is, with reference to **Figure 3d**, $\beta_D = \left(w_D^{A_0} - w_D^{A_R}\right)/\overline{A_0 A_R}$.

[2]This example is carried out in case of IP motion, a similar diagram can be obtained in case of OOP motion by plotting the horizontal force component H_R against the corresponding horizontal platform relative displacement $u_{LP} - u_{RP}$.

Table 1. Essentials in damper diagrams.

This allows for the direct measurement of the tangential relative motion at the contact (as shown in **Figure 3d**): this constitutes a true improvement in the test rig capabilities since it allows, as described in Section 3, for the estimation of the tangential contact stiffness values.

2.3. Measurement protocol

Each experimental nominal condition is defined by: damper configuration (i.e. shape, platform angles, etc.), centrifugal load on the damper, excitation frequency, amplitude and direction of motion.

The analysis of the damper performance under each nominal experimental condition is operated through the cross-comparison of a series of quantities (whose graphical representation can be found in **Figure 3b–d**) organized into diagrams (summarized in **Table 1**, shown in **Figures 5** and **6** and further commented in Section 3.2). Both contact forces and damper/platform kinematics are taken into account for the purpose of uncovering the cross-relations existing between them and to estimate contact parameters. It should be noted that some of these quantities are directly measured (e.g. tangential and normal forces at the nonconforming contact T_R and N_R and all damper displacements), while other quantities are derived (e.g. tangential and normal forces at the conforming contact T_L and N_L are obtained through the damper equilibrium by neglecting inertia forces at frequencies where this is correct, as shown

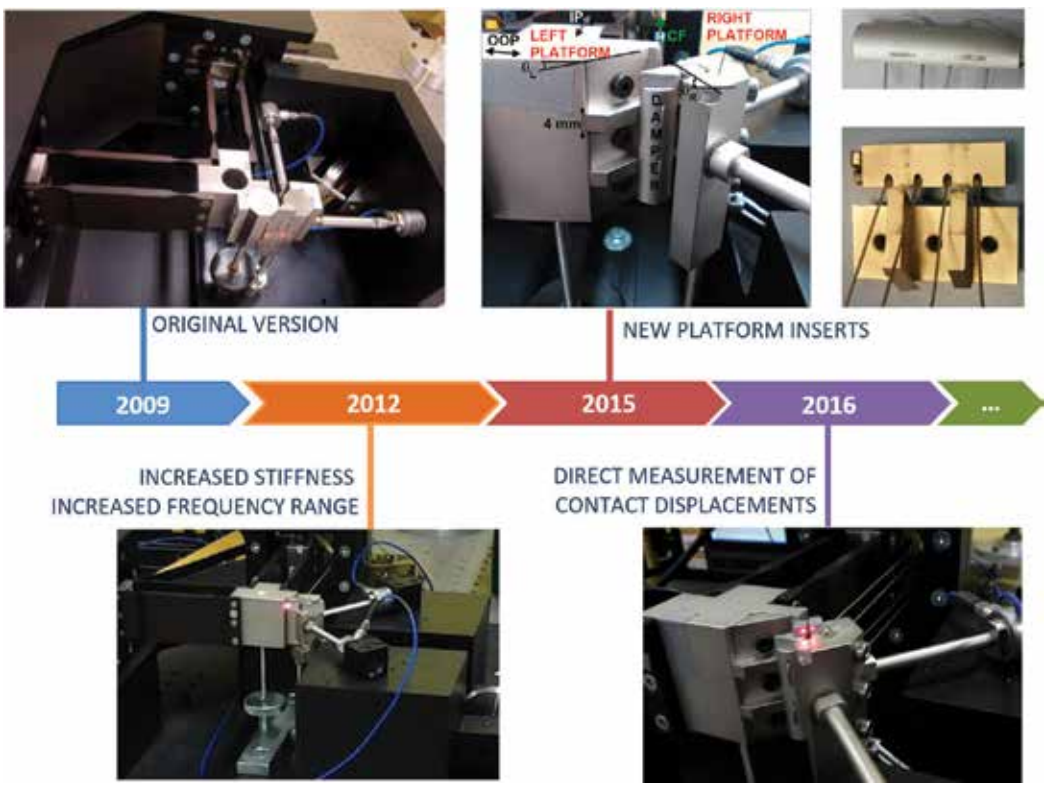

Figure 4. Piezo Damper Rig evolution.

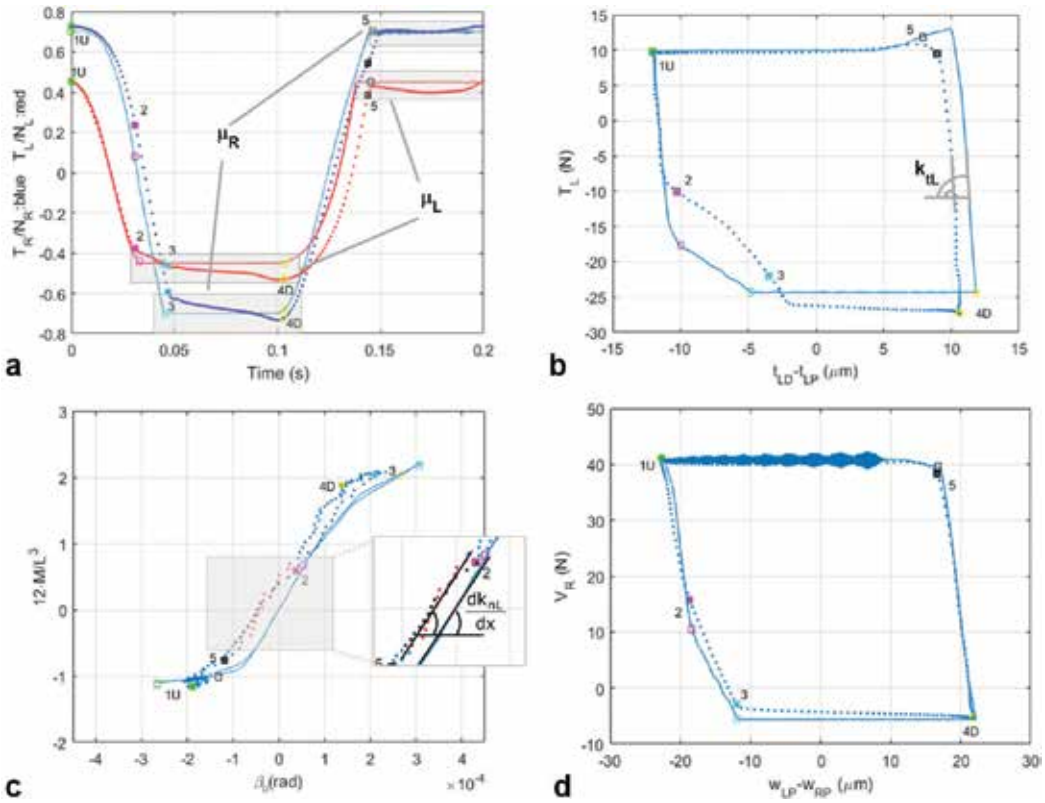

Figure 5. Measured vs. simulated. (a) T/N force ratio diagram. (b) Platform-to-damper hysteresis cycle at the flat-on-flat contact. (c) Moment vs. rotation diagram. (d) Platform-to-platform hysteresis cycle. Measured: dotted line, simulated: solid line. IP case, with CF = 4.65 kg.

in **Figure 3c**). Each quantity is equipped with a proper level of uncertainty. Measurement uncertainty, minimized through a purposely developed protocol, ensures significant trustworthy results (error up to 7%).

3. Numerical model and contact parameters estimation

The diagrams summarized in **Table 1** and shown in **Figures 5** and **6a** are represented together with the corresponding simulated counterpart, obtained using the numerical model shown in **Figure 3b**.[3] The numerical model represents the damper inside the test rig, however the same numerical routine can be incorporated into a code which substitutes the test rig presence with that of a FE bladed system [35].

[3]The springs representing the tripod and the mechanical structure hosting the piezo actuators have been experimentally measured as described in [39].

Only in-plane motion is addressed here (typical of blades bending modes, where dampers are most effective), however a more general 3D version of the same model is available for more complex cases. The general equilibrium equation to be solved at this stage is:

$$[M]\{\ddot{U}\} + [K]\{U\} = \{F_e\} + [T]\{F_C\} \tag{1}$$

where with reference to **Figure 3b**, $[M] = diag(m_D, m_D, m_D, m_{LP}, m_{LP}, m_{RP}, m_{RP})$, $[K] = diag\left(0, 0, 0, k_{uL}, k_{wL}, [k'_R]\right)$ with $[k'_R] = \begin{bmatrix} k'_{uR}\cos^2\alpha + k'_{wR}\sin^2\alpha & (k'_{uR} - k'_{wR})\sin\alpha\cos\alpha \\ (k'_{uR} - k'_{wR})\sin\alpha\cos\alpha & k'_{uR}\sin^2\alpha + k'_{wR}\cos^2\alpha \end{bmatrix}$, $\{U\} = \{u_D, w_D, \beta_D, u_{LP}, w_{LP}, u_{RP}, w_{RP}\}$, $\{F_E\} = \{0, -CF, 0, k_{uL}\cdot u_{vol}, k_{wL}\cdot w_{vol}, 0, 0\}$, $\{F_C\} = \{T_R, N_R, T_{L1}, N_{L1}, \ldots, T_{Ln_c}, N_{Ln_c}\}$ and $[T]$ is a transformation matrix. In detail, vector $\{F_C\}$ is the output of the contact elements which are fed by the correct relative displacements at the contact.

In this chapter, Direct Time Integration [40] is used to avoid approximations, however should a larger system be considered, multi-Harmonic Balance Method can be applied [35].

The reader will notice that the damper is modeled as a rigid body, a quite reasonable assumption given the bulkiness of the damper.

The contact elements here applied are state-of-the-art in the gross slip regime [11], which is the focus of this chapter's investigation. The nonconforming contact (cylinder-on-flat) is modeled using one element, while the conforming contact requires at least two contact elements (four in **Figure 3b**). Increasing the number of contact elements will smoothen the hysteresis shape but not change significantly the damper behavior. The position of the contact points is typically set at equal intervals along the flat interface using the two edges as limits (i.e. starting and ending points).

3.1. Definition of the unknowns

In principle, friction is a material property, therefore all interfaces, both conforming and nonconforming, should share the same contact parameter values. Friction is indeed a material property at microscopical level, therefore if a reliable and validated "realistic" model was available one could start from material properties and surface characteristics, and integration over the contact area would do the rest. However, since the selected contact elements are of the "heuristic" kind, other factors influence k_n, k_t and μ values.

In detail previous experience has shown that the geometry of the contact surface (line vs. area contact), contact surface kinematics and normal load play a significant role [37]. The influence of normal load will be addressed in Section 4, while, in order to take into account the influence of the contact areas different geometries and kinematics, it holds:

$$\begin{aligned} k_{nR} &\neq k_{nL} \\ k_{tR} &\neq k_{tL} \\ \mu_R &\neq \mu_L \end{aligned} \tag{2}$$

for a total of six unknowns (also represented in **Figure 3b**).

Contact parameters of the flat-on-flat interface are typically distributed uniformly among the contact points, for example, considering the normal contact spring:

$$k_{nLi} = \frac{k_{nL}}{n_C} \tag{3}$$

The validity of this assumption will be further assessed in Section 4.

3.2. Step-by-step contact parameter estimation procedure

Contact parameters are estimated starting from the experimental evidence, organized into diagrams as summarized in **Table 1**. In detail, for a given experimental nominal condition:

Step 1. Reference points on the diagrams in **Figure 5** have been marked by a symbol and a number: they are useful to guide the analysis of the cycle through cross-comparison.

Step 2. The cross-comparison of the T/N diagram (**Figure 5a**) and of the observed relative displacement at the contact interfaces can be used to make a hypothesis on the contact states experienced by the damper during one period of vibration. Namely, if, during a given portion of the cycle, the T/N force ratio is constant and the relative displacement at the contact is non-negligible, then that interface is assumed to be in slip condition. On the other hand, if the T/N force ratio is varying and the corresponding displacement at the contact is negligible, the damper is likely to be stuck to the platform. This allows the user to assign each stage of a cycle a given contact state (see **Table 2**).

Step 3. Based on the results of **Table 2**, friction coefficients at the right (cylinder-on-flat) and left (flat-on-flat) interface, μ_R and μ_L, are estimated using the time history of the correspondent T/N force ratio during slip (see **Figure 5a**).

Step 4. Based on the results of **Table 2**, the slopes of the platform-to-damper hysteresis cycles (referring to the stages identified as being in stick condition) can be used to estimate tangential contact stiffness values (k_{tR} and k_{tL}).

Step 5. The normal contact stiffness at the cylinder-on-flat interface k_{nR} is estimated using Brandlein's formula [28]. To this purpose only material properties and length of contact are needed. The new inserts equipped with contact "tracks" described in Section 2.2 ensure a controlled length of contact.

	Right interface			Left interface		
Stage	**T/N slope**	**Δt_R[1] (μm)**	**Contact state**	**T/N slope**	**Δt_L (μm)**	**Contact state**
1U–2	High	~1	Stick	High	1.8	Stick
2–3	High	<0.2	Stick	Medium	7.8	Partial slip
3–4D	Low	21.3	Slip	Low	13.1	Slip
4D–5	High	−0.6	Stick	High	−1.7	Stick
5–1U	Low	−21.7	Slip	Low	−21.03	Slip

[1]Δt_R of stage, for example 2–3, is defined as $\left(t_{RD}(\tau_3) - t_{RP}(\tau_3)\right) - \left(t_{RD}(\tau_2) - t_{RP}(\tau_2)\right)$, where τ is the time variable.

Table 2. Experimental contact states identification strategy.

The distribution of the normal contact stiffness at the flat-on-flat interface per unit length dk_{nL}/dx is obtained by linking the damper inclination (i.e. rotation angle β_D at a given instant in time) to the position of the left contact force resultant N_L. In other words, it is postulated that forces (i.e. moments) and displacements (i.e. rotation) are linearly linked. The technique also relies on two assumptions: (1) the normal contact stiffness is uniformly distributed along the flat interface (see Eq. 3 and **Figure 6b**); (2) the force per unit length q(x) related to the normal component of the left contact force resultant N_L has a linear distribution. In detail, with reference to **Figure 6b**, let us define a reference system x, parallel to the contact with its origin in O, the mid-point of the flat interface. As shown in **Figure 6a**, the normal component of the left contact force resultant N_L travels along the flat surface during the cycle. If, however N_L enters the inner third portion of the flat interface (see **Figure 6c**) the complete surface is in contact. Under this condition, the following holds:

$$M = N_L \cdot x = \frac{d\,k_{nL}}{dx}\frac{L^3}{12}\beta_D \tag{4}$$

This relation is graphically represented in **Figure 5c**, where the shaded are corresponds to the portion of the cycle during which N_L enters the inner third portion of the flat interface.

3.3. Remark on experimental evidence and validation

All experimental evidence shown and commented in this chapter has been represented together with its simulated counterpart for validation purposes. Some of the features of the diagrams (i.e. T/N levels during slip stages and slopes of the hysteresis cycles during stick stages) are meant to be similar because they are used as a calibration key in the contact parameter estimation process. Other features such as force trajectories and left contact force resultant application point (**Figure 6a**); the platform-to-platform hysteresis cycle (e.g. **Figure 5d**); the transition between contact states and the time instant at which they take place (e.g. **Figure 5a**); are not part of the calibration process. Therefore, the goodness of fit of these observed and simulated signals is a further proof of the soundness of the model and of the correctness of the contact parameters used to calibrate it.

4. Contact parameters variability and contact model adequacy

The purpose of this section is to detail the level of uncertainty of each of the contact parameters estimated in Section 3.2 and to investigate their variability. Results are summarized in **Table 3** and will be further commented on in the following subsections.

Contact parameter	μ_R	k_{tR} (N/μm)	μ_L	k_{tL} (N/μm)	dk_{nL}/dx (N/m²)
Uniform flat contact uncertainty bands	[0.6–0.75]	[25–35]	0.45–0.5	[20–30]	[0.8–1.2] × 10^{10}
Irregular flat contact uncertainty bands	[0.6–0.75]	[25–35]	0.45–0.6	[20–100]	[0.4–1.2] × 10^{10}
Normal load dependence	No	No	Yes	Yes	Yes

Table 3. Uncertainty bands and normal load dependence of contact parameters obtained at CF = 4.65 kg.

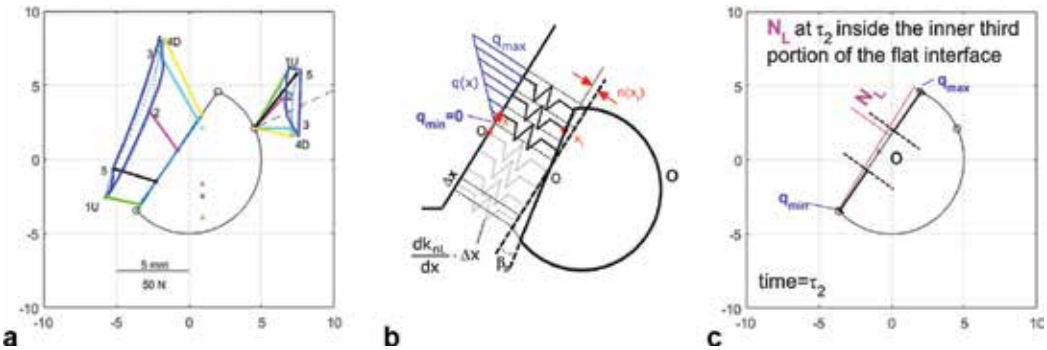

Figure 6. (a) Measured (dotted) vs. simulated (solid) contact forces diagram. (b) Representative scheme of the distribution of normal contact springs. (c) Derived position of N_L and resulting q(x) at stage 2.

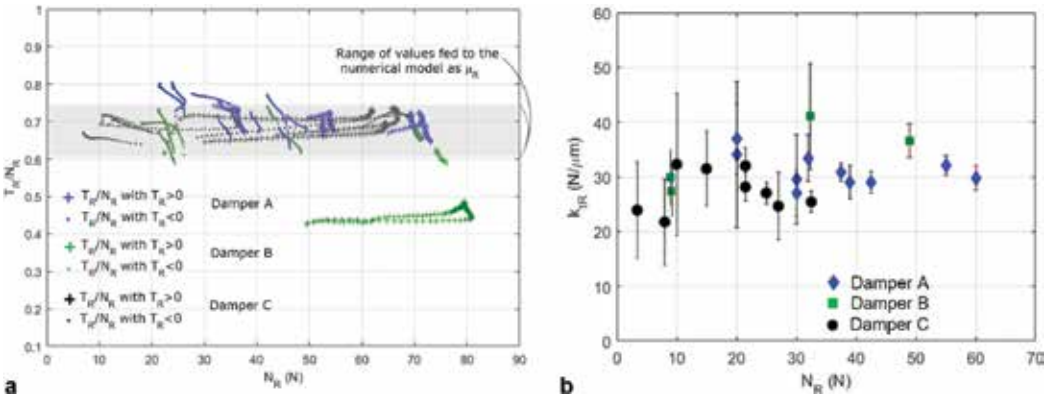

Figure 7. (a) T_R/N_R during slip as a function of N_R. (b) k_{tR} values as a function of the mean value of N_R during the corresponding stick stage. Three different damper samples are represented.

The level of uncertainty is estimated taking into account two contributions: measurement uncertainty and the uncertainty introduced by data processing techniques (e.g. reading error). Variability will be investigated at different levels in order to answer the following questions:

1. If the same damper is tested more than once under the same nominal conditions, do the estimated contact parameters change? 2. Are contact parameters dependent on the damper working conditions (e.g. normal contact pressure)?[4] 3. How different are contact parameters of different damper samples working under very similar working conditions?

The answer to point 3 is investigated using three pre-optimized damper configurations [40], that is, curved-flat dampers not affected by lift-off/rolling, jamming or partial detachment.

[4]The user-controlled working conditions investigated during this chapter are limited to a variation of centrifugal load on the damper (i.e. normal load at the contact). Other factors such as temperature, length/area of contact may affect the contacts. These dependences can and should be mapped in order to build a "database" and avoid testing each new component. This chapter should be intended as a first attempt in this direction.

4.1. Nonconforming (non-rolling) contacts

The uncertainty on μ_R is the combination of the uncertainty on T_R/N_R (3–5% from **Table 1**) and the reading error (typical values ≈ ±0.05 as shown in **Figure 5a**). The repeatability and sample-to-sample variability can be investigated by looking at **Figure 7a**.

Figure 7a shows the T_R/N_R force ratio during slip under increasing values of normal load N_R, achieved by increasing the centrifugal load (4.6–8.6 kg). Different dampers are represented with different colors and positive and negative slipping stages (see **Figure 7a** for sign convention) are represented using different symbols. "Clusters" of points of the same color and symbol belong to the same stage of the same experiment of the damper samples, represented with different colors.

Despite some inevitable variabilities (e.g. T/N ratios display minor variations during a single slip stage), μ_R can be set at a "unique value" for all investigated dampers. Furthermore, these variabilities are in the same range as the uncertainty introduced by the measuring and post-processing techniques. Choosing $\mu_R = 0.65$, a value mediated over all those encountered in **Figure 7a** is a perfectly adequate choice, which guarantees a controlled error on the equivalent stiffness and damping.

Similarly, k_{tR} (which is plotted as function of N_R in **Figure 7b**) is not influenced by the normal load[5] at the contact in the investigated range, is remarkably repeatable and no sample-to-sample variability is detected. In **Figure 7b**, the error bars are obtained by performing the least square fitting of the hysteresis slope.

It can therefore be concluded that contact parameters of the nonconforming contact are both repeatable and with a minor sample-to-sample variability.

4.2. Remark on rolling nonconforming contacts

The case of rolling contact is of scarce interest for curved-flat dampers, as it was demonstrated that large rotations (damper in lift-off) lead to a sharp decrease in dissipation capabilities [40]. However, purely cylindrical dampers are widely used and thus require a separate investigation.

The procedure to evaluate k_{tR} described in Section 3.2 cannot be operated if the damper is rotation is large (~10 times higher than that observed in **Figure 5c**). In fact, in that case, the reading "t_{RD}-t_{RP}" would give a false indication. As shown in **Figure 8a**, the laser, which is initially tracking point A ends up tracking point A*. However, the physical point initially corresponding to A is now A', not A*. This apparently minor difference, at micrometer level, impairs the effectiveness of this technique.

Fortunately, an alternative procedure based on the equivalent slopes of the platform-to-platform hysteresis cycle can be successfully carried out, both for cylindrical dampers and for curved-flat dampers [37, 39]. It is interesting to notice that the resulting k_{tR} values are 3.5–4 times lower than those obtained for non-rolling cylinder-on-flat contacts, all other parameters

[5]This is to be expected, as the cylinder-on-flat surface has a line contact, and an increase in normal load will lead to a number of asperities coming into contact which is proportionately much smaller than that obtained for a rectangular contact area (flat-on-flat contact).

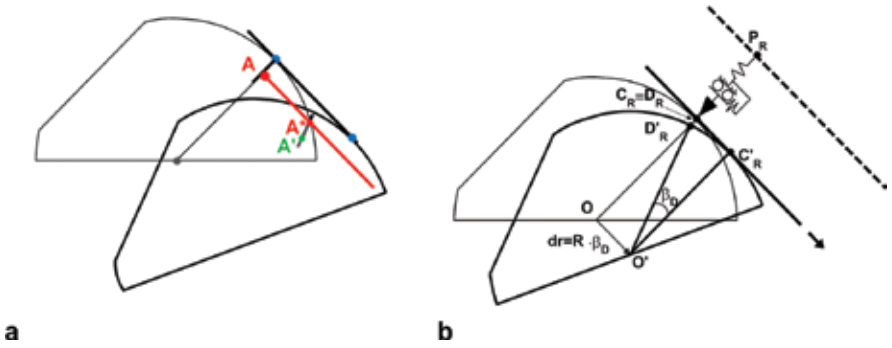

Figure 8. (a) Error committed by laser in case of large rolling motion mixed with sliding. (b) Behavior of the contact model in case of pure rolling motion.

(material, length of contact, radius, normal load, etc.) being equal (i.e. 8.5 N/μm vs. 30 N/μm for a 8 mm long contact). These predictions have been successfully validated both at damper [37] and at FRF level [34]. A possible explanation for this repeatable difference resides in the kinematics of the contact. In case of pure tangential translation (~0 rotation) the contact point coincides with the same physical point (same asperities) throughout the period of vibration. If larger rotations are at play, the "physical point" in contact keeps changing during rolling motion (as shown in **Figure 8b** contact point C_R initially coincident with physical point D_R, moves to C_R' and D_R, unloaded, moves to D_R'). This periodic unloading of contact regions may contribute to lower compenetration of the asperities, and therefore a lower k_{tR}. As shown in **Figure 8b**, the heuristic contact model applied here does not model this effect, therefore a case-specific calibration of k_{tR} is to be expected. In fact, during pure rolling motion, the contact model remains linked to the same nodes (physical points) P_R and D_R~D_R'.

4.3. Conforming contacts

Friction coefficient (μ_L) and contact stiffness values (k_{tL} and dk_{nL}/dx) of the flat-on-flat interface display a higher variability. Results for the same damper are very repeatable, but change from damper to damper.

Dampers B and C have repeatedly higher $\mu_L \approx 0.57$ with respect to Damper A, $\mu_L \approx 0.45$ (for all investigated normal loads) and the uncertainty levels (7% uncertainty and a 0.05 reading error) do not justify this marked and repeatable difference. Since the loading condition and kinematics of the flat interfaces are similar in all investigated cases, the cause of this difference may reside in the contact surfaces conditions.

In fact, Damper A, which has been tested for a higher number of cycles (it is completely "run-in") has a continuous wear trace (see **Figure 9c**). Unsurprisingly, it is easy to estimate k_{tL} (see **Figure 5b**). The same holds for dk_{nL}/dx (see **Figure 5c**) values. In other words, the uniform distribution of contact springs postulated in Section 3, is verified. Although both k_{tL} and k_{nL} values are positively correlated to normal loads (see **Figure 9a**). The adopted heuristic model does not take into account an increasing number of asperities coming into contact with increasing contact pressures. However, the normal load dependence can be easily mapped.

http://dx.doi.org/10.5772/intechopen.72676

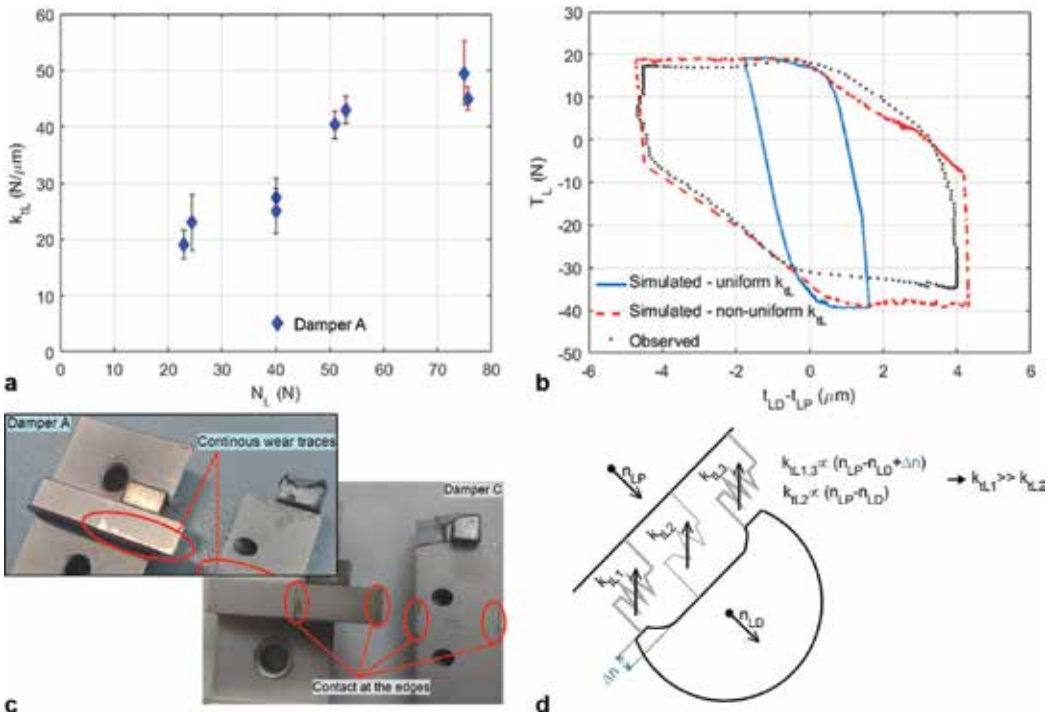

Figure 9. (a). k_{tL} as a function of N_L for Damper A. (b) Typical platform-to-damper flat-on-flat hysteresis cycle for damper C (similar to Damper B). (c) Contact surfaces of Damper A and C. (d) Representative scheme of Damper C's contact surfaces with non-uniform k_{tL} values.

On the other hand, Dampers B and C sport wear traces limited to the edges of the flat contact surfaces (see **Figure 9c**), therefore contact pressures are maximum at the two edges and much lower in the inner portion of the contact patch. As a result, friction coefficients increase (probably due to localized very high contact pressures) and the uniform distribution of contact springs assumption does not hold anymore. In fact, platform-to-damper hysteresis cycles (see **Figure 9b**), repeatedly display a non-unique slope during the stick stage. A minor gradual loss of stiffness could be explained by simple microslip, but this sharp two-slopes curve is simply not compatible with the uniform distribution of contact springs assumption.

Hysteresis cycles similar to those obtained for Dampers B and C can indeed be obtained in the simulation if one accepts to distribute the contact stiffness values in a non-uniform manner (see **Figure 9d**). The average height of Damper C's asperities is not the same throughout the entire nominal contact surface, rather it has two maxima at the edges. Therefore, for a given normal load, the equivalent stiffness at the edges is bound to be higher than that in the inner portion of the nominal contact surface. Therefore, if one wishes to represent the surface behavior with a limited number of equivalent macroslip elements the only option is to assign a different value to the different elements, depending on their position, as shown in **Figure 9d**. This strategy has been adopted to produce the very satisfactory match in **Figure 9b** (see dashed line). The procedure will have to be performed again if the mean value of normal load varies. Once again this "local fitting" (stiffness values vary with normal load and with

position now) denounces the inadequacy of the contact model. The inadequacy of the model forces the user to tune the contact stiffness values with increasing values of CF and, in some cases, with the contact point position.

5. Conclusions

A thorough review of contact models available for turbomachinery applications and the related calibration methods highlights the need for a method to solve the under-determinacy of the contact parameter estimation problem and, subsequently, to assess the adequacy of contact models. This chapter presents the evolution of the Piezo Damper Rig, a test facility for the experimental investigation of underplatform dampers. It was shown how its unique capability to provide kinematic and force related quantities while reproducing the real damper-platform kinematics allows for a trustworthy and univocal determination of contact parameters.

The measurement protocol and data processing technique ensure adequate uncertainty levels (i.e. <15%). The results can thus be used to perform safe and meaningful investigations on trends and variability of contact parameters.

The following conclusions can be drawn:

- independent experiments performed in the same nominal conditions (same damper, excitation, load etc.) are repeatable and consistent;
- contact parameter of nonconforming contacts display a remarkably low variability. No dependence on the contact pressure has been detected;
- contact parameters of conforming contacts display a higher variability caused by a difference in the surface conditions. In all cases, contact stiffness values increase with increasing contact pressures;
- the uniform distribution of contact stiffness along the flat contact surface, postulated in Section 3, is found to be adequate for run-in uniform surfaces (i.e. Damper A), but not for surfaces whose contact is “irregular” or “discontinuous”.

Heuristic models and sensible assumptions such as the uniformity of conforming contacts are nowadays considered a practical and adequate choice in turbomachinery applications. This is generally true, however special attention is required whenever a microscale phenomenon (e.g. nonuniform flat-on-flat contact, large rolling motion), not taken into account by the model, becomes prominent.

It was shown that the state-of-the-art heuristic contact model adopted in this chapter represents faultlessly run-in uniform flat-on-flat surfaces (i.e. Damper A). The same contact model CAN still be adapted to achieve simulated results matching the experimental evidence on dampers with irregular flat-on-flat contacts, but recalibrations are needed. For instance, a non-uniform distribution of k_{tL} among contact points, adjustments of the dk_{nL}/dx and μ_L values. Unfortunately, at design stage, when it is not possible to know “a-priori” the condition of

a given flat-on-flat contact surface, nor how long it will take for that surface to evolve towards a uniform distribution of contacts, this necessity for "adjustments" of contact parameters values translates into higher uncertainty levels. In other words, the state-of-the-art contact model used in this chapter is only partially adequate to represent all the complex phenomena observed. This adds its contribution to uncertainty.

On the other hand, other recalibrations (such as that needed for increasing normal loads at the flat-on-flat contact) or for very large rolling motions still signal that the heuristic model is not 100% adequate. Still, these dependences can be easily mapped and therefore do not add to the uncertainty.

One main outcome of this careful investigation, apart from the best fit values of the contact parameters (and the methodology used to obtain them), is an increased awareness of the limits and capabilities of heuristic contact models. The logical next step, the author is now working on, is the assessment of the influence that the uncertainty on contact parameters has at the blade response level.

Nomenclature

Variables, matrices and vectors

β	Rotation
CF	Centrifugal force
{F}	Generic force vector
k	Stiffness
M	Moment produced by left contact force
[M], [K]	Mass and stiffness matrices
μ	Friction coefficient
nc	Number of contact points used to represent the flat-on-flat contact
t, n	Tangential and normal displacements at the contact
T, N	Tangential and normal contact forces
[T]	Transformation matrix
θ	Platform angle
u, w	Horizontal and vertical displacements
{U}	Vector of displacements
R	Damper radius

Additional subscripts

C	Contact
D	Damper
E	External
L, R	Left and right
P	Platforms
t, n	Aligned along the normal and tangential direction, respectively

Author details

Chiara Gastaldi

Address all correspondence to: chiara.gastaldi@polito.it

AERMEC Laboratory, Politecnico di Torino, Torino, Italy

References

[1] AAVV. High cycle fatigue under high profile study [Internet]. Available from: http://www.cordis.europa.eu/result/rcn/80294_en.html [Accessed: 2017-09-23]

[2] Griffin JH. Friction damping of resonant stresses in gas turbine engine Airfoils. Journal of Engineering for Power. 1980;**102**(2):329-333. DOI: 10.1115/1.3230256

[3] Srinivasan AV. Flutter and resonant vibration characteristics of engine blades. Journal of Engineering for Gas Turbines and Power. 1997;**119**(4):742-775. DOI: 10.1115/1.2817053

[4] Krack M, Salles L, Thouverez F. Vibration prediction of bladed disks coupled by friction joints. Archives of Computational Methods in Engineering. 2017;**24**(3):589-636

[5] Schwingshackl CW, Petrov EP, Ewins DJ. Effects of contact interface parameters on vibration of turbine bladed disks with underplatform dampers. Journal of Engineering for Gas Turbines and Power. 2012;**134**(3):032507. DOI: 10.1115/1.4004721

[6] Nacivet S, Pierre C, Thouverez F, Jezequela L. A dynamic Lagrangian frequency–time method for the vibration of dry-friction-damped systems. Journal of Sound and Vibration. 2003;**265**(1):201-219. DOI: 10.1016/S0022-460X(02)01447-5

[7] Herzog A, Krack M, Panning-von Scheidt L, Wallaschek J. Comparison of two widely-used frequency-time domain contact models for the vibration simulation of shrouded turbine blades. In: ASME Turbo Expo; June 16-20, 2014; Düsseldorf, Germany. 2014. p. V07BT33A018. DOI: 10.1115/GT2014-26226

[8] Pesaresi L, Salles L, Jones A, Green JS, Schwingshackl CW. Modelling the nonlinear behaviour of an underplatform damper test rig for turbine applications. Mechanical Systems and Signal Processing. 2017;**85**:662-679. DOI: 10.1016/j.ymssp.2016.09.007

[9] De Moerlooze K, Al-Bender F, Van Brussel H. A generalised asperity-based friction model. Tribology Letters. 2010;**40**(1):113-130

[10] Yang BD, Menq CH. Characterization of 3D contact kinematics and prediction of resonant response of structures having 3D frictional constraint. Journal of Sound and Vibration. 1998;**217**(5):909-925. DOI: 10.1006/jsvi.1998.1802

[11] Yang BD, Chu ML, Menq CH. Stick–slip–separation analysis and non-linear stiffness and damping characterization of friction contacts having variable normal load. Journal of Sound and Vibration. 1998;**210**(4):461-481. DOI: 10.1006/jsvi.1997.1305

[12] Petrov EP, Ewins DJ. Analytical formulation of friction interface elements. Journal of Turbomachinery. 2003;**125**(2):364-371. DOI: 10.1115/1.1539868

[13] Panning L, Sextro W, Popp K. Spatial dynamics of tuned and mistuned bladed disks with cylindrical and wedge-shaped friction dampers. International Journal of Rotating Machinery. 2003;**9**(3):219-228

[14] Petrov EP. Explicit finite element models of friction dampers in forced response analysis of bladed disks. Journal of Engineering for Gas Turbines and Power. 2008;**130**(2):022502

[15] Afzal M. On efficient and adaptive modelling of friction damping in bladed disks [dissertation]. KTH: 2017

[16] Cattaneo C. Sul contatto di due corpi elastici: distribuzione locale degli sforzi. Accademia dei Lincei. 1938

[17] Mindlin RD, Deresiewicz H. Elastic spheres in contact under varying oblique forces. Journal of Applied Mechanics. 1953;**20**:327-344

[18] Gastaldi C, Gola MM. On the relevance of a microslip contact model for under-platform dampers. International Journal of Mechanical Sciences. 2016;**115**:145-156. DOI: 10.1016/j.ijmecsci.2016.06.015

[19] Iwan WD. A distributed-element model for hysteresis. Journal of Applied Mechanics. 1966;**33**(4):893-900. DOI: 10.1115/1.3625199

[20] Menq CH, Bielak J, Griffin JH. The influence of microslip on vibratory response, part I: A new microslip model. Journal of Sound and Vibration. 1986;**107**(2):279-293. DOI: 10.1016/0022-460X(86)90238-5

[21] Csaba G. Modelling of a microslip friction damper subjected to translation and rotation. In: ASME, Turbo Expo 1999; June 7-10, 1999; Indianapolis, Indiana, USA. 1999. p. V004T03A012. DOI: 10.1115/99-GT-149

[22] Gaul L, Nitsche R. The role of friction in mechanical joints. Applied Mechanics Reviews. 2001;**54**(2):93-106. DOI: 10.1115/1.3097294

[23] Segalman D. A four-parameter Iwan model for lap-type joints. Journal of Applied Mechanics. 2005;**72**(5):752-760. DOI: 10.1115/1.1989354

[24] Rajaei M, Ahmadian H. Development of generalized Iwan model to simulate frictional contacts with variable normal loads. Applied Mathematical Modelling. 2014;**38**(15-16):4006-4018. DOI: 10.1016/j.apm.2014.01.008

[25] Botto D, Lavella M, Gola MM. Measurement of contact parameters of flat on flat contact surfaces at high temperature. In: ASME, editor. Turbo Expo. 2012

[26] Šanliturk KY, Stanbridge AB, Ewins DJ. Friction dampers: Measurement, modelling and application to blade vibration control. In: ASME, editor. Proc. Des. Eng. Conf.; 1995

[27] Schwingshackl CW, Petrov EP, Ewins DJ. Validation of test rig measure measurements and prediction tools for friction interface modelling. In: Turbo Expo; 2010

[28] Brändlein J, Eschmann P, Hasbargen L, Ball K. editors. Ball and Roller Bearings: Theory, Design, and Application. John Wiley and Sons; 1999

[29] Szwedowicz J, Gibert C, Sommer TP, Kellerer R. Numerical and experimental damping assessment of a thin-walled friction damper in the rotating setup with high pressure turbine blades. Journal of Engineering for Gas Turbines and Power. 2008;**130**(1):10

[30] Szwedowicz J. Bladed Disks: Non linear Dynamics. Structural Design of Aircraft Engines: Key Objectives and Techniques. Belgium: Seinturier & Paniagua Edition; 2008

[31] Sextro W. Dynamical Contact Problems with Friction. 1st ed. Berlin: Springer; 2007

[32] Siewert C, Panning L, Schmidt-Fellner A, Kayser A. The Estimation of the Contact Stiffness for Directly and Indirectly Coupled Turbine Blading. In: ASME, editor. Turbo Expo; 2006

[33] Allara M. A model for the characterization of friction contacts in turbine blades. Journal of Sound and Vibration. 2009;**320**(3):527-544

[34] Gastaldi C, Grossi E, Berruti TM. On the choice of contact parameters for the forced response calculation of a bladed disk with underplatform dampers. Journal of the GPPS. 2017;**1**:1-8

[35] Gastaldi C, Berruti TM. Method to solve the efficiency-accuracy trade-off of multi-harmonic balance calculation of structures with friction contacts. International Journal of Non-Linear Mechanics. 2017;**92**:25-40

[36] Szwedowicz J, Slowik S, Mahler A, Hulme CJ. Nonlinear dynamic analyses of a gas turbine blade for attainment of reliable shroud coupling. In: ASME, editor. Turbo Expo; 2005

[37] Gastaldi C, Gola MM. A random sampling strategy for tuning contact parameters of underplatform dampers. In: ASME, editor. Turbo Expo; 2015

[38] Pesaresi L, Stender M, Ruffini V, Schwingshackl CW. DIC measurement of the kinematics of a friction damper. In: SEM, editor. Dynamics of Coupled Structures. Conference Proceedings of the SEM. Vol. 4. Springer; 2017

[39] Gola MM, Liu T. A direct experimental–numerical method for investigations of a laboratory under-platform damper behavior. International Journal of Solids and Structures. 2014;**51**(25-26):4245-4259

[40] Gastaldi C, Gola MM. Preoptimization of underplatform dampers. Journal of Engineering for Gas Turbines and Power. 2016;**139**(GTP-16-1229):9

Chapter 7

Single-Curvature Sandwich Panels with Aluminum Foam Cores under Impulsive Loading

Lin Jing, Zhihua Wang and Longmao Zhao

Additional information is available at the end of the chapter

http://dx.doi.org/10.5772/intechopen.70531

Abstract

Single-curvature sandwich panels combine the advantages of the shell and sandwich structure and are therefore envisaged to possess good potential to resist blast and shock or impact loads. This study presents a comprehensive report on the dynamic response and shock resistance of single-curvature sandwich panels, comprising two aluminum alloy face-sheets and an aluminum foam core, subjected to air-blast loading, in terms of the experimental investigation and numerical simulation. The deformation modes, shock resistance capability, and energy absorption performance are studied, and the influences of specimen curvature, blast impulse, and geometrical configuration are discussed. Results indicate that the deformation/failure, deflection response, and energy absorption of curved sandwich panels are sensitive to the loading intensity and geometric configuration. These results are significant to guide the engineering applications of sandwich structures with metallic foam cores subjected to air-blast loading.

Keywords: metallic foam, sandwich structure, single curvature, blast loading, shock resistance, energy absorption, deformation mode

1. Introduction

Light-weight cellular metallic foams possess good multifunctional combinations of mechanical, physical, and electromagnetic properties including the high specific stiffness, high specific strength, and superior energy dissipation capacity by plastic deformation of their cellular microstructures [1–3]. Since they can undergo the large plastic deformation at a constant nominal stress, resulting in a relatively long plateau stress in their stress versus strain response history curves shown in **Figure 1**, metallic foams are continually used in energy absorbers for the protective purpose [3]. More commonly, the metallic foams are extensively used as the cores of

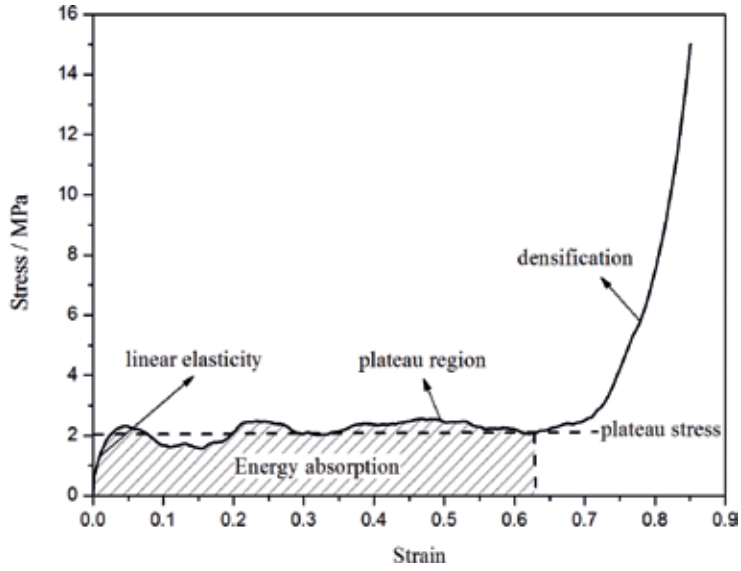

Figure 1. Stress versus strain response curve of the aluminum foam with 11% relative density.

sandwich structures to enhance the blast/shock resistance performance. The sandwich structure typically consists of two thinner but stiffer face-sheets and a softer crushable core, which is a special topology form comprising a combination of different materials that are bonded to each other so as to utilize the properties of each component for the structural advantage of the whole assembly. The face-sheets resist nearly all of the applied in-plane loads and bending moments, while the core sustains the transverse and shear loads mainly. The employment of flatted sandwich structures (i.e., the beam and panel) to resist blast/shock loadings still remains academic and engineering interests, and the responses of these sandwich structures to various loading cases have been widely investigated [4–12]. Some representative failure modes (e.g., face-sheet yielding and core compression or shear) have been experimentally observed [5, 7, 9–11], while the load-carrying capability and mechanisms of plastic failure and energy absorption have been predicted in theory and simulation [4, 6, 8, 12].

Curved sandwich panels, which better combine the advantages of shell and sandwich structures, are envisaged to possess good potential in withstanding blast or impact [13–15]. However, studies on curved metallic sandwich structures appear quite limited to date. Consequently, a comprehensive study on blast-loaded single-curvature sandwich panels with aluminum foam cores is conducted in experiment and simulation.

2. Air-blast experiments

2.1. Experimental procedure

2.1.1. Specimens

Single-curvature sandwich panel specimens, 310 mm long, with an arc length also of 310 mm, were fabricated from two thin LY-12 aluminum alloy face-sheets bonded to an aluminum foam

http://dx.doi.org/10.5772/intechopen.70531

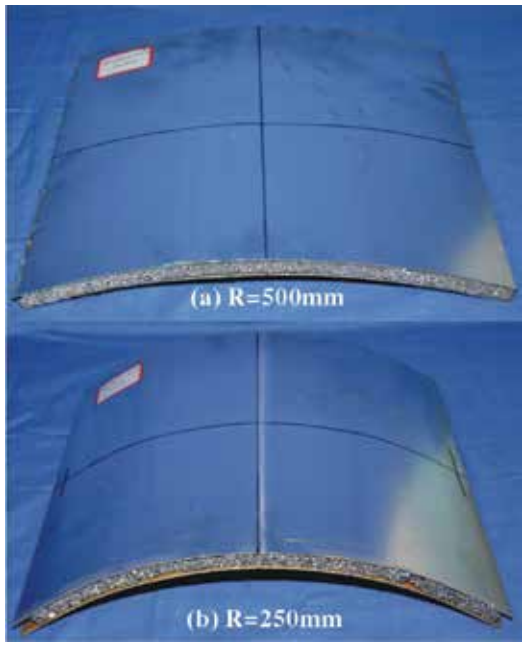

Figure 2. Photograph of specimens with the two radii of curvature.

core using commercially available adhesive. **Figure 2** shows the picture of single-curvature sandwich panels with two radii of curvature, that is, 250 and 500 mm. Three face-sheet thicknesses (i.e., 0.5, 0.8, and 1.0 mm) and three core relative densities (i.e., 11, 15, and 18%) were examined. The quasi-static mechanical properties of LY-12 aluminum alloy face-sheets with the density $\rho = 2780$ kg/m^3 are Young's modulus $E = 68$ GPa, Poisson's ratio $\nu = 0.33$, yield stress $\sigma_{fY} = 310$ MPa, and shear modulus $G = 28$ GPa.

The core material was closed-cell aluminum foam, and the typical quasi-static uniaxial compressive stress-strain responses for three different relative foam densities are shown in **Figure 3**. Here, an energy efficiency-based approach is proposed to calculate the plateau stress and densification strain. Energy absorption efficiency η (ε_a) is defined as the energy absorbed up to a given nominal strain ε_a normalized by the corresponding stress value σ_c (ε) [16]:

$$\eta(\varepsilon_a) = \frac{\int_{\varepsilon_{cr}}^{\varepsilon_a} \sigma(\varepsilon) d\varepsilon}{\sigma(\varepsilon)_{\varepsilon=\varepsilon_a}} \tag{1}$$

where ε_{cr} is the strain at the yield point corresponding to commencement of the plateau regime. The densification strain ε_D is the strain value corresponding to the stationary point in the efficiency-strain curve, that is, where the efficiency is a global maximum:

$$\left.\frac{d\eta(\varepsilon)}{d\varepsilon}\right|_{\varepsilon=\varepsilon_D} = 0 \tag{2}$$

The energy absorption efficiency curves of the aluminum foams are also depicted in **Figure 3**, and the plateau stress is obtained from

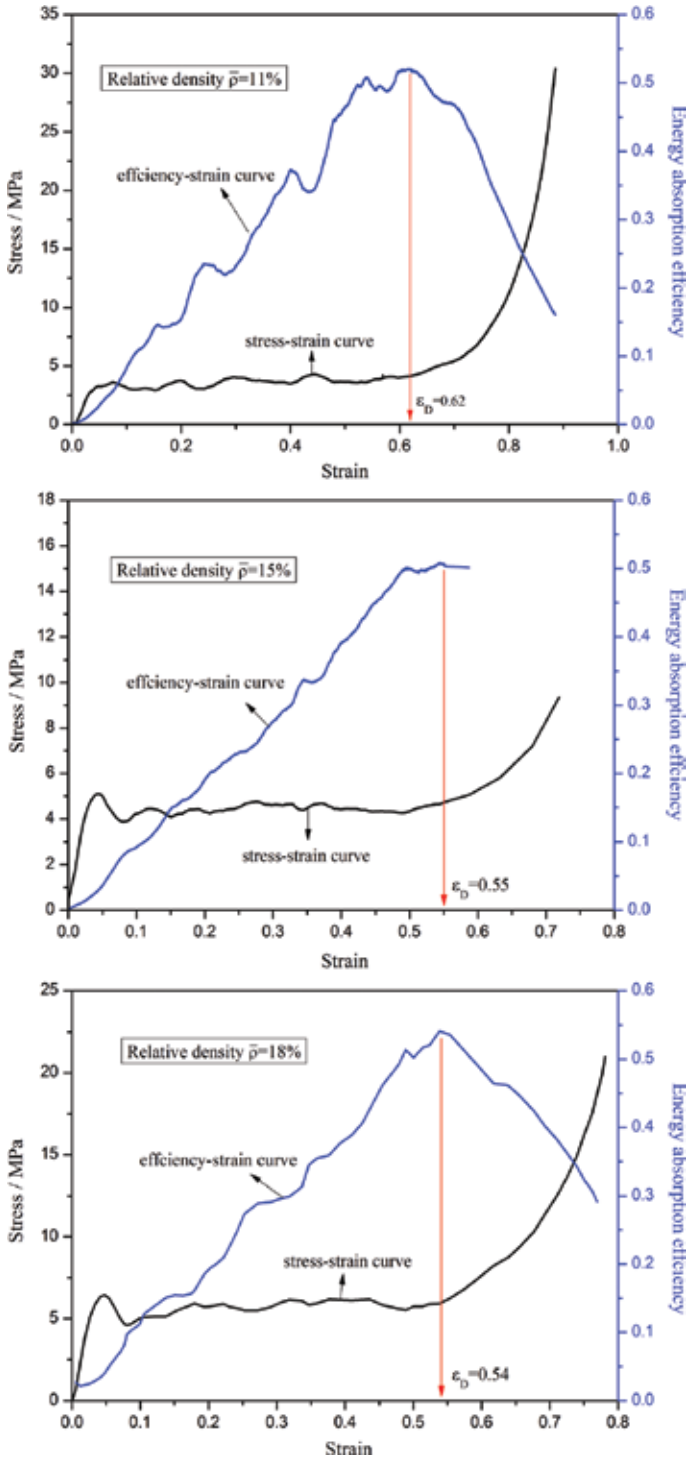

Figure 3. Stress versus strain response and energy absorption efficiency versus strain curves of aluminum foam cores.

$$\sigma_{pl} = \frac{\int_{\varepsilon_{cr}}^{\varepsilon_D} \sigma_c(\varepsilon) d\varepsilon}{\varepsilon_D - \varepsilon_{cr}} \tag{3}$$

By calculating, the plateau stress σ_{pl} and densification strain ε_D of aluminum foams with three various relative densities are σ_{pl} = 5.30 MPa and ε_D = 0.62 (for 11% relative density), σ_{pl} = 5.49 MPa and ε_D = 0.55 (for 15% relative density), and σ_{pl} = 7.11 MPa and ε_D = 0.54 (for 18% relative density), respectively.

A total of 48 specimens were fabricated, and for each blast condition, two nominally identical specimens were tested. All specimens were uniquely labeled—the label R500-H0.5-C10-ρ15%-f1 represents the specimen with a 500 mm radius of curvature, 0.5 mm face-sheet thickness, 10 mm core thickness, and 15% core relative density, which is the first specimen used for exploring the influence of face-sheet thickness on the dynamic response. The specimens were arranged into four groups; each group was designated for examining the effect of one or two parameters on the structural response.

2.1.2. TNT charge

Blast loading was applied to the specimens by detonating a cylindrical TNT charge with a density of 1.55 g/cm^3; a photograph is shown in **Figure 4**. Seven various mass charges (i.e., 10, 15, 20, 25, 30, 35, and 40 g) with an approximate height-to-diameter ratio of 1 were fabricated by changing the diameter and height of the charges.

2.1.3. Ballistic pendulum system

The specimen-frame assembly was attached to a four-cable ballistic pendulum system, which was employed to measure the impulse imparted to the front face of the specimen, as shown in **Figure 5**. The charges were mounted in front of the center of specimens, at various standoff

Figure 4. Picture of cylindrical TNT charge.

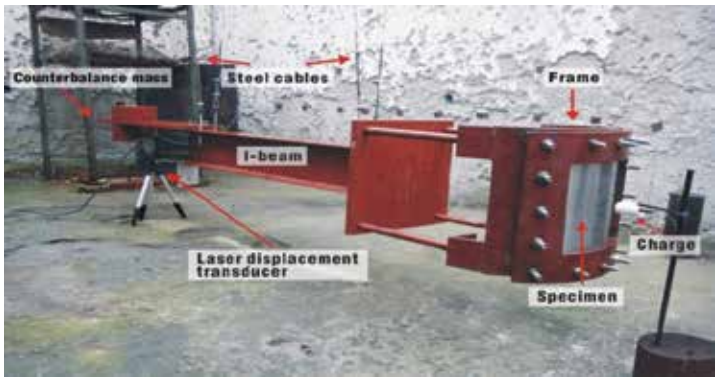

Figure 5. Photograph of the overall experimental setup.

distances. The movement of the pendulum was measured by a laser displacement transducer. Each single-curvature sandwich panel was clamped peripherally by steel frames, leaving an effective exposed curved area of 250 × 250 mm.

When the TNT charge is detonated, the impulsive load produced causes the pendulum to move, and its motion corresponds to that of a simple pendulum, described by the following equation:

$$M\frac{d^2x}{dt^2} + C\frac{dx}{dt} + \frac{Mg}{R}x = 0 \tag{4}$$

where M is the total mass, x the horizontal displacement, C the damping coefficient, and R is the cable length. Suppose $2\beta = C/M$ and $\omega_n^2 = g/R$, then Eq. (4) is simplified by

$$\ddot{x} + 2\beta\dot{x} + \omega_n^2 x = 0 \tag{5}$$

Introducing the damping ratio $\xi = \beta/\omega_n$, the solution of Eq. (5) is given by

$$x = Ae^{-\beta t}\sin(\omega t + \varphi) \tag{6}$$

where $\omega = \sqrt{\omega_n^2 - \beta^2}$, $A = \sqrt{x_0^2 + \frac{(\dot{x}_0 + \beta x_0^2)}{\omega^2}}$, and $\tan\varphi = \frac{x_0\omega}{\dot{x}_0 + \beta x_0}$.

With the initial condition $x_0 = 0$, Eq. (5) can be written as

$$x = \frac{\dot{x}_0}{\omega}e^{-\beta t}\sin\omega t \tag{7}$$

The period of the oscillation of the pendulum $T = 2\pi/\omega$; if x_1 is the displacement of the pendulum for a period of $t = T/4$ and x_2 for a period of $t = 3\ T/4$, then

$$x_1 = \frac{T}{2\pi}e^{-\frac{\beta T}{4}}\dot{x}_0 \tag{8}$$

$$x_2 = \frac{T}{2\pi} e^{-\frac{3\beta T}{4}} \dot{x}_0 \tag{9}$$

$$\beta = \frac{2\ln(x_1/x_2)}{T} \tag{10}$$

If the values of β, x_1, and x_2 are known, then the initial velocity of the pendulum is given by

$$\dot{x}_0 = \frac{2\pi}{T} e^{\frac{\beta T}{4}} x_1 \tag{11}$$

The impulse imparted into the pendulum is generally given by

$$I = M \cdot \dot{x}_0 \tag{12}$$

where M is the total mass of the pendulum. By introducing (11) into Eq. (12), given by

$$I = M x_1 \frac{2\pi}{T} e^{\frac{\beta T}{4}} \tag{13}$$

In the present tests, β = 0.031, M = 151.3 kg, T = 3.12 s, and R = 2.69 m. Generally, the rotation angle (θ) should be less than 5°; in this study, θ is approximately 2.1°, which is acceptable.

2.2. Experimental results and discussion

The blast impulse is calculated by Eq. (13), according to the ballistic pendulum movement measured by the laser displacement transducer, as shown in **Figure 6**. The permanent deflection of the center of the back face-sheet was also examined by the posttest measurements. Here, the experimental results are classified and presented in the following subsections, in terms of typical deformation/failure modes and influences of some key parameters on the final permanent deflection (since the resistance to blast loading is quantified by the permanent deflection of the central point of the back face-sheet).

2.2.1. Deformation modes

The deformation and failure modes of the single-curvature sandwich panels can be classified into that of the front face-sheet, core, and back face-sheet, respectively, although all the sandwich panels present the evident global deformation with the various local failures.

The front face-sheet of single-curvature sandwich panels subjected to blast loading mainly fails in the local indentation, transverse tearing, and petal-like tearing, as shown in **Figure 7**. Indentation failure shown in **Figure 7(a)** is the localized severe deformation without rupture, and the indentation depth is related with the load magnitude. When deformation of the face-sheet exceeds its ductility at larger loads, failure is dominated by tearing. The transverse tearing may occur for a certain range of blast loads, as shown in **Figure 7(b)**. With the increase of blast loading, the petal-like tearing mode shown in **Figure 7(c)** will be caused.

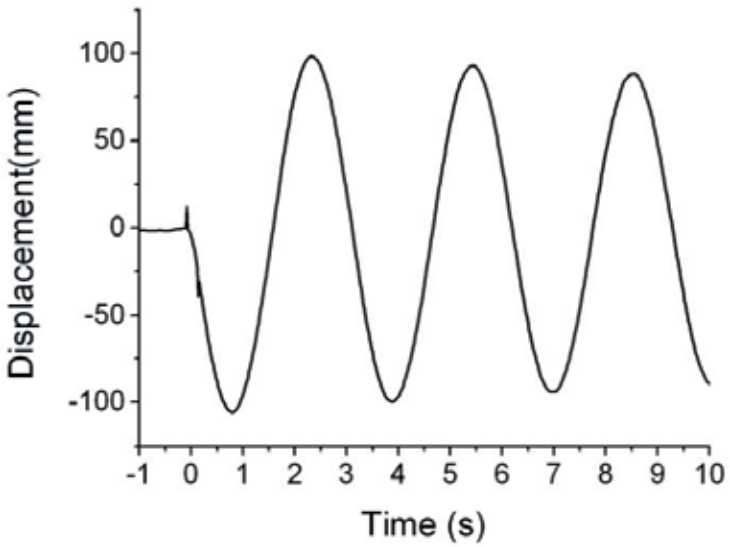

Figure 6. Typical displacement-time response of ballistic pendulum in a blast test.

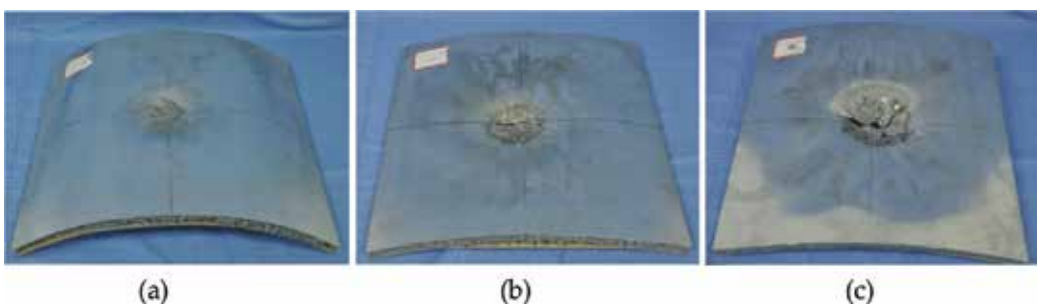

Figure 7. Three deformation and failure patterns in front face-sheets: (a) indentation failure, (b) transverse tearing, and (c) petal-like tearing.

Figure 8 illustrates the typical cross-sectional profiles of blast-loaded sandwich specimens with two radii of curvature. Each specimen can be split into three regions (i.e., core crushing region, shear failure region, and an uncompressed region) from the mid-span to the clamped end, according to the deformation degree of the core. Core crushing is considered as the generation of a hole in the specimen central zone, as shown in **Figure 8(a)**. The fracture of core in the central zone may be observed for some specimens as shown in **Figure 8(b)**. The core also can be failed by core shear under the transverse shear force. Moreover, the delamination between the crushed core and face-sheets can be found in the core shear region. In those regions far away from the loading area, the cores are generally uncompressed.

The deformation/failure of the back face-sheet corresponds to Mode I (gross inelastic deformation), Mode II (gross inelastic deformation with tensile tearing at the edges), and tearing. The deformation profile of the back face-sheet for the typical Mode I response is dome-shaped at the center, and with obvious plastic hinges extending from the plate corner to the base of the

http://dx.doi.org/10.5772/intechopen.70531

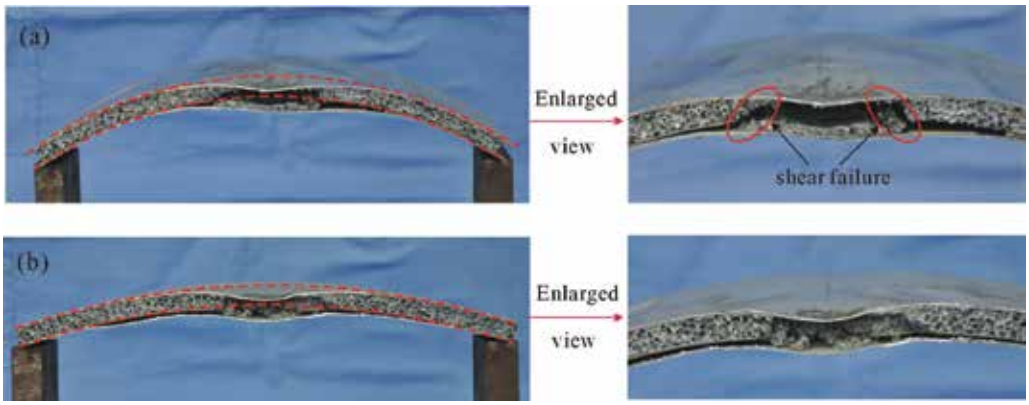

Figure 8. Collapse patterns of the foam core: (a) progressive compression with shear failure in central area and (b) fracture of central core.

dome, as shown in **Figure 9(a)**. **Figure 9(b)** shows significant inelastic deformation with tensile tearing at the clamped edges of the curved sandwich panel. For the thinner specimen subjected to a larger impulse, tearing of the back face-sheet was observed, as shown in **Figure 9(c)**.

2.2.2. Influence of blast impulse on the shock resistance

The maximum center-point deflection of curved sandwich panels (H = 0.8 mm, C = 10 mm, relative density = 15%) and curved monolithic plates of equivalent mass (H = 3.0 mm) are plotted in **Figure 10**, as a function of impulse for different blast distances and six charge masses (10, 15, 20, 25, 30, and 35 g). As expected, the central deflection increases with impulse for all test configurations. By applying a linear fit to the data, the relationship between the central deflection and the blast impulse can be written as

$$W = kI + b \tag{14}$$

where W and I are, respectively, the central deflection in mm and impulse in Ns; k and b are the two constants with the values of 1.22 mm/Ns and −9.03 mm for R = 500 mm curved sandwich panels and 1.85 mm/Ns and −10.66 mm for R = 250 mm sandwich specimens, respectively.

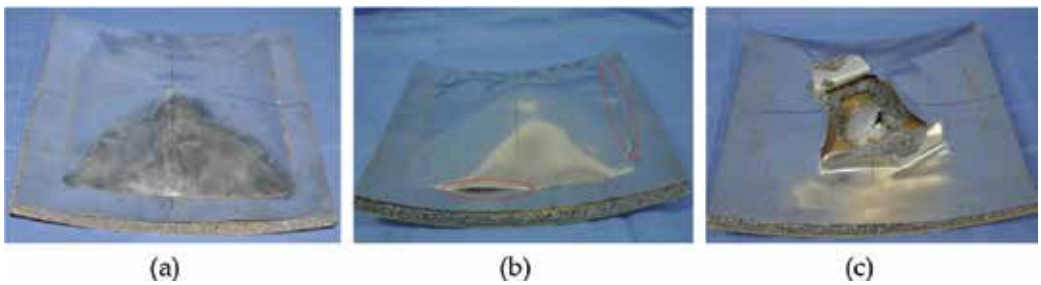

Figure 9. The deformation/failure of the back face-sheet: (a) Mode I (gross inelastic deformation), (b) Mode II (gross inelastic deformation with tensile tearing), and (c) tearing failure.

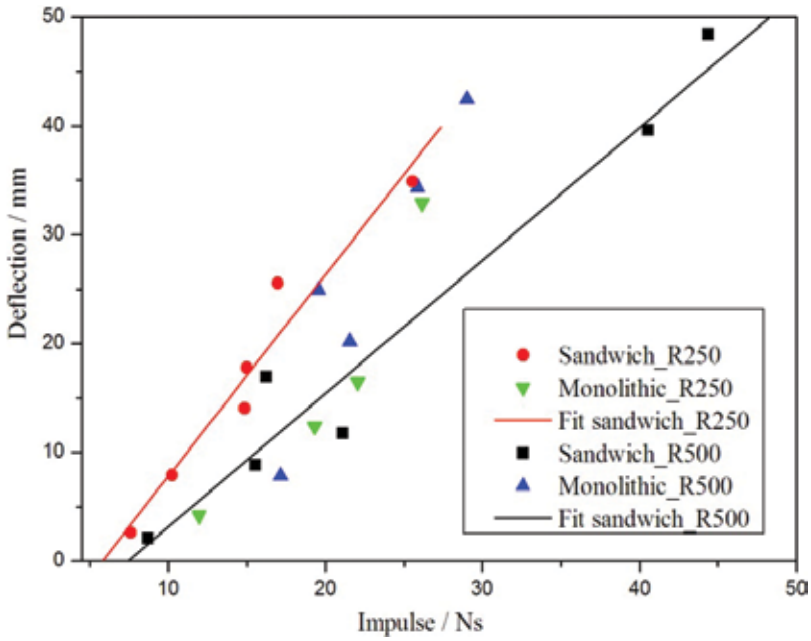

Figure 10. Relationship between central deflection and blast impulse.

A comparison of the blast resistance between curved sandwich panels and monolithic plates of equivalent mass is also shown in **Figure 10**. Those R = 500 mm sandwich panel specimens show the better resistance to blast loading compared to the solid shells with the equivalent mass. However, the central deflection of R = 250 mm curved sandwich panels were larger than that of solid counterparts. This may be explained that the deformation of the smaller radius of curvature specimens is governed by the local failure, which may decrease the energy absorption capability of the foam cores; however, the deformation of the solid shell counterparts is dominated by the global bending.

2.2.3. Influence of face-sheet thickness on the shock resistance

The dependence of the central deflection of the back face-sheet on face-sheet thickness is shown in **Figure 11**, where additional data corresponding to the same conditions are included to show the possible general trend. The central point deflection decreases with the increased face-sheet thickness, as expected. For R = 250 mm curved sandwich panels, those specimens with 0.8-mm- and 1.0-mm-thick face-sheets show the smaller deflections than curved panels with the 0.5 mm face-sheets, by 28.3 and 56.3%, respectively. This is also the case for the R = 500 mm specimens, whereby the deflections are, respectively, 48.5 and 68.8% smaller.

2.2.4. Influence of core relative density on the shock resistance

The central point deflection of specimens is plotted in **Figure 12** as a function of core relative density. For both curvatures, the specimens with the larger core relative density results in the smaller deflections. Taking the core relative density of 11% as a reference, R = 250 mm

http://dx.doi.org/10.5772/intechopen.70531

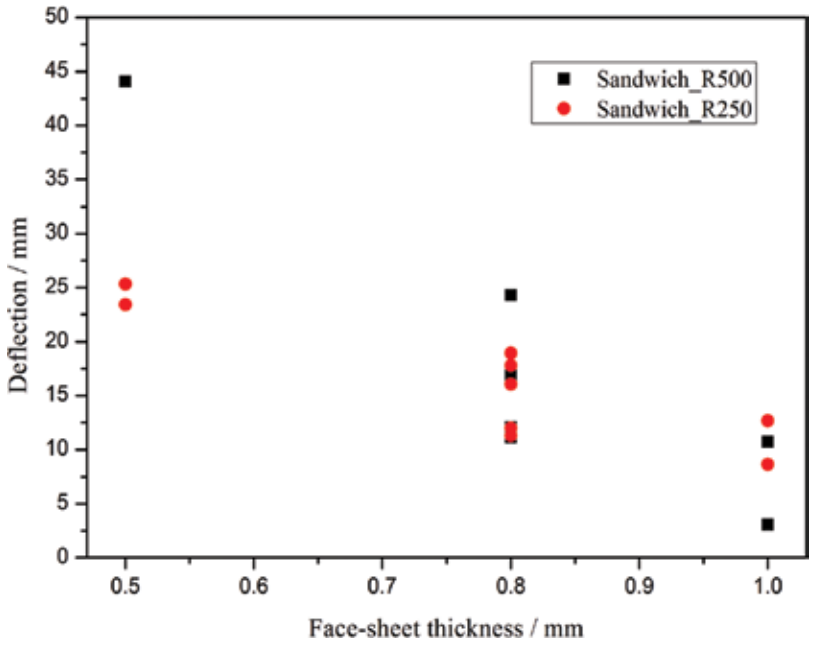

Figure 11. Effect of face-sheet thickness on central deflection of curved sandwich panels.

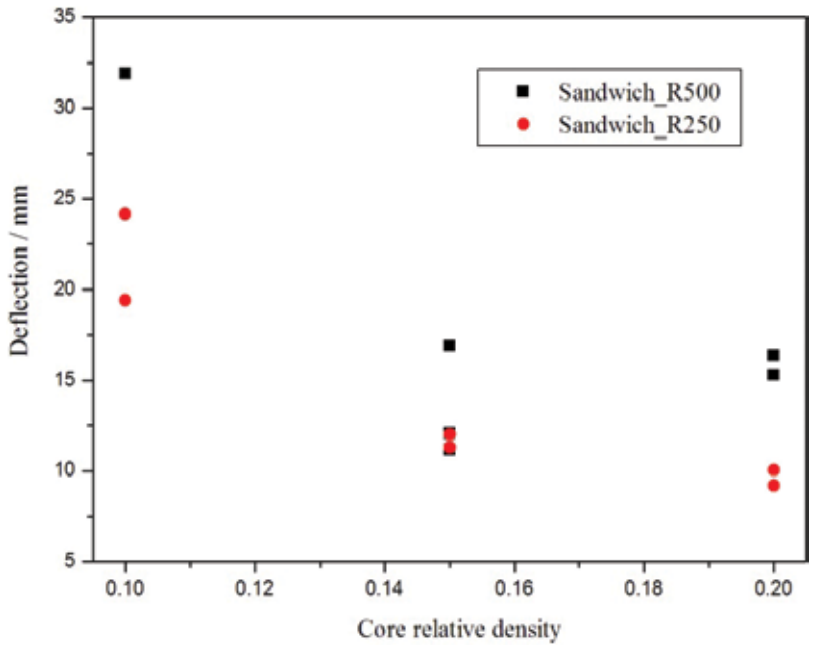

Figure 12. Effect of core relative density on central deflection of curved sandwich panels.

sandwich panels with higher relative densities (15 and 18%) can decrease the average deflection, by 46.6 and 55.9%, respectively. However, for R = 500 mm sandwich panels, it is difficult to quantify the effect of core relative density on the structural response of specimens, due to the large variability in both impulse and deflection.

2.2.5. Influence of specimen curvature on the shock resistance

The influence of curvature is deduced primarily from **Figure 10**. Two major influences can be identified: (i) the blast resistance of single-curvature sandwich panels with the larger radius of curvature is better, and (ii) a comparison between the response of the curved sandwich panels and the solid shell counterparts with the same mass is made, as stated in Section 2.2.2. Obviously, the deformation of curved sandwich panels with the smaller radius of curvature is governed by local penetration failure, while the deformation of the larger radius of curvature specimens is the global deformation with bending and stretching dominants. The larger deformation zone of the latter appears to contribute the greater plastic energy absorption and thus enhances the resistance to blast loading.

3. Finite element simulations

Based on the experiments, corresponding finite element (FE) simulations have been undertaken by employing the nonlinear, explicit finite element code LS-DYNA 970.

3.1. FE model

Since the curved sandwich panel is symmetric about x-z and y-z planes, only a quarter of the curved panel was modeled, as shown in **Figure 13**. The entire model comprises 53,166 nodes and 61,257 elements. The LY-12 face-sheets were modeled by Belytschko-Tsay shell element,

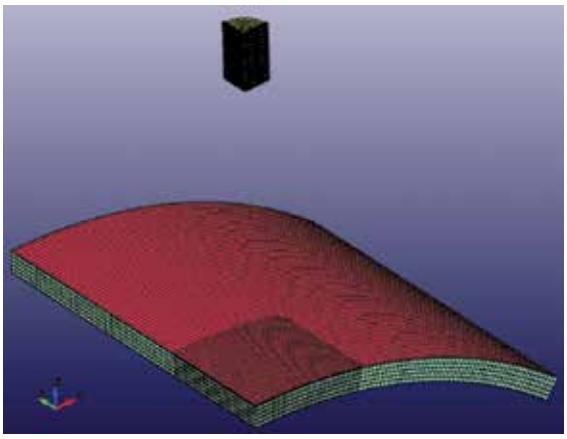

Figure 13. FE model of the 1/4 curved sandwich panel and charge.

while the foam core was modeled by the default brick element. Similarly, one quarter of the charge was modeled shown in **Figure 13**, and eight-node brick elements with arbitrary Lagrange-Eulerian (ALE) formulation were adopted.

The mechanical behavior of face-sheets were represented by material model 3 of LS-DYNA (*MAT_PLASTIC_KINEMATIC), while the aluminum foam core was modeled by material model 63 of LS-DYNA (*MAT_CRUSHALBE_FOAM). A high-explosive material model (*MAT_HIGH_EXPLOSIVE_BURN) incorporating the JWL equation of state (EOS_JWL) was used to describe the material property of the TNT charge:

$$p = A\left(1 - \frac{\omega}{R_1 V}\right)e^{-R_1 V} + B\left(1 - \frac{\omega}{R_2 V}\right)e^{-R_2 V} + \frac{\omega E}{V} \tag{15}$$

where p is the blast pressure, E is the internal energy per initial volume, V is the initial relative volume, and ω, A, B, R_1, and R_2 are the material constants, respectively. The material parameters of the curved sandwich panel and TNT charge are kept the same as experimental ones.

The bolts used in the tests to clamp the curved panels to the fixture were represented by nodal constraints in the numerical model. Symmetric boundary conditions about x-z and y-z planes were imposed. The blast load imparted on the front face-sheet of curved sandwich panel was defined with algorithm of *CONTACT_ERODING_SURFACE_TO_SURFACE. Automatic, surface-to-surface contact options were generally used for curved sandwich panels.

3.2. Simulation results and discussion

3.2.1. Explosion and structural response process

The whole response can be divided into three stages: Stage I (expansion of the explosive), Stage II (explosive product interacts with the curved sandwich panel), and Stage III (plastic deformation of the curved sandwich panel under the inertia).

3.2.1.1. Stage I: expansion of the explosive

The expansion of the explosive starts at the point of detonation (central point of the top surface of charge), as shown in **Figure 14**. The detonation of a high-performance explosive is achieved by compressing and heating of its constituents, resulting that a chemical reaction is triggered and then it is supersonically propagated through the explosive at the Chapman-Jouguet velocity. Whereafter, a strong shock wave, generated by the violent expansion of the gaseous products, propagates into the ambient medium. Since the sound speed increases with the increased temperature in the compressible flow, shock waves are generated. The detonation wave generated by the cylindrical charge presents an obvious directionality and a cross distribution shape. The axial propagation speed is larger than the radial propagation speed, so the axial pressure is also greater than that of radial direction due to the proportional relationship between the wave speed and intensity in air medium.

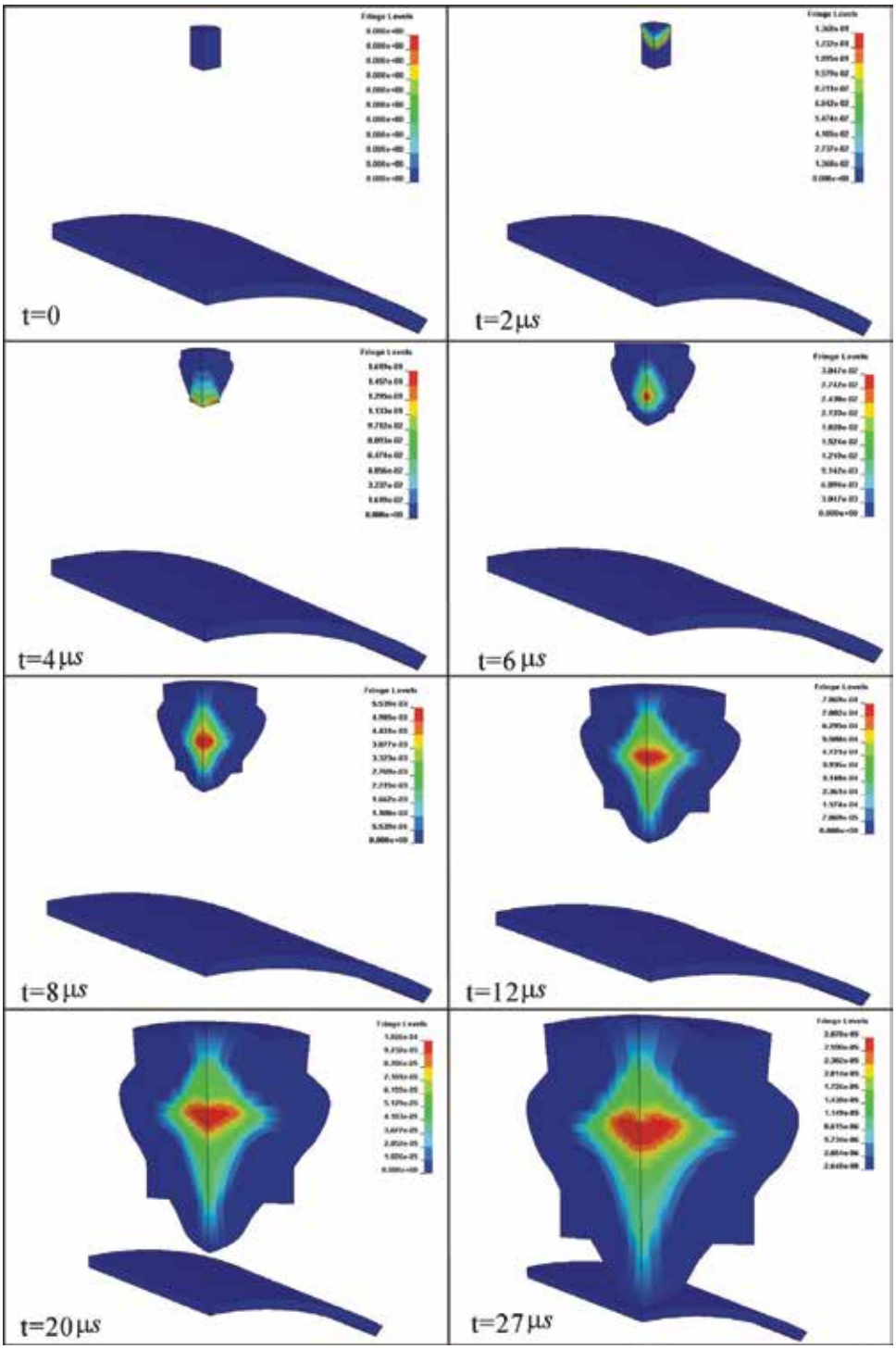

Figure 14. A typical process of the charge detonation.

http://dx.doi.org/10.5772/intechopen.70531

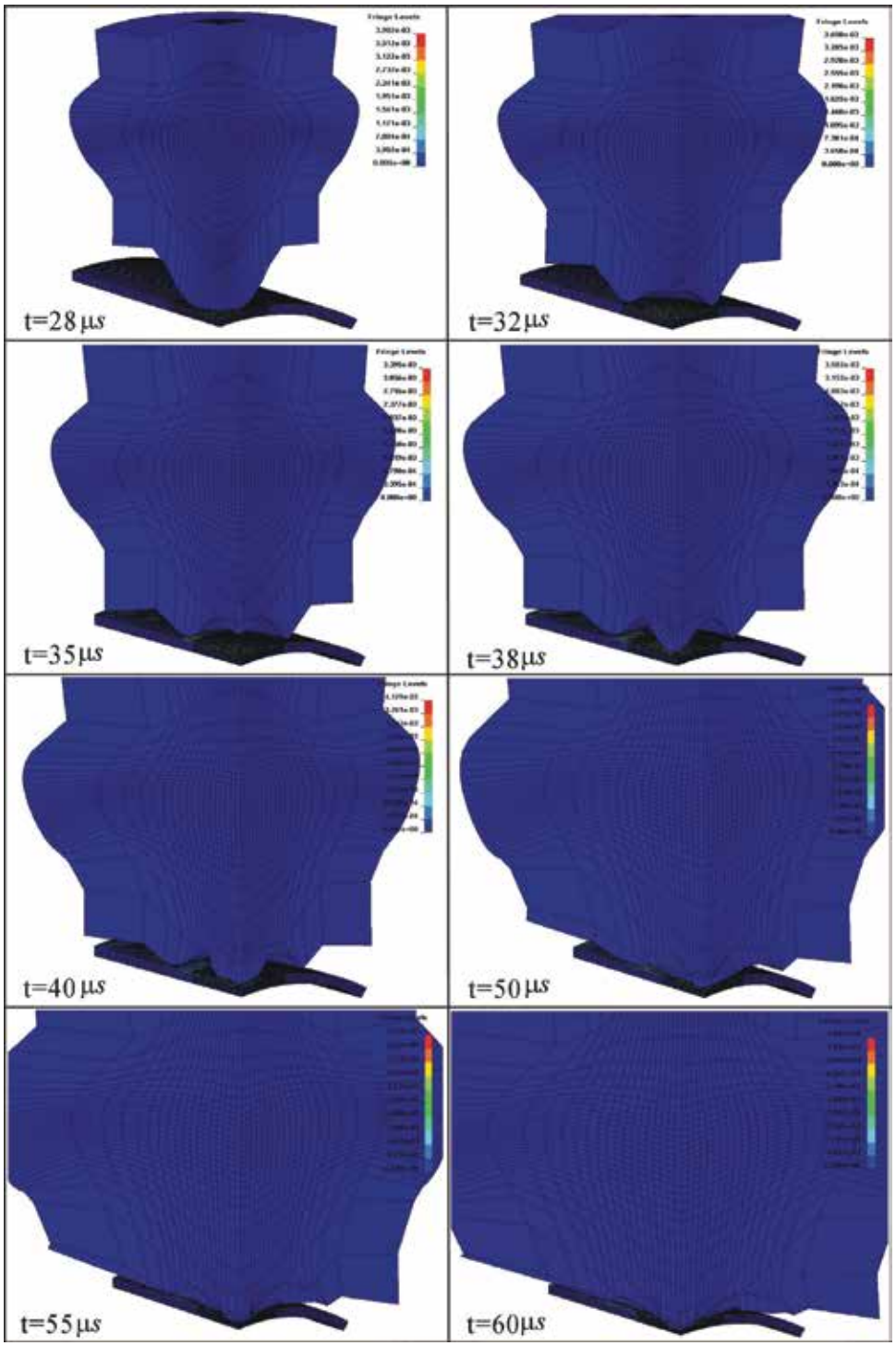

Figure 15. A typical process of explosive product-structure interaction.

3.2.1.2. Stage II: explosive product-curved panel interaction

The expansion of the explosive begins to interact with the front face-sheet of curved sandwich panel at this stage. It is seen from **Figure 15** that the explosive product-curved panel interaction lasts over a time period of approximately 32 μs, from approximately t = 28 μs to t = 60 μs, corresponding the duration of the contact force between the explosive product and target structure almost becomes to zero. **Figure 15** shows the interaction of the explosive product with the curved panel, accompanied with the upward distortion as a result of the reflection from the curved target panel. Indentation deformation is first occurred in the central region of

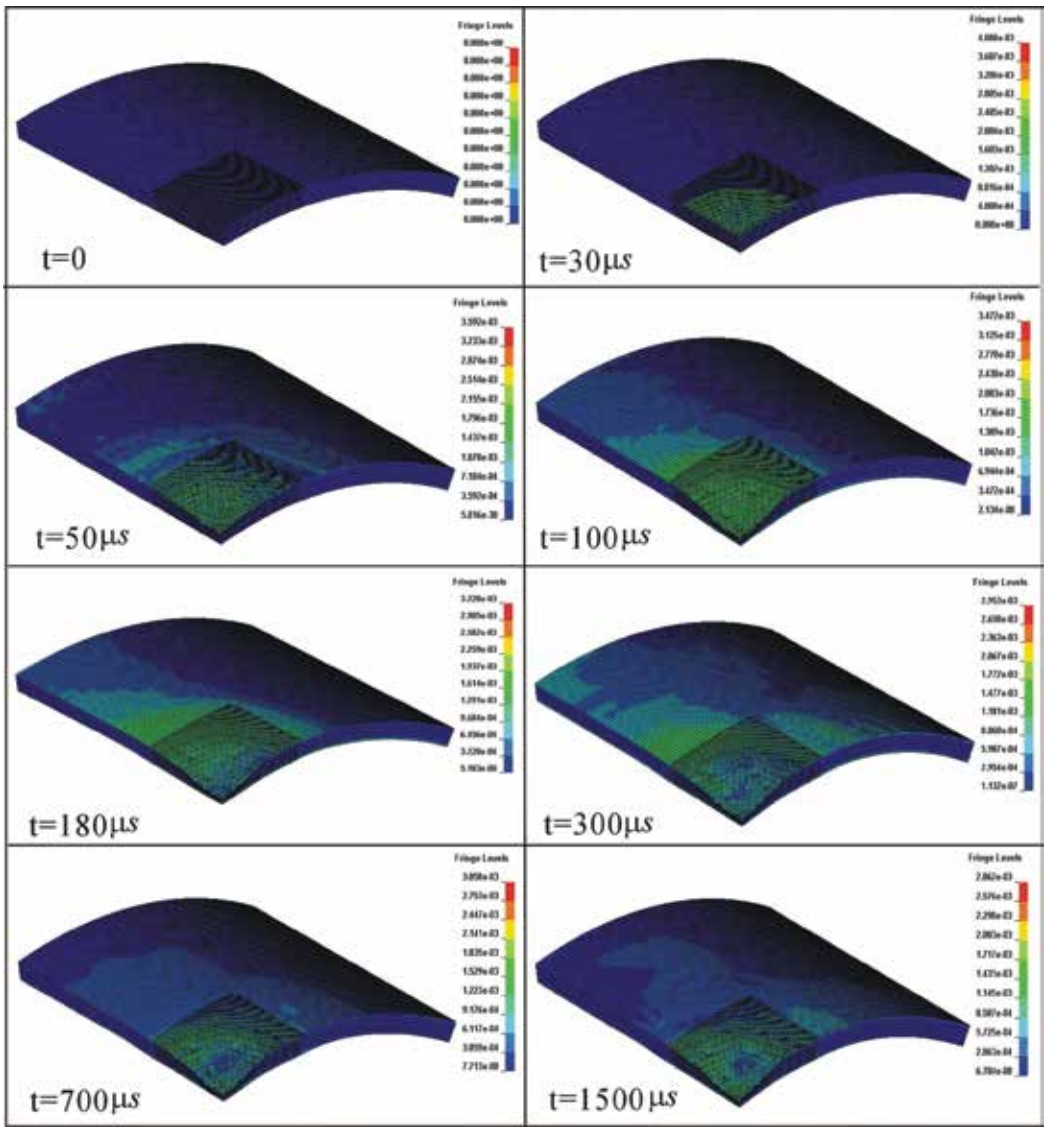

Figure 16. A typical process of curved sandwich panel deformation.

front face-sheet of the specimen, and then it extends both outward and downward with the transfer of blast impulse. Back face-sheet of the specimen has little deformation at this stage. Once the coupling interaction is completed (i.e., the contact force becomes to zero at $t = 60$ μs), the high-explosive model should be manually deleted from the finite element code.

3.2.1.3. Stage III: deformation of curved sandwich panel under its own inertia

In this stage, there is no coupling effect between the explosive product and the structure, and the curved sandwich panel remained to deform under the inertia, as shown in **Figure 16**. The central indentation failure of the front face-sheet is formed by gradually compressing the foam core, and the deformation extends outward until to the external clamped boundaries by traveling plastic hinges. The deformation of the curved sandwich panel structure is mainly governed by the plastic bending and stretching, accompanied with the slight oscillation. The whole curved sandwich panel finally presents a global dishing shape, and the maximum deflection of the back face-sheet occurs at the central point of the specimen.

3.2.2. Deflection response of the back face-sheet

Figure 17 compares the experimental and simulated permanent deflection at the central point of the back face-sheet. It is shown that all data points are close to the line of perfect match, which represents that the simulated data are agreed well with the experimental results. In order to better understand the deformation mechanism of curved sandwich panel, the progressions of deflections at several key nodes (as shown in **Figure 18**) along the central

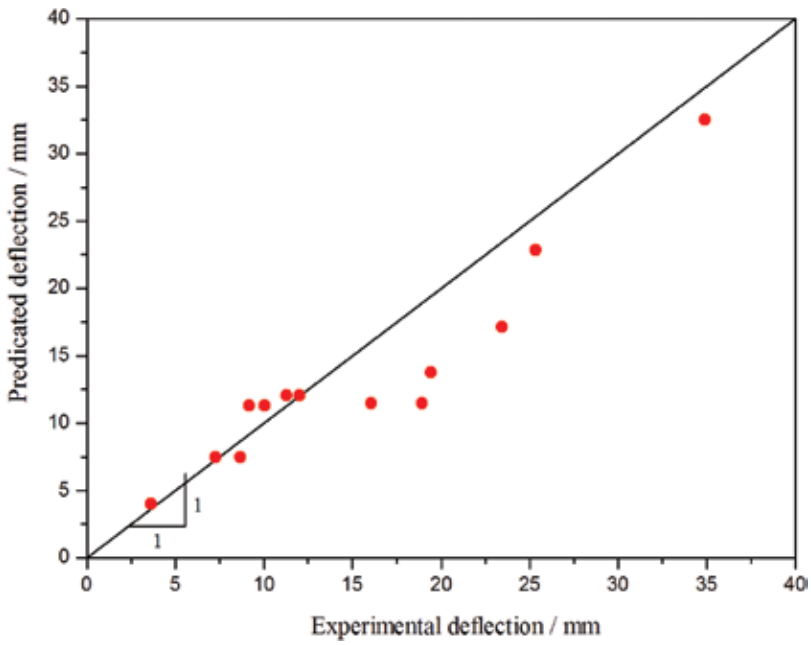

Figure 17. Comparison of experimental and numerical back-face deflection.

circumferential and longitudinal directions are presented in **Figure 19**. Both circumferential and longitudinal nodes for the front and back face-sheets have the similar deformation trend. At ~300 μs, all the nodes, except the node C5, have the maximum transient deflections, and then the deflection of these nodes decreases obviously due to the rebound of the elastic

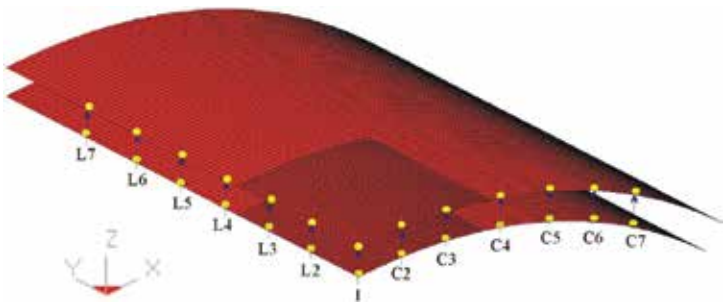

Figure 18. Locations of the circumferential and longitudinal nodes on the face-sheets.

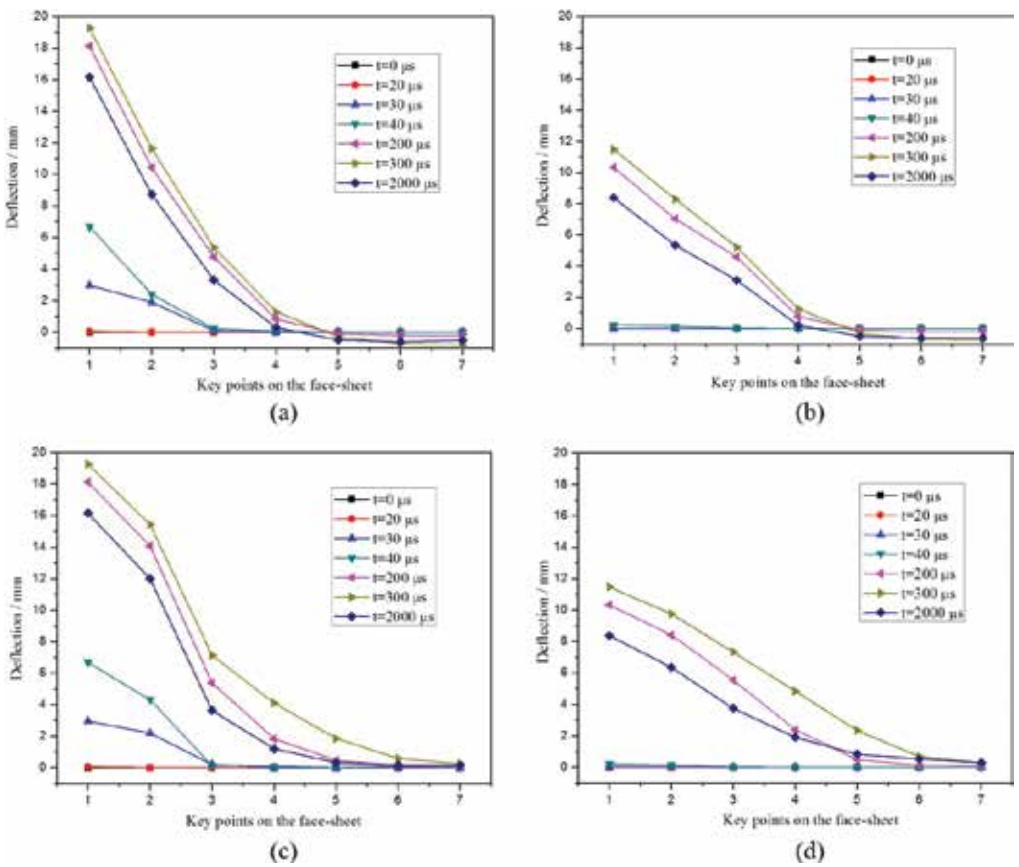

Figure 19. Deflection variation of key points on the face-sheets of the curved sandwich panel. (a) Circumferential (front face-sheet), (b) circumferential (back face-sheet), (c) longitudinal (front face-sheet), and (d) longitudinal (back face-sheet).

deformation until the whole deformation process is finished. The deformation of the back face-sheet obviously lags behind that of the front face-sheet, and the central point deflection of back face-sheet is also smaller than that of front face-sheet due to the foam core compression.

3.2.3. Energy absorption capability

Figure 20 shows the histories of plastic dissipation of the components of a curved sandwich panel (R250-h0.8-C10-ρ15%-B3) subjected to blast loading. In the early stage of the response, the front face-sheet compresses the aluminum foam core, resulting in core crushing and significant energy dissipation. It can be found from **Figure 20** that most of energy is dissipated by the large deformation of front face-sheet and core compression and core constitutes a major contribution, which is about 60% of total dissipation.

Effects of the impulse level and geometric configuration on the energy absorption of the components of the curved sandwich panels were indicated in a stack bar diagram in **Figure 21**. The partition of energy absorption of specimens is compared and analyzed in terms of the impulse level (specimen nos. 1–3), face-sheet thickness (specimen nos. 4–6), and core relative density (specimen nos. 7–9). The increase of impulse leads to a rise of total plastic energy dissipation in the specimens. Most of energy dissipation is attributed to large plastic deformation of front face-sheet and core compression. The energy absorption does not present a monotonic relationship with the face-sheet thickness. The specimen with 0.8-mm-thick face-sheets has the best energy absorption performance, followed by that of 0.5-mm-thick face-sheet, and the worst is that of 1.0-mm-thick face-sheet. This can be explained as follows: the

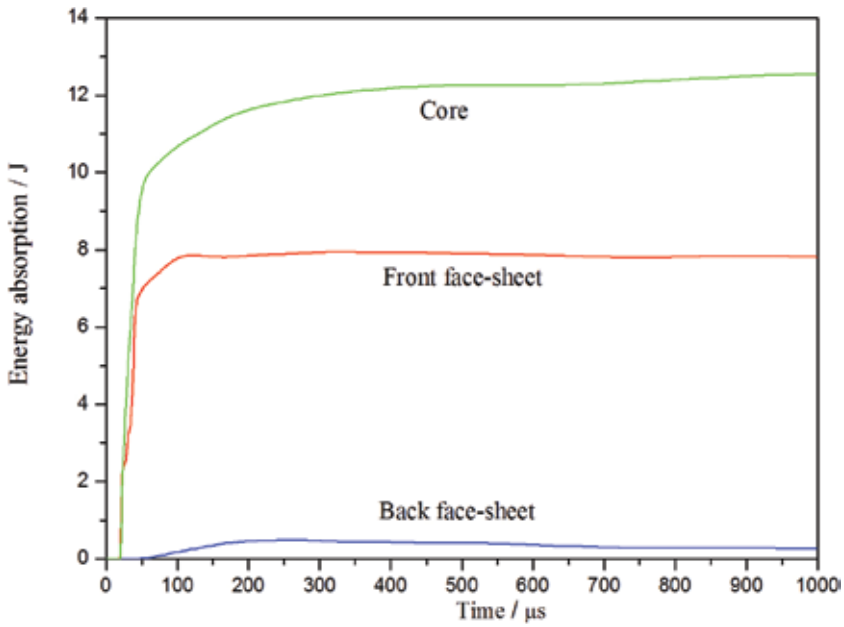

Figure 20. History of plastic dissipation of sandwich specimen during plastic deformation.

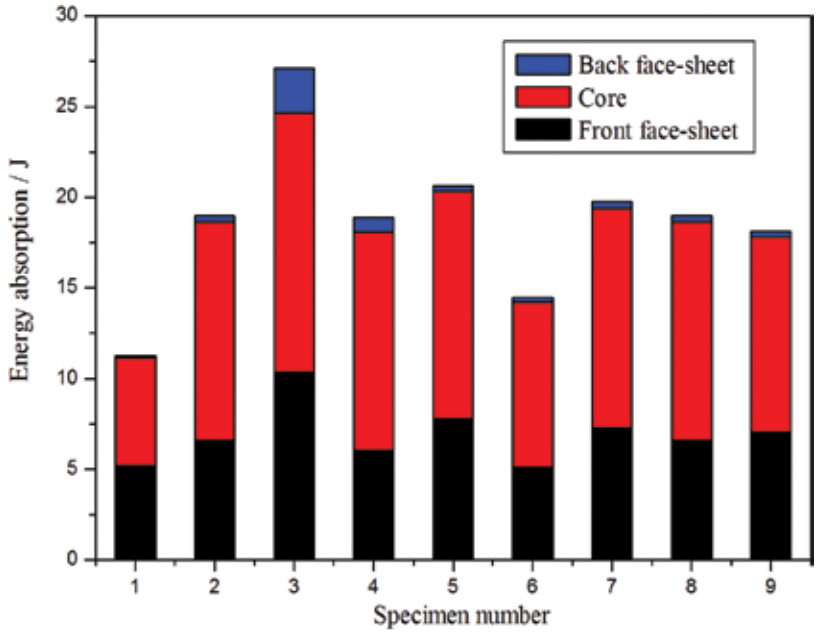

Figure 21. Plastic energy dissipation by the components of curved sandwich panels.

curved sandwich panel with thicker face-sheets deforms smaller due to the relatively larger structural stiffness; however, the severe damage may occur at the thinner front face-sheet under the large blast loading. Moreover, the total energy absorption amount of the curved sandwich panels decreases with the increased core relative density. Compared to the sandwich panels with the 10% core relative density, those specimens with 15 and 20% core density display relatively smaller energy absorption values, by 3.95 and 8.3%, respectively. This is attributed that the core compression values decrease with the increased core relative density, and the dominant deformation/failure mode of curved sandwich specimens is converted from the local core compression to global bending deformation, resulting in a weaker energy absorption capability.

4. Conclusions

Single-curvature sandwich panels with closed-cell aluminum foam cores, which include two radii of curvature (i.e., 250 and 500 mm), three face-sheet thicknesses (i.e., 0.5, 0.8, and 1.0 mm), and six different arrangements of foam core layers, were tested under air-blast loadings of various magnitudes. A total of 48 curved sandwich panels were examined, and the typical deformation and failure modes and the quantitative blast impulse and specimen deflection results were obtained and discussed. Based on the experiments, the corresponding finite element simulations were conducted using LS-DYNA software. The explosion and structural

response process, back face-sheet deflection response, and energy absorption capability were explored. Experimental results show that permanent central point deflection linearly increases with blast impulse for all the specimen configurations and blast resistance of specimens can be enhanced by increasing the face-sheet thickness or the core density. The weaker blast resistance of R = 250 mm curved sandwich panels, compared to monolithic plates with the same mass, and the R = 500 mm sandwich panels, which are attributed to the different dominant deformation mechanisms. Simulation results present that the deformation modes, deflection responses, and energy absorption capability of curved sandwich panels are related with the loading intensity and geometric configuration. Energy absorption capability of curved sandwich specimens is monotonically increasing with the increased blast impulse and decreasing with the increase of core relative density. However, it does not monotonically change with the face-sheet thickness.

Acknowledgements

The reported research is financially supported by the China National Natural Science Fundation under grant number 11402216.

Author details

Lin Jing[1]*, Zhihua Wang[2] and Longmao Zhao[2]

*Address all correspondence to: jinglin_426@163.com

1 State Key Laboratory of Traction Power, Southwest Jiaotong University, Chengdu, China

2 Institute of Applied Mechanics and Biomedical Engineering, Taiyuan University of Technology, Taiyuan, China

References

[1] Ashby MF, Evans AG, Fleck NA, Gibson LJ, Hutchinson JW, Wadley HNG. Metal Foams: A Design Guide. Oxford: Butterworth-Heinemann; 2000

[2] Lu G, Yu TX. Energy Absorption of Structures and Materials. Cambridge: Woodhead Publishing Ltd.; 2003

[3] Gibson LJ, Ashby MF. Cellular Solids: Structure and Properties. 2nd ed. Cambridge: Cambridge University Press; 1997

[4] Deshpande VS, Fleck NA. Collapse of truss core sandwich beams in 3-point bending. International Journal of Solids and Structures. 2001;**38**:6275-6305

[5] Jing L, Wang ZH, Ning JG, Zhao LM. The dynamic response of sandwich beams with open-cell metal foam cores. Composites: Part B. 2011;**42**:1-10

[6] Qiu X, Deshpande VS, Fleck NA. Impulsive loading of clamped monolithic and sandwich beam over a central patch. Journal of the Mechanics and Physics of Solids. 2005;**53**:1015-1061

[7] Wang ZH, Jing L, Ning JG, Zhao LM. The structural response of clamped sandwich beams subjected to impact loading. Composite Structures. 2011;**93**:1300-1308

[8] Jing L, Wang ZH, Zhao LM. The dynamic response of sandwich panels with cellular metal cores to localized impulsive loading. Composites Part B Engineering. 2016;**94**:52-63

[9] Foo CC, Chai GB, Seah LK. Quasi-static and low-velocity impact failure of aluminum honeycomb sandwich panels. Proceedings of the Institution of Mechanical Engineers, Part L: Journal of Materials: Design and Applications. 2006;**220**:53-66

[10] Radford DD, McShane GJ, Deshpande VS, Fleck NA. The response of clamped sandwich plates with metallic foam cores to simulated blast loading. International Journal of Solids and Structures. 2006;**43**:2243-2259

[11] Zhu F, Zhao LM, Lu GX, Wang ZH. Deformation and failure of blast-loaded metallic sandwich panels-experimental investigations. International Journal of Impact Engineering. 2008;**35**:937-951

[12] Qiu X, Deshpande VS, Fleck NA. Dynamic response of a clamped circular sandwich plate subject to shock loading. Journal of Applied Mechanics. 2004;**71**:637-645

[13] Jing L, Wang ZH, Shim VPW, Zhao LM. An experimental study of the dynamic response of cylindrical sandwich shells with metallic foam cores subjected to blast loading. International Journal of Impact Engineering. 2014;**71**:60-72

[14] Jing L, Wang ZH, Zhao LM. An approximate theoretical analysis for clamped cylindrical sandwich shells with metallic foam cores subjected to impulsive loading. Composites Part B: Engineering. 2014;**60**(4):150-157

[15] Jing L, Wang ZH, Zhao LM. Dynamic response of cylindrical sandwich shells with metallic foam cores under blast loading—Numerical simulations. Composite Structures. 2013;**99**:213-223

[16] Li QM, Magkiriadies I, Harrigan JJ. Compressive strain at the onset of densification of cellular solids. Journal of Cellular Plastics. 2006;**42**:371-392

Section 2

Fracture Mechanics

Chapter 8

Fracture Toughness Determination with the Use of Miniaturized Specimens

Jan Dzugan, Pavel Konopik and Martin Rund

Additional information is available at the end of the chapter

http://dx.doi.org/10.5772/intechopen.73093

Abstract

Fracture mechanics has been used for decades nowadays, and methods have been well established in the community especially for standard-sized specimens. As it was mainly developed for large structure assessment against the brittle failure, standardized specimens are of large size at present. However, in many cases, these standard specimens are not possible to apply due to size requirements of the available experimental material or the size of the component considered. These can be cases of residual service life assessment of in-service components, local properties determination (e.g., across weld), anisotropy determination and assessment of mechanical properties of newly developed materials under laboratory conditions (e.g., SPD processed materials, etc.). Therefore, development of new methods using significantly smaller specimens has to be carried out, and procedures using smaller-sized specimens together with their validity limits and relation to standardly obtained results have to be provided in order to provide solution for wide applications.

Keywords: fracture mechanics, ductile fracture, brittle fracture, miniature specimens, local properties, anisotropy assessment

1. Introduction

Fracture toughness properties yield very essential information on the material behavior with the presence of the sharp crack. This information is in many cases crucial for design or decision about the further use or discarding the component from service. However in many such important cases, there is shortage of the experimental material, and thus assessment has to be done based on miniaturized specimen testing. Examples of the cases when shortage of the

experimental material is only available can be residual service life assessment of in-service components, when the experimental material only by semi-destructive approach can be obtained. Cases during development of new materials, generally preparation of the materials with limited volume such as severe plastic deformation processes for bulk nanomaterials preparation. Recently, also for the assessment of the parts produced by additive manufacturing techniques are application for small-size specimen testing.

This chapter is going to provide overview of reporting values of the results obtained with the use of miniaturized specimens with hints how can be small-size-based results related to the standard-sized specimen results. These techniques enable assessment of the fracture behavior from small material volumes allowing, for example, also local anisotropy assessment. In the first part of the chapter, some theoretical background for small-size specimen testing is provided for different fracture regime behaviors ranging from brittle up to full ductile behavior. Several mini specimens' geometries are demonstrated here that are subsequently applied on the experimental materials. Three materials are presented here, ferritic steel used for Master Curve-based assessment and then stainless steel and Ti-alloy produced by additive manufacturing technology. The results are summarized in order to provide inside into the facture behavior assessment with the use of miniaturized specimens providing background for practical application of these approaches.

2. Specimen size and geometry influence on fracture toughness parameters

The effect of the specimen size and the geometry is variable with the material fracture behavior. Most of the technical materials exhibit transition behavior, and thus three basic regions can be distinguished: the lower shelf, transition and upper shelf.

Holzmann and Vlach [1, 2] suggested schematic diagram of fracture toughness behavior with temperature (see **Figure 1**), where following fracture toughness parameters are used for an analysis of the fracture behavior:

$K_{J0.2}$—fracture toughness after 0.2 mm of blunting and crack extension.

K_{Jm}—value of K_J at the maximum load F_{max} for stable fracture behavior and nonlinear test record.

K_{Ju}—post-ductile tearing cleavage fracture toughness; only J_c-tests terminated by cleavage prior to attaining the maximum load F_{max} were taken into account.

K_{JC}—fracture toughness for the onset of cleavage fracture after elastic-plastic deformation, but with no prior ductile tearing.

K_C—the fracture toughness at the onset of brittle fracture; test record linear or with no significant deviation from linearity, but size validity requirements of ASTM E399 are not met.

K_{IC}—plane strain fracture toughness.

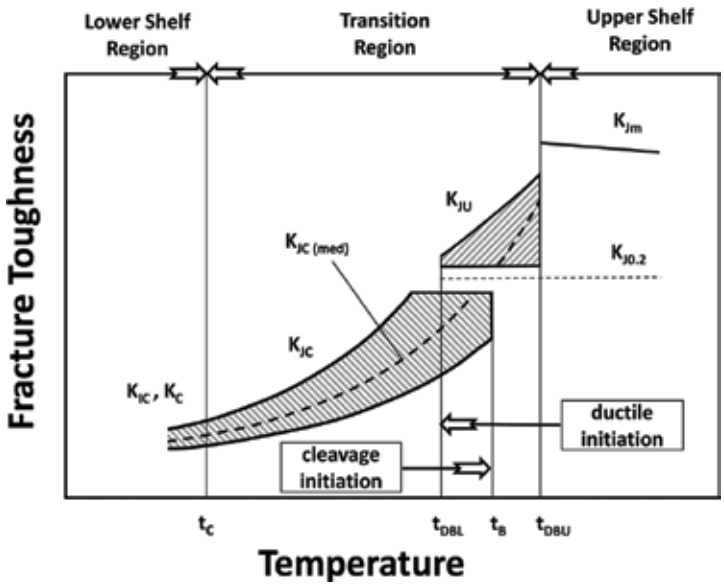

Figure 1. Schematic representation of fracture toughness-temperature dependence.

All values of K_J could be obtained by conversion from J-values using Eq. (1):

$$K_J = \sqrt{\frac{J.E}{(1-\nu^2)}} \tag{1}$$

The following transition temperatures are denoted in the diagrams:

t_{DBU}—ductile-brittle upper; the cleavage fracture occurs after certain amount of ductile tearing but prior to attaining the maximum load (the onset of the transition region).

t_{DBL}—ductile-brittle lower; the end of the region with the above fracture mode.

t_B—brittle-fracture transition temperature; the onset of the region, where cleavage fracture is initiated ahead of the blunted crack tip but without prior ductile tearing. Due to inherent scatter of material properties, t_B could be within the (t_{DBL}-t_{DBU}) region.

t_C—the lower shelf fracture toughness regime is below this temperature.

2.1. Brittle region (lower shelf region)

When a material behaves in a linear elastic manner prior to failure, such that the plastic zone is small compared to the specimen dimensions, a critical value of the Mode I stress intensity factor K_{Ic} may be an appropriate fracture parameter. In the ASTM E 399 [3] and similar test methods, K_{Ic} is referred to as "plane strain fracture toughness." Four specimen configurations are permitted for the fracture toughness determination by the current version of E 399: the compact tension (CT), single edge-notched bend bar (SE(B)), arc-shaped and disc-shaped specimens. However,

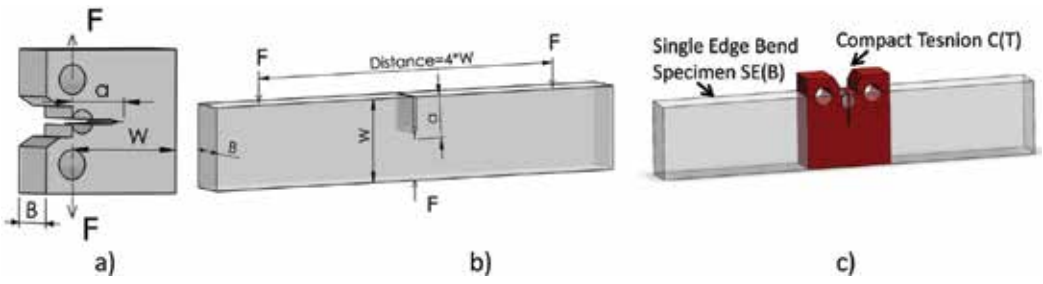

Figure 2. Comparison of the profiles of CT and SE(B) specimens with the same in-plane characteristic dimensions (*B, W, a*).

the vast majority of fracture toughness tests are performed on either CT or SE(B) specimens. **Figure 2** shows basic dimensions of both types of specimens of these two specimen types, assuming the same characteristic dimensions (*B, W, a*). It can be seen that the specimen design is such that all of the key dimensions (i.e., a, *B* and $W - a$) are approximately equal and, thus, geometry selection is only question of less material consumption from semi-product.

In order to fulfill the size requirements for size-independent fracture toughness value determination according to the ASTM E399, the minimal specimen thickness is 1.6 mm, while the specimen ligament size (*W-a*) must be not less than $2.5(K_{Ic}/\sigma_{YS})^2$, where σ_{YS} is the 0.2% offset yield strength. Considering recommended proportion of the thickness *B* which is nominally one-half the specimen width *W* and crack length, *a*, is nominally between 0.45 and 0.55 times the width *W*, the thickness must be also not less than $2.5(K_{Ic}/\sigma_{YS})^2$. These limits could be expressed using Eq. (2), which is not literally listed in the standard ASTM E399 but is noted in Anderson [4]:

$$B, a, (W-a) \geq 2,5 \cdot \left(\frac{K_{\mathrm{IC}}}{\sigma_{YS}}\right)^2 0.45 \leq a/W \leq 0.55 \tag{2}$$

Because the size requirements of ASTM E 399 are very stringent, it is very difficult and sometimes impossible to measure a valid K_{Ic} for most of the structural materials. As an example, we can consider structural steel with σ_{YS} = 330 MPa and typical K_{Ic} values of 210 MPa.m$^{0.5}$. According to Eq. (2), the required thickness must be higher than 1 m, and the width (since $a/W = 0.5$) must be more than 2 m (see **Table 1**). Materials are seldom available in such dimensions, and if yes, machining and testing would have to be done using special machine, and all investigation would be extremely expensive. On the other hand, material such as tool steels exhibits high yield strength and low fracture toughness, and **Table 1** shows combination of these two values for obtaining valid fracture toughness value under plain

Example	σ_{YS}	K_{Ic}	B, a	B, a
	MPa	MPa.m$^{0.5}$	m	mm
Steel_1	330	210	1012	1012.4
Steel_2	1600	40	0.002	1.6

Table 1. Examples of the calculated thickness *B* for given σ_{YS} and K_{Ic} values.

strain condition for thickness 1.6 mm. Considering investigated material in this chapter, **Table 2** shows hypothetic K_{Ic} value under plain strain condition for different specimen geometries and sizes. Note that the toughness level calculated here corresponds to the lower shelf for these materials. Thus valid K_{Ic} tests on these materials would be possible only at low temperatures, where the materials are too brittle for most structural applications.

In ASTM E 399 it is listed that "Variation in the value of K_{Ic} can be expected within the allowable range of specimen proportions, a/W and W/B. K_{Ic} may also be expected to rise with increasing ligament size. Notwithstanding these variations, however, K_{Ic} is believed to represent a lower limiting value of fracture toughness (for 2 % apparent crack extension) in the environment and at the speed and temperature of the test."

Therefore, valid K_{Ic} is generally accepted as size-independent value though some minor deviation could not be avoided. As it can be seen from **Tables 1** and **2**, it is very difficult to obtain valid fracture toughness values with the use of subsized specimens in this region, except for very brittle materials. Therefore, subsided specimens will most yield size-dependent values of the fracture toughness.

2.2. Ductile-brittle transition region

In this region, micro-mechanisms of cleavage fracture cause that the cleavage toughness data tend to be highly scattered when compared to the lower shelf region, and thus a statistical analysis must be performed as shown in **Table 3**. Rather than single value of toughness at a particular temperature, the material has a toughness distribution. Research over the past three decades on the fracture of ferritic steels in the ductile-brittle transition region has led to two important conclusions:

Material	Specimen geometry and size	σ_{YS}	B, a	Requested K_{Ic}
		MPa	mm	$MPa.m^{0.5}$
15CH2NMFA	1 T-CT	502	25.0	50.2
	M-CT		4.0	20.1
	CVN 10 × 10 × 55		10.0	31.7
	KLST 4 × 2 × 27		2.0	14.2
AISI 304	1 T-CT	657	25.0	65.7
	M-CT		4.0	26.3
	CVN 10 × 10 × 55		10.0	41.6
	KLST 4 × 2 × 27		2.0	18.6
AM Ti6Al4V	1 T-CT	927	25.0	92.7
	M-CT		4.0	37.1
	CVN 10 × 10 × 55		10.0	58.6
	KLST 4 × 2 × 27		2.0	26.2

Table 2. Calculated requested parameter K_{Ic} for valid plain strain condition considering investigated material in this chapter.

Material	Tests							Region of fracture toughness results
	Tensile tests		Facture toughness tests					
	Standard	Mini	1 T-CT	0.16 T-CT	CVN	KLST	2 T-CT	
15CH2NMFA	X	X	X	X	X	X	X	Transition region
AISI 304	X	X	X	X	X	X		Upper shelf
Ti6AL4V		X		X	X			Upper shelf

Note: CVN, standard Charpy V-notched specimen ($10 \times 10 \times 55$ mm^3).

Table 3. Test matrix for the fracture toughness tests.

1. Scatter in fracture toughness data in the transition region follows a characteristic statistical distribution that is very similar for all ferritic steels.
2. The shape of the fracture toughness vs. temperature curve in the transition range is virtually identical for all ferritic steels. The only difference between steels is the absolute position of this curve on the temperature axis.

ASTM E1921 [5] implements this knowledge, and the standard outlines a fracture toughness test method that is based on the Master Curve concept for ferritic steels with yield strengths ranging from 275 to 825 MPa. Thanks to previous research, methodology for determination of toughness distribution is greatly simplified including size effect prediction. In order to directly compare toughness data obtained from different thickness specimens, a statistical size correction is employed to equilibrate the highly stressed material volume sampled at the crack tip by cleavage. The following Eq. (3), derived from ASTM E1921, shall be used for conversion to an equivalent value of $K_{Jc(1T)}$ for a reference 1 T specimen with thickness of $B_{1T} = 25$ mm:

$$K_{Jc(1T)} = 20 + \left(K_{Jc(X)} - 20\right).\left(\frac{B_X}{B_{1T}}\right)^{1/4} \tag{3}$$

where $K_{Jc(X)}$ is measured fracture toughness of the tested specimen and Bx refers to the nominal thickness of the tested specimen in millimeters, regardless of side grooves. Once toughness values at a fixed temperature have been converted to 1 T equivalent values, the further evaluation which leads to a reference transition temperature T_0 is performed according to standard as for 1 T specimen.

The reference temperature T_0 should be relatively independent of the test temperature that has been selected. Hence, data that are distributed over a restricted temperature range, namely, $T_0 \pm 50°C$, can be used to determine T_0. This temperature range together with the specimen size requirement (see Eq. (4)) provides a validity window for application of the Master Curve methodology. As an example, such a validity window for Charpy-size fracture specimens (W = B = 10 mm, a/W = 0.5) is shown in **Figure 3**.

$$K_{JC(\mathrm{lim}it)} = \sqrt{\frac{Eb_0\sigma_{ys}}{30.(1-\nu^2)}} \tag{4}$$

where E is the Young's modulus, σ_{ys} is the material yield strength at the test temperature and b_0 is ligament W-a.

It should be also mentioned that specimens can have side grooves, but they are optional (see **Figure 4**). In fact, side grooving may be indispensable as a means for controlling crack front straightness in bend bars of square cross section. The total side-grooved depth shall not exceed 0.25B. Side grooves with an included angle of 45° and a root radius of 0.5 ± 0.2 mm usually produce the desired results.

In the ASTM E1921 is noted that at high values of fracture toughness relative to specimen size and material flow properties, the values of K_{Jc} that meet the requirements of Eq. (3) may not always provide a unique description of the crack front stress strain fields due to some loss of constraint caused by excessive plastic flow. The application which played a key role for development of small specimen test technology (SSTT) was the evaluation of properties of irradiated materials. For example, many investigations for integrity assessments of nuclear components were done in VTT in Finland where also Master Curve method was developed [7] and validated [8]. Wallin et al. were further developing SSTT for Master Curve determination using mini-Charpy specimen (KLST) since 1997 [9]. Scibetta et al. [10] investigated different reactor pressure vessel steels using standard and miniature specimens. The reference temperatures obtained from subsize SE(B) and C(T) geometry tend to give a lower reference temperature by about −8.5°C than larger specimens which was considered as a consequence of the constraint loss. Kima et al. [11] investigated effects of specimen size on fracture toughness using 1 CT, 1/2 CT and 1/4 CT. It was found that small specimen test technique for F82H steel can be applicable to evaluate the fracture toughness properties due to no substantial effects of specimen size.

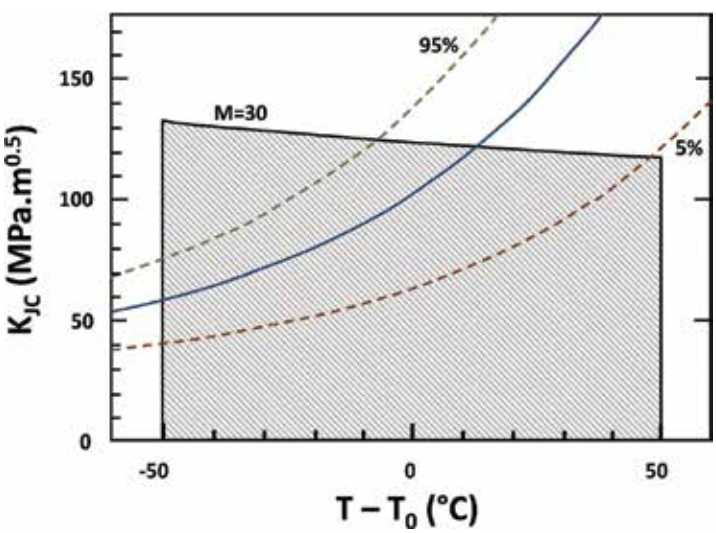

Figure 3. Validity window of the Master Curves for the ferritic materials [6].

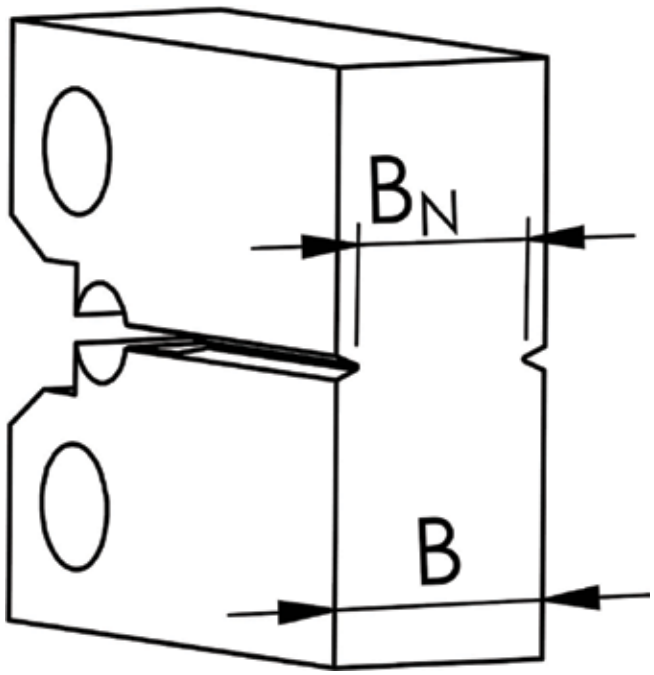

Figure 4. Side grooves in a fracture mechanics test specimen.

Recently, great attention is focused on mini-CT (0.16 T-CT) specimen geometry that can be made out of the broken halves of standard Charpy specimens. In 2014, round robin program focused on verification of the reliability and robustness of experimental data of the mini-CT was carried out among different laboratories. The results of the round robin confirmed that the mini-CT specimens offer a very attractive opportunity to derive the same fracture toughness reference temperature values, T_0, as those derived by larger fracture toughness specimens [12].

Sokolov [13, 14] tested in 2016 and 2017 the mini-CT specimens with dimension of $10 \times 10 \times 4\,mm^3$ (see **Figure 5**) on materials HSST Plate 13B and un-irradiated Linde 80 WF-70 weld, respectively. The T_0 value derived from a relatively small number of mini-CT specimens in these studies is in remarkable agreement with the T_0 value previously reported from a much larger number of conventional fracture toughness specimens. At the same time, these studies indicate that in the real practice, it is highly advisable to use much larger number of specimens than the minimum amount prescribed in ASTM E1921, when mini specimens are employed.

Also Wallin in work [15] focused his attention on mini-CT specimen. His work indicates that miniature C(T) specimens fulfilling the ASTM E1921 size requirement behave like larger specimens loaded to the same proportional loading. Side grooving was found to have a minor effect on the initiator locations and was not significantly affected by the side groove geometry.

For completeness, it should be noted that three different methods to quantify constraint have also been proposed, *J* small scale yielding correction, *Q*-parameter and the *T*-stress. [16]. Also Wallin considers *Q*-parameter and the *T*-stress for Master Curve reference temperature T_0

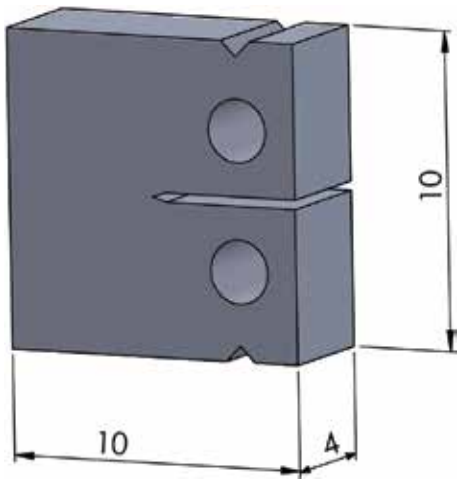

Figure 5. Layout of mini-0.16 T-CT specimens that can be extracted out of the broken halves of Charpy specimens and its overall dimensions.

correction [15, 17]. However closer description of these approaches is out of the scope of the current chapter.

2.3. Ductile region

In the case of ductile materials, first the blunting of preexisting cracks occurs during loading followed by formation of voids ahead of the crack tip at the critical strain. These voids finally coalesce with the crack tip leading to the crack propagation. Hence, the ductile crack initiation cannot be defined as a point in the *J-Δa* curve but rather as a process which occurs over a range. For a *J-R* curve determination, it is necessary to know the crack length at corresponding loading level. There are basically two approaches: single-specimen and multiple specimen methods. For the multiple specimen test method, several "identical" specimens are loaded to different levels, and the achieved crack lengths are usually measured visually at the fracture surface. In the case of the single-specimen method, in order to obtain a full range pf crack lengths for *J-R* curve determination from only one specimen, three widely used single-specimen test methods were developed with the crack lengths being monitored during the test. One is the elastic unloading compliance method that is the most often used out of the single-specimen methods. Another technique is the electrical potential drop method and also the normalization method, both described in the ASTM 1820 [18].

From a *J-R* curve, the characteristic values of elastic-plastic fracture mechanics are determined. One of the significant parameters is the plane strain initiation toughness J_{Ic} that provides a measure of the crack growth resistance near the onset of stable crack growth for mode-I cracks. Since it is difficult to define the instance of crack initiation in ductile metals, different definitions of the initiation toughness were used in different test standards. ASTM E1820 adopts an engineering definition of J_{Ic} at the intersection of a 0.2-mm offset construction line and the *J-R* curve, as shown by J_Q in **Figure 6**.

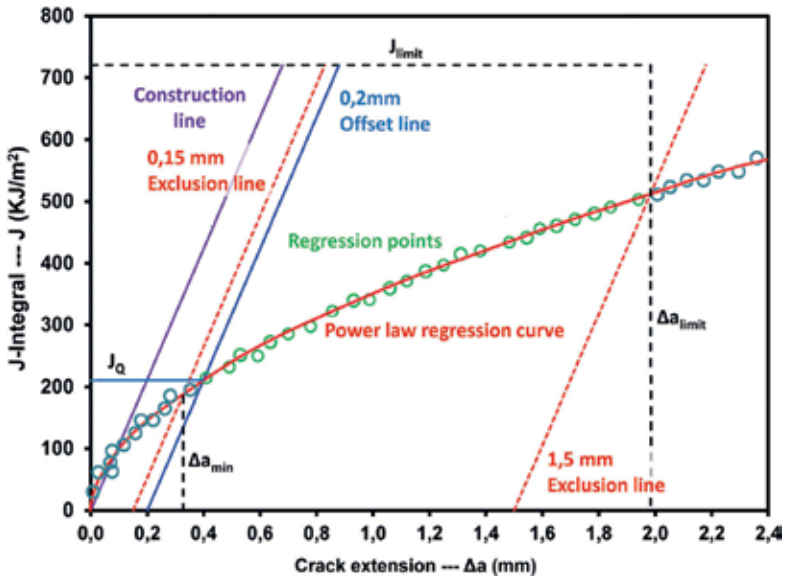

Figure 6. A typical J-R curve with test data points, construction lines and limitation bounds required by ASTM E1820.

A valid J-R curve consists of the measured data points in a region defined by the coordinate axis and the J_{max} and Δa_{max} limits. These two limits describe the measurement capacity of test specimen. The maximum J-integral capacity for a specimen is given by the smaller of:

$$J_{max} = b\sigma_Y/10 \text{ or } J_{max} = B\sigma_Y/10 \tag{5}$$

where σ_Y is an effective yield strength assumed as the average of the 0.2% offset yield strength σ_{YS} and the ultimate tensile strength σ_{tS}. The maximum crack extension capacity for a specimen was defined as

$$\Delta a_{max} = 0.25\, b_0 \tag{6}$$

where b_0 is the initial crack ligament.

Application of fracture mechanics methods to engineering design and structural integrity assessment requires fracture toughness values to be transferred from the laboratory test to a structural application. Experiments have shown that the crack depth, section thickness, specimen size, crack geometry and loading configuration all can have a strong effect on the fracture toughness measurements (K, G, J and d). These effects are referred to as "constraint effect." Joyce and Link [19] tested SE(B) specimens with various a/W ratios to investigate the constraint effect on J-R curves. **Figure 7** shows that significant differences exist between the J-R curves for deep and shallow cracks. Similar trend can be observed when only one type of geometry with the same ratio of a/W but with different sizes is used.

Ono et al. [20] tested JLF-1 steel using 1 CT, 1/2 CT and 1/4 CT in the upper shelf region. Obtained J-R curve are very illustrative and showed shallow shape with decreasing size; see

Figure 8. Specimen size effects were interpreted here in terms of an increase in the plain stress state region and plastic zone size at the crack tip in the specimen. From the point of specimen thickness effect, this work summarized that the fracture toughness increased as the specimen thickness decreased. From the point of ligament size effect, the fracture toughness decreases when the specimens were miniaturized while keeping the same proportions.

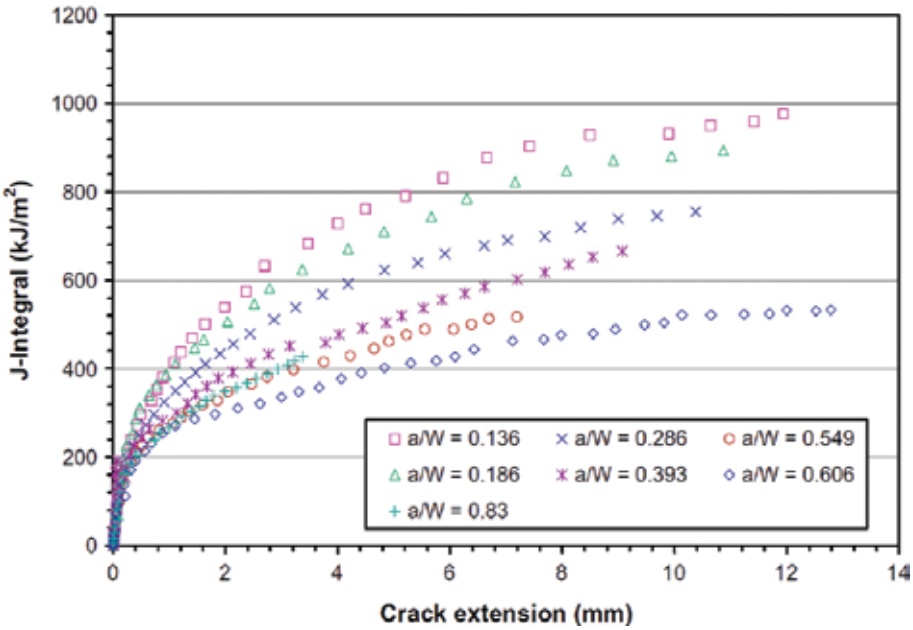

Figure 7. The J-R curve dependency on the a/W ratio for HY80 steel obtained by Zhu and Joyce [19] using SE(B) specimens and normalization method.

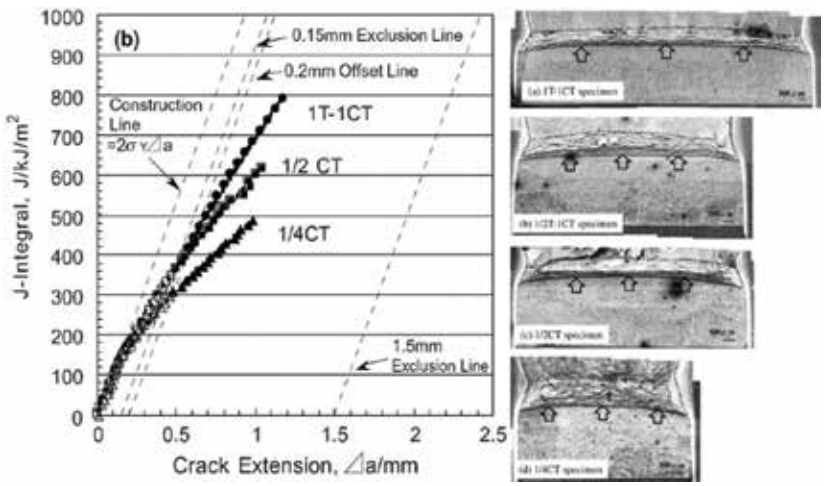

Figure 8. J-R curves of JLF-1 steel (left) and corresponded specimen size (right) [20].

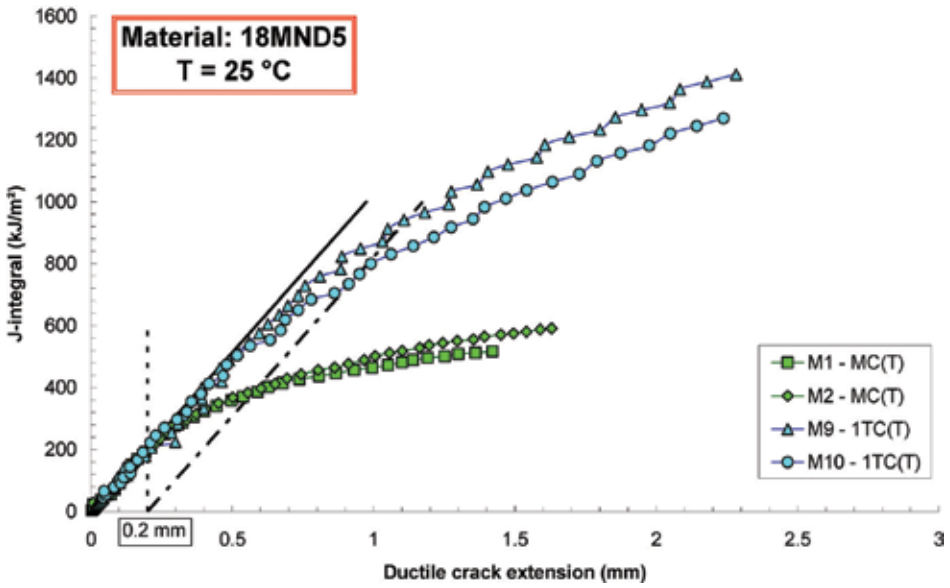

Figure 9. Results obtained at room temperature from mini-CT and 1 T-CT specimens of 18MND5 steel [24].

Seok et al. [21] investigated effect of specimen configurations using 0.5–2 T CT and further specimens with constant width (101.6 mm) but different thickness plus specimens with same thickness but different width. Therefore, the effect of plane size, specimen size and thickness could be investigated. Moreover, the effect of the crack length and side grooves was discussed as well. The resulting *J-R* curve increased with increasing plane size, though there is a difference of increasing amount according to the material states, base or weld metal and stainless or carbon steel. The resulting *J-R* curves decreased with increasing crack length and showed that the effect of the crack length was significant. However, relatively weak influence was observed from the change of the specimen thickness and size. It was also observed that *the J-R* curve decreased by applying the side grooves and the effect of side groove was related to material properties.

Lucon et al. [22–24] investigated mini-CT specimen ($10 \times 10 \times 4.15$ mm^3) applicability for fracture toughness determination in the upper shelf region. As a general conclusion, in these investigations it was observed that mini-CT specimens consistently and systematically underestimate elastic-plastic fracture toughness as measured from 1 T-CT specimens, in terms of both ductile initiation and tearing resistance. **Figure 9** shows an example of such a behavior and also shows that, below approximately J = 200 kJ/m^2, no significant deviation was observed between data measured from mini-CT and 1 T-CT specimen; below this threshold, mini-CT could therefore provide a reliable measurement of the material's toughness.

3. Small size experimental specimen testing

Examples of fracture toughness test with the use of miniature test specimens are going to be presented in this chapter. Results obtained on three experimental materials are shown here.

Namely, RPV steel GOST 15Ch2NMFA with ferritic-martensitic microstructure, austenitic stainless steel EN X5CrNi18-10 (AISI 304) and Ti-Alloy Ti6Al4V produced by Additive Manufacturing (AM) technology are employed in this study. Ductile and brittle materials facture behavior is investigated here with the use of miniaturized specimens applying J-R curve and Master Curve assessment approaches.

As the assessment of the fracture toughness parameters requires also tensile test data as input parameters for the evaluation, determination of tensile properties with the use of miniature tensile test (M-TT) specimens is also demonstrated here.

3.1. Experimental materials

Material GOST 15Ch2NMFA were delivered in a form of rod with diameter of 130 mm and length 150 mm. At first, three 2 T-CT specimens were produced in R-C orientation (according to the standard ASTM E399-09 [3]). Technical drawing of 2 T-CT specimens is depicted in **Figure 10**. Broken halves of the 2 T-CT specimens were subsequently used for production of the other specimens (tensile test specimens, Charpy specimens, etc.).

Material EN X5CrNi18-10 (AISI 304) was delivered in the form of hot rolled rod with quadratic cross section of dimensions 60 × 30 × 400 mm^3. All specimens were produced in T-L orientation according to standard [3].

Material Ti6Al4V was investigated in the form of bar with dimension of 10 × 20 × 100 mm^3. Designation of specimen orientation was done according to the standard [25]. Where the first letter represents the direction normal to the crack plane and second latter represents the expected direction of crack extension. Orientation and its designation of the specimens in the prism are depicted in **Figure 11**.

3.2. Tensile tests

Tensile test were carried out on standard- and miniature-sized specimens at room temperature under quasi-static loading conditions for demonstration of comparable results obtained with the use of miniaturized specimens. Tests were following procedure according to standard (ISO CSN EN 6892-1) in the case of the full-size specimen testing. Testing procedure based on

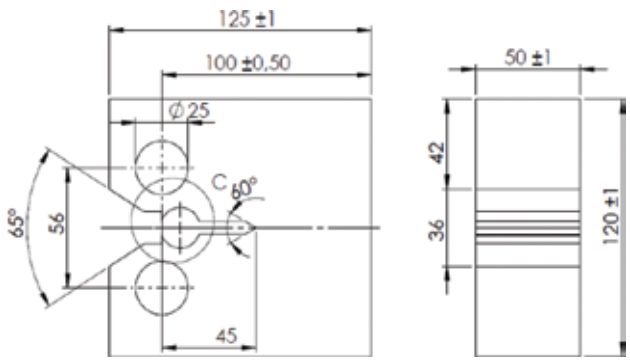

Figure 10. 2 T-CT specimen geometry.

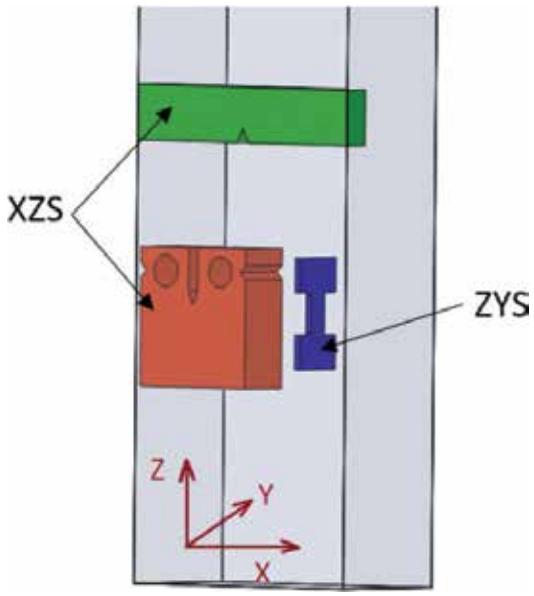

Figure 11. Orientation and designation of the specimens for the material Ti6Al4V produced SLM AM technology (Z = building direction).

standard developed in [26, 27] was employed for mini tensile test (M-TT) specimens. Specimen geometry used for the current investigations is displayed in **Figure 13**. Full size specimens (**Figure 12c**) were tested with the use of electromechanical testing system Zwick Z250 with

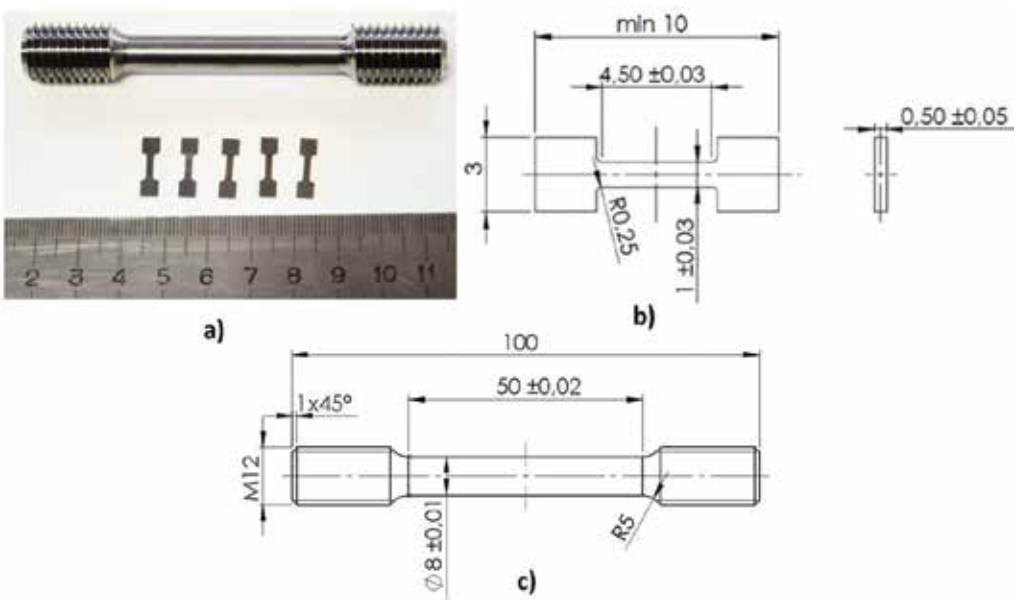

Figure 12. Tensile test specimen geometries. (a) Comparison of the standard and miniature tensile test specimens. (b) Dimensions of mini tensile test (M-TT) specimen. (c) Standard size specimen.

mechanical extensometer for strain measurement. The M-TT specimens (**Figure 12b**) were tested with the use of small-sized linear drive-based testing system with capacity of 5 kN. Strain in the course of the M-TT test was measured using DIC system ARAMIS by GOM. Prior to tests, strain calibration with certified calibration blocks was performed. An appropriate pattern was applied on the specimen surface for the strain measurement by DIC system. M-TTs were done with constant crosshead velocity of 0.25 mm/min and 1 mm/min for the "standard" geometry. Three to five specimens were tested per batch. Specimens' dimensions were measured prior to tests and after tests in order to evaluate tensile test-specific parameters. Summarized test records obtained for the materials investigated are shown in **Figures 13–15**. Averaged test results for each material investigated are shown in **Table 4–6**.

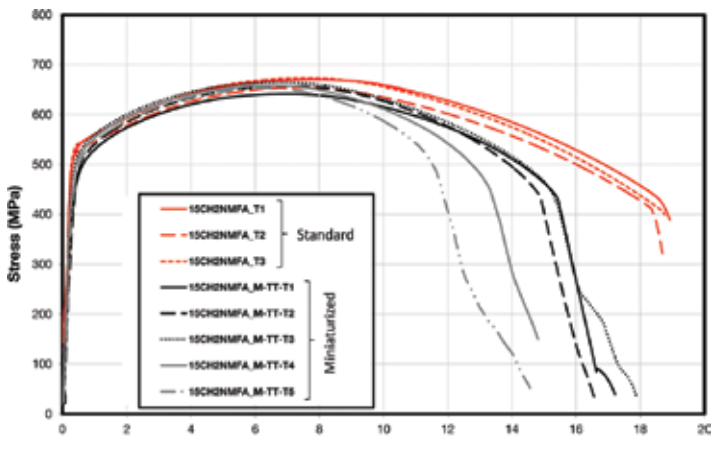

Figure 13. Tensile test results, material 15CH2NMFA, geometry: standard and miniaturized.

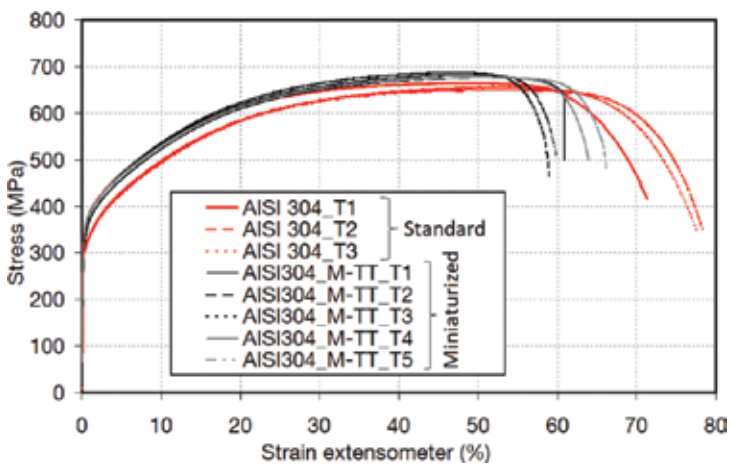

Figure 14. Tensile test results, material AISI304, geometry: standard and miniaturized.

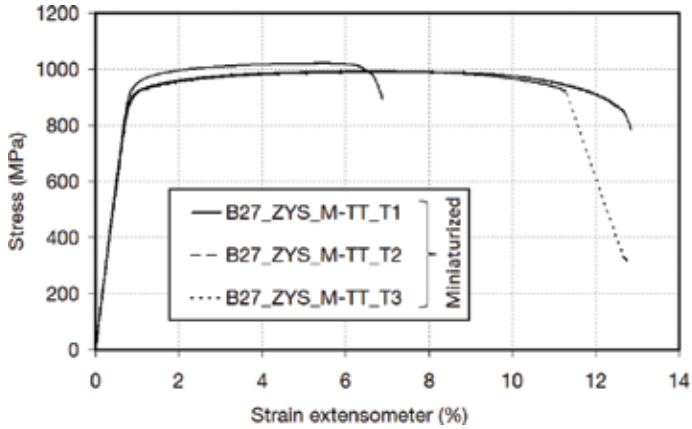

Figure 15. Tensile test results, material AM Ti6Al4V, geometry: M-TT.

Specimen		E	YS	UTS	El_u	El	RA
		GPa	MPa	MPa	%	%	%
AISI304_standard	Avg.	167.6	316.2	657.1	49.1	63.7	82.5
	St. dev.	16.9	27.6	6.8	1.2	2.1	1.8
AISI304_miniaturized	Avg.	141.9	340.7	679.1	49.3	62.0	75.7
	St. dev.	8.1	9.9	4.8	1.3	3.0	1.7

Table 4. Tensile test results, material AISI 304, geometry: standard and miniaturized.

Specimen		E	YS	UTS	El_u	El	RA
		GPa	MPa	MPa	%	%	%
15CH2NMFA_standard	Avg.	195.4	502.0	647.9	8.0	20.8	70.1
	St. dev.	9.5	21.4	13,1	1.1	1.4	0.4
15CH2NMFA_miniaturized	Avg.	159.8	503.4	655,1	6.3	16.2	66.0
	St. dev.	27.9	11.7	8,3	0.3	1.4	5.2

Table 5. Tensile test results, material 15CH2NMFA, geometry: standard and miniaturized.

Specimen		E	YS	UTS	El_u	El	RA
		GPa	MPa	MPa	%	%	%
B27_ZYS_miniaturized	Avg.	114.6	927.3	1000.7	5.5	10.8	43.3
	St. dev.	2.0	20.2	17.1	0.8	3,4	2.1

Table 6. Tensile test results, material AM Ti6Al4V, geometry: miniaturized.

3.3. Fracture toughness measurements

Based on theoretical and experimental analyses of possible fracture toughness specimen downsizing, several geometries were proposed as it was discussed before. Demonstration of the fracture toughness property measurement with the use of miniaturize specimens is shown here on samples of several geometries here. The geometries employed here are miniature compact tension specimen (0.16 T-CT) (**Figure 16**) and miniature Charpy specimens (half Charpy specimen typically 4 × 3 × 22, KLST); see **Figure 17**. These specimens' geometries are utilized for brittle and ductile fracture description.

As the input data for the fracture toughness tests are used, results of tensile tests for pre-cracking parameter determination and subsequent evaluation of validity limits and J-R curves.

The effect of the temperature on fracture toughness is known for many years. It is a question of the material if it will exhibit sharp or gentle change. As it was mentioned above, the fracture toughness-temperature dependency can be divided in several regions, and the current tests are covering most of them.

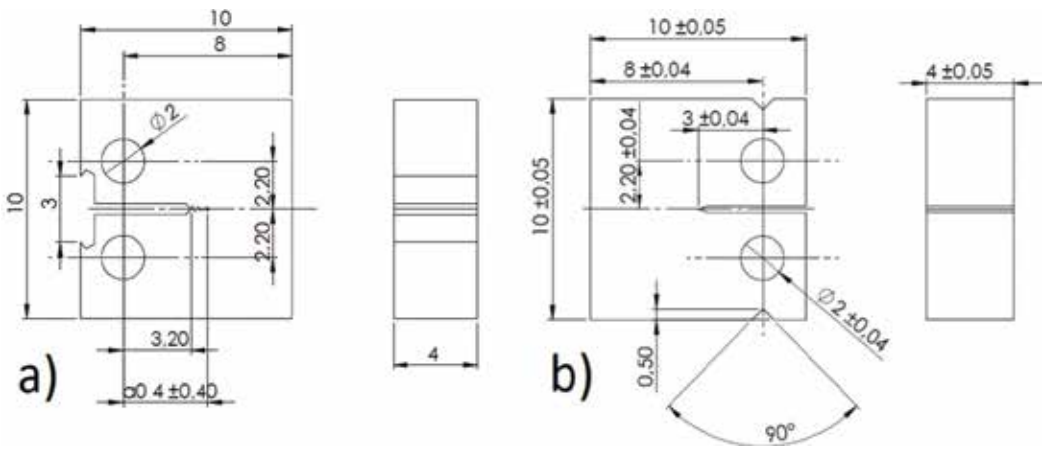

Figure 16. Miniature compact tension specimen (0.16 T-CT): (a) front face geometry and (b) the "top and bottom" geometry.

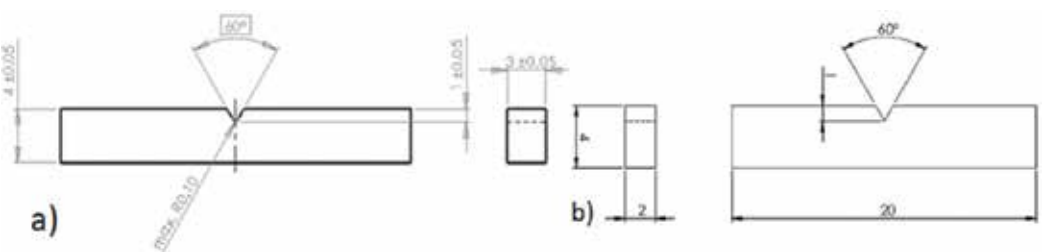

Figure 17. Miniature Charpy specimen (KLST): (a) geometry 4 × 3 × 22 mm^3 and (b) geometry 4 × 2 × 20 mm^3.

3.4. Testing in the transition region

Master Curve concept according to the standard ASTM 1921-17a [5] was applied on material 15CH2NMFA. The aim of this investigation was to show the shift of the reference temperature T_0 with regard to the geometry of the specimen and size of the specimen. Therefore, compact tension specimens of different sizes (2 T-CT, 1 T-CT and 0.16 T-CT) and three-point bend specimens' geometries (CVN, standard Charpy specimen $10 \times 10 \times 55$ mm^3, and miniaturized Charpy specimen, KLST ($3 \times 4 \times 22$ mm^3)) were produced.

Pre-crack of all specimens was done on magnetic resonance testing machine RUMUL; the initial crack size was 0.5 *W* with the final stress intensity factor of 16 MPa.m$^{0.5}$. After pre-cracking, 20% side groves were introduced. The final tests were performed on servo-hydraulic testing machine MTS 810 with load capacity of 250 kN (in a case of 2 T-CT and 1 T-CT specimens) and servo-hydraulic testing machine Instron with load capacity 80 kN (in a case of CVN, KLST specimens), respectively. Both machines were equipped with environmental chamber for cooling of the specimens. In all cases specimens were held on testing temperature for 15 min before the tests. Deformation of the specimens was measured by means of COD extensometer on the load-line position. Testing setup for KLST samples is depicted in **Figure 18**.

The first estimation of the T_0 was done according to the (7) presented in [5]. For this purpose ten standard Charpy specimens were produced, and value $TK_{28J} = -34.7$ J was determined. The estimated reference temperature T_0 was evaluated according to the (7) as -52.7°C. This estimation provides reference temperature with standard deviation of 15°C [5]:

$$T_0 = TK_{28J} - 18^{\circ}C \tag{7}$$

For measurement and calculation of reference temperature T_0, the multi-temperature approach was applied. All measured data were censored through crack front criterion defined in (8):

$$K_{Jc(limit)} = \sqrt{\frac{Eb_0\sigma_{YS}}{30(1-v^2)}} \tag{8}$$

where E is Young modulus, $b_0 = W\text{-}a_0$ (a_0 = initial crack size), σ_{YS} is yield strength and v is Poisson ratio. For the final evaluation, all fracture toughness results were recalculated to K_{JC_1T} using Eq. (3).

Measured data which fulfill the limit stated in (8) were marked as $r_i = 1$. If evaluated facture toughness values exceed limit (8) value, they were marked as $r_i = 0$, respectively.

Crack lengths were measured through area measurement method. Example of fracture area measurement is presented in **Figure 19**.

Summarization of the reference temperature T_0 determination is shown in **Table 7**. Master Curve with all measured data is depicted in **Figure 20**.

It is clear from **Table 7** that evaluated reference temperature using the KLST specimens and 2 T-CT specimens does not fulfill the validity criteria $\sum r_i n_i > 1$, and these reference temperatures can be taken as provisional reference temperature T_{0Q}.

Figure 18. KLST specimens ($4 \times 3 \times 22$ mm^3) from material 15CH2NMFA.

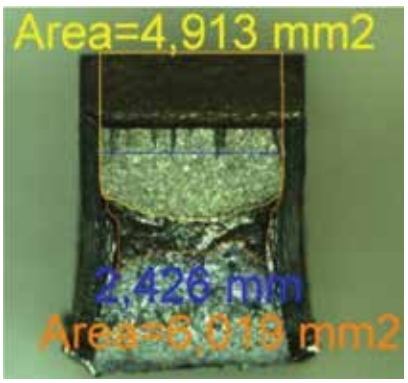

Figure 19. Example of crack size measurement.

Specimen	**Number of specimen**	**T_0/T_{0q}**	**$r_i.n_i$**	**Diff.T_0**
		°C	**—**	**°C**
1 T-CT	6	−41,3	1	−23,7
0.16 T-CT	9	−62,6	1,5	−2,4
CVN	14	−73,1	2,33	8,1
KLST	14	−51,8	0,56	−13,2
2 T-CT	3	−27,9	0,5	−37,1
All specimens	46	**−65,0**	**5,9**	—

Table 7. Summarization of Master Curve results, material 15CH2NMFA.

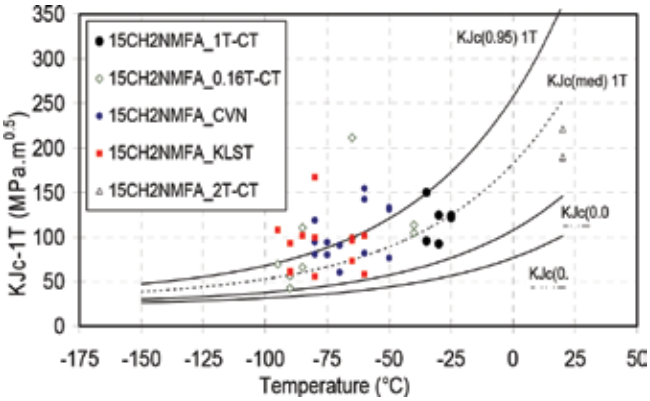

Figure 20. Comparison of the Master Curve evaluation for various samples' geometries.

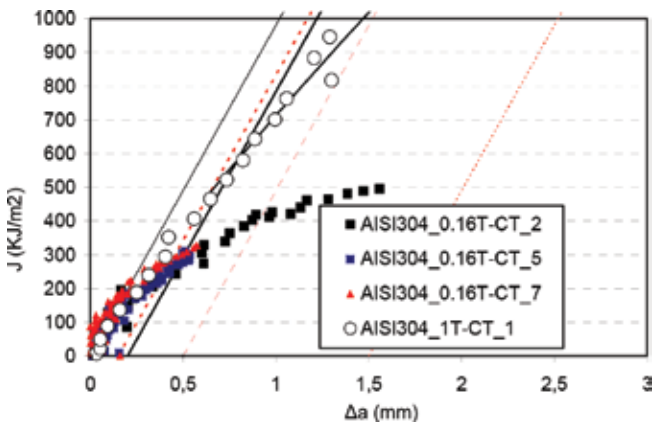

Figure 21. Comparison of J-R curves; material AISI 304; geometry of the specimens, 1 T-CT vs. 0.16 T-CT; unloading compliance method of measurement.

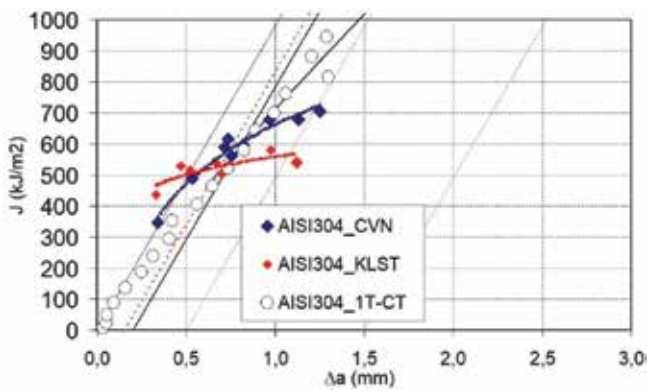

Figure 22. Comparison of J-R curves, material AISI 304, geometry of the specimens: 1 T-CT (unloading compliance method) vs. CVN and KLST (multiple specimen method).

3.5. Testing in the ductile region

Testing in ductile region was done according the standard ASTM 1820-17 [18] where concept of J-R curve was applied with in order to evaluate the crack initiation and propagation of material AISI 304 and material Ti6Al4V produced by AM technology. It compared J-R measured using unloading compliance method (for CT specimen) and multiple specimen method (for three-point-bend specimens); simultaneous size of the specimens was taken into the account. Compact tension specimen (1 T-CT and 0.16 T-CT) was compared with standard Charpy specimen (CVN) and miniaturized Charpy specimens (KLST).

Specimens were pre-cracked at first up to the final initial crack size 0.5 W with the final stress intensity factor of 16 MPa.m$^{0.5}$. After the pre-cracking 20% side groves were introduced, and magnetic resonance machine RUMUL was used for pre-cracking. Testing of 1 T-CT was carried out on servo-hydraulic testing machine MTS 810 with load capacity 250 kN. *J-R* curve tests of CVN, KLST and 0.16 T-CT specimens were carried out on servo-hydraulic testing machine Instron with the load capacity of 80 kN. In the scope of the multiple testing procedures, specimens were heat tinted after the tests and consequently cooled down in liquid nitrogen. The cooled specimens were then broken, and crack sizes were measured through area measurement method; see in **Figure 19**. *J-R* curve evaluation was done with the slope of construction line according to (9):

$$J = 2\sigma_{YS}\Delta a \tag{9}$$

Results of the *J-R* testing are present in **Figures 21–23** and summarized in **Table 8**. Summarization of *J-R* curve tests on material Ti6Al4V produced by Additive Manufacturing technology is in **Table 9**. Comparison of J-R curves obtained for 0.16 T–CT and KLST (4 × 2 × 20 mm^3) is depicted in **Figure 23**.

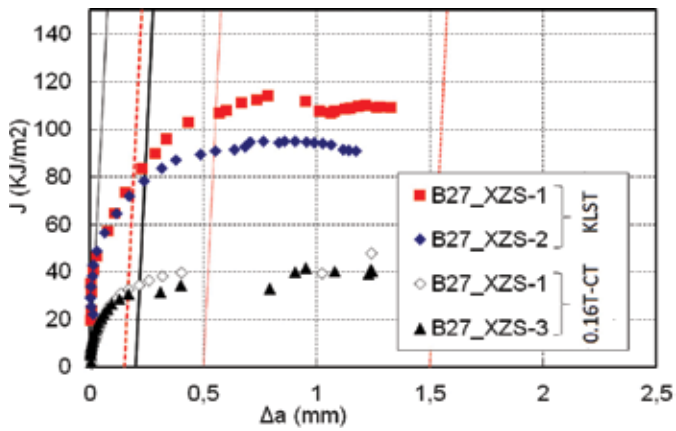

Figure 23. Comparison of J-R curves; material, AM Ti6Al4V; geometry of the specimens, 0.16 T-CT vs. KLST (4 × 2 × 20 mm^3); unloading compliance method of measurement.

Specimen	J_{IC} kJ/m^2	Number of specimens	Specimen
1 T-CT	598,3	3,0	UC
0.16 T-CT	345,2	7,0	UC
CVN	573,1	10,0	MS
KLST	513,6	14,0	MS

(UC = Unloading Compliance; MS = Multiple specimen method)

Table 8. Summarization of average values of fracture toughness results, material AISI 304.

Specimen	O.16 T-CT		KLST (4 × 2 × 20 mm^3)	
	Avg.	St. dev.	Avg.	St. dev.
J_{IC} kJ/m^2	31,9	2,5	85,7	9,1

Table 9. Comparison of fracture toughness results; material AM Ti6Al4V; geometry, 0.16 T-CT vs. KLST (4 × 2 × 20 mm^3); unloading compliance method of measurement.

4. Result discussion and conclusions

The chapter presented here gives basic overview on issues related to small-size specimen testing in the field of the fracture mechanics tests. Some theoretical background and the relation between values obtained on small- and full-sized specimens for all regimes of the fracture behavior ranging from the lower shelf behavior up to the upper shelf region are shown. Some possibilities on how to resolve the size issue influence of the fracture toughness parameters and the reasons for differences obtained during the evaluation in the first chapter part were presented. An overview of size requirements for a valid value determination of the fracture toughness is also given. The subsequent experimental part is demonstrating results of the fracture toughness determination for three materials covering transition and upper shelf region behavior. As an important part of the fracture toughness tests are tensile properties determination. The chapter is dealing with miniature specimen testing; thus mini tensile tests are presented here for the basic property determination that is necessary for fracture toughness test preparation, execution and assessment.

Testing in the transition region and evaluation with the use of the Master Curve approach yielded very good result comparability between miniaturized and full-size specimens for the material investigated. Testing program spanning over five specimens' geometries agrees very well with published results and confirms reliable result determination in this region even with the use of the miniaturized specimens including 4-mm-thick mini-CT specimens and three-point-bend specimens of cross section 2 × 4 mm^2. The upper shelf behavior with the stable crack extension was investigated for stainless steel and Ti-alloy produced by the additive manufacturing process. In the case of the stainless steel, four specimens' geometries were

investigated, and multiple specimens' as well as single specimens' approaches were applied. Standard-sized specimen results yielded very good agreement with the results achieved for subsized three-point bend specimens, while the mini-CT specimen yielded values of about 60% of those ones obtained for standard-sized specimens. In the case of Ti-alloy, due to very limited amount of the experimental material, typically, e.g., for AM parts, mini specimens were investigated only. Both considered specimens' geometries yielded repeatable results. However, the CT specimens yielded significantly lower fracture toughness values of about 40% of those obtained for three-point-bend specimens. Large difference between these specimens' geometries results is in agreement with other published studies and results presented here for the stainless steel.

The results obtained here point out the fact that there is currently no available general solution for size effect description in the fracture toughness determination approaches so far. Varying agreement is found for various materials. Therefore, for a reliable "size-independent" value determination, the material of the interest has to be investigated and size effect quantified. It seems that the *J*-integral-based assessment has rather limited reporting value and better description has to be established for size-independent fracture toughness evaluation in the upper shelf. Lower transition region is well described by the Master Curve approach including size effect in the evaluation. Generally considered, there is no need in all cases to obtain size-independent values. These can be the case such as property assessment of the components of small wall thickness, where plain strain condition is in reality not predominant. Cases when local property anisotropy is being evaluated, just ratio among different locations and/or orientations, are considered. Typical examples of the materials produced with small wall thickness exhibiting high ration of property anisotropy are materials and components produced by the additive manufacturing processes. In these cases, there is generally hardly any chance to obtain "size-independent material properties" due to the reason that if produced in different wall thicknesses, different properties are achieved, and thus considered wall thickness has to be directly assessed.

As it can be seen in many cases, no real size-independent values are possible to achieve for the material, and thus small-size techniques are the only way to characterize the properties. These values are related just to the component and the process considered; however, valuable information are provided allowing component design and process optimization. Miniaturized specimen-based techniques for the fracture toughness determination were demonstrated here as a tool providing deeper insight into the material fracture behavior for better understanding of the material behavior in cases when limited amount of the experimental is available.

Acknowledgements

This chapter was created with support of the projects TH02020448S service life assessment with the use of miniaturized test specimens, 2017–2020, and Development of West-Bohemian Centre of Materials and Metallurgy No. LO1412, financed by the MEYS of the Czech Rep.

Author details

Jan Dzugan*, Pavel Konopik and Martin Rund

*Address all correspondence to: jan.dzugan@comtesfht.cz

COMTES FHT a.s., Dobrany, Czech Republic

References

[1] Holzmann M, Vlach B, Man J. R-curves and fracture toughness transition behaviour at static, rapid and impact loading of Cr-Ni-Mo-V reactor pressure vessel steel. International Journal of Pressure Vessels and Piping. 1995:39-47

[2] Holzmann M, Vlach B, Brumovský M. Measurement of fracture toughness transition behaviour of Cr-Ni-Mo-V pressure vessel steel using pre-cracked Charpy specimens. International Journal of Pressure Vessels and Piping. 1999;**76**:591-598

[3] ASTM E399-09. Standard Test Method for Linear-Elastic Plane-Strain Fracture Toughness KIc of Metallic Materials. West Conshohocken, PA: ASTM Int; 2009

[4] Anderson TL. Fracture Mechanics – Fundamentals and Applications. 3rd ed. Boca Raton: CRC Press; 2005

[5] ASTM E1921-17a. Standard Test Method for Determination of Reference Temperature, to, for Ferritic Steels in the Transition Range. West Conshohocken, PA: ASTM International; 2017 www.astm.org

[6] Feilitzen CF, Sattari-Far I. Implementation of the Master Curve method in ProSACC; 2012, ISSN: 2000-0456

[7] Sattari-Far I, Wallin K. Application of Master Curve Methodology for Structural Integrity Assessments of Nuclear Components, October 2005, ISSN 1104-1374

[8] Wallin K. Master curve analysis of ductile to brittle transition region fracture toughness round robin data, The "EURO" fracture toughness curve, VTT manufacturing Technology; 1998, ISNN 1455-0849

[9] Wallin K, Valo M, Planman T, Rintamaa R. Applicability of Smaller than Charpy Specimens for Fracture Toughness Characterization with the VTT Method. Finland: VTT Manufacturing Technology, FIN-02044 VTT (Espoo); 1997

[10] Scibetta M, Lucon E, Walle E. Optimum use of broken Charpy specimens from surveillance programs for the application of the master curve approach. International Journal of Fracture. 2002;**116**:231-244

[11] Kima BJ, Kasadaa R, Kimuraa A, Tanigawab H. Effects of specimen size on fracture toughness of phosphorous added F82H steels. Fusion Engineering and Design. 2011;**86**(9):2403-2408

[12] Sokolov MA. Results of fracture toughness tests for the round robin test program using mini-compact specimens. In Sokolov MA. ORNL report, ORNL/LTR-2014/686; December 2014

[13] Sokolov MA. Development of Mini-Compact Tension Test Method for Determining Fracture Toughness Master Curves for Reactor Pressure Vessel Steels. Materials Science and Technology Division, Oak Ridge National Laboratory; 2017

[14] Sokolov MA, Nanstad RK. The Assessment and Validation of Mini-Compact Tension Test Specimen Geometry. Materials Science and Technology Division, Oak Ridge National Laboratory; 2016

[15] Wallin K, Yamamoto M, Ehrnstén U. Location of initiation sites in fracture toughness testing specimens - the effect of size and side grooves. Proceedings of the ASME 2016 PVP2016, Vancouver, British Columbia, Canada

[16] Nevalainen MJ. The effect of specimen and flaw dimensions on fracture toughness. VTT Publications 314: Espoo. Technical Research Centre of Finland; 1997

[17] Wallin K. Quantifying T_{stress} controlled constraint by the master curve transition temperature T_0. Engineering Fracture Mechanics. 2001;**68**:303-328

[18] ASTM E1820-17. Standard Test Method for Measurement of Fracture Toughness. West Conshohocken, PA: ASTM International; 2017 www.astm.org

[19] Zhu WK, Joyce JA. Review of fracture toughness (G, K, J, CTOD, CTOA) testing and standardization. U.S. Navy Research. Paper 49; 2012

[20] Ono H, Kasada R, Kimura A. Specimen size effects on fracture toughness of JLF-1 reduced-activation ferritic steel. Journal of Nuclear Materials. 2004;**329–333**:1117-1121

[21] Seok CS, Kim SY. Effect of specimen configurations on the fracture resistance curve. Nuclear Engineering and Design. 2002;**214**:47-56

[22] Lucon E, Scibetta M. Miniature compact tension specimens for upper shelf fracture toughness measurements on RPV steels. American Society for Testing and Materials. 2009;**5**:18-31. ASTM STP 1502

[23] Lucon E, Scibetta M, Vandermeulen W. Additional Investigations on the Applicability of Miniature Compact Tension Specimens for Fracture Toughness Measurements in the Upper Shelf Regime; 2005

[24] Lucon E, Scibetta M, Chaouadi R, van Walle E. Use of Miniaturized Compact Tension Specimens for Fracture Toughness Measurements in the Upper Shelf Regime, OPEN REPORT OF THE BELGIAN NUCLEAR RESEARCH CENTRE, SCK.CEN-BLG-1009; April 2005. online: http://publications.sckcen.be/dspace/bitstream/10038/240/1/blg_1009_text.pdf

[25] ASTM WK49229, Standard Guide for Orientation and Location Dependence Mechanical Properties for Metal Additive Manufacturing; 2017. Work in Progress. http://www.astm.org/DATABASE.CART/WORKITEMS/WK49229.htm

[26] Džugan J, Procházka R, Konopík P. Micro -Tensile Test Technique Development and Application to Mechanical Property Determination. In: Sokolov MA, Lucon E, eds. Small Specimen Test Techniques. Vol. 6, STP 1576. pp. 12-29. doi: 10.1520/STP157620140022

[27] Dzugan J, Konopik P, Rund M, Prochazka R. Determination of Local Tensile and Fatigue Properties with the Use of Sub-Sized Specimens, ASME PVP 2015. Vol. 1A. USA: Codes and Standards, Boston, Massachusetts; 2015. ISBN: 978-0-7918-5692-5, Paper No. PVP2015-45958, pp. V01AT01A066; 8 pages. DOI: 10.1115/PVP2015-45958

Chapter 9

Fatigue Fracture of Functionally Graded Materials Under Elastic-Plastic Loading Conditions Using Extended Finite Element Method

Somnath Bhattacharya, Kamal Sharma and Vaibhav Sonkar

Additional information is available at the end of the chapter

http://dx.doi.org/10.5772/intechopen.72778

Abstract

In this chapter, extended finite element method (XFEM) has been used to simulate the fatigue crack growth problems in functionally graded material (FGM) in the presence of hole, inclusion and minor crack under elastic and plastic conditions. The fatigue crack growth analysis of alloy/ceramic FGMs, alloy and equivalent composite is done by XFEM in the presence of multiple discontinuities under mode-I mechanical load. The validity of linear elastic fracture mechanics (LEFM) theory is limited to the brittle materials. Therefore, the elastic plastic fracture mechanics (EPFM) theory needs to be utilized to characterize the plastic behavior of the material. A generalized Ramberg-Osgood material model has been used to model the stress-strain behavior of the material. Plasticity has been checked by Von Mises Yield criteria. J-integral has been used to calculate the SIF. Crack growth direction is determined by maximum principal stress criteria.

Keywords: FGM, composite materials XFEM, elastic-plastic loading, fatigue fracture, crack propagation, discontinuities, inclusions, holes, minor cracks

1. Introduction

Development of novel materials improves performance and efficiency of the structures, and also leads to development of advanced and sophisticated structures. This complex process of materials, structures and technology has led to the development of composite materials. Strength and stiffness plays a key role in evaluating the worth of the material. These characteristics provide strength to the structure to retain its desired shape and size under loading or any other external action.

Cracks/flaws are inevitable in all engineering materials. Loading under severe environmental conditions may either initiate new cracks or may cause the propagation of pre-existing cracks in the structures. Theoretically, fracture can be defined as the breaking or rupturing of a material resulting into its separation into two or more pieces.

Composite materials manifested in the middle of the twentieth century. Composites are naturally occurring or engineered materials made from two or more constituents with different chemical or physical properties distinct boundary among constituents. Lightweight composite materials with high strength to weight and stiffness to weight ratios have been used successfully in aircraft industry and other engineering applications. Under high temperature conditions the strength of the metal is deteriorated whereas, ceramics have excellent resistance to heat.

FGMs can be referred as multiphase composite materials in which the composition or microstructure or both are spatially varied which lead to a certain gradation in the local material properties. FGMs can be defined as multi-phase composites. FGMs are synthesized such that they own continuous variations in volume fractions of their components in space to return a pre-established composition. FGMs possess continuously varying properties in one or more than one direction and the form non-homogeneous macrostructure due to these variations. By gradually varying the volume fraction of the constituents, FGMs exhibit a smooth and continuous change from one surface to another, thus reducing interface problems, and minimizing thermal stress concentrations. The ceramic phase of FGMs provides a good resistance to heat, while the metal phase provides a strong mechanical performance and hence reduces the possibility of catastrophic failure.

The major advantages of FGM over conventional materials are firstly, FGM satisfies the working conditions for which it is specifically developed. Secondly, it is economical as it reduces material costs for particular engineering applications. Thirdly, it can reduce the magnitude of residual and thermal stresses generated under working conditions. Finally, FGMs exhibit better fracture toughness and bond strength. This is normally achieved by using a ceramic layer connected with a metallic layer. FGMs have wide area of engineering applications like in the computer circuit and aerospace industries. FGMs have typical applications is in aircraft and automotive industries as thermal barrier coatings (TBCs).

In general, all structural components are subjected to thermo-mechanical cyclic load. The fatigue life of these components is generally predicted without considering the effect of defects/discontinuities present in component. However, FGMs are commonly made by sintering process, which are porous in nature. These discontinuities at the vicinity of a major crack tip lead to increase the effective SIF at the major crack tip due to which the life of the components get depreciated. Hence, the analysis of FGMs in the vicinity of discontinuities becomes very important from the design point of view. To widen the spectrum of applications of FGMs, the fatigue/fracture behavior should be properly evaluated.

Over the years, greater understanding of fracture mechanics has undoubtedly prevented a significant number of structural failures. Fracture mechanics approach for the design of structures includes flaw size as one of the key variables. Fracture toughness replaces strength of material as a relevant material attribute, and its evaluation is mainly done in composites using the *J*-integral approach [1]. Failure of FGM has always been a trending domain of research for scientists and engineers due to the wide spectra of their engineering applications.

http://dx.doi.org/10.5772/intechopen.72778

Fatigue and quasi-static fracture are two forms of crack growth phenomenon. Fatigue fracture refers to the slow propagation of cracks under cyclic loading conditions where the stress intensity factors are below the fracture toughness of the material. Quasi-static fracture is observed near the end of the fatigue life when the increased crack length leads to stress intensity factors which are above the fracture toughness [2, 3].

In many cases, multiple cracks may exist in the components. There interaction resulting in the variation of stress intensity factor, stress distribution and propagation direction of the major crack. In the past, the failure of structures was analyzed in the presence of multiple cracks [4]. Some efforts have been made using analytical, experimental and simulation techniques to analyze the effect of interaction among multiple cracks [5–7].

Although, many analytical [8, 9] and experimental methods [10, 11] have been explored for the calculation of fracture parameters even then the drawbacks associated with experimental investigation and scarcity of analytical solution have impelled the analysts towards alternative techniques. Numerical methods hold the promise in this regard.

Many numerical methods are available to simulate the problems of fatigue failure in materials. These include finite element method (FEM), boundary element method, hybrid boundary node method [12, 13], meshfree methods [14–18] and extended finite element method [19, 20]. Out of these methods, FEM has been widely used for solving a wide variety of engineering and industrial problems [21–26]. It has achieved a remarkable success in solving various linear and non-linear problems [27–34]. Despite its numerous advantages and unparalleled success, it is not well-suited for solving the problems involving crack propagation. In crack growth problems, element edges provide natural lines along which a crack can grow. This is advantageous if the crack path is known a priori, but in most of the fracture phenomenon, the crack path is unknown. Thus, FEM requires a conformal mesh and re-meshing to ensure that the element boundaries coincide with the moving discontinuities (crack). Moreover, crack tip singularity cannot be accurately modeled by standard finite element approximation. Therefore, the modeling of crack growth becomes quite tedious and time consuming due to the modification in mesh topology at each stage of crack propagation. To overcome this difficulty, a new method known as extended finite element method (XFEM) has been developed to model arbitrary discontinuities without a need of conformal mesh or re-meshing. Level set method (LSM) is used in conjunction with XFEM for defining as well as tracking the geometry of cracks and other discontinuities like holes and inclusions. To cope up with these problems, XFEM has been adopted as a tool for the analysis of fatigue crack propagation in FGM.

2. Calculation of SIF for FGM

A domain based interaction integral approach can be used for calculating the stress intensity factors for homogeneous, bi-layer and functionally graded materials under thermal as well as mechanical loading. In this chapter, interaction integral approach will be extended to calculate the SIFs for FGM and bi-layered FGM under mechanical loads. The interaction integral is calculated based on *J*-integral. The *J*-integral for an elastic body subjected to thermo-mechanical load is given as,

$$J = \oint_{\Gamma_o} \left(\tilde{W}\, \delta_{1j} - \sigma_{ij} \frac{\partial u_i}{\partial x_1} \right) n_j d\Gamma \tag{1}$$

For the interaction integral calculation of an elastic body, consider two equilibrium states i.e. state 1, the actual state with given boundary conditions and state 2, an auxiliary state of the cracked body. The parameters for auxiliary state are represented with superscript *a*. The final expression for the interaction integral takes the form [35]

$$\begin{aligned} M_{12} = & \int_{A_o} \left(\sigma_{ij} \frac{\partial u_i^a}{\partial x_1} + \sigma_{ij}^a \frac{\partial u_i}{\partial x_1} - \sigma_{ik}^a \varepsilon_{ik}^m \delta_{1j} \right) \frac{\partial q}{\partial x_j} dA + \\ & \int_{A_o} \left(\sigma_{ij} \left(S_{ijkl}^{tip} - S_{ijkl}(\mathbf{x}) \right) \frac{\partial \sigma_{kl}^a}{\partial x_1} \right) q\, dA \end{aligned} \tag{2}$$

where, the auxiliary field for the FGM may be taken from [36] as.

$$\sigma_{ij}^a = C_{ijkl}^{tip} \frac{1}{2} \left(\frac{\partial u_k^a}{\partial x_l} + \frac{\partial u_l^a}{\partial x_k} \right), \varepsilon_{ij}^a = S_{ijkl}(\mathbf{x}) \sigma_{kl}^a \text{ and } \varepsilon_{ij}^a \neq \frac{1}{2} \left(\frac{\partial u_i^a}{\partial x_j} + \frac{\partial u_j^a}{\partial x_i} \right) \tag{3}$$

The SIFs are calculated from the interaction integral as [36]:

Mode-I SIF is given as,

$$K_I = \frac{M_{12} E^* \cosh^2 \left(\pi \varepsilon^{tip} \right)}{2} \text{ with } K_I^a = 1 \text{ and } K_{II}^a = 0 \tag{4a}$$

Mode-II SIF is given as,

$$K_{II} = \frac{M_{12} E^* \cosh^2 \left(\pi \varepsilon^{tip} \right)}{2} \text{ with } K_I^a = 0 \text{ and } K_{II}^a = 1 \tag{4b}$$

where, $E^* = \frac{2\overline{E}_1 \overline{E}_2}{\overline{E}_1 + \overline{E}_2}$ with $\overline{E}_i = \begin{cases} E_i^{tip} & \text{for plane stress} \\ E_i^{tip} / \left(1 - \left(\nu_i^{tip} \right)^2 \right) & \text{for plane strain} \end{cases}$ with $i = 1, 2$

3. Fatigue crack growth

Here we use Paris law for stable crack propagation, the generalized Paris's law is given as:

$$\frac{da}{dN} = C \left(\Delta K_{Ieq} \right)^m \tag{5}$$

http://dx.doi.org/10.5772/intechopen.72778

Where, a is the crack length and N is the number of loading cycles. C and m are material properties to find the rate of crack growth. At each crack tip, the local direction of crack growth θ_c can be calculated by the maximum principal stress theory [37]. Crack is assumed to grow in a direction perpendicular to the maximum principal stress. Thus, by enforcing the condition that the local shear stress is zero for $\theta = \theta_c$,

$$K_I \sin\theta_c + K_{II}(3\cos\theta_c - 1) = 0 \tag{6}$$

The solution of Eq. (6) gives

$$\theta_c = 2\tan^{-1}\left(\frac{K_I - \sqrt{K_I^2 + 8K_{II}^2}}{4K_{II}}\right) \tag{7}$$

According to this criterion, the equivalent mode-I SIF is obtained as

$$K_{Ieq} = K_I \cos^3\left(\frac{\theta_c}{2}\right) - 3K_{II}\cos^2\left(\frac{\theta_c}{2}\right)\sin\left(\frac{\theta_c}{2}\right) \tag{8}$$

For stable crack propagation, the generalized Paris' law for FGM is given as

$$\frac{da}{dN} = C(\mathbf{x})\left(\Delta K_{Ieq}\right)^{m(\mathbf{x})} \tag{9}$$

where, $C(\mathbf{x})$ and $m(\mathbf{x})$ are the functions of the location.

In the numerical example, the crack growth value Δa is assumed and the corresponding number of cycles ΔN is computed from Eq. (9). When multiple crack tips are present, the crack growth value Δa is assumed for the most dominant crack tip, corresponding ΔN is computed and then at the other crack tips the crack growth is computed corresponding to ΔN. Eventually, when the maximum value of K_{Ieq} for any crack tip becomes more than the fracture toughness K_{IC} at corresponding location then the simulation is terminated. At this point, the total number of cycles elapsed is the fatigue life of the FGM.

4. Modeling of the properties of FGM

In this chapter, the results have been presented for a FGM plate as shown in **Figure 1**. The FGM plate is manufactured by reinforcing an alloy with ceramic. The volume fraction of ceramic is varied in the x-direction to get a material property variation in the x-direction. It is assumed that at $x = 0$ the FGM have the properties of the alloy and at $x = L$ properties of ceramic. The major crack is always taken at the center of the FGM plate in the x-direction. The interface, when present is also in the same direction. The material properties of the aluminum alloy and alumina used in FGM are tabulated in **Table 1** [38, 39].

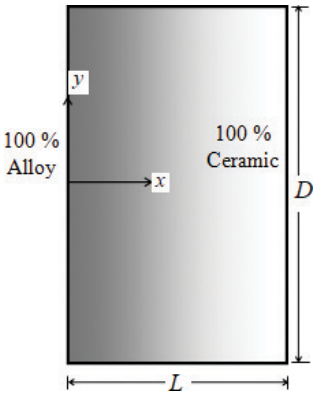

Figure 1. Geometry of the FGM plate along with its dimensions.

Material properties	**Aluminum alloy**	**Alumina**
Elastic modulus E(GPa)	70	300
Poisson's ratio, ν	0.33	0.21
Coefficient of thermal expansion γ ($/^{\circ}$C)	25×10^{-6}	8.2×10^{-6}
Fracture toughness K_{IC}(MPa$\sqrt{m}$)	29	3.5
Paris law parameter C in $m/cycle$(MPa$\sqrt{m}$)$^{-m}$	10^{-12}	2.8×10^{-10}
Paris law parameter, $m(\mathbf{x})$	3	10

Table 1. Material properties of aluminum alloy and alumina.

The variation of the elastic modulus for FGM is modeled as

$$E(x) = E_{alloy}e^{\alpha x} \text{ where } \alpha \text{ is given as } \alpha = \frac{1}{L}\ln\left(\frac{E_{ceramic}}{E_{alloy}}\right) \tag{10}$$

A plot of $E(\mathbf{x})$ for $L = 100$ mm is shown in **Figure 2**. The fatigue life of FGM has been compared with the same of the aluminum alloy and an equivalent composite of aluminum alloy/alumina. The equivalent composite considered in this example has the same overall volume fractions of aluminum alloy and ceramic as the FGM. The volume fractions of ceramic and aluminum alloy in the FGM are obtained as

$$V_{ceramic}^{FGM}(x) = \frac{E(x) - E_{alloy}}{E_{ceramic} - E_{alloy}} = \frac{E_{alloy}e^{\alpha x} - E_{alloy}}{E_{ceramic} - E_{alloy}} \tag{11a}$$

$$V_{alloy}^{FGM}(x) = 1 - V_{ceramic}^{FGM}(x) \tag{11b}$$

In this example, the equivalent composite is assumed to have the same amount of metal and ceramic. The volume fraction of alumina in the equivalent composite is calculated as

$$V_{ceramic}^{composite} = \frac{1}{L}\int_0^L V_{ceramic}^{FGM}(x)\,dx \tag{11c}$$

where, L is the length of the plate. For $L = 100$ mm, $V_{ceramic}^{composite} = 38.28\%$ and $V_{alloy}^{composite} = 61.72\%$. The variation in volume fraction of ceramic (alumina) in the FGM is shown in **Figure 3**. The volume fraction for the equivalent composite has also been indicated. Now, using the rule of mixtures for the equivalent composite

$$E_{composite} = E_{alloy}\,V_{alloy}^{composite} + E_{ceramic}V_{ceramic}^{composite} \tag{12}$$

we get $E_{composite} = 158.04$ GPa. The Poisson's ratio for the equivalent composite as well as for the FGM may be calculated as [40]

$$\nu(x) = \frac{\nu_{alloy}V_{alloy}^{FGM}(x)\,E_{ceramic} + \nu_{ceramic}V_{ceramic}^{FGM}(x)\,E_{alloy}}{V_{alloy}^{FGM}(x)\,E_{ceramic} + V_{ceramic}^{FGM}(x)\,E_{alloy}} \tag{13a}$$

$$\text{and } \nu_{composite} = \frac{\nu_{alloy}V_{alloy}^{composite}E_{ceramic} + \nu_{ceramic}V_{ceramic}^{composite}E_{alloy}}{V_{alloy}^{composite}E_{ceramic} + V_{ceramic}^{composite}E_{alloy}} \tag{13b}$$

The Poisson's ratio is shown in **Figure 4**.

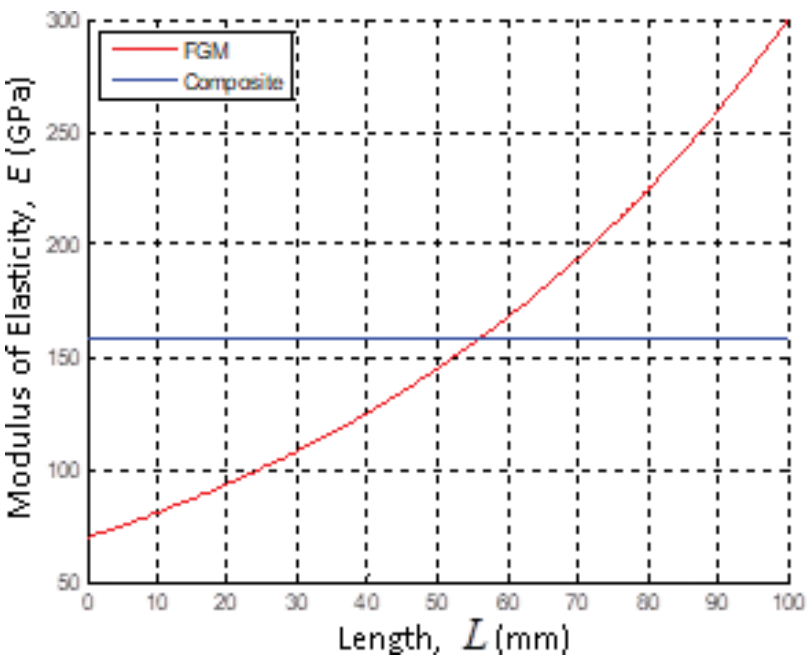

Figure 2. Variation of modulus of elasticity along the length of the plate.

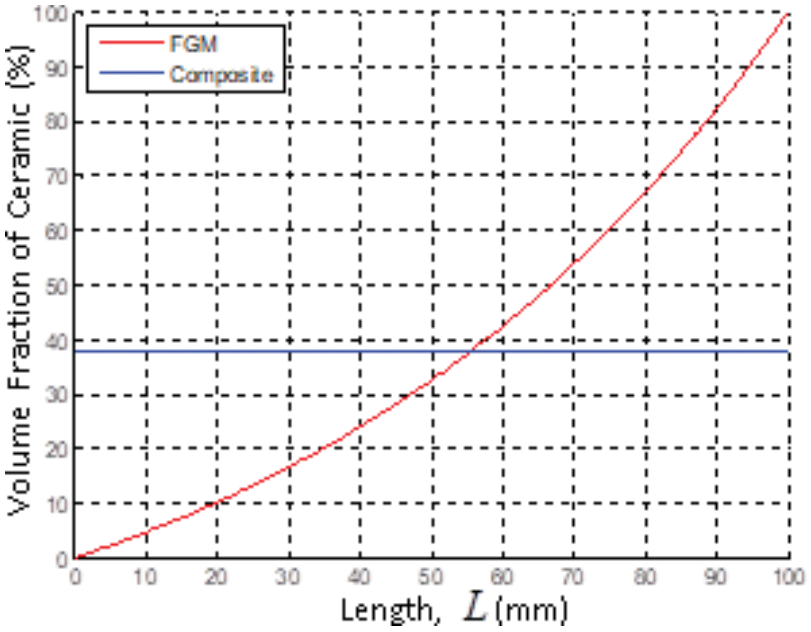

Figure 3. Variation of volume fraction of ceramic along the length of the plate.

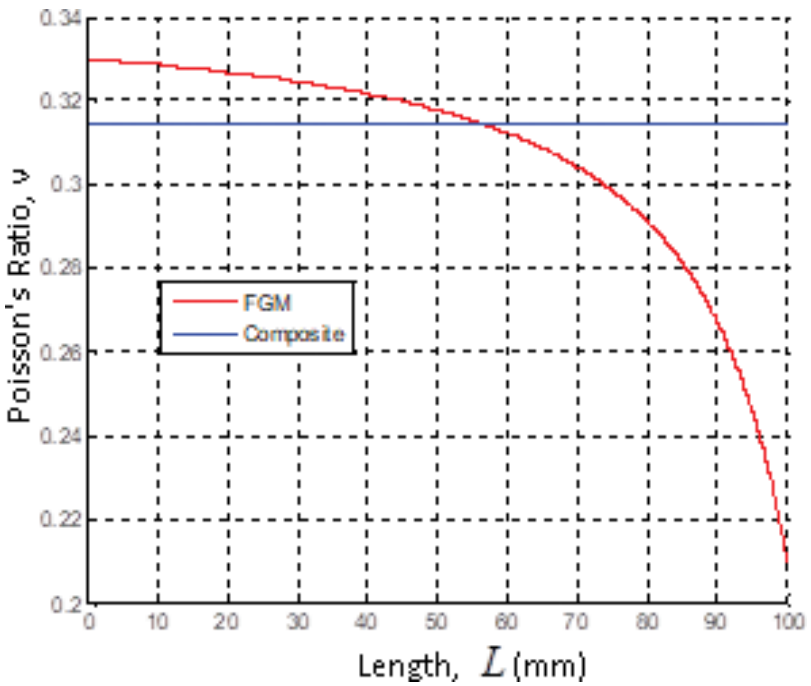

Figure 4. Variation of Poisson's ratio along the length of the plate.

http://dx.doi.org/10.5772/intechopen.72778

The coefficient of thermal expansion for the FGM by the rule of mixtures is calculated as

$$\gamma(x) \ = \gamma_{alloy} V_{alloy}^{FGM}(x) + \gamma_{ceramic} V_{ceramic}^{FGM}(x) \tag{14a}$$

The coefficient of thermal expansion for the equivalent composite is given by

$$\gamma_{composite} \ = \gamma_{alloy} V_{alloy}^{composite} + \gamma_{ceramic} V_{ceramic}^{composite} \tag{14b}$$

The value of the coefficient of thermal expansion for the equivalent composite is calculated using Eq. (14b) and is found to be $\gamma_{composite} = 18.57 \times 10^{-6}/^{\circ}\mathrm{C}$. A variation of coefficient of thermal expansion for the FGM is shown in **Figure 5**.

The fracture toughness of the FGM as well as the equivalent composite may be expressed as a function of the volume fraction of the ceramic by the following formula given by [41]

$$\begin{aligned} K_{IC}(x) = & \frac{K_{IC}^{alloy} + K_{IC}^{ceramic}}{2} \\ & + \frac{K_{IC}^{alloy} - K_{IC}^{ceramic}}{2} \left(\sqrt{1 - V_{ceramic}^{FGM}(x)} - \sqrt{V_{ceramic}^{FGM}(x)} \right) \end{aligned} \tag{15a}$$

$$\begin{aligned} K_{IC}^{composite} = & \frac{K_{IC}^{alloy} + K_{IC}^{ceramic}}{2} \\ & + \frac{K_{IC}^{alloy} - K_{IC}^{ceramic}}{2} \left(\sqrt{1 - V_{ceramic}^{composite}} - \sqrt{V_{ceramic}^{composite}} \right) \end{aligned} \tag{15b}$$

The variation of fracture toughness is shown in **Figure 6**.

The Paris law parameters are assumed to have exponential variation in a manner similar to the elastic modulus. Thus, the variation in the parameters of Paris equation is taken as

$$C(x) = C_{alloy} e^{\vartheta x}, \text{ where, } \vartheta = \frac{1}{L} \ln \left(\frac{C_{ceramic}}{C_{alloy}} \right) \tag{16}$$

$$m(x) = m_{alloy} e^{\varsigma x}, \text{ where, } \varsigma = \frac{1}{L} \ln \left(\frac{m_{ceramic}}{m_{alloy}} \right) \tag{17}$$

For the equivalent composite, we find the location at which the volume fraction of ceramic in the FGM is same as that of the equivalent composite. This location $\overline{x}$ may be found by either **Figure 5** or by using the formula $\overline{x} = \frac{1}{\alpha} \ln \left(\frac{E_{composite}}{E_{alloy}} \right)$, where α is defined in Eq. (10). For the present example $\overline{x} = 56$ mm. The Paris law parameters of the equivalent composite is assumed to be same as that of the FGM at $x = \overline{x}$. Thus,

$$C_{composite} = C_{alloy} e^{\vartheta \overline{x}} \tag{18a}$$

$$m_{composite} = m_{alloy} e^{\varsigma \overline{x}} \tag{18b}$$

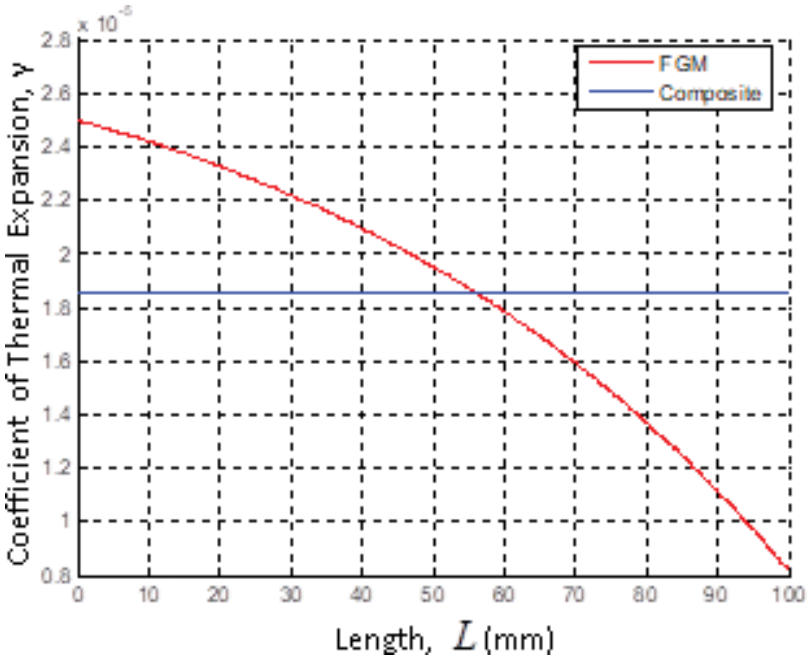

Figure 5. Variation of coefficient of thermal expansion along the length of the plate.

The values of C and m for the equivalent composite comes out to be $C_{composite} = 2.34 \times 10^{-11}$ m/cycle $(\text{MPa}\sqrt{\text{m}})^{-\text{m}}$ and $m_{composite} = 5.88$. The variation of C and m are shown in **Figures 7** and **8** respectively.

Plastic behaviour for FGM can be modeled using Ramberg Osgood equation [42]

$$\varepsilon = \frac{\sigma}{E} + \left(\frac{\sigma}{H}\right)^{1/n} \tag{19}$$

Here, H is the strength coefficient and n is the strain hardening exponent. The value of $n = 0.0946$ is used for the present example. The values of the parameters of Paris equation are taken as $C = 3 \times 10^{-11}$ and $m = 3$. In actual case the path of crack growth is curved but in this study the linear crack growth path is taken. Linear crack extension length Δa for an edge crack is kept constant. For a center crack maximum crack extension length Δa_{max} is kept on principal crack tip. The principle crack tip is the crack tip where ΔK_{Ieq} maximum. Crack increment at the other crack tip is given by:

$$\Delta a = \Delta a_{max} \left(\frac{\Delta K_{Ieq}}{\Delta K_{Ieq\ max}}\right)^{m} \tag{20}$$

The crack tip extension at the principal crack tip is Δa_{max} and at the other crack tip extension is smaller. The crack extension takes place $K_{Ieq\ max} < K_{IC}$. Crack becomes unstable when

http://dx.doi.org/10.5772/intechopen.72778

$K_{Ieq\ max} > K_{IC}$. Simulation continues until this condition is met. Here, $K_{Ieq\ max}$ is the equivalent SIF for mode-I at principal crack tip and K_{IC} is the material property called fracture toughness or critical SIF. K_{IC} for FGM is given by [35]

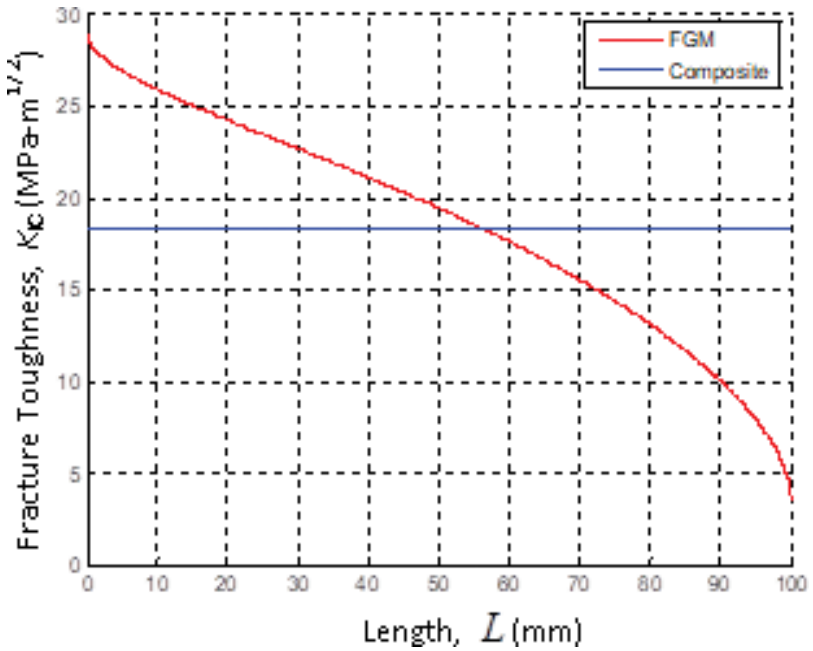

Figure 6. Variation of fracture toughness along the length of the plate.

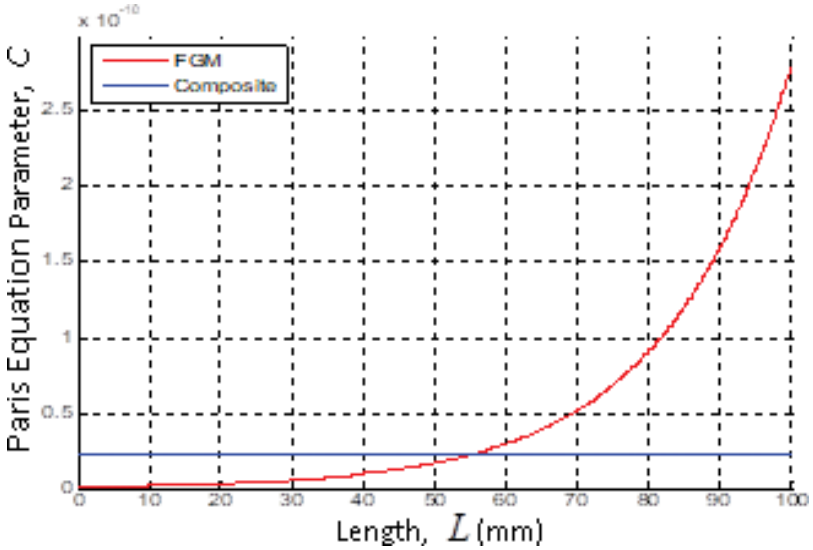

Figure 7. Variation of $C(\mathbf{x})$ along the length of the plate.

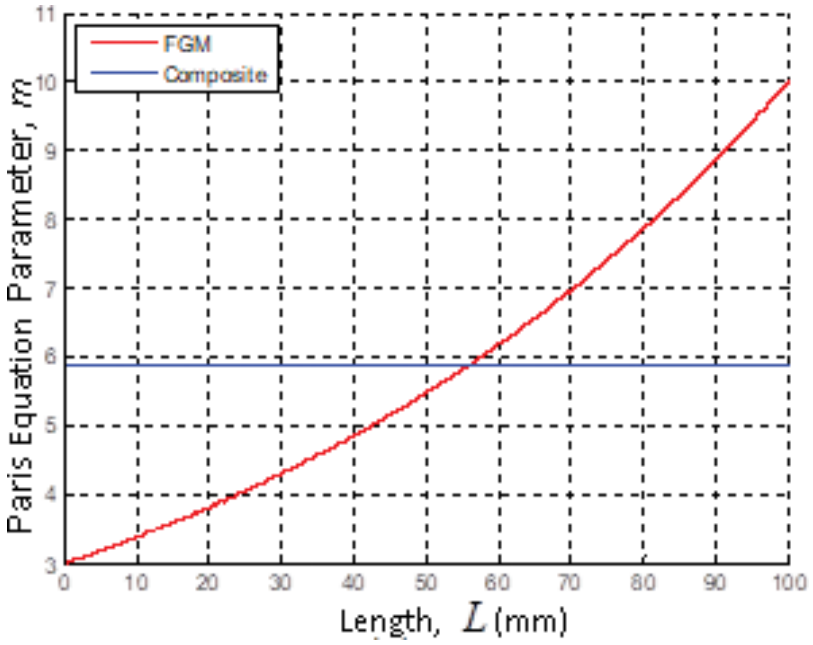

Figure 8. Variation of $m(\mathbf{x})$ along the length of the plate.

$$K_{IC}(x) = K_{IC}^{ceramic}\left[\frac{E(x)}{1-\nu_{FGM}^2}\left\{V_m(x)\frac{1-\nu_{alloy}^2}{E_{alloy}}\left(\frac{K_{IC}^{alloy}}{K_{IC}^{ceramic}}\right)^2 + (1-V_m(x))\frac{1-\nu_{ceramic}^2}{E_{ceramic}}\right\}\right]^{1/2} \tag{21}$$

where $K_{IC}(x)$ is the fracture toughness of the FGM at point x. K_{IC}^{alloy} and $K_{IC}^{ceramic}$ are the fracture toughness of the alloy and ceramic, while valloy and vceramic are Poisson's ratios for the alloy and ceramic respectively. $V_m(x)$ denotes the volume fraction for the alloy at point x.

The constitutive relation for the elastic-plastic material is given as

$$\sigma(u) = D_{ep}(\mathrm{x})\varepsilon(u) \tag{22}$$

where x is the vector of x and y-coordinates, $D_{ep}(\mathrm{x})$ is elastic-plastic constitutive matrix varying in x-direction. The elastic constitutive matrix can be written for plane stress condition as

$$D_e(\mathbf{x}) = \frac{E(\mathbf{x})}{\left\{1-\nu(\mathbf{x})^2\right\}}\begin{bmatrix} 1 & \nu(\mathbf{x}) & 0 \\ \nu(\mathbf{x}) & 1 & 0 \\ 0 & 0 & \dfrac{1-\nu(\mathbf{x})}{2} \end{bmatrix} = D \tag{23a}$$

and for plane strain condition as

http://dx.doi.org/10.5772/intechopen.72778

$$D_e(\mathbf{x}) = \frac{E(\mathbf{x})}{\{1-2\nu(\mathbf{x})\}\{1+\nu(\mathbf{x})\}} \begin{bmatrix} 1-\nu(\mathbf{x}) & \nu(\mathbf{x}) & 0 \\ \nu(\mathbf{x}) & 1-\nu(\mathbf{x}) & 0 \\ 0 & 0 & \dfrac{1-2\nu(\mathbf{x})}{2} \end{bmatrix} = D \tag{23b}$$

The incremental theory of plasticity [43] has been used to model the elastic-plastic constitutive relation for a material. An incremental stress vector $d\sigma$ and incremental strain vector $d\varepsilon$ are such that $d\sigma = D_{ep}.d\varepsilon$. Where D_{ep} is the elastic-plastic constitutive matrix, which is determined as discussed under:

Total strain increment is the sum of elastic and plastic strains

$$d\varepsilon = d\varepsilon_e + d\varepsilon_p \tag{24}$$

Elastic incremental strain and stress is determined

$$d\sigma = D_e d\varepsilon_e \tag{25}$$

$$F(\sigma) = f(\overline{\sigma}) \tag{26}$$

where σ is the stress tensor and $\overline{\sigma}$ is the equivalent stress, F and f are two different failure functions. By the flow rule the incremental strain is related to the gradient of a function known plastic potential. If the plastic potential function and the failure function is same, then the following relation is obtained,

$$d\varepsilon_p = \nabla F.d\,\lambda \tag{27}$$

Plastic modulus H is given as

$$H = \frac{d\overline{\sigma}}{d\overline{\varepsilon}_p} \tag{28}$$

For a given strain energy δw, and according to the definitionof $d\varepsilon_p$ we must have,

$$\delta w = \overline{\sigma}.d\overline{\varepsilon}_p \tag{29}$$

According to the Von Mises criteria, $F = J_2$, where J_2 is the second invariant of deviatoric stress tensor. So, we must have $F(\overline{\sigma}) = \frac{\overline{\sigma}^2}{3}$, Thus Eqs. (26) and (27) result in

$$d\sigma = D_e\{d\varepsilon - d\varepsilon_p\} \tag{30}$$

After taking the derivatives from both sides of failure criteria equation

$$\left(\frac{\partial F}{\partial \sigma} d\sigma\right) = \left(\frac{\partial f}{\partial \overline{\sigma}} \cdot \frac{\partial \overline{\sigma}}{\partial \overline{\varepsilon}_p} \cdot \frac{\partial \overline{\varepsilon}_p}{\partial w} \cdot \frac{\partial w}{\partial \overline{\varepsilon}_p} .\partial \varepsilon_p\right) \tag{31}$$

For simplicity we take $\frac{\partial F}{\partial \sigma} = a$, $\frac{\partial f}{\partial \overline{\sigma}} = \overline{a}$

$$a.d\sigma = \overline{a}.H.\left(\frac{1}{\sigma}\right)\sigma.d\varepsilon_p \tag{32}$$

$d\lambda$ is calculated by omitting $d\sigma$ between Eqs. (30) and (31) and substituting $d\varepsilon_p$ from Eq. (27). By substituting $d\lambda$ in Eq. (27), the final form of material matrix is obtained as [43]

$$D_{ep} = D_e - D_p \tag{33}$$

$$\text{where } D_p = \frac{Da\ a^T D}{\frac{\overline{a}}{\overline{\sigma}} H\sigma^T + a^T Da} \tag{34}$$

5. XFEM: Introduction and formulation for cracks and discontinuities in FGM

XFEM or the extended finite element method is a numerical technique which allows crack modeling irrespective of the mesh, and eliminates the cumbersome process of remeshing in problems involving change in the crack geometry like crack growth. XFEM models a crack by enriching the standard finite element approximation with some functions, which are obtained from the theoretical background of the problem. Moving discontinuities are tracked by the level set method. XFEM is a numerical method, based on the finite element method (FEM) that is especially designed for treating discontinuities. The formulation is done as discussed in [35, 44]. The solution of FGM differs from homogeneous materials only in the spatial gradation in the material properties. After calculating the values of stress and strain, the SIF is determined.

6. Numerical examples and discussion

The FGM plate considered in all the numerical simulations has 100% aluminum alloy on one side and 100% alumina on the other side. The volume fraction of alumina changes from 0% on one side to 100% on the other side so as to produce an FGM. The equivalent composite is equivalent to the FGM in the sense that both the FGM and the composite plate contain the same amount of aluminum alloy and alumina. The fatigue crack growth analysis of alloy/ceramic FGMs, aluminum alloy and equivalent composite is done by XFEM in the presence of multiple cracks, holes and inclusions under mode-I mechanical load and their fatigue life are compared. The constituents of the FGM plate are aluminum alloy and alumina. A major crack of large initial length is assumed to exist at the edge of the plate. The major crack is assumed to be in the direction of material gradation. The fatigue crack growth analyses of the FGM, the equivalent composite and the aluminum alloy plates have been carried out in the presence of minor cracks, holes and inclusions till the final failure of the plate under mode-I mechanical load. The effect of these small defects on the fatigue life as well as on the crack path has been investigated in detail.

http://dx.doi.org/10.5772/intechopen.72778

6.1. Example 1

A rectangular FGM plate of length (L) 100 mm. and height (D) 200 mm. with 100% aluminum alloy on left side and 100% ceramic (alumina) on right side is considered. Property variation is taken in x-direction, where x = 0 to x = 100 mm. The plate with a major edge crack of length a = 20 mm is analyzed under plane strain condition in the presence of multiple discontinuities. In all simulations, the plate dimensions, initial crack length and material properties are taken to be same. The properties of FGM, composites and aluminum alloy are already described in **Table 1**. The material properties of the inclusions are taken as $E = 20$ GPa and $\nu = 0.2$. The plate domain is discretized using uniformly distributed 117 nodes in x-direction and 235 nodes in y-direction. The fatigue crack growth analysis is performed by taking a crack increment of $\Delta a = \frac{a}{10} = 2$ mm. A cyclic tensile load varying from $\sigma_{\max} = 70$ MPa to $\sigma_{\min} = 0$ MPa is applied in all the simulations. The geometric discontinuities like holes, inclusions and minor cracks are added in the plate in addition to the major edge or center crack to analyze their effect on the fatigue life of the material. The fatigue life of the FGM, equivalent composite and aluminum alloy are obtained under mode-I loading, and are compared with each other.

6.2. Plate with a major edge crack under linear elastic condition

Figures 9 and **10** show a plate with a major edge crack of length a = 20 mm at the left and right edge respectively. These plates have been analyzed under plane strain condition using a uniform mesh of 117 by 235 nodes. The plots of the fatigue life for different materials are shown in **Figure 11**. From these figures, it is seen that the equivalent composite withstands 7885 cycles before it fails while the FGM with crack on alloy side undergoes 15,561 cycles and

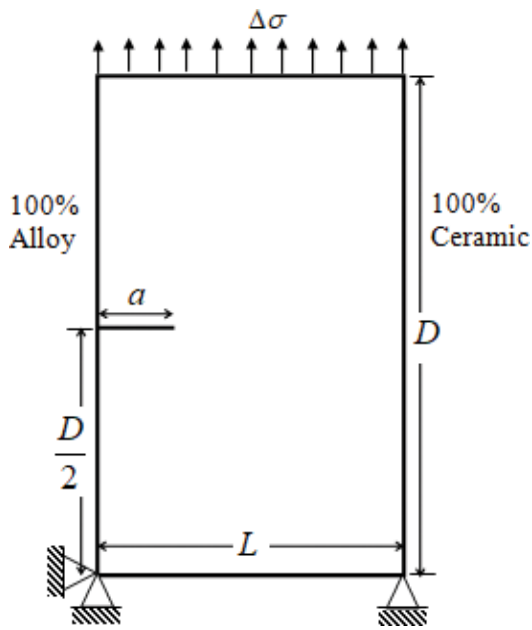

Figure 9. Plate with an edge crack on the alloy rich side under mode-I loading.

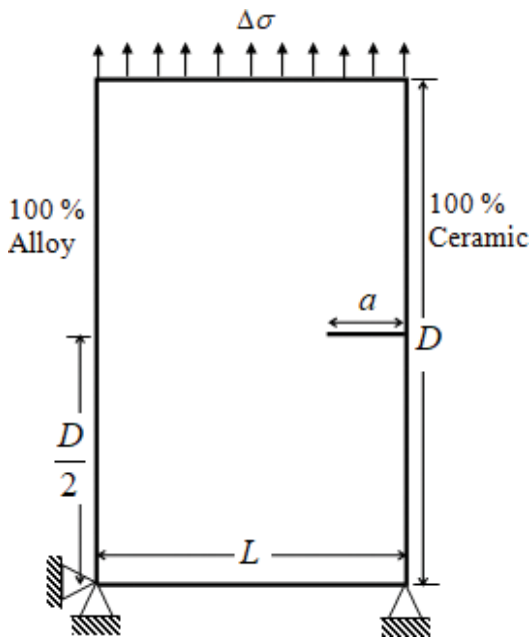

Figure 10. Plate with an edge crack on the ceramic rich side under mode-I loading.

pure aluminum alloy undergoes 19,145 cycles before failure. It is also observed that when a major crack initiates from the ceramic (alumina) rich side then it fails much earlier (4872 cycles) as compared to when the crack initiates from the aluminum alloy side.

These plots show that when a crack is present on the ceramic rich side, the life diminishes by a considerable extent as compared to when a crack is present on the alloy rich side. The equivalent composite shows the minimum life except in case when a crack is present on the ceramic side. It is also observed that the crack follows nearly a straight path in all the materials.

6.3. Plate with a major edge crack, minor cracks, holes and inclusions under linear elastic condition

In this case, a major crack of length a = 20 mm. is taken at the left and the right edge of the plate (100 × 200 mm) as shown in **Figures 12** and **13** respectively. In addition to the major edge crack, 36 minor cracks, 15 holes and 15 inclusions are randomly distributed in the plate. The length of the minor cracks varies from 3.5 to 4.5 mm, and orientation varies from 0 to 60° randomly. The holes and inclusions have variations in their radii from 3 to 4.5 mm randomly. A cyclic mode-I mechanical load is applied at the top edge of the plate. The plots for crack extension with number of cycles are shown in **Figure 14**.

It is also observed that the crack deflects in all the materials. Moreover, it is seen that the number of cycles to failure in case of aluminum alloy is about 18,111 cycles whereas in case of FGM with crack on the alloy and ceramic rich sides is 14,622 cycles and 3111 cycles respectively. The fatigue life of the composite plate is found to 6956 cycles. Thus, it can be stated that

http://dx.doi.org/10.5772/intechopen.72778

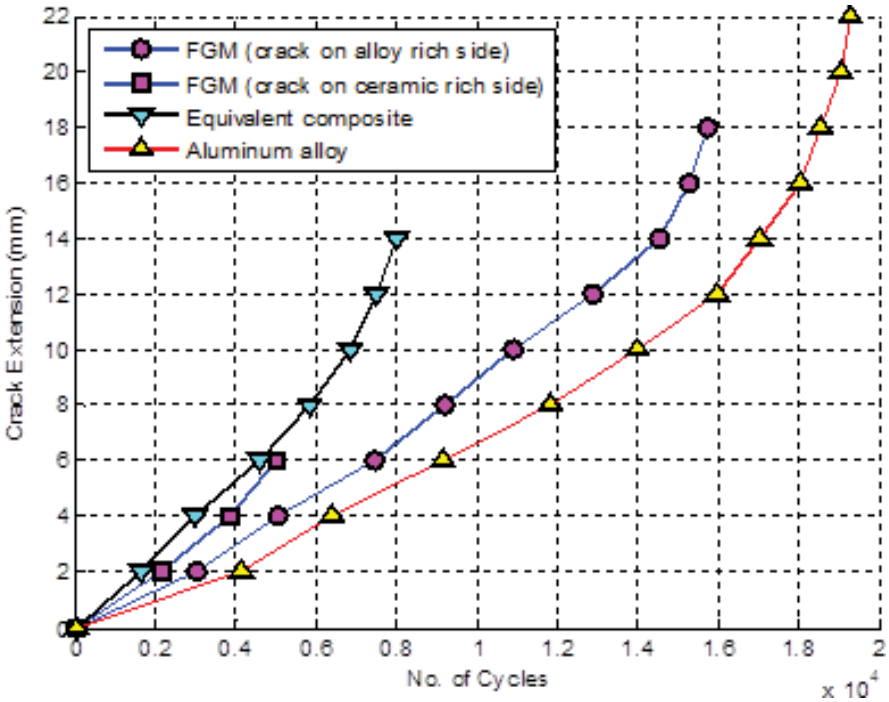

Figure 11. A plot of crack extension with number of cycles.

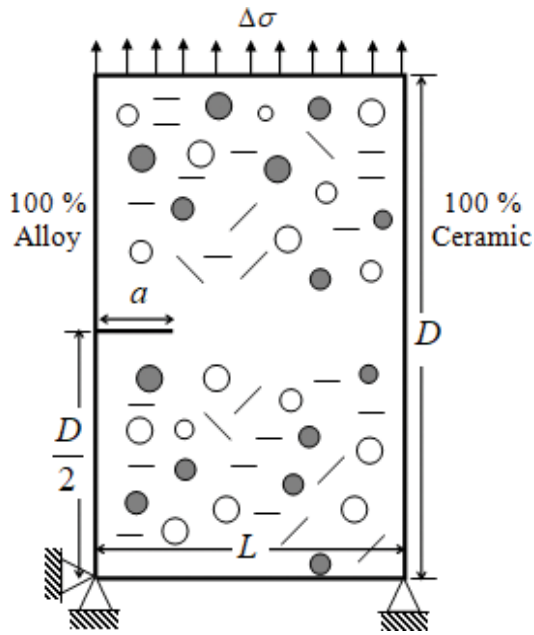

Figure 12. Plate with an edge crack on the alloy rich side under mode-I loading.

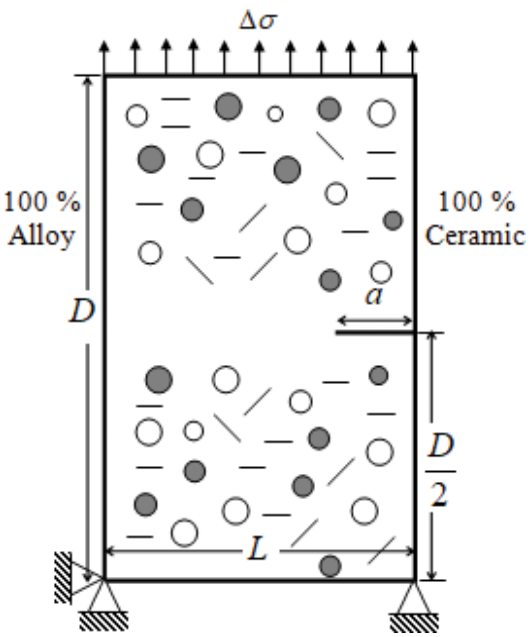

Figure 13. Plate with an edge crack on the ceramic rich side under mode-I loading.

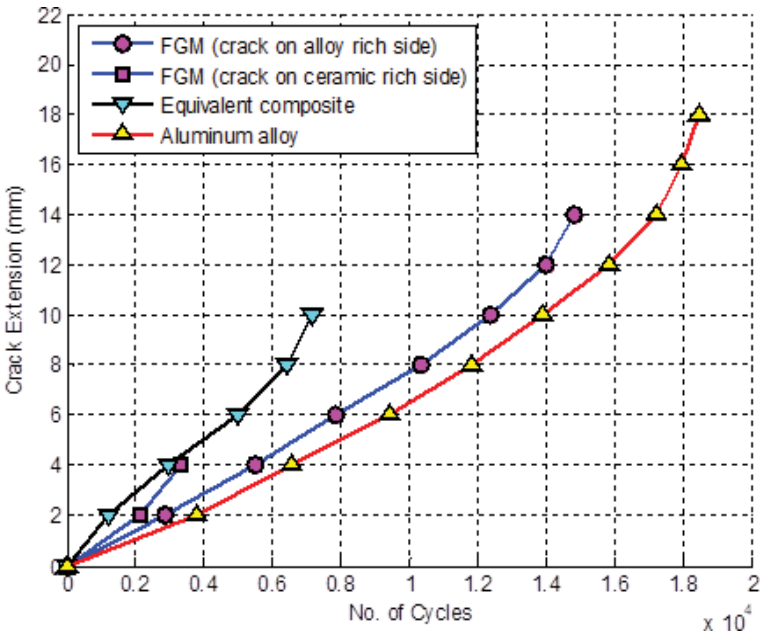

Figure 14. A plot of crack extension with number of cycles.

due to the presence of minor cracks, holes and inclusions, the life of the aluminum alloy is reduced by about 5.42%, whereas the fatigue life of the FGM with crack on the alloy and ceramic rich sides goes down by 6.03 and 36.15% respectively. The fatigue life of the equivalent composite is reduced by 11.78%.

6.4. Example 2

A rectangular FGM plate of length (*Lt*) 100 mm. and height (*Ht*) 200 mm. with 100% copper nickel alloy on left side and 100% ceramic (alumina) on right side is considered. Property variation is taken in x-direction, where x varies from x = 0 to x = 100 mm. A uniform traction of 100 MPa is applied on the top edge of the rectangular domain along y direction. Cyclic loading is applied at top edge of the plate with a maximum value of $\sigma_{max} = 100$ MPa and minimum value of $\sigma_{min} = 0$ MPa. A uniform mesh of size 117 × 235 nodes is used for the analysis in each case. The values of SIFs are computed at the tip of the major crack. The variation of SIF with crack length is plotted in each case. The material properties are taken from **Table 2** [43].

6.5. A major crack in FGM plate under elastic: Plastic loading condition

In this case, a major crack of length $a = 20$ mm is taken at the edge of the domain (100 × 200 mm) as shown in **Figure 15**. Cyclic loading is applied at the top edge of the FGM plate, and a crack propagates due to this loading. The plots of SIF with crack length for an crack configuration is shown in **Figure 16**. The failure crack length obtained for edge crack is 0.0402 m.

Material properties	**Values**
Elastic modulus of copper nickel alloy E_{alloy}(GPa)	160
Elastic modulus of alumina (ceramic) $E_{ceramic}$(GPa)	386
Elastic modulus of soft inclusion $E_{inclusion}$(GPa)	100
Elastic modulus of Hard inclusion $E_{inclusion}$(GPa)	400
Poisson's ratio of copper nickel alloy ν_{alloy}	0.35
Poisson's ratio of alumina (ceramic) $\nu_{ceramic}$	0.21
Poisson's ratio of inclusion $\nu_{inclusion}$	0.3
Poisson's ratio of inclusion ν_{FGM}	0.23
Fracture toughness of copper nickel alloy K_{IC}^{alloy}(MPa$\sqrt{m}$)	79
Fracture toughness of alumina (ceramic) $K_{IC}^{ceramic}$(MPa$\sqrt{m}$)	5
Paris constant C in $m/cycle$(MPa$\sqrt{m}$)$^{-m}$	3×10^{-11}
Paris exponent m	3

Table 2. Material property table.

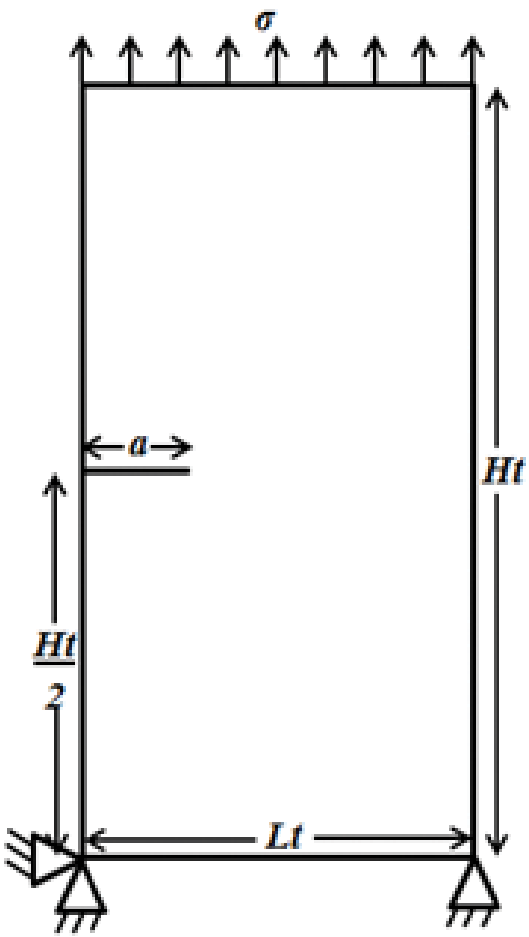

Figure 15. FGM plate with an edge crack.

6.6. A major edge crack in FGM plate with holes, inclusions and minor cracks under elastic-Plastic loading condition

In this case, a major crack of length $a = 20$ mm is taken at the edge of the domain (100 $\times$ 200 mm) is taken as shown in **Figure 17**. Minor cracks, holes and inclusions are randomly distributed in the plate. All 36 minor cracks have varying length randomly from 3.5 to 4.5 mm, with varying orientation from 0 to 60°. In addition to these 15 inclusions are also distributed in the domain randomly. The holes and inclusions have variation in their radii from 3 to 4.5 mm. A cyclic mode-I loading is applied due to which the major crack propagates. The plots for SIF variation with crack length of edge crack is shown in **Figures 18** and **19** for soft and hard inclusions respectively. The failure crack length for edge crack is obtained 0.0384 and 0.0392 m. for soft and hard inclusions respectively.

http://dx.doi.org/10.5772/intechopen.72778

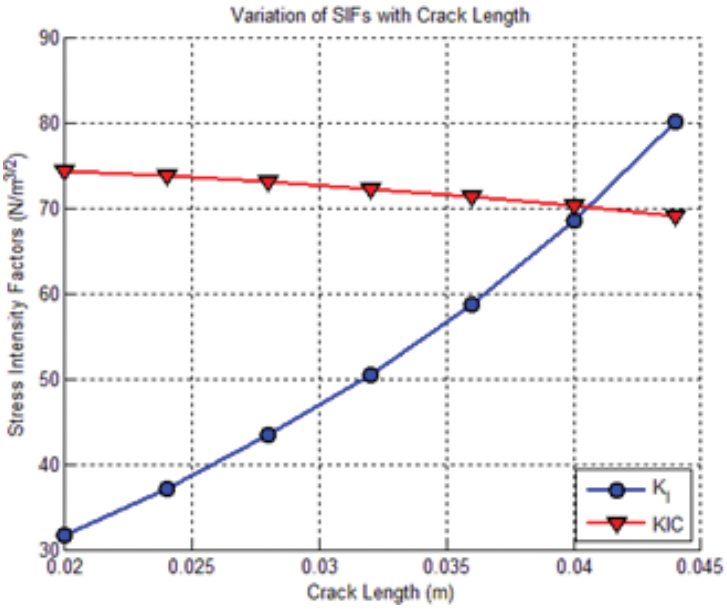

Figure 16. Plot for variation of SIF with crack length.

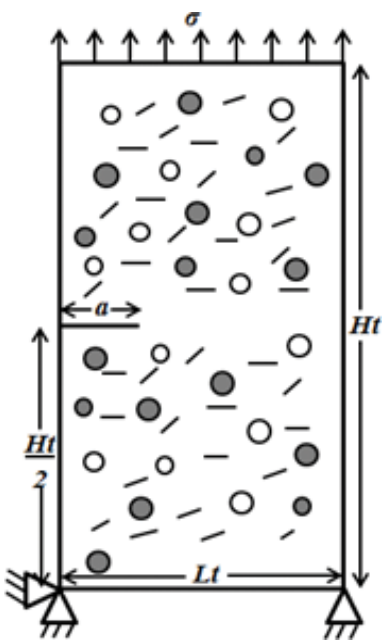

Figure 17. FGM plate with an edge crack, 15 inclusions, 15 holes and 36 minor cracks.

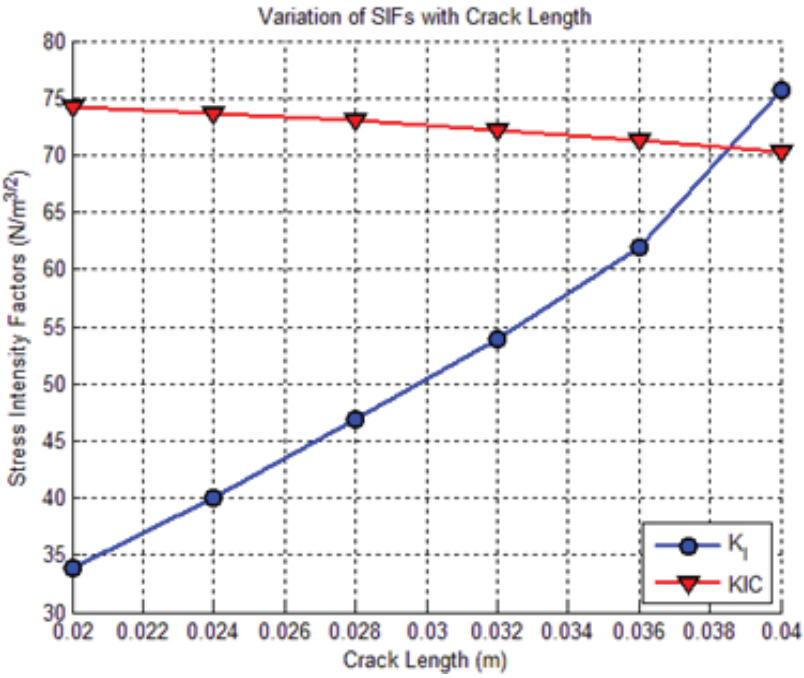

Figure 18. Plot for variation of SIF with crack length for soft inclusions.

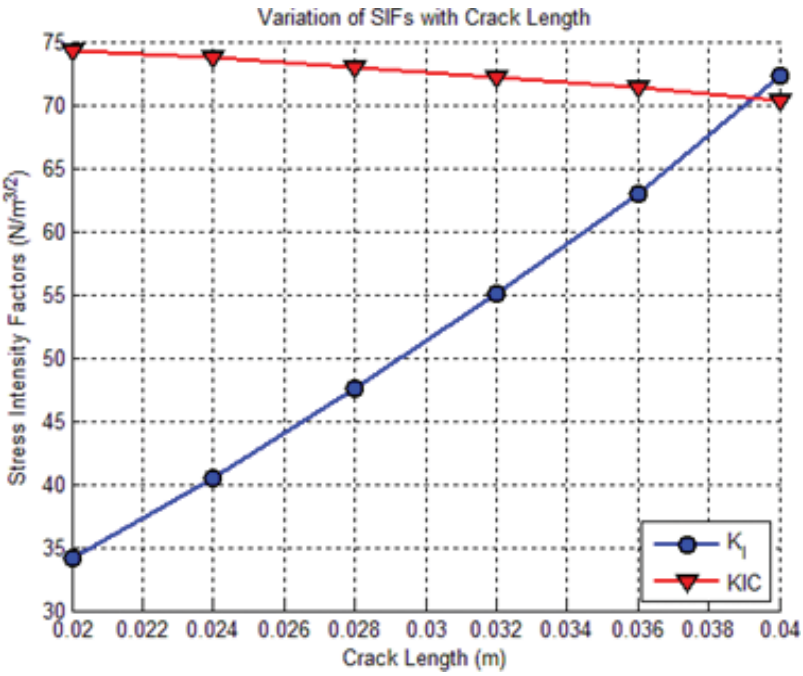

Figure 19. Plot for variation of SIF with crack length for hard inclusions.

7. Conclusions

In this chapter we have discussed the simulation of cracks in a FGM plate has been carried out in the presence of multiple inhomogeneities by XFEM using both linear elastic as well as elastic-plastic formulations. SIF has been calculated at the tip of the major crack using interaction integral approach. The variation in the SIF at the tip of the major crack has been studied when multiple inhomogeneities are present in the domain. From this study it is observed that minor cracks have least effect in the FGM plate's failure crack length, whereas soft inclusions have moderate effect and holes have the most severe effect. It is found that the FGM plate's life increases in each case when soft inclusions are replaced by hard inclusions. Hence the presence of the hard inclusions in the plate increases the failure crack length of the plate i.e. plate survives more.

Nomenclatures

$\tilde{W}$: Strain energy

σ: Stress

ε: Strain

u: Deformation

C: Compliance matrix

E: Modulus of elasticity

γ: Coefficient of thermal expansion

K_{IC}: Critical stress intensity factor (Fracture toughness)

Author details

Somnath Bhattacharya[1]*, Kamal Sharma[2] and Vaibhav Sonkar[1]

*Address all correspondence to: somnathb.iitr@gmail.com

1 Department of Mechanical Engineering, NIT, Raipur, India

2 BARC, Mumbai, India

References

[1] Agarwal BD, Kumar P, Khanna SK. Determination of the fracture toughness of fabric reinforced composites by the *J*-integral approach. Composites Science and Technology. 1986;**25**:311-323

[2] Chowdhury SR, Narasimhan R. A finite element analysis of quasi-static crack growth in a pressure sensitive constrained ductile layer. Engineering Fracture Mechanics. 2000;**66**:551-571

[3] Partheepan G, Sehgal DK, Pandey RK. Fracture toughness evaluation using miniature specimen test and neural network. Computational Materials Science. 2008;**44**:523-530

[4] Patil DP, Maiti SK. Detection of multiple cracks using frequency measurements. Engineering Fracture Mechanics. 2003;**70**:1553-1572

[5] Cheung Y, Wang Y, Woo C. A general method for multiple crack problems in a finite plate. Computational Mechanics. 1992;**10**:335-343

[6] Ang WT, Gumel AB. Multiple interacting planar cracks in an anisotropic multilayered medium under an antiplane shear stress: A hypersingular integral approach. Engineering Analysis with Boundary Elements. 1996;**18**:297-303

[7] Denda M, Dong YF. Complex variable approach to the BEM for multiple crack problems. Computer Methods in Applied Mechanics and Engineering. 1997;**141**:247-264

[8] Rice JR. A path independent integral and the approximate analysis of strain concentration by notches and cracks. Journal of Applied Mechanics. 1968;**35**:379-386

[9] Sills BL, Dolev O. The conservative M-integral for thermal-elastic problems. International Journal of Fracture. 2004;**125**:149-170

[10] Choubey A, Sehgal DK, Tandon N. Finite element analysis of vessels to study changes in natural frequencies due to cracks. International Journal of Pressure Vessels and Piping. 2006;**83**:181-187

[11] Khanna SK, Shukla A. Energy absorption mechanisms during dynamic fracturing of fibre-reinforced composites. Journal of Materials Science. 1993;**28**:3722-3730

[12] Zhang J, Yao Z, Tanaka M. The meshless regular hybrid boundary node method for 2-D linear elasticity. Engineering Analysis with Boundary Elements. 2003;**27**:259-268

[13] Zhang J, Yao Z. The regular hybrid boundary node method for three-dimensional linear elasticity. Engineering Analysis with Boundary Elements. 2004;**28**:525-534

[14] Singh IV, Sandeep K, Prakash R. Heat transfer analysis of two-dimensional fins using meshless element-free Galerkin method. Numerical Heat Transfer: Part A. 2003;**44**:73-84

[15] Singh IV, Sandeep K, Prakash R. Application of meshless element free Galerkin method in two-dimensional heat conduction problems. Computer Assisted Mechanics and Engineering Sciences. 2004;**11**:265-274

[16] Rao BN, Rahman S. An efficient meshless method for fracture analysis of cracks. Computational Mechanics. 2000;**26**:398-408

[17] Rao BN, Rahman S. An enriched meshless method for nonlinear fracture mechanics. International Journal for Numerical Methods in Engineering. 2004;**59**:197-223

[18] Bui QT, Nguyen NM, Zhang C. An efficient meshfree method for analysis of two-dimensional piezoelectric structures. Smart Materials and Structures. 2011;**20**:065016

[19] Belytschko T, Black T. Elastic crack growth in finite elements with minimal remeshing. International Journal for Numerical Methods in Engineering. 1999;**45**:601-620

[20] Belytschko T, Parimi C, Moes N, Sukumar N, Usui S. Structured extended finite element methods for solids defined by implicit surfaces. International Journal for Numerical Methods in Engineering. 2003;**56**:609-635

[21] Giudice SD, Comini G, Mikhailov MD. Finite element analysis of combined free and forced convection. International Journal of Heat Mass Transfer. 1978;**21**:1619-1621

[22] Reddy JN, Chao WC. Finite element analysis of laminated bi-modulus composite- material plates. Computers and Structures. 1980;**12**:245-251

[23] Kant T, Menon MP. A finite element-difference computational model for stress analysis of layered composite cylindrical shells. Finite Elements in Analysis and Design. 1993;**14**:55-71

[24] Sze KY, Wang HT. A simple finite element formulation for computing stress singularities at bi-material interfaces. Finite Elements in Analysis and Design. 2000;**35**:97-118

[25] Armentani E, Citarella R. DBEM and FEM analysis on non-linear multiple crack propagation in an aeronautic doubler-skin assembly. International Journal of Fatigue. 2006;**28**: 598-608

[26] Yoon JW, Cardoso RPR, Dick RE. Puncture fracture in an aluminum beverage can. International Journal of Impact Engineering. 2010;**37**:150-160

[27] Deodatis G. Stochastic FEM sensitivity analysis for non-linear dynamic problems. Probabilistic Engineering Mechanics. 1989;**4**:135-141

[28] Kant T, Arora CP, Varaiya JH. Finite element transient analysis of composite and sandwich plates based on a refined theory and a mode superposition method. Composite Structures. 1992;**22**:109-120

[29] Yoon JW, Song IS, Yang DY, Chung K, Barlat F. Finite element method for sheet forming based on an anisotropic strain-rate potential and the convected coordinate system. International Journal of Mechanical Science. 1995;**37**:733-752

[30] Yoon JW, Yang DY, Chung K. Elasto-plastic finite element method based on incremental deformation theory and continuum based shell elements for planar anisotropic sheet materials. Computer Methods in Applied Mechanics and Engineering. 1999;**174**:23-56

[31] Andreev K, Harmuth H. FEM simulation of the thermo-mechanical behaviour and failure of refractories-a case study. Journal of Materials Processing Technology. 2003;**143-144**:72-77

[32] Huang ZM. Failure analysis of laminated structures by FEM based on nonlinear constitutive relationship. Composite Structures. 2007;**77**:270-279

[33] Dias AMPG, Kuilen JWVD, Lopes S, Cruz H. A non-linear 3D FEM model to simulate timber–concrete joints. Advances in Engineering Software. 2007;**38**:522-530

[34] Coda HB. A solid-like FEM for geometrically non-linear 3D frames. Computer Methods in Applied Mechanics and Engineering. 2009;**198**:3712-3722

[35] Bhattacharya S, Singh IV, Mishra BK. Mixed-mode fatigue crack growth analysis of functionally graded materials by XFEM. International Journal of Fracture. 2013;**183**:81-97

[36] Yu H, Wu L, Guo L, He Q, Du S. Interaction integral method for the interfacial fracture problems of two non-homogeneous materials. Mechanics of Materials. 2010;**42**:435-450

[37] Sukumar N, Prevost J. Modeling quasi-static crack growth with the extended finite element method part I: Computer implementation. International Journal of Solids and Structures. 2003;**40**:7513-7537

[38] Arola D, Huang MP, Sultan MB. The failure of amalgam dental restorations due to cyclic fatigue crack growth. Journal of Materials Science: Materials in Medicine. 1999;**10**:319-327

[39] Roylance D. Fatigue, Department of Materials Science and Engineering, Cambridge: Massachusetts Institute of Technology. 2001;Vol. 02139

[40] Hsieh CL, Tuang WH. Poisson's ratio of two phase composites. Materials Science and Engineering A. 2005;**396**:202-205

[41] Raveendran KV, Vermam AP, Rao CVSK. Effective fracture toughness of composites. Interntionl Journal of Fracture. 1991;**47**:63-65

[42] Shedbale AS, Singh IV, Mishra BK. Nonlinear simulation of an embedded crack in the presence of holes and inclusions by XFEM. Procedia Engineering. 2013;**64**:642-651

[43] Bhattacharya S, Sharma K, Sonkar V. Numerical simulation of elastic plastic fatigue crack growth in functionally graded material using the extended finite element method. Mechanics of Advanced Materials and Structures. 2017 http://dx.doi.org/10.1080/15376494.2016.1227511

[44] Bhattacharya S, Singh IV, Mishra BK, Bui TQ. Fatigue crack growth simulations of interfacial cracks in bi-layered FGMs using XFEM. Computational Mechanics. 2013b;**52**:799-814

Chapter 10

Fretting: Review on the Numerical Simulation and Modeling of Wear, Fatigue and Fracture

Iñigo Llavori, Jon Ander Esnaola, Alaitz Zabala,
Miren Larrañaga and Xabier Gomez

Additional information is available at the end of the chapter

http://dx.doi.org/10.5772/intechopen.72675

Abstract

This chapter presents a general background and the state of the art of numerical simulation and modeling of fretting phenomenon in terms of wear, fatigue and fracture. First, an introduction of fretting and its implications is exposed. Second, different methodologies for wear modeling and simulation are described and discussed. Afterwards, fatigue and fracture analysis approaches are revised. To that end, multiaxial fatigue parameters are introduced putting an emphasis on the physical basis of the fretting phenomena and the suitability of each model. On the other hand, the propagation phase based on linear elastic fracture mechanics (LEFM) via the finite element method (FEM) and the eXtended finite element method (X-FEM) analysis methods is presented and compared. Finally, different approaches and latest developments for fretting fatigue lifetime prediction are presented and discussed.

Keywords: fretting, wear, fatigue, fracture, numerical simulation

1. Introduction

Fretting phenomena arises when two bodies are in contact subjected to relative movement of small amplitude (0–300 μm), producing damage on the contact surface [1]. Since virtually all machines vibrate, fretting failure can occur in a variety of mechanical components (even the ones that are not intended to move), such as aircraft engine blade housings, ropes, flexible couplings, bearing housings and even orthopedic devices.

It has been reported that up to 50 variables might influence the magnitude and rate of the fretting process [2]; however, Drobomirski [3] identified the slip amplitude, the contact pressure

and the coefficient of friction as the most influential ones. Different regimes can be determined depending on the slip amplitude, which is related to different failure types [4]:

- Stick regime: no slip occurs between the surfaces due to the accommodation of the displacement by elastic deformation. The damage in the surface is very low.
- Partial-slip regime: the central zone of the contact interface is motionless or stuck while the outer one is sliding. In this case, there is a minimum wear, and fatigue failure occurs due to crack incubation and growth (fretting fatigue).
- Gross-slip regime: the contact interface is in slip regime. The failure mainly occurs due to wear (fretting wear).

Depending on the magnitude of stresses, fretting can cause catastrophic failure of mechanical components. It is noteworthy mentioning that fretting fatigue may reduce the lifetime of a component by half or even more, in comparison to plain fatigue [5].

Despite the considerable progress made in the understanding of fretting fatigue over the last decades, it is still one of the modern issues for industrial machinery [6]. Accordingly, there is an increasing interest in the use of the finite element method (FEM) to analyze fretting phenomena, since it provides data which currently cannot be obtained through experimental testing or analytical solutions. This chapter presents a general background and the state of the art of numerical simulation and modeling of fretting in terms of wear, fatigue and fracture.

2. Methodologies for wear modeling and simulation

Many wear models have been developed throughout history aimed to describe and predict the phenomena. Those models are extensively reviewed in the literature [7–10] and can be broadly classified into two main categories, namely, (1) mechanistic models, based on material failure mechanism and (2) phenomenological models, based on contact mechanics.

The most popular and most used among them is the phenomenological Archard and Hirst model [11]:

$$V = kPs \tag{1}$$

where V represents the worn volume, k the wear coefficient (obtained experimentally), s the sliding distance and P the contact force. It is noteworthy that the wear coefficient depends on the contact force and sliding amplitude, requiring its determination for each test condition.

On the other hand, Fouvry et al. [12] proposed a new model based on the energy dissipated on the contact surface:

$$V = \alpha \sum_{i=1}^{N} E_{\mathrm{d},i} \tag{2}$$

where α is the energy wear coefficient and $E_{\mathrm{d},i}$ is the dissipated energy of the ith cycle.

Fouvry highlighted the benefits of the energy-based wear model over the classically applied Archard's approach. This new model requires a unique experimental campaign due to the independence of the energy wear coefficient to the contact force and sliding amplitude. Both models predict the same wear under gross slip condition, since the tangential force follows the equation: $Q = \mu P$ where μ is the coefficient of friction. However, results differ under partial sliding condition, where $Q < \mu P$. It is, therefore, concluded that Fouvry's model is superior due to the independency of contact force and sliding amplitude.

With the aim to solve wear modeling in more complex configurations and contact conditions, the FEM wear modeling has appeared as a good alternative in the last decade. Contact surface evolves progressively during wear phenomena, which generates an evolution in the stress state. This being so, the strategies for wear simulations consist of updating the geometry at discrete time increments, based on semi-empiric wear models.

McColl et al. [13] introduced a methodology for numerical wear simulation based on the local implementation of the previously mentioned Archard model (the so-called modified Archard's model):

$$\Delta h(x, t) = k_1 p(x, t) \Delta s(x, t) \tag{3}$$

where Δh is the incremental wear depth, k_1 is the local Archard coefficient, p is the local contact pressure and Δs is the relative slip distance increment.

As shown in **Figure 1**, the simulation consists of an iterative process where the local Archard's model is solved through contact pressures and sliding distributions obtained by the numerical simulation at discrete time increments. The wear value obtained at each increment is then used to update the worn geometry at the end of the cycle and the process is repeated till a predefined maximum sliding distance is reached.

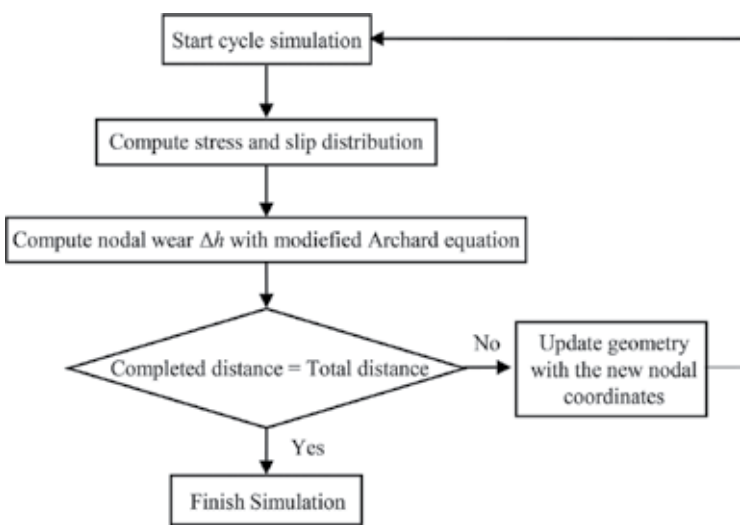

Figure 1. Simplified wear simulation flowchart of the McColl's approach.

Since contact problems are nonlinear, the computational demand is considerable, especially in three spatial dimensions where this problem is highly magnified. Among the strategies to optimize wear simulations, the use of the cycle jumping technique should be highlighted. This approach allows to speed up the wear simulation under the assumption that wear remains constant for a small number of cycles. Therefore, a cycle jumping factor N multiplying the incremental wear allows using one computational wear cycle to model the material removal of N actual cycles [13].

A further improvement on the computational time was presented by Madge et al. [14] who programed the spatial adjustment of the contact nodes through the user defined subroutine UMESHMOTION (available on the commercial FE code Abaqus FEA). This subroutine works in an adaptive meshing constrain framework in order to adapt the mesh to the evolving geometries.

Among the several benefits of using UMESHMOUTION subroutine, it should be highlighted that the updating is done incrementally through the fretting cycle, providing more stable results comparing to the updates done at the end of the cycle. Larger cycle jumps can therefore be used, decreasing significantly the computation time. However, the subroutine gives access to the pressure data of only one of the bodies, avoiding the possibility to compute wear on both parts. Cruzado et al. [15–17] overcame this limitation by transferring the available contact pressure data to the other part by interpolation techniques.

It should be highlighted that recent publications [18, 19] proposed the use of the energy wear approach instead of the Archard's local equation. Following the previously explained framework proposed by Madge, the energy equation is computed locally as:

$$\Delta h(x, t) = \alpha q(x, t) \Delta s(x, t) \tag{4}$$

As mentioned earlier, Fouvry's model shows the independency of contact force and sliding amplitude being more versatile than the commonly used Archard's equation.

3. Fatigue analysis approaches

Material fatigue refers to a progressive degradation of a material caused by loading and unloading cycles. The stress fluctuations suffered over time weakens or breaks the material even at stresses lower than the yielding value. Accordingly, a lot of effort has been directed at developing fatigue-life prediction models.

Fatigue is characterized with a high scatter of the lifetime. Probabilistic approaches are recently arising in the literature to address this problem [20, 21]. However, the majority of the models currently used analyze fatigue in a deterministic way, that is, a structure fails if a given parameter reaches a critical value.

Nowadays, a variety of different approaches for fatigue life prediction exist, such as approaches based on multiaxial fatigue criteria, damage mechanics or micromechanics, which are extensively reviewed in literature [22–33]. The present review focuses on the most widely used classical methodologies, that is, multiaxial fatigue criteria.

Multiaxial fatigue criteria reduce the multiaxial stresses (usually computed by FEM analysis) to an equivalent uniaxial stress state. This way, the results can be compared to an experimental fitting curve obtained from uniaxial fatigue data. A crucial step when selecting a multiaxial criterion is to check whether the simplification from multiaxial stress state to an equivalent uniaxial stress state is acceptable or valid. This task is not simple and requires the detailed study of the evolution of stresses and strains along the loading cycle.

The book published by Socie and Marquis [22] presents a wide and detailed study about the principal multiaxial parameters, also known as Fatigue Indicator Parameters (FIPs). Those parameters can be broadly classified into three groups: strain-based, stress-based and energy-based FIPs. Strain-based FIPs [34, 35] are generally related with Low-Cycle Fatigue (LCF) where plastic deformation may be predominant. Stress-based FIPs [36, 37] are associated with High-Cycle Fatigue (HCF), where the stresses usually remain in the elastic domain. Finally, energy-based models [38–40] relate the product of stresses and strains to quantify fatigue life, which generally are applicable to both LCF and HCF regime.

Additionally, fatigue can be categorized into proportional (fixed principal directions along a loading cycle) and nonproportional loading (rotation of the principal directions along a loading cycle). **Figure 2** shows the evolution of the stresses at the contact surface along fretting

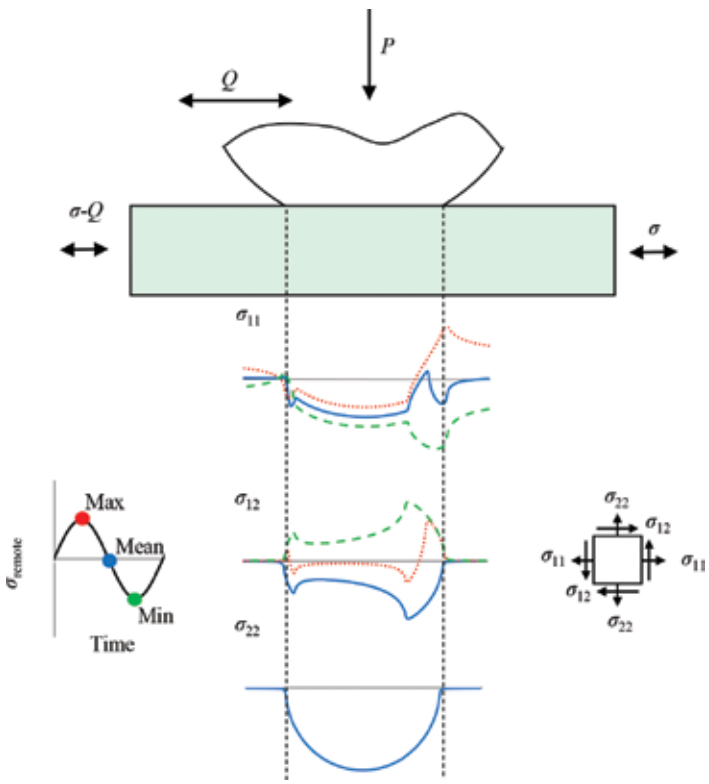

Figure 2. Nonproportional stresses in fretting fatigue during a loading cycle: distribution of the principal stress components (σ_{11}, σ_{12}, and σ_{22}) along the contact interface for different loading time steps (dotted red line, dashed green line, solid blue line).

fatigue cycle at three different stages of the loading cycle (maximum, mean and minimum). It can be observed that the normal stress σ_{11} and the shear stress σ_{12} fluctuate along the cycle while the stress σ_{22} remains unaltered. Consequently, principal directions rotate along the cycle generating nonproportional stresses under proportional remote loading. Therefore, the equivalent stress and strain approaches such as Von Mises criterion developed for proportional loading are not applicable in fretting since the problem is highly nonlinear and nonproportional.

For these complex stresses or loading states, other approaches such as the critical plane method are more suitable [41–43]. The critical plane method has been developed from the experimental observation of nucleation and crack growth under multiaxial loading. The critical plane models include the dominant parameters that govern the type of crack initiation and propagation. An adequate model must be one that estimates correctly both fatigue life and the dominant failure plane. However, several failure modes exist, and there is not a unique parameter that suits all.

A great deal of critical plane based FIPs have been used in the literature to assess fretting fatigue life [44–49]. Nonetheless, the most popular parameters are the energetic criteria known as Fatemi-Socie (*FS*) [39] and Smith-Watson-Topper (*SWT*) [40].

The *SWT* parameter is applied in those materials where the crack growth occurs in mode I. The critical plane is defined as the one where the product of maximum normal stress ($\sigma_{\mathrm{n,\,max}}$) and normal strain amplitude ($\varepsilon_{\mathrm{n,\,a}}$) is maximum.

$$SWT = \left(\sigma_{\mathrm{n,\,max}}\,\varepsilon_{\mathrm{n,\,a}}\right)_{\max} \tag{5}$$

Under shear loading condition, crack lip surfaces generate frictional forces that reduce stresses at the crack tip, thus increasing fatigue life. However, tensile stresses and strains will separate the crack surfaces, reducing the friction forces. The energetic FIP *FS* can be understood as the cyclic shear strain to include the crack closure effect multiplied by normal stress to take into account the opening of the crack.

$$FS = \frac{\Delta\gamma_{\max}}{2}\left(1 + k_{\mathrm{FS}}\frac{\sigma_{\mathrm{n,\,max}}}{\sigma_{\mathrm{y}}}\right) \tag{6}$$

where $\Delta\gamma_{\max}$ is the maximum range of shear strain on any plane, $\sigma_{\mathrm{n,\,max}}$ is the maximum normal stress in that particular plane, σ_{y} is the material yield stress, k_{FS} is a material dependent factor.

Vázquez et al. [50] recently compared both parameters for the analysis of the initial crack path in cylindrical fretting contact, concluding that the *SWT* parameter gives much better correlation than the *FS* parameter.

It should be mentioned that these parameters give a local life prediction and seek to find the hot spot to give the minimum life estimation. However, when high stress gradient events appear, for example, fretting case, an over-estimation of crack nucleation is predicted at the hot spot. Consequently, a nonlocal approach such as the Theory of Critical Distances (TCD) [51] used extensively in notched fatigue is recommended [52].

http://dx.doi.org/10.5772/intechopen.72675

4. Fracture modeling and simulation

Fracture mechanics is the field of mechanics concerned with the study of structures integrity in the presence of cracks. Within this field, there are several approaches, such as the linear elastic fracture mechanics (LEFM), the non linear fracture mechanics (NLFM) or the elasto-plastic fracture mechanics (EPFM) [53–55]. This chapter focuses on the most widely used one, the LEFM approach.

From a fully elastic point of view, Williams [56] presented an eigen function expansion method that provides a framework for the description of the stress state near a crack-tip. For each cracked configuration, a sequence of coefficients depending on the geometry and load describes the stress state with respect to the radius of circumference r and angle θ (see **Figure 3**).

Irwin identified the first physically valid term in this infinite series, the K field [57]:

$$\sigma(r,\theta) = \sum_i K_i \frac{1}{\sqrt{2\pi r}} f_i(\theta) \tag{7}$$

where K_I is the Stress Intensity Factor (SIF) for each of the fracture mode. The use of SIFs assumes that the singular stresses dominate the stress field near the crack front, thus neglecting higher order terms of the Williams series. It can be easily seen that the stress field shows a singularity when r tends toward zero.

As far as fatigue crack growth behavior is concerned, this is usually described by the relationship between the crack growth length increase per cycle (da/dN) as a function of the SIF range (ΔK). The typical log-log plot of crack growth behavior is shown schematically in **Figure 4**, which may be divided into three regimes:

- Regime I: the near threshold region—below the threshold value of SIF (ΔK_{th}) cracks will not propagate.

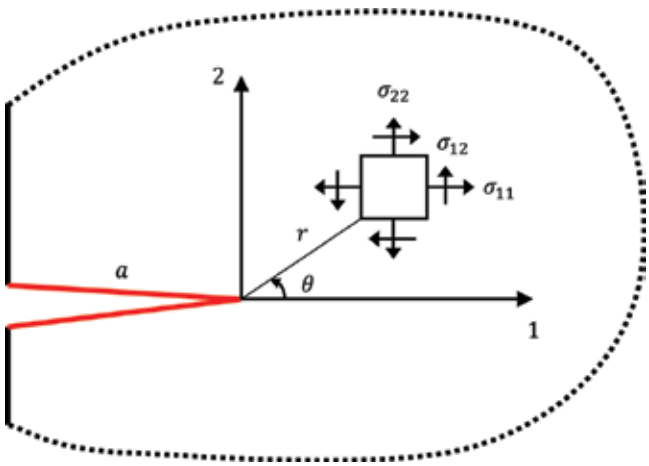

Figure 3. Singular stress field around the crack-tip.

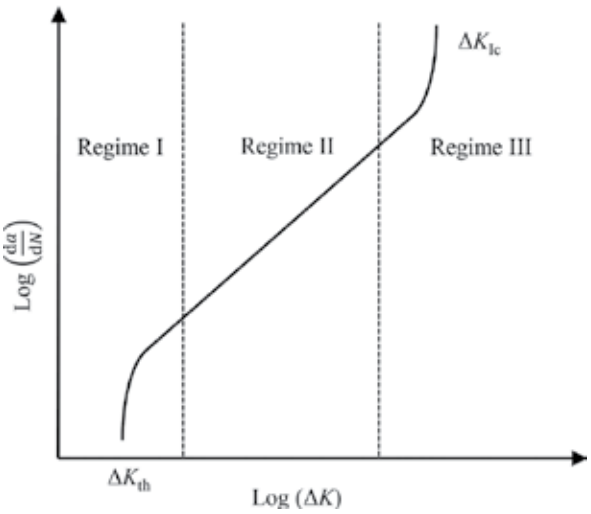

Figure 4. Schematic representation of a typical fatigue crack growth rate curve plotted in log-log scale.

- Regime II: stable crack growth region—the curve is essentially linear (log-log scale), widely known as the Paris regime.
- Regime III: rapid unstable crack growth leading to catastrophic fracture.

Regarding the simulation and modeling of crack growth behavior, the computation of the SIFs have been a priority in fracture mechanics, which has given rise to a great diversity of techniques (discussed in Section 4.1). In cases where the SIF range overcomes the threshold value ($\Delta K > \Delta K_{th}$), the velocity and direction of the crack growth should be computed.

Crack propagation rate is usually described by means of a phenomenological law of the type $da/dN = f(\Delta K)$. A comprehensive analysis of crack propagation velocity models in fretting fatigue was carried out by Navarro et al. [58] who analyzed nine of the fatigue crack growth models for an aluminum alloy Al7075. This study concluded that the Paris law [59] and the modified SIF model [60] were the most suitable ones for the experimental campaign carried out.

Concerning crack orientation criteria, they are generally based on the analysis of the stress and strain fields. The suitability of each criterion mainly depends on the evolution of the stresses and strains along a loading cycle. It should be noted that fretting fatigue usually induces friction between crack faces prone to slip motion during the loading cycle. The problem is therefore nonproportional, and the classical orientation criteria for proportional loading such as the maximum circumferential stress [61] or the minimum of the strain energy density factor S [62] among others are not applicable. Giner et al. [63] analyzed the suitability of the nonproportional loading criteria available in the literature for fretting fatigue problem, concluding that the prediction of the crack path observed in the complete contact experiments did not present a good agreement with the models available. Therefore, they developed the criterion of the minimum shear stress range, which is a generalization for nonproportional loading of the so-called criterion of local symmetry well established for proportional loading. The numerical results obtained by this new criterion were in good agreement with the experimental observation.

4.1. Stress intensity factor computation

Many of the initial analytical approaches initially developed for SIFs calculation [64–67] have been now outdated by the versatility offered by numerical methods. In this regard, one of the main methods is the interaction integral [68] through the equivalent domain integral [69] (nowadays implemented in commercial finite element codes such as Abaqus FEA). The interaction integral is an extension of the well-known J integral proposed by Rice [70], which is capable of extracting SIFs for each mode separately (K_{I}, K_{II} and K_{III}).

The computation of the interaction integral requires first to compute the stresses and strains by means of the FEM. However, the study of the singular problem through the FEM presents several drawbacks. On the one hand, in the classical formulation of the FEM the element edges need to conform to the crack boundaries, which require the use of cumbersome meshing techniques. On the other hand, the shape functions employed are generally of low-order polynomials, leading to the use of very refined mesh to compute reliable stresses and strains around the crack tip. Additionally, fatigue crack requires remeshing techniques to conform to the new crack boundaries.

Once Melenk and Babuška [71] showed that the finite elements could be enriched with additional functions to represent a given function, Möes et al. [72] proposed the eXtended finite element method (X-FEM) as a solution to overcome these issues.

In the X-FEM it is not necessary to have a mesh that conforms to the crack geometry, thus the finite element mesh is independent of the crack shape. To this end, the FEM model is enriched with additional degrees of freedom. On the one hand, the Heaviside function ($H(\mathbf{x}) = \pm 1$) is used to introduce discontinuity along the crack faces. On the other hand, the FEM model is additionally enriched with the asymptotic function derived by Irwin, and, therefore, can reproduce the singular behavior of LEFM by the following expression:

$$\{F^L(\mathbf{x})\} \equiv \sqrt{r}\left\{\sin\left(\frac{\theta}{2}\right), \cos\left(\frac{\theta}{2}\right), \sin\left(\frac{\theta}{2}\right)\sin(\theta), \cos\left(\frac{\theta}{2}\right)\sin(\theta)\right\} \tag{8}$$

where r, θ represents the polar coordinates defined with respect to the local reference system at the crack tip (see **Figure 3**).

Therefore, the classical FEM displacement definition is enriched to obtain the X-FEM approximation to the displacement field, defined as:

$$\mathbf{u}^{\text{X-FEM}}(\mathbf{x}) = \sum_{i \in I} \mathbf{u}_i N_i(\mathbf{x}) + \sum_{i \in L} \mathbf{a}_i N_i(\mathbf{x}) H(\mathbf{x}) + \sum_{i \in K} N_i(\mathbf{x}) \left(\sum_{l=1}^{4} \mathbf{b}_i^l F^l(\mathbf{x}) \right) \tag{9}$$

where I is the set of all nodes in the mesh, L and K are the sets of the enriched nodes, N_i is the shape function, $\mathbf{u}_i$ is the classical degree of freedom of the FEM and $\mathbf{a}_i$ and $\mathbf{b}_i^l$ are respectively the degrees of freedom of the enriched nodes.

Another important aspect of the X-FEM is the geometrical representation of the evolving cracks and the definition of the elements and nodes to be enriched. There are several methods to perform this task and can be divided into two groups: (1) implicit methods, such as the Level Set Method (LSM) [73] or the fast version called the Fast Marching Method (FMM) and (2) explicit methods, such as geometric predicates [74] or other approaches [72]. The suitability

of each of the method depends on whether the problem is two or three-dimensional. Although the benefits of the LSM or FMM are not overwhelming in 2D, the use of implicit methods becomes necessary in 3D since the explicit representation can be quite difficult to discretize [75, 76].

5. Fretting fatigue numerical simulation

Over the years, a significant number of different methodologies for fretting fatigue life prediction have been presented. First models were purely analytical, and numerical models appeared as computers evolved. Nowadays the preferred approaches can be classified into hybrid (combining analytical and numerical methods) or fully numerical methods.

Fretting fatigue life estimation has become an object of interest in the literature of the field. In general, the study of fretting is divided into two stages, the crack initiation (N_i) and its subsequent propagation (N_p). Therefore, the sum of the two stages gives a total life prediction:

$$N_f = N_i + N_p \tag{10}$$

In those situations in which the initiation phase dominates over propagation, some authors propose to estimate life considering only the initiation stage [77]. Conversely, for cases where crack growth stage dominates the components' life, the initiation phase is sometimes neglected [78]. Nonetheless, most current approaches combine both phases in order to provide a total life prediction, and this chapter is therefore centered on those combined models.

The number of cycles to initiate a crack is typically obtained with a FIP (the reader is referred to Section 3 for multiaxial criterion details). Crack propagation is subsequently considered using different fatigue crack growth laws, which require the definition of an initial crack length.

It is noteworthy that the development of a combined initiation-propagation model involves two critical steps: (1) the selection of the stress-deformation analysis location and (2) the definition of the initial crack length. On the one hand, due to the high stress gradient that characterizes fretting (see **Figure 5(a)**), the predicted crack nucleation cycles will increase as the location is further from the contact (see **Figure 5(b)**. On the other hand, longer cracks grow faster, leading to a lower number of propagation cycles (see **Figure 5(c)**).

Among the different methodologies presented for fretting fatigue lifetime prediction, the simplest approach is to perform the multiaxial analysis at the hot spot (i.e., at the surface), which results in a conservative crack initiation prediction [79]. Once the condition of crack initiation is reached, a predefined crack length is introduced in the numerical model [44, 79]. Alternatively, other authors perform the multiaxial analysis at a certain distance from the surface instead of at the hot spot, obtaining less conservative life estimations [14, 78, 80, 81]. However, the selected distance is usually arbitrary and there is no consensus in the literature.

A further improvement was introduced by Navarro et al. [82] who presented a nonarbitrary criteria. In this methodology, both the initiation and propagation phases are computed

http://dx.doi.org/10.5772/intechopen.72675

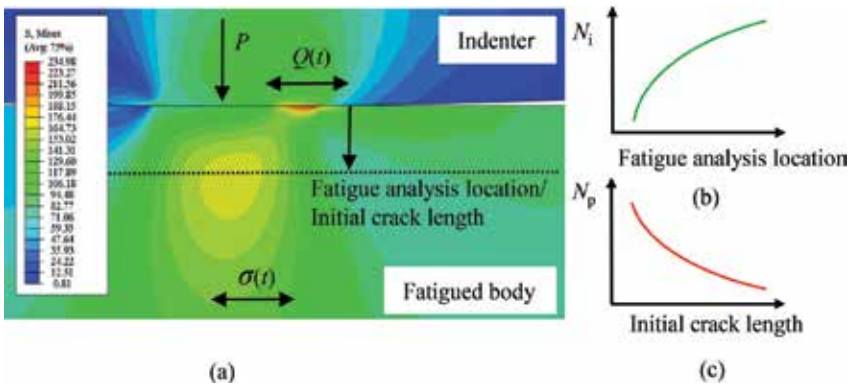

Figure 5. Dependency of fatigue analysis location and initial crack length in fretting fatigue lifetime. (a) Von Mises stress contour showing the high stress gradient present in fatigue phenomena. (b) and (c) Schematic representation of the influence of fatigue analysis location in the crack initiation cycle prediction (N_i) and the influence of initial crack length in the propagation cycle estimation (N_p), respectively.

separately for a set of points at different depths, considering the distance from the surface to the point under analysis as the initial crack length. Fretting fatigue life estimation is then calculated for each point ($N_i + N_p$) and the minimum of those predictions is considered the estimated life. This methodology combines the FEM for crack initiation analysis and analytical models for crack propagation phase. It has been shown that the use of the X-FEM for crack propagation analysis following the same framework gives a better correlation in fatigue life prediction [47].

More recently, the use of nonlocal methods such as the TCD (the reader is referred to Section 3) was suggested by some authors in order to define the location of the multiaxial analysis and to set the initial crack length [49, 83].

Despite fretting wear and fretting fatigue being frequently linked, most of the approaches, such as the ones mentioned earlier, neglect wear phenomena. A further improvement is therefore to consider the wear simulation in order to study the effect of wear on fatigue life.

In this regard, one of the most prominent work was presented by Madge et al. [84] In this work, the 2D numerical simulation of material removal process is performed first under the UMESHMOTION framework (the reader is referred to the Section 2). Then, the multiaxial fatigue analysis coupled with a damage accumulation framework is carried out in order to account for the effect of wear on fatigue lifetime. Finally, the propagation phase is analyzed via submodeling technique, which allows to transfer the stress state of the contact surface from global wear model to crack submodel. It should be noted that this approach does not account for the explicit interaction between the fretting contact and the crack. This study showed that the linkage of wear modeling with fatigue analysis is a key factor to successfully predict the increase in life in the gross sliding regime.

A further improvement of the previous approach was recently published by the present authors [85] by combining wear, fatigue and fracture phenomena in a single numerical model. **Figure 6** shows the flow chart of the coupled numerical analysis approach.

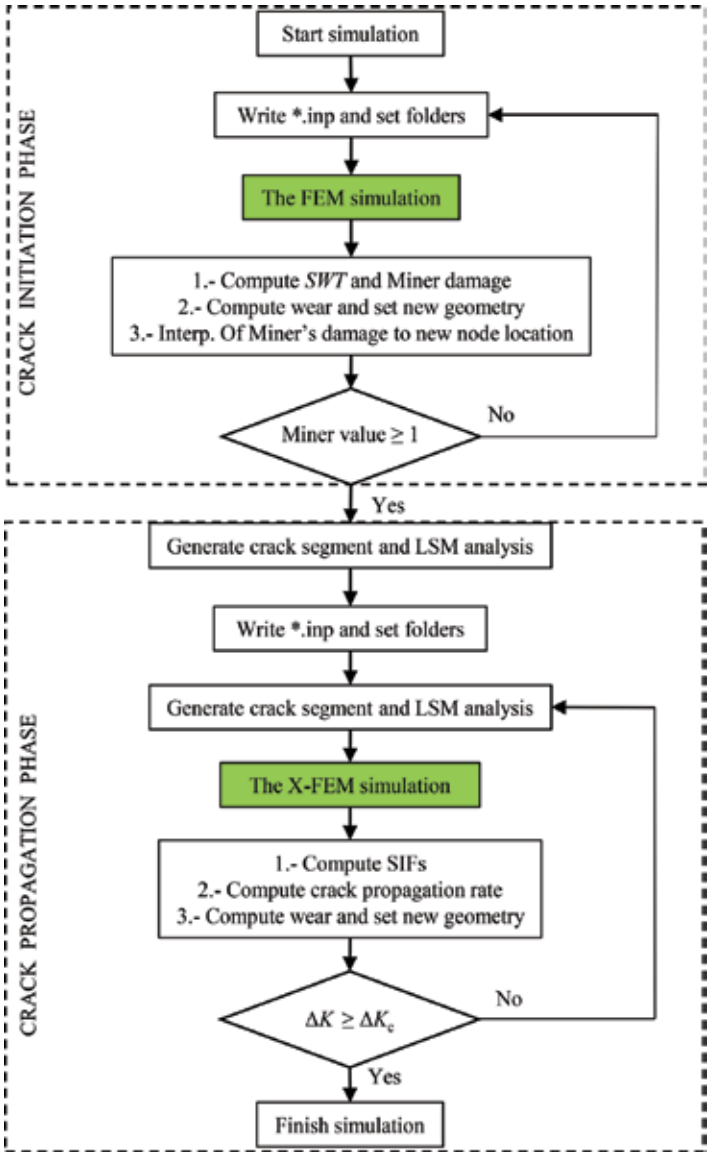

Figure 6. Flowchart showing computational sequence of the coupled wear, fatigue and fracture in fretting numerical analysis developed by [85].

The simulation algorithm is divided into two blocks corresponding to initiation and propagation stages, respectively. The first stage runs under the FEM framework, where the accumulated damage is computed during wear simulation iteratively. This process is repeated until the accumulated damage value reaches the value of 1 (Miner ≥ 1), that is, up to concluding the initiation phase. Afterwards, the propagation is computed through X-FEM code published by Giner et al. [76]. In this stage, the crack propagation is calculated during wear simulation iteratively up to reaching the failure criteria ($\Delta K \geq \Delta K_c$). The presented model allows the

study of the fretting phenomena as a whole, allowing to model explicitly the interaction between the fretting contact and the crack. It is expected that further analysis using this framework will allow a better understanding of the synergies between wear, fatigue and fracture phenomena.

6. Summary and concluding remarks

The complex nature of the physical phenomenon of fretting involves the mixture of different fields of engineering such as fatigue, fracture and tribology. This chapter has introduced the state of the art of the currently available modeling and simulation methods to analyze fretting phenomenon. The benefits and drawbacks of each reviewed technique have been highlighted. Finally, a numerical architecture of coupled wear, fatigue and fracture methodology has been introduced, which allows to analyze the fretting phenomenon as a whole.

Among the main open challenges identified, a predominant role is taken by the need to compare the increasing amount of methodologies to assess fretting lifetime, and it is likely to become the subject of considerable debate in the research community in the near future.

Author details

Iñigo Llavori[1,2]*, Jon Ander Esnaola[2], Alaitz Zabala[1], Miren Larrañaga[2] and Xabier Gomez[1]

*Address all correspondence to: illavori@mondragon.edu

1 Surface Technologies, Engineering Faculty, Mondragon Unibertsitatea, Arrasate-Mondragon, Spain

2 Structural Mechanics and Design, Engineering Faculty, Mondragon Unibertsitatea, Arrasate-Mondragon, Spain

References

[1] Waterhouse RB. Fretting wear. Wear. 1984;**100**:107-118

[2] Collins JA, Marco SM. The effect of stress direction during fretting on subsequent fatigue life. Proceedings of ASTM. 1964;**64**:547-560

[3] Dobromirski JM. Variables in the Fretting Process: Are There 50 of Them? Philadelphia, PA: ASTM; 1992

[4] Vingsbo O, Söderberg S. On fretting maps. Wear. 1988;**126**:131-147

[5] Hills DA, Nowell D. Mechanics of Fretting Fatigue. 1st ed. Springer Nederlands: Kluwer Academic Publisher; 1994

[6] Sato J. Rercent trend in studies of fretting wear. Transaction of JSLE. 1995;**30**:853-855

[7] Meng HC. Wear modelling: evaluation and categorization of wear models [thesis]. Ann Arbor: University of Michigan, USA; 1994

[8] Meng HC, Ludema KC. Wear models and predictive equations: Their form and content. Wear. 1995;**181-183**:443-457

[9] Hsu SM, Shen MC, Ruff AW. Wear prediction for metals. Tribology International. 1997;**30**(5):377-383. PII: S0301-679X(96)00067-9

[10] Blau PJ. Fifty years of research on the wear of metals. Tribology International. 1997;**30**(5): 321-331. PII: S0301-679X(96)00062-X

[11] Archard JF, Hirst W. The wear of metals under unlubricated conditions. Proceedings of the Royal Society. 1956;**A236**:387-400

[12] Fouvry S, Liskiewicz T, Kapsa P, Hannel S, Sauger E. An energy description of wear mechanisms and its applications to oscillating sliding contacts. Wear. 2003;**255**:287-298. DOI: 10.1016S0043-1648(03)00117-0

[13] McColl IR, Ding J, Leen SB. Finite element simulation and experimental validation of fretting wear. Wear. 2004;**256**:1114-1127. DOI: 10.1016/j.wear.2003.07.001

[14] Madge JJ, Leen SB, McColl IR, Shipway PH. Contact-evolution based prediction of fretting fatigue life: Effect of slip amplitude. Wear. 2007;**262**:1159-1170. DOI: 10.1016/j.wear.2006.11.004

[15] Cruzado A, Urchegui MA, Gómez X. Finite element modelling and experimental validation of fretting wear scars in thin steel wires. Wear. 2012;**289**:26-38

[16] Cruzado A, Leen SB, Urchegui MA, Gómez X. Finite element simulation of fretting wear and fatigue in thin steel wires. International Journal of Fatigue. 2013;**55**:7-21

[17] Cruzado A, Urchegui MA, Gómez X. Finite element modeling of fretting wear scars in the thin steel wires: Application in crossed cylinder arrangement. Wear. 2014;**318**:98-105

[18] Zhang T, Harrison NM, McDonnell PF, McHugh PE, Leen SB. A finite element methodology for wear-fatigue analysis for modular hip himplants. Tribology International. 2013;**65**:113-127

[19] Tongyan Y, Wahab MA. Finite element analysis of stress singularity in partial slip and gros sliding regimes in fretting wear. Wear. 2014;**321**:53-63

[20] Castillo E, Fernández Canteli A. A Unified Statistical Methodology for Modelling Fatigue Damage. Springer; 2009

[21] Muñiz Calvente M, Blasón S, de Jesús A, Correia J, Fernández Canteli A. A probabilistic approach for multiaxial fatigue criteria. In: Proceedings of the International Conference on Multiaxial Fatigue and Fracture (ICMFF11); June 2016; Sevilla

[22] Socie D, Marquis G. Multiaxial Fatigue. Warrendale, PA: SAE; 2000. ISBN: 978-0768004533

[23] Goh CH, Wallace JM, Neu RW, McDowell DL. Polycrystal plasticity simulations of fretting fatigue. International Journal of Fatigue. 2001;**23**:S423-S435. PII: S0142-1123(01)00150-5

[24] Goh CH, Neu RW, McDowell DL. Crystallographic plasticity in fretting of Ti-6AL-4V. International Journal of Plasticity. 2003;**19**:1627-1650. PII: S0749-6419(02)00039-6

[25] McDowell DL, Dunne FPE. Microstructure-sensitive computational modeling of fatigue crack formation. International Journal of Fatigue. 2010;**32**:1521-1542. DOI: 10.1016/j.ijfatigue.2010.01.003

[26] McCarthy OJ, McGarry JP, Leen SB. A finite element study of microstructure-sensitive plasticity and crack nucleation in fretting. Computational Materials Science. 2011;**50**:2439-2458. DOI: 10.1016/j.commatsci.2011.03.026

[27] McCarthy OJ, McGarry JP, Leen SB. Micro-mechanical modelling of fretting fatigue crack initiation and wear in Ti-6Al-4V. International Journal of Fatigue. 2014;**62**:180-193. DOI: 10.1016/j.ijfatigue.2013.04.019

[28] McCarthy OJ, McGarry JP, Leen SB. Microstructure-sensitive prediction and experimental validation of fretting fatigue. Wear. 2013;**305**:100-114. DOI: 10.1016/j.wear.2013.05.012

[29] McCarthy OJ, McGarry JP, Leen SB. The effect of grain orientation on fretting fatigue plasticity and life prediction. Tribology International. 2014;**76**:100-115. DOI: 10.1016/j.triboint.2013.09.023

[30] Ashton PJ, Harte AM, Leen SB. Statistical grain size effects in fretting crack initiation. Tribology International. 2017;**108**:75-86. DOI: 10.1016/j.triboint.2016.09.022

[31] Zhang T, McHugh PE, Leen SB. Finite element implementation of multiaxial continuum damage mechanics for plain and fretting fatigue. International Journal of Fatigue. 2012;**44**:260-272. DOI: 10.1016/j.ijfatigue.2012.04.011

[32] Hojjati-Talemi R, Wahab MA. Fretting fatigue crack initiation lifetime predictor tool: Using damage mechanics approach. Tribology International. 2013;**60**:176-186. DOI: 10.1016/j.triboint.2012.10.028

[33] Hojjati-Talemi R, Wahab MA, De Pauw J, De Baets P. Prediction of fretting fatigue crack initiation and propagation lifetime for cylindrical contact configuration. Tribology International. 2013;**76**:73-91. DOI: 10.1016/j.triboint.2014.02.017

[34] Yokobori T, Yamanouchi H, Yamamoto S. Low cycle fatigue of thin-walled hollow cylindrical specimens of mild steel in uni-axial and torsional tests at constant strain amplitude. International Journal of Fracture Mechanics. 1965;**1**(1):3-13. DOI: 10.1007/BF00184149

[35] Socie DF, Shield TW. Mean stress effects in biaxial fatigue of Inconel 718. ASME. 1984;**106**:227-232

[36] McDiarmid DL. A shear stress based critical-plane criterion of multiaxial fatigue failure for design and life prediction. Fatigue & Fracture of Engineering Materials & Structures. 1994;**17**(12):1475-1484

[37] Findley WN. A theory for the effect of mean stress on fatigue of metals and their combined torsion and axial load or bending. Journal of Engineering for Industry. 1959:301-306

[38] Brown MW, Miller KJ. A theory for fatigue failure under multiaxial stress-strain conditions. Proceedings of the Institution of Mechanical Engineers. 1973;**187**(1):65-73

[39] Fatemi A, Socie DF. A critical plane approach to multiaxial fatigue damage including out-of-phase loading. Fatigue & Fracture of Engineering Materials & Structures. 1988;**11**(3):149-165

[40] Smith RN, Watson P, Topper TH. A stress-strain parameter for the fatigue of metals. Journal of Materials. 1970;**5**(4):767-778

[41] You BR, Lee SB. A critical review on multiaxial fatigue assessments of metals. International Journal of Fatigue. 1996;**18**(4):235-244. PII: S0142-1123(96)00002-3

[42] Das J, Sivakumar SM. An evaluation of multiaxial fatigue life assessment methods of engineering components. International Journal of Pressure Vessels and Piping. 1999;**76**:741-746 PII: S0308-0161(99)00053-8

[43] Araújo JA, Nowell D. The effect of rapidly varying contact stress fields on fretting fatigue. International Journal of Fatigue. 2002;**24**:763-775. PII: S0142-1123(01)00191-8

[44] Szolwinski MP, Farris TN. Mechanics of fretting fatigue crack formation. Wear. 1996;**198**: 93-107. PII: S0043-1648(96)06937-2

[45] Nowell D, Dini Dm Hills DA. Recent developments in the understanding of fretting fatigue. Engineering Fracture Mechanics. 2006;**73**:207-222. DOI: 10.1016/j.engfracmech. 2005.01.013

[46] Navarro C, Muñoz S, Domínguez J. On the use of multiaxial fatigue criteria for fretting fatigue life assessment. International Journal of Fatigue. 2008;**30**:32-44. DOI: 10.1016/j. ijfatigue.2008.02.018

[47] Giner E, Navarro C, Sabsabi M, Tur M, Domínguez J, Fuenmayor FJ. Fretting fatigue life prediction using the extended finite element method. International Journal of Mechanical Sciences. 2011;**53**:217-225. DOI: 10.1016/j.ijmecsci.2011.01.002

[48] Gandiolle C, Garcin S, Fouvry S. A non-collinear fretting-fatigue experiment to compare multiaxial fatigue criteria: Critical shear plane strategy is better than invariant formulations. Tribology International. 2017;**108**:57-68. DOI: 10.1016/j.triboint.2016.09.011

[49] Araújo JA, Susmel L, Pires MST, Castro FC. A multiaxial stress-based critical distance methodology to estimate fretting fatigue life. Tribology International. 2017;**108**:2-6. DOI: 10.1016/j.triboint.2016.07.028

[50] Vázquez J, Navarro C, Domínguez J. Analysis of fretting fatigue initial crack path in Al7075-T651 using cylindrical contact. Tribology International. 2017;**108**:87-94. DOI: 10.1016/j.triboint.2016.09.023

[51] Taylor D. The Theory of Critical Distances. A New Perspective in Fracture Mechanics. 1st ed. Oxford: Elsevier; 2017. ISBN: 978-0-08-044478-9

[52] Susmel L. Multiaxial Notch Fatigue. From Nominal to Local Stress/Strain Quantities. 1st ed. Cambridge: Woodhead Publishing Limited; 2009. ISBN: 978-1-84569-582-8

[53] Anderson TL. Fracture Mechanics. Fundamentals and Applications. 3rd ed. Boca Raton: CRC Press; 2005. ISBN: 978-1-4200-5821-5

[54] Gdoutos EE. Fracture Mechanics. An Introduction. 2nd ed. Netherlands: Springer; 2005. ISBN: 1-4020-2863-6

[55] Saxena A. Nonlinear Fracture Mechanics for Engineers. 1st ed. Boca Raton: CRC Press; 1998. ISBN: 0-8493-9496-1

[56] Williams ML. On the stress distribution at the base of a stationary crack. Journal of Applied Mechanics. 1957;**24**(1):109-114

[57] Irwin GR. Analysis of stresses and strains near the end of a crack traversing a plate. Journal of Applied Mechanics. 1957;**24**(1):361-364

[58] Navarro C, Muñoz S, Domínguez J. Propagation in fretting fatigue from a surface defect. Tribology International. 2006;**39**:1149-1157. DOI: 10.1016/j.triboint.2006.02.004

[59] Paris PC, Erdogan F. A critical analysis of crack propagation laws. Journal of Basic Engineering. ASME. 1963;**85**(4):528-533

[60] Hatthori T, Nakamura M, Watanabe T. Simulation of fretting-fatigue life using stress-singularity parameters and fracture mechanics. Tribology International. 2003;**36**:87-97. PII: S0301-679X(02)00141-X

[61] Erdogan F, Sih GC. On the crack extension path in plates under loading and transverse shear. Journal of Basic Engineering. ASME. 1963;**85**:519-527

[62] Sih GC. Strain-energy-density factor applied to mixed mode crack problems. International Journal of Fracture. 1974;**10**(3):305-321

[63] Giner E, Sabsabi M, Ródenas JJ, Fuenmayor FJ. Direction of crack propagation in a complete contact fretting-fatigue problem. International Journal of Fatigue. 2014;**58**:172-180. DOI: 10.1016/j.ijfatigue.2013.03.001

[64] Murakami Y. Stress Intensity Factors Handbook. 1st ed. Oxford: Pergamon Press; 1987. ISBN: 0080348092

[65] Fett T. Stress Intensity Factors and Weight Functions for Special Crack Problems. 1st ed. Forschungszentrum Karlsruhe GmbH: Karlsruhe; 1997

[66] Laham SA. Stress Intensity Factor and Limit Load Handbook. 2nd ed. British Energy Generation: Barnwood; 1998

[67] Tada H, Paris PC, Irwin GR. The Stress Analysis of Cracks Handbook. 3rd ed. New York: ASME Press. 2000. ISBN: 0-7918-0153-5

[68] Yau JF, Wang SS, Corten HT. A mixed-mode crack analysis of isotropic solids using conservation laws of elasticity. Journal of Applied Mechanics. 1980;**47**:335-341

[69] Li FZ, Shih CF, Needleman A. A comparison of methods for calculating energy release rates. Engineering Fracture Mechanics. 1985;**21**(2):405-421

[70] Rice JR. A path independent integral and the approximate analysis of strain concentration by notches and cracks. Journal of Applied Mechanics. 1968;**35**(2):379-386

[71] Melenk JM, Babuska I. The partition of unity finite element method: Basic theory and applications. Computer Methods in Applied Mechanics and Engineering. 1996;**139**:289-314

[72] Moës N, Dolbow J, Belytschko T. A finite element method for crack growth without remeshing. International Journal for Numerical Methods in Engineering. 1999;**46**:131-150

[73] Osher S, Sethian JA. Fronts propagating with curvature-dependent speed: Algorithms based on Hamilton-Jacobi formulations. Journal of Computational Physics. 1988;**79**:12-49

[74] Huang R, Sukumar N, Prévost JH. Modeling quasi-static crack growth with the extended finite element method part II: Numerical applications. International Journal of Solids and Structures. 2003;**40**:7539-7552. DOI: 10.1016/j.ijsolstr.2003.08.001

[75] Osher S, Fedkiw R. Level Set Methods and Dynamic Implicit Surfaces. 1st ed. New York: Springer; 2000. 7-8 p. ISBN: 0-387-95482-1

[76] Giner E, Sukumar N, Tarancón JE, Fuenmayor FJ. An Abaqus implementation of the extended finite element method. Engineering Fracture Mechanics. 2009;**76**:347-368

[77] Giannakopoulos AE, Suresh S. A three-dimensional analysis of fretting fatigue. Acta Materialia. 1998;**46**(1):177-192. PII: S1359-6454(97)00210-3

[78] Giannakopoulos AE, Lindley TC, Suresh S. Application of Fracture Mechanics in Fretting Fatigue Life Assessment. 1st ed. Philadelphia: ASTM; 2000. 80-99 p. DOI: 10.1520/STP14723S

[79] Szolwinski MP, Farris TN. Observation, analysis and prediction of fretting fatigue in 2024-T351 aluminum alloy. Wear. 1998;**221**:24-36

[80] Sum WS, Williams EJ, Leen SB. Finite element, critical-plane, fatigue life prediction of simple and complex contact configurations. International Journal of Fatigue. 2005;**27**:403-416

[81] Houghton D, Wavish PM, Williams EJ, Leen SB. Multiaxial fretting fatigue testing and predicition for esplined couplings. International Jounal of Fatigue. 2009;**31**:1805-1815

[82] Navarro C, Vázquez J, Domínguez J. A general model to estimate life in notches and fretting fatigue. Engineering Fracture Mechanics. 2011;**78**:1590-1601. DOI: 10.1016/j.engfracmech.2011.01.011

[83] Gandiolle C, Fouvry S. Stability of critical distance approach to predict fretting fatigue cracking: A "l_{opt}-b_{opt}" concept. International Journal of Fatigue. 2016;**82**:199-210. DOI: 10.1016/j.ijfatigue.2015.07.016

[84] Madge JJ, Leen SB, Shipway PH. A combined wear and crack nucleation-propagation methodology for fretting fatigue prediction. International Journal of Fatigue. 2008;**30**:1509-1528. DOI: 10.1016/j.ijfatigue.2008.01.002

[85] Llavori I, Urchegui MA, Tato W, Gomez X. An all-in-one numerical methodology for fretting wear and fatigue life assessment. Frattura ed Integrità Strutturale (Fracture and Structural Integrity). 2016;**37**:87-93

Chapter 11

Determination of Fracture Toughness Characteristics of Small-Size Chevron-Notched Specimens

Yevgeny Deryugin

Additional information is available at the end of the chapter

http://dx.doi.org/10.5772/intechopen.72643

Abstract

A new method is proposed to determine fracture toughness of structural materials according to the test data of non-standard small-size chevron-notched specimens. During the tests, loading diagrams and photographic images of the specimens taken in time intervals are obtained. The crack length is measured in the process of its initiation and propagation. The analytical expressions are obtained being based and derived from the constitutive equations of engineering fracture mechanics to determine the crack-driving force (specific fracture energy) and the stress intensity factor. The method allows us to exclude the periodic unloading of the specimen applied under standard test conditions to determine the change in specimen compliance, which is taken into account in constitutive equations at crack length increase. All necessary calculation parameters are determined according to the experimental data. The method allows us to certify fracture toughness of the material without restrictions regarding the amount of plastic deformation and in front of the crack tip and in the specimen as a whole. The examples are given to calculate the fracture toughness criteria for a number of structural materials characterized by the ability to plastic deformation and by the Young's modulus value.

Keywords: fracture toughness, non-standard small-size chevron-notched specimens, analytical expressions, specific fracture energy, stress intensity factor, compliance

1. Introduction

Various methods for determining fracture toughness of materials are well-known and widely used when testing standard specimens with induced fatigue crack [1–3], when testing the Charpy notched specimens for fracture toughness [4], by the micro indentation method [5–7], et al.

An essential feature of these methods is that the characteristics of loading diagrams and the existing fracture length are measured, and then fracture toughness characteristics of the material are calculated by the semi-empirical formulas. As a rule, the critical stress intensity factor

(SIF) of the 1st kind K_{Ic} (for cleavage crack) is taken for the main fracture toughness characteristics of the material. The plane strain state condition of the loaded specimen is required in the experiments. In this regard, standard tests are conducted on specimens at least 10 mm thick.

Disadvantages of used methods are as follows:

1. There is no possibility to assess the fracture toughness of the material when testing the small thickness specimens;
2. Complexity of the mechanical processing and manufacturing of specimens;
3. Requirement for the fatigue pre-cracking on the notch;
4. Availability of special test equipment;
5. Use of significant amount of the complex-shaped specimens (cut out by layers, holes, notches);
6. Need for the high power load device;
7. High steel intensity of test specimens.
8. Need for periodic unloading of the specimen to determine the change in specimen compliance under loading.
9. Availability of phenomenological constants in constitutive equations, taking into account the geometric shape and boundary loading conditions.

As a rule, during a fracture toughness test of small-size specimens, the chevron-notched specimens are used [7–11]. The specimens with this configuration do not require the preliminary fatigue crack. When testing the small-size chevron-notched specimens, many of the above-mentioned problems are absent.

This chapter proposes a new method for fracture toughness determination of structural materials using the small-size chevron-notched specimens. The method allows us to determine fracture toughness characteristics without severe restrictions on the specimen ability to plastic deformation. There are no phenomenological dependencies and empirical constants in the calculations.

The fracture toughness characteristics comply with the conditions of continuous loading of specimens, without using the "loading-unloading" operation.

The important calculation works were carried out associated with the use of chevron-notched specimens during testing.

2. Fracture toughness calculation of straight-through notched specimens

To determine the global failure conditions, irrespective of the material state and geometrical dimensions of the specimen, the energy approach is appropriate [12]. The key point of the energy fracture criterion in fracture mechanics is formulated as follows: the crack growth can

occur if the system can release energy required to initiate crack propagation to the elementary distance *dl*. The energy needed for crack growth, appears only due to the elastic deformation energy that occurs in-side the material under the applied external force.

The reliable fracture toughness characteristic is the critical value of the elastic energy release rate (ERR) during the crack propagation G_c. In the two-dimensional version, this characteristic is equivalent to the value of the J-integral [13, 14]. For brevity, the value of *G* will be called specific fracture energy. The specific fracture energy (SFE) is defined as energy that is spent on the formation of the crack surface with area 1 m^2. The unit of measurement for SFE is J/m^2.

In practice, there is a decrease in specimen stiffness or structure at initiation and propagation of the crack. The specimen stiffness M is defined as the ratio of load *P*, applied to the specimen, to the displacement of load application point λ_e at elastic deformation of the specimen: $M = P/\lambda_e$.

The reciprocal of the stiffness is defined as a specimen compliance η: $\eta = \lambda_e/P$.

The necessary condition for through-crack propagation in the flat specimen of unit thickness obeys the equation [12–14]

$$G = \frac{P^2 d\eta}{2dl}, \tag{1}$$

where $d\eta/dl$ is the change in specimen ductility during crack propagation, *dl* is the short distance, to which a straight-line crack front propagates. At the stage of stable crack propagation, this value characterizes the fracture toughness G_c of the material. As follows from Eq. (1), elastic energy per unit of new crack surface at its propagation to *dl* in the specimen in thickness *a* is equal to

$$G = \frac{P^2 d\eta}{2adl} = \frac{P^2 d\eta}{dS}, \tag{2}$$

where $dS = 2adl$ is the elementary increment of the crack surface area.

There is a classic example for calculating the stress intensity factor K_I to test a double cantilever beam specimen with a straight-through notch [15]. The relation between *G* and K_I for the plane stress state obeys the equation

$$G = K_I^2(1 - \nu^2)/E. \tag{3}$$

Let us consider the case of double-cantilever beam specimens with a straight-through notch in detail, since the result will be used in the calculation of *G* for the chevron-notched specimens.

Figure 1 presents the double-cantilever beam specimens with a straight-through notch. Distance from the load application point *P* to the crack front is the initial crack length *l*. As follows from the cantilever bending theory, displacement of the load application point λ_e (**Figure 1**) is equal to $\lambda_e = \frac{4P}{Ea}\left(\frac{l}{b}\right)^3$, where *E* is the Young's modulus, *b* is the cantilever thickness. For the double cantilever beam specimen, displacement of load application points ζ is $2\lambda_e$. Therefore, the specimen ductility η is $\eta = \frac{\zeta}{P} = \frac{8}{Ea}\left(\frac{l}{b}\right)^3$.

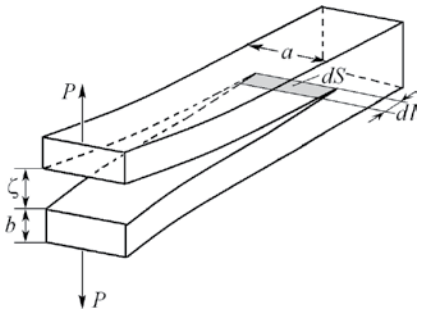

Figure 1. Straight-through-notched specimen.

The ductility derivative by the crack length is equal to

$$\frac{d\eta}{dl} = \frac{24l^2}{Eab^3}. \tag{4}$$

Substitution of Eq. (4) into Eq. (1) leads to the following expression for SFE [13, 15]

$$G = \frac{12P^2l^2}{Eb^3a^2}. \tag{5}$$

According to Ref. [14], the displacement λ_e of the cantilever end under elastic deformation for the specimen in thickness of a with a crack length l is provided by the load:

$$P = \frac{E\lambda_e a}{4}\left(\frac{b}{l}\right)^3. \tag{5a}$$

Substituting this expression into Eq. (4), we obtain the equation for G that allows us to calculate fracture energy by the crack length l and by the elastic opening value of the notch tips λ_e [16]:

$$G = \frac{3\lambda_e^2 b^3 E}{4l^4}. \tag{6}$$

In the given representation, the value of G does not depend on the specimen thickness a.

Eq. (5) determines SFE by the crack length l, and by the external load value P, at which spontaneous crack propagation begins. Basically, SFE can be calculated according to Eq. (6) when testing the small-size specimens. It should be noted that there are no any empirical constants in Eq. (6). All necessary values can be taken from the experiment. To maintain the experimental integrity, one can grow a fatigue crack at the tip of the notch. However, this method has several disadvantages.

Eq. (5) gives only a rough approximation of the SFE value. There is a certain divergence due to the fact that the cantilevers' ends are fixed not absolutely rigidly, as in the cantilever embedded in the rigid base. But this is not the most important thing. The main disadvantage is that in practice crack propagation along the notch plane is not guaranteed. Consequently, deviations in crack propagation direction cause shear deformations. Besides, crack front straightness is not preserved. To some extent, this problem is solved by using the chevron-notched specimens.

3. Fracture toughness calculation of the chevron-notched specimens

When testing the small-size specimens, generally, the chevron-notched specimens are used [7, 17]. For the first time, a chevron-notched specimen was proposed by L.M. Barker in 1977 to determine fracture toughness under plane strain conditions [17].

Standard tests of the chevron-notched specimen are conducted according to the scheme presented in **Figure 2**.

Figure 3 shows examples of the chevron-notched specimens. The specimens of this configuration do not require the preliminary guidance of a fatigue crack to the tip of the notch. From the moment of loading, there is a high stress concentration at the tip of the chevron notch that is sufficient to crack initiation. It is assumed that the development of plastic deformation in the chevron zone satisfies the plane strain state condition. The crack initiated at the tip of the chevron, can propagate only along the notch plane. At the same time, there is a high probability that the crack front during propagation, at the average, maintains a straight shape. The chevron notch geometry allows us to fix and extend the stable crack propagation stage and, thus, to calculate the beginning of the specimen catastrophic failure more accurately.

As a rule, short circular specimens are used in the experiments (**Figure 3*a***). The disadvantage of the standard method for measuring fracture toughness of the chevron-notched specimens is that in order to determine the change in specimen ductility, the "loading-unloading" condition

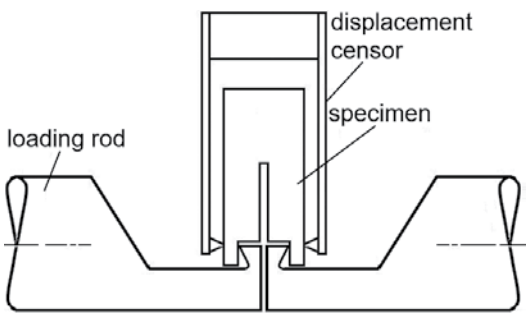

Figure 2. Loading configuration of the chevron-notched specimen.

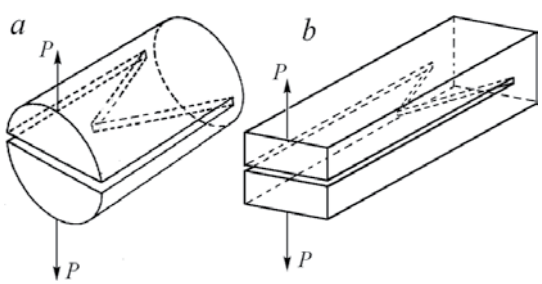

Figure 3. The chevron-notched specimens: short circular specimen (*a*) and elongated rectangular specimen (*b*).

should be carried out. For this reason, the calculation formulas include adjustable coefficients considering the non-linear behavior of the material and a complex geometric shape of the notch.

This section provides a new method for calculating the fracture toughness characteristics of materials when testing the chevron-notched specimens. The novelty is in the fact that the calculation of SFE is based on calculation of the energy and power parameters of the specimen taking into account the complex geometry of a chevron notch according to the strict laws of solid mechanics. It is convenient to make calculations and experiments for the elongated rectangular specimen (**Figure 3*b***). In this case, the chevron-notched specimen has a shape of a double cantilever beam configuration.

Let us determine the relation of the external force P with an elastic deflection λ_e of the single cantilever of the specimen. The cantilever can be represented as a set of elementary cantilevers (minicantilevers) of the infinitely small width dx. **Figure 4** shows the projections of the chevron-notched specimens. The minicantilever length at a distance x from the symmetry axis of the specimen is $l(x) = l_0 + x \cdot \mathrm{ctg}(\alpha/2)$, where l_0 is the minimum distance from the load application point to the chevron notch, α is the chevron angle (**Figure 4**). For each minicantilever in the set, the well-known elasticity theory formula is valid [14]:

$$\lambda_e = \frac{4dP(x)}{Edx}\left(\frac{l(x)}{b}\right)^3, \tag{7}$$

where λ_e is the elastic deflection of the minicantilever, dP is the elementary load, under the action of which the cantilever in thickness of dx is deflected to the value of λ_e, b is the thickness of the minicantilever. In view of this, from Eq. (6) we obtain the elementary load dependence dP, applied to the end of the minicantilever on its width dx:

$$dP(x) = \frac{\lambda_e E}{4}\left(\frac{b}{l(x)}\right)^3 dx. \tag{8}$$

Integration of elementary forces (7), affecting each minicantilever across the specimen width a, will clearly determine the actual load P, providing the minicantilever's deflection by λ_e:

$$P = \frac{\lambda_e b^3 E}{4}\int_{-\frac{a}{2}}^{\frac{a}{2}} dx/\left(l_0 + x\cdot\ \mathrm{ctg}\,\frac{\alpha}{2}\right)^3, \text{ or } P = \frac{E\lambda_e a}{4}\left(\frac{b}{l_0}\right)^3\left[4 + \frac{a}{l_0}\,\mathrm{ctg}\,\frac{\alpha}{2}\right]\Big/\left[2 + \frac{a}{l_0}\,\mathrm{ctg}\,\frac{\alpha}{2}\right]^2 = \frac{E\lambda_e a}{4}\left(\frac{b}{l_0}\right)^3 k' \tag{9}$$

This equation differs from Eq. (5) from the straight-through notch only by the factor

$$k' = l_0[4l_0 + a\,\mathrm{ctg}\,(\alpha/2)][2l_0 + a\mathrm{ctg}\alpha/2]^{-2}. \tag{10}$$

According to Eq. (9), a single cantilever elastic deflection of a double cantilever beam specimen with a chevron notch is $\lambda_e(l_0) = \frac{4P}{Ea}\left(\frac{l_0}{b}\right)^3 k'^{-1}$.

During the loading, the moment of crack initiation occurs at the tip of the chevron notch. Propagation of the initiated crack to the distance Δl increases the effective fracture length. Let us present the crack front as a straight line (**Figure 5**). The length of this line is $h = 2\Delta l \cdot \mathrm{tg}(\alpha/2)$.

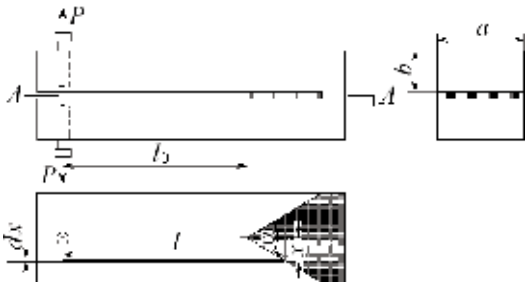

Figure 4. Projections of chevron-notched specimen.

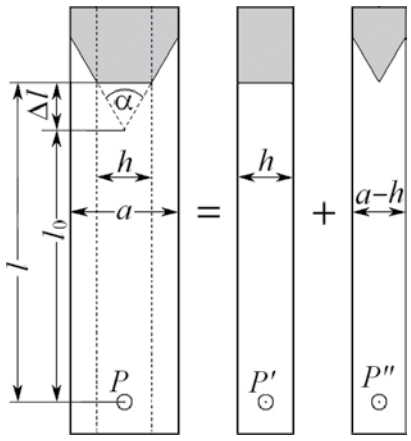

Figure 5. Presentation of the specimen with a crack in the form of straight-through and chevron-notched specimens.

Basically, this specimen with a crack is a set of two specimens: with a straight-through notch in width of h and with a chevron notch in width of $a - h$ (**Figure 5**). Let us determine the forces P' and P'' for these specimens, respectively, causing identical deflection λ_e. Using Eq. (5), we find an expression for P' acting on a straight-through notched specimen in width of $h = 2\Delta l \cdot \mathrm{tg}(\alpha/2)$:

$$P' = \frac{\lambda_e E \Delta l}{4} \mathrm{tg}\,\frac{\alpha}{2}\left(\frac{b}{l}\right)^3. \tag{11}$$

According to Eq. (9), for the chevron-notched specimen in width of $a - h$, we obtain an expression for P'':

$$P'' = \frac{\lambda_e \Delta l \cdot \mathrm{tg}\,\frac{\alpha}{2} E}{4}\left(\frac{b}{l}\right)^3\left(1 - \frac{2\Delta l}{a}\mathrm{tg}\,\frac{\alpha}{2}\right)\frac{l}{l_0}\left[4 + \frac{a}{l_0}\,\mathrm{ctg}\,\frac{\alpha}{2} + \frac{2\Delta l}{l_0}\right] \Big/ \left[2 + \frac{a}{l_0}\,\mathrm{ctg}\,\frac{\alpha}{2}\right]^2. \tag{12}$$

On the basis of Eqs. (11) and (12), an expression for λ_e is determined:

$$\lambda_e(l) = \frac{4P}{Ea}\left(\frac{l}{b}\right)^3 k^{-1}, \tag{13}$$

where $P = P' + P''$, $l = l_0 + \Delta l$ and k is

$$k = \frac{2\Delta l}{a}\,\mathrm{tg}\,\frac{\alpha}{2} + \frac{l}{l_0}\left(1 - \frac{2\Delta l}{a}\,\mathrm{tg}\,\frac{\alpha}{2}\right)\left(4 + \frac{a}{l_0}\,\mathrm{ctg}\,\frac{\alpha}{2} + \frac{2\Delta l}{l_0}\right)\left[2 + \frac{a}{l_0}\,\mathrm{ctg}\,\frac{\alpha}{2}\right]^{-2}.$$

It is easy to verify that at $\Delta l \to 0$, the value of $k \to k'$.

Substituting Eq. (13) for λ_e into Eq. (6), we obtain the expression for SFE:

$$G = \frac{12P^2l^2}{Eb^3a^2}k^{-2}. \tag{14}$$

This equation differs from the similar one for the straight-through notch only by k^{-2}. In particular, if $\alpha = \pi$, Eq. (14) goes over into Eq. (5) for the straight-through notch, since then k is 1.

As follows from Eq. (14), the characteristic of G depends on the Young's modulus E. The higher E is, the lower is the SFE value under all other conditions being equal. In contrast, according to Eq. (2), characteristic of K_I does not depend on E, i.e. SIF is invariant in relation to the Young's modulus.

4. Theoretical determination of elastic crack opening δ_e

The specimen presentation in the form of a double cantilever configuration allows us to determine the elastic crack opening initiated at the tip of the chevron. It is known that the elastic displacements of the cantilever points obey equation [14]:

$$\upsilon_e(x) = \frac{P}{Ea}\left[2\left(\frac{x}{b}\right)^3 - 6\frac{x}{b}\left(\frac{l}{b}\right)^2 + 4\left(\frac{l}{b}\right)^3\right], \tag{15}$$

where the x axis is directed along the cantilever. At $x = 0$, Eq. (15) determines the elastic deflection λ_e of the load application point P.

Eq. (15) is also valid for the double cantilever beam specimen with a straight-through notch. Then elastic notch opening in the point x is $\delta_e(x) = 2\upsilon_e(x)$. The cantilever displacement in the point $x = l_0$ is equal to

$$\upsilon_e(l_0) = \frac{2Pl_0\Delta l^2}{Eab^3}\left[3 + 2\frac{\Delta l}{l_0}\right]. \tag{16}$$

Substituting Eq. (5a) for P into Eq. (16), we obtain the cantilever displacement in the point $x = l_0$ for the straight-through notched specimen:

$$\upsilon_e = \lambda_e\frac{\Delta l^2[3l_0 + 2\Delta l]}{2(l_0 + \Delta l)^3}. \tag{17}$$

Let us find the cantilever displacement in the point $x = l_0$ for the chevron-notched specimen. For this, we use Eq. (16), where we place the value of P' instead of P according to Eq. (11), and

the width of the specimen central part $h = 2\Delta l \cdot \mathrm{tg}(\alpha/2)$ shown in **Figure 5** instead of a. Let us find the cantilever deflection in the load application point P':

$$\lambda_e = \frac{2P'}{E\Delta l \cdot \mathrm{tg}\,(\alpha/2)} \left(\frac{l_0 + \Delta l}{b}\right)^3. \tag{18}$$

Alternately, as follows from Eq. (17),

$$\lambda_e = \frac{\upsilon_e 2(l_0 + \Delta l)^3}{(3l_0 + 2\Delta l)\Delta l^2}. \tag{19}$$

From Eqs. (18) and (19), we obtain an expression for P':

$$P' = \frac{\upsilon_e E b^3 \,\mathrm{tg}\,(\alpha/2)}{(3l_0 + 2\Delta l)\Delta l}. \tag{20}$$

As follows from Eq. (12), $\lambda_e = \frac{4l^2 \cdot \mathrm{ctg}\,(\alpha/2)(P-P')}{Eb^3[a-2\Delta l\,\mathrm{tg}\,(\alpha/2)]} \frac{[2l_0+a\,\mathrm{ctg}\,(\alpha/2)]^2}{[4l_0+a\mathrm{ctg}\alpha/2+2\Delta l]}$.

Taking into account Eq. (20), we find a cantilever point displacement at a distance l_0 from the load application point P:

$$\upsilon_e = \frac{P(l_0 + 2l)\Delta l}{Eb^3\,\mathrm{tg}\,(\alpha/2)} - \frac{\lambda_e \Delta l(l_0 + 2l)[a - 2\Delta l\,\mathrm{tg}\,(\alpha/2)][4l_0 + a\,\mathrm{ctg}\,(\alpha/2) + 2\Delta l]}{4l^2\,\mathrm{tg}\,(\alpha/2)[2l_0 + a\,\mathrm{ctg}\,(\alpha/2)]^2}. \tag{21}$$

The value of $\delta_e(l_0) = 2\upsilon_e$ determines the crack opening initiated at the chevron.

During the crack propagation, the increment of the single cantilever elastic deflection occurs in the load application point P. The increment

$$\Delta\lambda_e = \lambda_e(l_0 + \Delta l) - \lambda_e(l_0), \tag{22}$$

corresponds to the crack length Δl.

Figure 6 presents the curves of the υ_e dependence on the crack length Δl and on the increment of the single cantilever elastic deflection $\Delta\lambda_e$ obtained using Eq. (21), at following values of the parameters: $E = 110$ GPa, $l_0 = 18.12$ mm, $\Delta l = 3.77$ mm, $P = 822$ H, $\alpha = \pi/9$ (20°), $a = b = 4.35$ mm. The calculations show that there is a parabolic dependence between Δl and υ_e, which can be written as $\upsilon_e = A\Delta l^2$, where A is the constant, which depends on the assignment of concrete parametric values in Eq. (21). In this case, A is equal to 2.58. As seen from the plot, there is a linear dependence $\Delta\lambda_e = B\upsilon_e$ between $\Delta\lambda_e$ and υ_e. The proportionality factor for the assigned values of B is 5.969.

The equations given above are derived from the constitutive equations of engineering fracture mechanics for the first time and can be used for the calculation of SFE for the chevron-notched specimens.

The processes of plastic deformation affect the cantilever deflection value and opening of crack sides in the point of its initiation. For this reason, the experimentally measured values of the

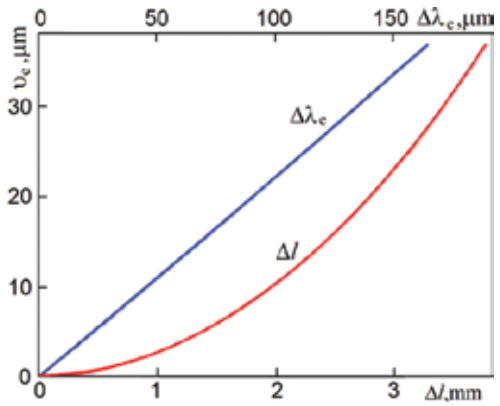

Figure 6. Dependence υ_e on Δl and $\Delta\lambda_e$.

cantilever deflection λ, except for λ_e, contain a part of the equation $\lambda_p = \lambda - \lambda_e$ that is not related to the change in specimen ductility. The crack opening values of υ measured in the same way contain the plastic deformation contribution $\upsilon_p = \upsilon - \upsilon_e$. The values of λ_p and υ_p are very important when simulating the fracture process in the chevron-notched zone.

Using Eq. (13), according to the experimentally measured value of cantilever deflection λ (**Figure 7**), one can determine the relative value of $(\lambda-\lambda_e)/\lambda_e = \lambda_p/\lambda_e$ as an additional fracture toughness characteristic. It is obvious that the more ductile a material is, the higher is its fracture toughness. The value of λ_p is not associated with change in specimen ductility since it is determined only by the elastic deflection of the specimen. The stress distribution in the plastic deformation zone is significantly different from the stress field in an elastic medium with a crack. On the way of crack propagation, the material is always subjected to a certain degree of plastic deformation. This means that crack is always surrounded by a layer of the plastically deformed material. The calculations made in Ref. [21] by the method of relaxation elements showed that stress field in the plastic deformation zone differs significantly from the crack stress field in the elastically deformable medium. Plastic deformation leads to stress relaxation. For this reason, there is no singularity in the crack mouth. The maximum stress concentration is observed in the plastic deformation zone.

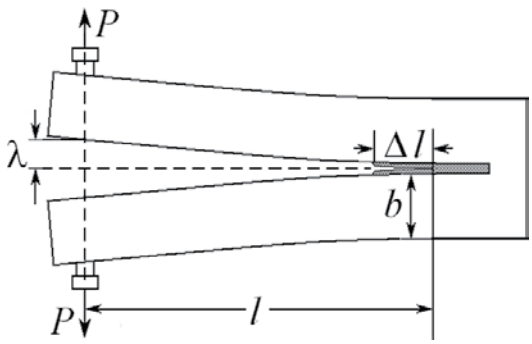

Figure 7. Scheme of the cantilever deflection.

The above equations are derived without any assumptions about the plastic properties of the material. Therefore, they can be used to calculate fracture toughness of any structural materials wherein the crack initiation at the tip of the chevron notch is observed. The product of $EG/(1-\nu^2)$ does not depend on the Young's modulus since SFE G is inversely proportional to the Young's modulus value E (see Eq. (14)). Therefore, irrespective of plastic properties of the material, the equation

$$K_I = \sqrt{\frac{EG}{(1-\nu^2)}} = \frac{2Pl}{ab^{3/2}k}\sqrt{\frac{3}{1-\nu^2}} \tag{23}$$

determines the stress intensity factor (SIF) for the small-size chevron-notched specimens.

The standard test on ductility change of the chevron-notched specimens is made using the "loading-unloading" operations [7, 8, 18–20]. As a result, the fracture toughness of the material is determined under the low-cycle loading conditions, rather than under constant loading. It is known that the curve type "load-displacement" changes significantly depending on the previous loading history. This is due to the fact that the plastic deformation rate and strain hardening of the material essentially depend on the external load and time during which the load is acting. To define the mechanisms of failure of structural materials, first of all, the values of SFE and SIF under continuous loading are significant. Eqs. (13) and (15) allow us to calculate these characteristics with-out using the load-unload condition. It is enough to know the crack length Δl initiated at the chevron.

The examples of the fracture toughness analysis of a number of structural materials, which differ in their ability to crack formation and the Young's modulus, are presented below.

5. Fracture toughness of structural materials

This section presents the calculation results of the fracture toughness characteristics of VT6 (Ti + 6%Al + 4%V) alloy, Fe-35.4% Ni and 12GBA tube steel.

The specimens 21 × 10 × 6 mm^3 in size were cut from the work piece by the electroerosion method. Then a notch 0.3 mm thick was made with a chevron angle $\alpha = 60^\circ$ (see **Figure 4**). The crack length at the pre-fracture stage was determined by the specimen images. Alloys with different ability to plastic deformation and with different values of the Young's modulus E were tested. The loading of specimens made of VT6 and Fe + 34.6%Ni alloys was performed by the intrusion of a narrow wedge into the notch at a motion rate of 5 μm/s (**Figure 8**). The 12GBA tube steel loadings were performed by application of opposite forces to the tips of the notch (**Figure 7**).

Figure 8 shows the scheme of the specimen wedging. The constant motion rate of the wedge provides the prolonged stage of stable crack propagation initiated at the chevron. The equation for the calculation of P bending the cantilever is obtained from the condition of equilibrium of forces:

$$P = \frac{F \cdot \cos\gamma}{2\left[\sin(\beta/2) + \kappa \cdot \cos(\beta/2)\right]}, \tag{24}$$

where F is the load on the wedge, κ and γ are the friction factor and interplanar angle between the wedge and cantilever, respectively, β is the angle of wedge opening.

As seen from Eq. (19), in order to determine the bending force P, it is important to calculate the friction factor κ. Substituting Eq. (22) into Eq. (8) instead of P, we obtain the following equation for κ:

$$\kappa = \frac{\Delta F}{\Delta L} \frac{2\cos\gamma[2l_0 + a\,\mathrm{ctg}\,(\alpha/2)]^2}{\sin(\beta/2)(4l_0 + a\,\mathrm{ctg}\,(\alpha/2))aEl_0} \left(\frac{b}{l_0}\right)^3 - \mathrm{tg}\,\frac{\beta}{2}, \tag{25}$$

where $\Delta F/\Delta L$ is the decline of the initial elastic segment of the experimental loading diagram "load P–wedge displacement L".

The calculations showed that κ is equal to 0.08 to an accuracy of 10%.

Table 1 shows the fracture toughness characteristics of the studied materials.

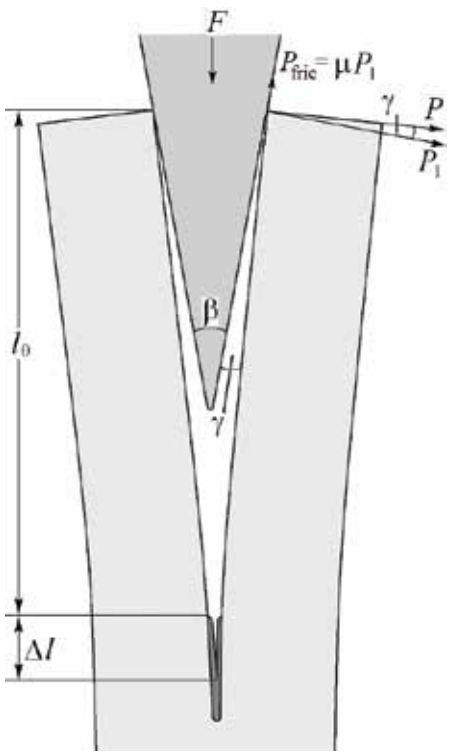

Figure 8. The scheme of the chevron-notched specimen wedging.

Alloy	*P*, N	λ_e, mm	λ, mm	λ_p/λ_e	υ_e, μm	υ, μm	υ_p/υ_e	*G*, kJ/m^2	K_I, MPa·m$^{1/2}$
VT6 UFG	277.7 (max)	0.453	0.453	0	0	0	–	11.9	35.5
	193.1 (stable)	0.407	0.374	0.09	15.1	23.8	0.53	4.58	22.5
VT6 CC	522.6 ($\Delta l = 0$)	0.827	1.275	0.54	0	0	–	43.04	68.81
	584.1 (max)	1.162	2.100	0.81	39.6	162.5	3.10	43.40	69.09
Ni-Fe	936.0 ($\Delta l = 0$)	0.426	0.474	0.11	0	0	–	23.63	70.44
	1175.2 (max)	0.695	1.038	0.49	30.8	89.9	1.92	30.27	75.51
12GBA	2776 (max)	0.095	0.379	2.6	0	0	–	51.7	104.2

Table 1. Fracture toughness characteristics of structural materials.

5.1. VT6 alloy (Ti–6Al–4V)

The structural VT6 alloy is mainly used for the manufacturing of large welded and built-up air-craft structures, balloons working under internal pressure over a wide temperature range from 196 to 450°C, and a number of other structural elements.

The studies were conducted using the material in the initial coarse-crystalline (CC) state (grain size of 7–5 μm) and with ultra-fine grained (UFG) structure (grain size of 500 nm) obtained by the severe plastic deformation [22]. The loading was carried out by a wedge with β equal 20° (**Figure 8**).

Figure 9 shows a typical loading diagram of the UFG VT6 alloy. The load-peak corresponds to the moment of crack initiation at the tip of the chevron. A sudden stress drop is caused by the spontaneous crack propagation to a certain length along the chevron notch. After that there is slow and stable crack propagation to the critical length, which determines the final fracture of the material. In the calculations for the VT6 alloy, *E* was equal to 110 GPa [23–25].

The measured values of l_0 and Δl are equal to 18.12 and 3.767 mm, respectively, $a = b = 4.35$ mm. The same values were used for calculating the fracture toughness of the VT6 alloy in the coarse-crystalline state (CC).

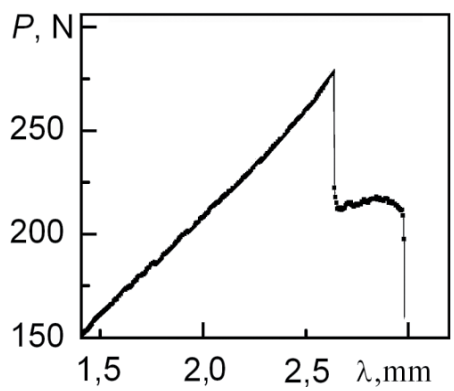

Figure 9. Loading diagram of UFG VT6 alloy.

Table 1 shows that plastic deformation does not affect the displacement of the notch sides prior to the crack initiation in the UFG VT6 alloy ($\lambda_p/\lambda_e = 0$). This means that the specimen is deformed only elastically prior to crack initiation. At the stage of pre-fracture, the influence of plastic deformation was observed: $\lambda_p/\lambda_e = 0.09$. The contribution of plastic deformation to the crack opening at the tip of the chevron is comparable with that of elastic deformation: $\upsilon_p/\upsilon_e = 0.53$.

Spontaneous crack propagation from the moment of its initiation is accompanied by the reduction in the elastic deflection λ_e of a single cantilever of the specimen and reduction in the fracture tough-ness characteristics of G and K_I. This alloy shows quite different fracture regularities in the coarse-crystalline state. A qualitative view of the loading diagrams and consistent patterns of crack propagation in the chevron-notch zone (**Figure 10**) show the following. The beginning of crack initiation and propagation occurs long before the external load reaches a maximum. This is marked with an arrow 1 shown in **Figure 10**. Crack initiation is preceded by the plastic deformation of the material in the chevron-notch zone. The contribution of plastic deformation λ_p to the displacement of load application point P up to the moment of crack initiation is comparable with that of elastic deformation: $\lambda_p/\lambda_e = 0.54$ (see **Table 1**).

Peaks and plateaus on the loading diagram are caused by abrupt nature of crack propagation. The specific fracture energy of G and K_I is almost unchanged until it reaches the maximum load P_{max} marked with an arrow 2 in **Figure 10**. Thus, a fracture toughness criterion for the CC VT6 alloy are the values of SFE $G_c = 43.2 \pm 0.2$ kJ/m^2 and SIF $K_{Ic} = 68.9 \pm 0.2$ MPa·m$^{1/2}$. The SIF value coincides with the value of 66.4 MPa·m$^{1/2}$ to an accuracy of 3.6% in Ref. [24] for standard test conditions.

During crack propagation, a contribution of plastic deformation to the displacement of the notch tips increases. The equation $\lambda_p/\lambda_e = 0.81$ corresponds to the maximum load. The contribution of plastic deformation to the crack opening at the tip of the chevron is 3 times higher than that of elastic deformation: $\upsilon_p/\upsilon_e = 3.1$. The subsequent loading leads to a drop in the external load and to the reduction of G and K_I characteristics. In this case, the λ_p/λ_e ratio goes up due to the λ_p increase and λ_e decrease.

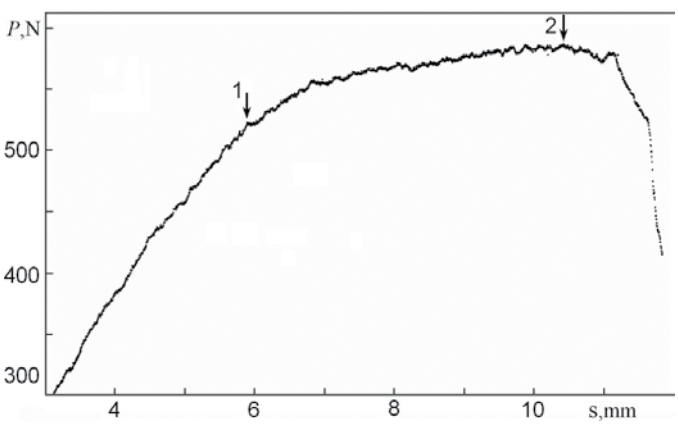

Figure 10. Loading diagram of the CC VT6 alloy.

A comparison shows that the method used to obtain the UFG structure in the VT6 alloy leads to a strong decrease in ductility, crack initiation stress (two-fold) and stress of stable crack propagation (three-fold). For this reason, the SMC VT6 alloy is characterized by the low fracture toughness. The behavior of the SMC VT6 alloy can be explained as follows. The low ductility of the alloy practically eliminates the stress relaxation factor in the chevron-notch zone and, as a consequence, reduces the crack initiation stress in the chevron. Stable propagation is determined by the stress con-centration at the tip of the crack, which is higher than that at the tip of the chevron prior to crack initiation. In this connection, a stress decrease takes place. The calculations have shown that the fracture toughness criteria for the SMC VT6 alloy are the values of SFE $G_c = 4.58 \pm 0.2$ kJ/m^2 and SIF $K_{Ic} = 22.5 \pm 0.2$ MPa·m$^{1/2}$ at the stage of stable crack propagation.

5.2. The Fe + 34.6%Ni-alloy

Table 1 also includes the data for the iron-nickel invar Fe + 34.6% Ni, which is widely used in modern industry and technology as an alloy with thermal linear expansion coefficient (TLEC) close to zero. When loading the specimen, a wedge with $\beta = 40^\circ$ was used.

The structural state of the alloy corresponds to that after the multi-axial forging. The alloy has a polycrystalline structure with an average crystallite size d equal 8 μm. The value of Young's modulus E in the calculation is 210 GPa. **Figure 11** shows a loading diagram of this alloy. The moment of crack initiation at the tip of the chevron is marked with an arrow 1. The beginning of crack initiation and propagation occurs long before the external load reaches a maximum. According to Eq. (13), the SFE from the moment of crack propagation (at $\Delta l = 0$) is equal to $G = 23.6 \pm 0.20$ kJ/m^2. The corresponding value of K_I is 70.5 ± 0.1 MPa·m$^{1/2}$.

The intermittent nature of the loading curve demonstrates that crack propagation occurs abruptly. Experimentally measured displacement of the load application point up to the moment of crack initiation is $\lambda = 0.47 \pm 0.02$ mm. According to Eq. (12), the portion of displacement that takes place due to the specimen elastic deformation is $\lambda_e = 0.43 \pm 0.02$ mm. Therefore, within the limits of the experimental error, the relative value of λ_p/λ_e does not exceed 10%. Thus, the plastic deformation prior to the moment of crack initiation in the chevron makes a minor contribution to the displacement of the load application point.

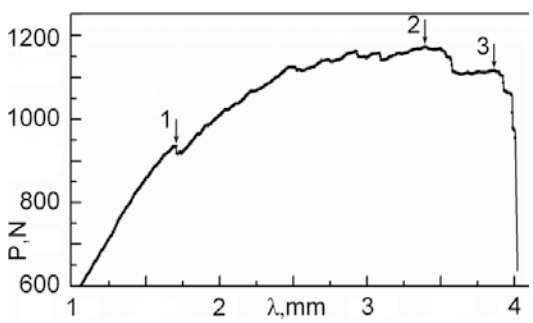

Figure 11. Loading diagram of the Fe-Ni alloy.

The observations show that the crack propagates along a complex trajectory, sharply changing the motion direction (**Figure 12**). The maximum value of SFE $G_c = 30.8 \pm 0.3$ kJ/m^2 corresponds to the maximum load. The corresponding value of K_{Ic} is equal to 80.4 ± 0.2 MPa·m$^{1/2}$. Note that the value obtained practically coincides with those of $K_c = 81.2$ MPa·m$^{1/2}$, obtained for the Fe-17%Ni alloy [26]. The critical value of crack opening $\delta_e = 2\upsilon_e = 61.56$ μm can also be used as a fracture toughness characteristic. The experimental value of δ is 179.8 μm. Hence, υ_p/υ_e is equal to 1.92. Thus, at the stage of prefracture, the crack opening in the chevron-notch zone contains a significant contribution related to the plastic deformation, which is almost twice greater than that of the elastic deformation of the specimen. A subsequent increase in crack length leads to a drop in the values of G_c and K_{Ic}. In this case, the υ_p/υ_e ratio increases due to the increase of υ_p contribution and decrease in υ_e contribution.

5.3. The 12GBA tube steel

The low-carbon low-alloy 12GBA steel is widely used in the construction of main oil and gas pipelines. The material was subjected to plastic deformation by rolling to the finite cross-section of bars of 8×8 mm^2 for several passes with step-like temperature decrease from 750 to 550°C [27]. After severe plastic deformation, the steel has a fibrous UFG structure with a lateral fragment size of 0.5 μm. In the longitudinal direction, the length of fragments is 15–20 μm.

The 12GBA tube steel loading was performed by opening of the chevron-notch sides (**Figure 6**).

Figure 13 shows a loading diagram "force P – displacement of notch tips λ" for the 12GBA tube steel. Crack initiation at the tip of the chevron notch is preceded by considerable plastic deformation. A crack initiates at the moment when the load reaches practically reaches a maximum (marked with an arrow). First, the crack slowly grows, and then its propagation

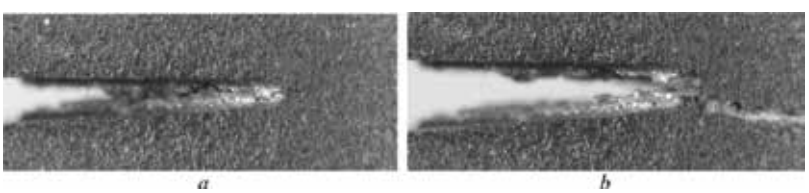

Figure 12. Crack in the chevron-notch zone prior to the fracture (*a*) and the specimen fracture after 4 s (*b*).

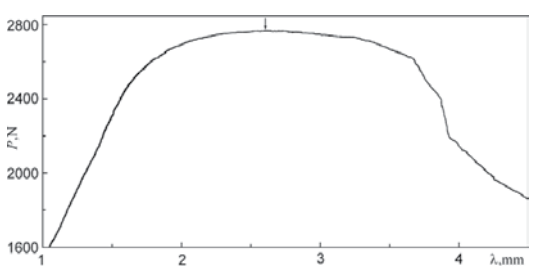

Figure 13. Loading diagram for the 12GBA steel.

Figure 14. Crack propagation in the chevron-notched zone. The 12GBA tube steel in the UFG state.

velocity increases sharply. The calculations by Eq. (5) determine the value of K_{Ic} = 104 kJ·m$^{1/2}$ for 12GBA, which is much higher than for the Fe-Ni alloy (75.51 MPa·m$^{1/2}$).

In contrast to the titanium-based alloys, significant processes of plastic deformation are developed in the SMC 12GBA steel in the chevron-notch zone resulting to the extremely viscous fracture behavior. **Figure 14** illustrates the consistent patterns of crack propagation in the chevron-notch zone. From the moment of crack initiation, this process is accompanied by a monotonous drop in the external load (**Figure 13**).

The λ_p/λ_e ratio can serve as a quantitative characteristic of viscosity. For these materials, it differs quite considerably, in particular, at the load peak λ_p/λ_e is 2.6 for 12GBA and λ_p/λ_e is 0.81 for the CC VT6 alloy.

These examples show that at fracture toughness certification of the material, except for SFE, it is important to know the characteristics of λ_p/λ_e and υ_p/υ_e, which determine the effect of plastic deformation on the displacement of load application points and crack opening, respectively. The proposed method allows us to study the fracture toughness of materials without restrictions on the plastic zone size at the crack tip.

6. Conclusion

This chapter presents a new method for determining fracture toughness of materials according to the test data of non-standard small-size chevron-notched specimens. The analytical expressions are obtained being based and derived from the constitutive equations of engineering fracture mechanics to determine the crack-driving force G (specific fracture energy) and the stress intensity factor (SIF) K_{Ic}. Experimental determination of crack length Δl is of principle importance in calculations. During testing, loading diagrams and photographic images of the specimens taken in time intervals are obtained. The displacement of the notch sides, crack opening at the tip of the chevron notch and crack length during its initiation and propagation are measured. This allows us to distinguish the plastic deformation contribution to the displacements that is not related to the change in specimen ductility and therefore does not affect the fracture toughness characteristics of the material.

Due to the fact that change in specimen ductility with increase in the crack length is analytically considered in constitutive relations, the periodic unloading of the specimen applied under standard test conditions of the chevron-notched specimens is excluded in the experiments.

There are no empirical constants and phenomenological dependencies in the calculations. All necessary calculation parameters are determined according to the experimental data. The

method allows us to use the low-power test machines and does not require large amounts of material for the production of specimens, as well as fatigue precracking. The method allows us to certify fracture toughness of the material without restrictions regarding the amount of plastic deformation and in front of the crack tip and in the specimen as a whole. The theoretical analysis has shown that G_c compared to K_{Ic} depends on the Young's modulus E of the material. The higher E is, the lower is G_c under all other conditions being equal. For this reason, the relative values of G_c and K_{Ic} characteristics can differ essentially. Thus, the value of G_c for the Fe-Ni alloy is lower that for the CC VT6 alloy, and the value of K_{Ic} is, on the contrary, higher (**Table 1**).

It is proposed to consider the λ_p/λ_e ratio as an additional fracture toughness characteristic that determines the plastic deformation contribution to the displacement of load application point in relation to the elastic deformation.

Therefore, in order to make fracture toughness certification of the material more complete, it is recommended to determine three fracture toughness characteristics of the material: SIF, SFE and the λ_p/λ_e ratio. According to this method, the fracture toughness characteristics of the VT6, Fe-35.4%Ni alloy and the 12GBA tube steel are determined, which differ in the ability to fracture toughness and the Young's modulus.

Acknowledgements

The authors would like to acknowledge the financial support of the Russian Foundation for Basic Research according to the research project № 17-08-00377.

Author details

Yevgeny Deryugin

Address all correspondence to: dee@ispms.tsc.ru

Institute of Strength Physics and Materials Science of the SB RAS, Tomsk, Russia

References

[1] ASTM Designation E 399-09: Standard Test Method for Linear-Elastic Plane-Strain Fracture Toughness K_{Ic} of Metallic Materials. PA, USA: West Conshohocken; 2009

[2] Methods of Mechanical Testing of Metals. Determination of Fracture Toughness Characteristics under Static Loading. GOST 25.506-85. Moskow: Izdatelstvo standartov; 1985

[3] GOST 4647-80 (ST SEV 1491-79). Moskow: IPK Izdatelstvo standartov; 1998

[4] Ali MB, Abdullah S, Nuawi MZ, Ariffin AK, Nopiah ZM. Evaluating instrumented charpy impact strain signals using curve fitting equations. Journal of Central South University. 2014;**21**:600-609. DOI: 10.1007/s11771-014-1979-3

[5] Miyazaki H, Hyuga H, Yoshizawa YI, Hirao K, Ohji T. Relationship between fracture toughness determined by surface crack in flexure and fracture resistance measured by indentation fracture for silicon nitride ceramics with various microstructures. Ceramics International. 2009;**35**:493-501. DOI: 10.1016/j.ceramint.2008.01.006

[6] Bončina T, Zupanič F, Čekada M, Markoli B. Microindentation of dispersed phases in an Al94Mn 2Be2Cu2 alloy. Journal of Alloys and Compounds. 2010;**505**:486-491. DOI: 10.1016/j.jallcom.2010.06.111

[7] Barker LM. Theory for determining K_{Ic} from small, non-LEFM specimens, supported by experiments on aluminum. International Journal of Fracture. 1979;**16**:515-536. DOI: 10/1007/BF00019921

[8] Wang CT, Pillar RM. Short-rod elastic-plastic fracture toughness test using miniature specimens. Journal of Materials Science. 1989;**24**:2391-2400. DOI: 10.1007/BF01174501

[9] Grant TJ, Weber L, Mortensen A. Plasticity in Chevron-notch fracture toughness testing. Engineering Fracture Mechanics. 2000;**67**:263-276. DOI: 10.1016/S0013-7944(00)00061-8

[10] Soderholm K-J. Review of the fracture toughness approach. Dental Materials. 2010;**26**: e63-e77. DOI: 10.1016/j.dental.2009.11.151

[11] Rakhimkulov RR. Matching of fracture toughness values of K_{1c}, obtained in chevron-notched specimens and based on standard technique for a steel St3sp. Neftegazovoe delo. 2010;**2**:1-10. Available from: http://www.ogbus.ru/authors/Rakhimkulov/Rakhimkulov_1.pdf

[12] Hertzberg RW. Deformation and Fracture Mechanics of Engineering Materials. 3rd ed. New York: Wiley; 1989

[13] Matvienko YG. Models and Criteria of Fracture Mechanics. Moskow: FIZMATLIT; 2006

[14] Timoschenko S, Goodier JN. Theory of Elasticity. New York, Toronto: McGraw-Hill Book Company; 1951

[15] Broek D. Elementary Engineering Fracture Mechanics. Leyden, Netherlands: Noordhoff International Publishing; 1974

[16] Salem JA, Shannon JI Jr, Jenkins MG. Some observations in fracture toughness and fatigue testing with chevron-notched specimens. In: Brown K, Baratta F, editors. Chevron-Notch Fracture Test Experience: Metals and Non-Metals. ASTM STP 1172. Philadelphia: American Society for Testing and Materials; 1992. pp. 9-25

[17] Barker LM. A simplified method for measuring plane strain fracture toughness. Engineering Fracture Mechanics. 1977;**9**:361-369. DOI: 10.1016/0013-7944(77)90028-5

[18] Ruggieri C, Mathias L. Fracture-resistance testing of pipeline girth welds using bend and tensile fracture specimens. Journal of Pipeline Engineering. 2013;**12**:217-227

[19] Roy H, Ray A, Barat K, et al. Structural variations ahead of crack tip during monotonic and cyclic fracture tests of AISI 304LN stainless steel. Materials Science & Engineering, A. 2013;**561**:88-99. DOI: 10.1016/msea.2012.10.074

[20] Bartisch M, Zang ZF, Scheu C, et al. Fracture parameters of chevron-notched Al_2O_3/Nb sandwich specimens. Zeitschrift Fur Metallkunde. 2004;**95**:779-784

[21] Deryugin EE. Improved model of the Griffith crack. Journal of Applied Mechanics and Technical Physics. 1998;**39**:934-942. DOI: 10.1007/BF02468227

[22] Zherebtsov SV et al. Production of submicrocrystalline structure in large scale Ti-6Al-4V billet by warm severe deformation processing. Scripta Materialia. 2004;**51**:1147-1151. DOI: 10.1016/j.scriptamat.2004.08.018

[23] Grigor'ev IS, Meilikhova BZ, editors. Physical Quantities. Handbook. Moscow: Energoatomizdat; 1991

[24] Titanium Alloys. Composition, Structure, Properties. Reference Book. Moscow: VILS-MATI; 2009. 520 p

[25] Deryugin EE, Suvorov BI. Defining the fracture toughness for small-sized samples of materials with submicrostructure. Vestnik SamGU. Technical Sciences. 2012;**36**:123-129

[26] Prokopovich KA. Static fracture toughness of the extraterrestrial Fe-17%Ni alloy. In: Works of XII International Scientific and Technical Ural School-Seminar of Metallographers-Young Metal Science Scientists; Russia. Ekaterinburg: UrFU; 2011. pp. 288-290

[27] Safarov IM, Sergeev SN, Korznikov AV, et al. Fibrous ultrafinegrained structure and properties of rolled low carbon steel 12 GBA. Letters on Materials. 2013;**3**:3-6. DOI: 10.22226/2410-3535-2013-1-3-6

Chapter 12

Numerical Analysis Methods of Structural Fatigue and Fracture Problems

Qiu Zhiping, Zhang Zesheng and Wang Lei

Additional information is available at the end of the chapter

http://dx.doi.org/10.5772/intechopen.72285

Abstract

Fatigue and fracture problems, which lead to 95% of structural failure, have attracted much attention of engineers and researchers all over the world. Compared with experimental method, numerical simulation method based on empirical models shows its remarkable advantages in structure design because of less cost and higher efficiency. However, the application of numerical simulation method in fatigue lifetime prediction is restricted by low accuracy and poor applicability in some circumstances. Most numerical method is based on empirical models. This chapter first reviews various kinds of empirical models of fatigue and fracture problems, including some modifying methods of basic empirical models, which have been widely applied to fatigue lifetime prediction and indicated their advantages and disadvantages. Then, FEM is introduced as an important method to obtain stress intensity factor or crack growth route. At last, this chapter is finished with existing problems and current trends in fatigue lifetime prediction via numerical method.

Keywords: fatigue lifetime prediction, crack propagation, numerical method, empirical model, Paris law, perturbation approach, extended finite element method, fractal geometry

1. Introduction

With the development of mechanical engineering and manufacturing technology, engineering structures applied in aircrafts and huge machines become much more complex. These structures usually bear constantly changing loads in tour of duty. Although the max stress in structure caused by these dynamic loads is much lower than yield limit and ultimate strength of material, structure is destroyed after a long time. Internal defects in engineering structures appear in producing, processing, and assembling process. Internal defects lead to stress concentration, crack initiation, and propagation and even fatigue failure under dynamic load.

According to statistical data, loss caused by improper structural fatigue lifetime design in America equals 4.4% of gross national product, and 95% of structure failures are related to fatigue break caused by alternating dynamic loads [1]. There are numerous historical examples that result in great loss of human life and economic value. For example, two Comet aircraft crashed in 1954, and the main reason is fatigue of fuselage structure [2]. Mechanical failure caused by fatigue, which concentrates much attention of engineers and researches, has been studied for more than 150 years [3]. However, it is still much difficult to prevent fatigue failure because fatigue of materials is far from being completely comprehended [4].

Metallic materials are widely applied in design of structures and parts in present days; therefore, fatigue of metals is a problem deserving efforts. In fact, the fatigue process is constitutive of crack initiation and crack propagation to total failure, as shown in **Figure 1**, and fatigue lifetime should conclude crack initiation life and crack propagation life.

On one hand, it is widely accepted that the crack initiation phase costs a majority of fatigue lifetime in a high-cycle fatigue regime [5]. Furthermore, crack initiation behavior has a great influence on crack growth prediction in a unified approach for fatigue lifetime prediction [6]. Therefore, knowledge and technology of crack initiation life prediction are significant for evaluation of fatigue lifetime of structures and deserve our efforts to study deeply. On the other hand, there are frequently small cracks and defects in engineering structures due to manufacturing and environment factors; therefore, fatigue crack propagation prediction plays an important role in estimating the structural safety under dynamic loads.

Therefore, people divide structural life prediction problem into two problems: fatigue problem and fracture problem. People pay attention to crack initiation life in fatigue problem and make efforts to construct the relationship between structure life and stress or strain in structure. It is assumed in fatigue problem that there is a small crack existing in structure, and crack propagation behavior is studied in order to predict the remaining life of structure. These two problems have aroused widespread concern nowadays.

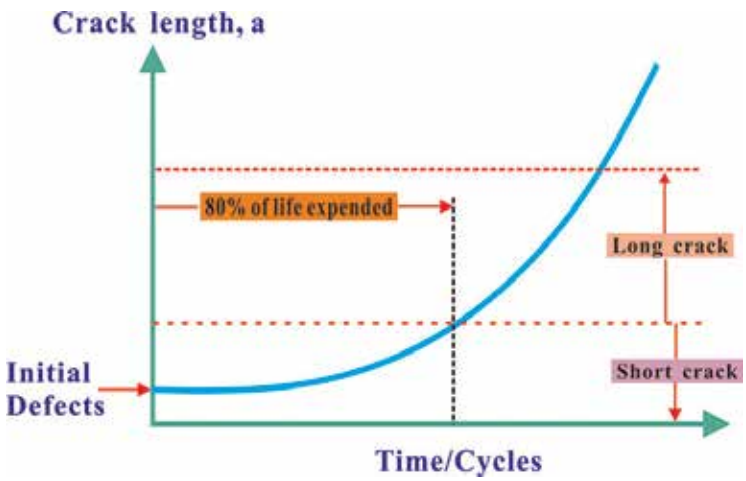

Figure 1. Schematic illustration of crack length versus time/cycles.

Experimental method and numerical method are two significant ways to analyze fatigue lifetime of structures. Experimental method has been widely applied since a long time ago. However, it is much expensive to predict structural life via experimental method. Furthermore, it is difficult to execute experiments for some complicated structures. Therefore, numerical method based on empirical models becomes much more popular in structural life prediction, and in some cases, those do not need high accuracy because of less cost and higher efficiency.

2. Empirical models in fatigue problem

Approaches to predict fatigue initiation life in literature can be classified into several types. These approaches study the fatigue problem from different perspectives, involving the average or local values of stresses and strains, the initiation of crack and defects, and macro- and microanalysis [7]. Nevertheless, people prefer to use phenomenological models, which reflect general material response at macroscopic scale under cyclic loads, rather than complex micro- or mesoscopic model of material fatigue behavior in structure design [8].

2.1. Empirical models of high-cycle fatigue

Wöhler is the pioneer in this field, who established the traditional stress-based approach in the nineteenth century [9]. He carried out a few fatigue experiments on metallic materials and indicated the relationship between fatigue crack initiation life and cyclic stress. He proposed to apply $S-N$ curves in description of fatigue behavior of metals in his paper. Effectiveness of this method in high-cycle fatigue analysis is demonstrated afterward by many researchers. There are several kinds of expression of $S-N$ curve, mainly including exponential function expression and power function expression. Basquin was the first person who suggested using exponential function to construct the expression of $S-N$ curve in the twentieth century. The typical exponential function expression is written as follows:

$$e^{mS_{\max}}N = C \tag{1}$$

where m and C are constants, which can be determined based on experiment data, N stands for the number of loading cycles, and $S_{\max}$ is the maximum value of stress at specific stress ratio. The power function expression with two parameters is usually expressed in the following form:

$$S_a^m N = C \tag{2}$$

where S_a is the stress amplitude at specific ratio. The power function expression with three parameters is expressed as

$$(S_{\max} - C)^m N = D \tag{3}$$

or

$$S_{\max} = C\left(1 + \frac{A}{N^{\alpha}}\right) \tag{4}$$

where D, A, and α are constants. The parameter C in Eqs. (3) and (4) nearly equals fatigue limit.

2.2. Empirical models of low-cycle fatigue

Stress level is usually high in low-cycle fatigue, and the maximum value of stress is nearly close to the ultimate strength of material. The number of loading cycles in low-cycle fatigue, which is not more than 10^3 times, is much less than that in high-cycle fatigue. Plastic deformation plays an important role in low-cycle fatigue, in which the accumulation of plastic deformation results in structural failure. Because low-cycle fatigue lifetime is much sensitive to the change of stress level, $S - N$ curve is unable to reflect the low-cycle fatigue performance of material. Therefore, $\varepsilon - N$ curve is applied to low-cycle fatigue analysis. The most widely accepted low-cycle fatigue lifetime model based on $\varepsilon - N$ curve is proposed by Basquin [10], which is expressed as follows:

$$\varepsilon_e = \frac{\sigma_a}{E} = \frac{\sigma_f'}{E}\left(2N_f\right)^b \tag{5}$$

where ε_e is the amplitude of elastic strain, E is the elasticity modulus of material, σ_f' is the fatigue strength coefficient of material, and b is the fatigue strength exponent. Because the relationship between plastic strain and fatigue lifetime is not taken into consideration in Basquin formula, Coffin [11] and Manson [12] proposed an empirical model when studying the relationship between fatigue lifetime and plastic strain amplitude. The expression of Coffin-Manson model is.

$$\varepsilon_a = \frac{\sigma_f'}{E}\left(2N_f\right)^b + \varepsilon_f'(2N)^c \tag{6}$$

in which ε_a stands for the amplitude of total strain and ε_f' and c stand for the fatigue ductility coefficient and fatigue ductility exponent separately. The relationships between plastic strain, elastic strain, total strain, and fatigue lifetime are shown in **Figure 2**.

2.3. Improved models considering mean stress or stress ratio

There are many factors, such as residual stress, temperature, multiaxial stress, and geometrical feature, that influence structural fatigue lifetime, in which mean stress or stress ratio concentrates the most attention.

2.3.1. Walker formula

Mean stress and stress ratio are of great significance for structural fatigue lifetime. Walker formula considers sensitivity of different materials to mean stress; therefore, it shows well

http://dx.doi.org/10.5772/intechopen.72285

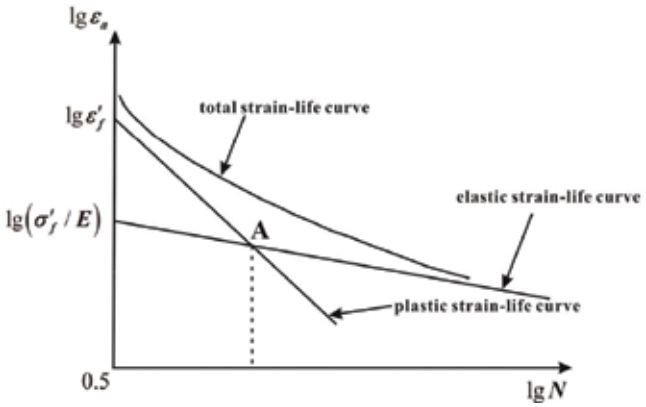

Figure 2. Elastic strain-life curve and plastic strain-life curve.

effect for all materials [13, 14]. An equivalent local strain parameter is defined in Walker formula; its expression is

$$\varepsilon_{eq} = (2\varepsilon_a)^r \left(\frac{\sigma_{\max}}{E}\right)^{1-r} \tag{7}$$

r is the material parameter. In order to construct the relationship between Walker formula and fatigue lifetime, Jaske et al. [15] carried out many experiments on different kinds of materials and proposed following expression based on experimental data:

$$\log N_f = A_0 + A_1 \tanh^{-1}\left[\frac{\log\left(\varepsilon_u \varepsilon_e / \varepsilon_{eq}^2\right)}{\log\left(\varepsilon_u / \varepsilon_e\right)}\right] \tag{8}$$

where A_0 and A_1 are regression coefficients and ε_u and ε_e are the upper and lower limits of this reverse hyperbolic tangent function, respectively. The strain-life curve is shown in **Figure 3**.

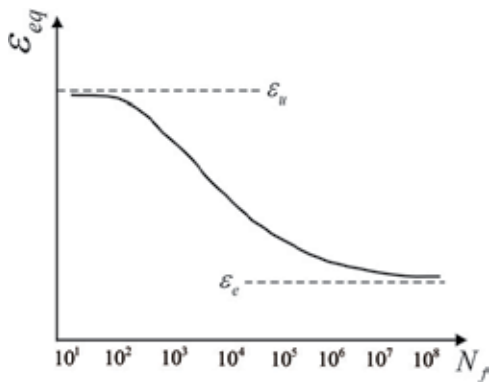

Figure 3. Strain-life curve of Walker formula.

There are too many parameters to be fitted in this method, which need plenty of experimental data. That disadvantage constricts badly the application of Walker formula in engineering.

2.3.2. Morrow's modifying method

Morrow's modifying method and SWT modifying method are two commonly used methods. Morrow mean stress modifying formula is shown as follows [16]:

$$\varepsilon_a = \frac{\sigma_f'}{E}\left(1 - \frac{\sigma_m}{\sigma_f'}\right)(2N_f)^b + \varepsilon_f'\left(1 - \frac{\sigma_m}{\sigma_f'}\right)(2N_f)^c \tag{9}$$

Considering the greater influence made by mean stress in long life period, further modifying method is given:

$$\varepsilon_a = \frac{\sigma_f'}{E}\left(1 - \frac{\sigma_m}{\sigma_f'}\right)(2N_f)^b + \varepsilon_f'(2N_f)^c \tag{10}$$

where ε_a is strain amplitude and σ_m is mean stress. Morrow's modifying method aims at elastic strain; therefore, it is only suitable when stress amplitude is constant or mean stress is compression stress.

2.3.3. SWT modifying method

Expression of Smith-Watson-Topper (SWT) parameter modifying method is [17]

$$\sigma_{\max}\varepsilon_a = \frac{\sigma_f'^2}{E}(2N_f)^{2b} + \sigma_f'(2N_f)^{b+c} \tag{11}$$

where

$$\sigma_{\max} = \sigma_m + \sigma_a \tag{12}$$

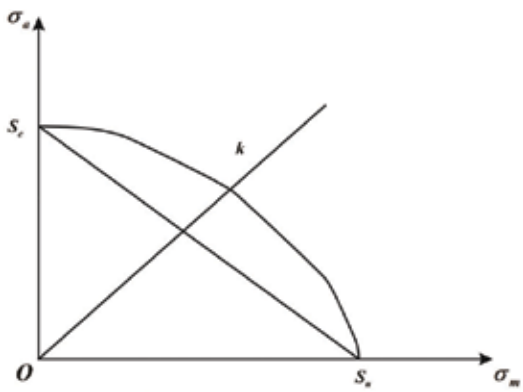

Figure 4. Fatigue limit curve and Goodman simplified straight line.

SWT mean stress modifying method is not valid for compression mean stress, and it will obtain too conservative result when the stretching mean stress is large.

2.3.4. Goodman's modifying method

We can acquire the fatigue limit points of material at different stress ratio $r = \sigma_{\min}/\sigma_{\max}$ under infinite life requirement with the support of large amount of experimental data. Draw these points in rectangular coordinate system whose X-axis is mean stress $\sigma_m = (\sigma_{\min} + \sigma_{\max})/2$ and Y-axis is stress amplitude $\sigma_a = (\sigma_{\max} - \sigma_{\min})/2$; thus, the fatigue limit curve is fitted based on these points. It is unpractical to carry out many experiments on all materials and structures in engineering, so we usually use a simplified straight line to replace the fatigue limit curve. Goodman simplified straight line, which is one of these straight lines, is widely accepted due to its simplicity and conservative estimation [18], as shown in **Figure 4**. Goodman simplified straight line can be expressed in the following relationship:

$$\frac{\sigma_a}{S_e} + \frac{\sigma_m}{S_u} = 1 \tag{13}$$

where S_e stands for the fatigue strength of material and S_u stands for the ultimate tensile strength of material. However, it has been proved that Goodman modifying method is only appropriate for low-ductility material, such as high-strength steel and cast iron.

3. Empirical models in fracture problem

3.1. Paris law

Paris et al. [19] made great contribution in this field who was pioneer suggesting that crack growth rate, da/dN, was a function of the maximum stress intensity factor $K_{\max}$ in 1961. Then, Liu [20] related the crack growth to the stress intensity factor range ΔK subsequently. Paris and Erdogan [21] proposed the well-known Paris law, which can be presented as follows:

$$\frac{da}{dN} = C(\Delta K)^m \tag{14}$$

where C and m can be obtained from experiment data, and they are usually considered as constants for a particular metal and environment [22]. Since then researchers have made efforts to study on Paris law and its deviation; however, we are still far from a complete comprehension [23].

It is believed that the relationship between crack propagation and ΔK can be divided into three distinct regions, as shown in **Figure 5**. The crack propagation is slow in region A, and concept of a fatigue threshold stress intensity factor range ΔK_{th} is proposed by Mcclintock [24], beneath which cracks are regarded not to grow. In region B, the "mid growth" range, crack propagation is stable, and Paris law is supposed to be held. Region C is associated with fast crack propagation leading to final failure. Therefore, calculation of number of loading cycles in region B, which could be gained from Paris law, is significant for prediction of fatigue crack growth life.

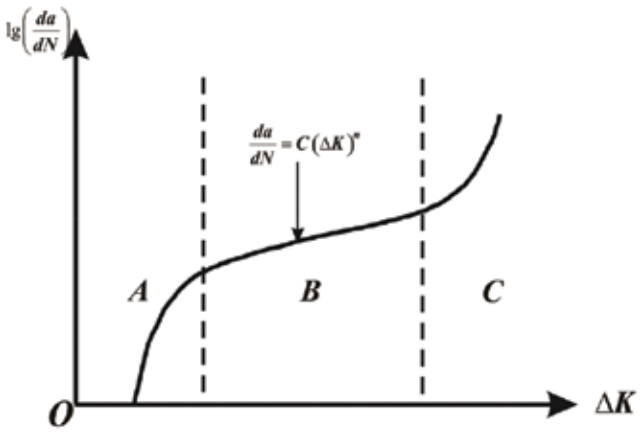

Figure 5. Schematic diagram of the relationship between crack growth and ΔK.

3.2. Improved models

3.2.1. Models considering mean stress or stress ratio

Since Paris law is proposed, much related work is done, and many modifying methods are put forward [22, 25–27]. It is commonly accepted that crack growth rate of material is related to mean stress or stress ratio. Several models, in which Forman formula [28] and Walker formula [29] are most famous, take this factor into consideration. Forman formula also considers the fracture toughness as an important factor; its expression is

$$\frac{da}{dN} = \frac{C(\Delta K)^m}{(1-R)K_c - \Delta K} \tag{15}$$

Forman formula is valid for dealing with experimental data of many kinds of materials, especially high-hardness alloy, but it is hard to obtain the fracture toughness K_c for high-ductility material. According to following relationship:

$$R = \frac{K_{\min}}{K_{\max}} \tag{16}$$

$$\Delta K = K_{\max} - K_{\min} \tag{17}$$

Forman formula can be transformed as follows:

$$\frac{da}{dN} = \frac{CK_{\max}(\Delta K)^{m-1}}{K_c - K_{\max}} \tag{18}$$

Forman formula explains the reason why crack growth enlarges sharply when stress intensity factor is close to fracture toughness.

Walker formula is another wide-applied crack propagation model in engineering, which expresses the influence made by stress ratio on crack growth rate. Furthermore, it takes maximum of stress intensity factor into consideration:

$$\frac{da}{dN} = C[(1-R)^m K_{\max}]^n \tag{19}$$

Three parameters C, m, and n can be acquired based on experimental data of crack propagation experiments with different stress ratios. Walker formula is valid when $R > 0$ and $R < 0$. According to the relationship between stress ratio and amplitude of stress intensity factor, another commonly used form of Walker formula is obtained:

$$\frac{da}{dN} = CK_{\max}^m (\Delta K)^n \tag{20}$$

3.2.2. Model based on crack closure theory

In 1971, Elber [30] found that crack opened completely only when the stress was larger than a certain value, and he developed a modified Paris law based on this theory. The stress when crack is completely open is defined as crack opening stress σ_{op}, and the stress when crack begins to close is defined as crack closing stress σ_{cl}. It has been demonstrated that crack opening stress is nearly equal to crack closing stress. The modified formula is written as follows:

$$\frac{da}{dN} = C\left(\Delta K_{eff}\right)^m \tag{21}$$

and

$$\frac{da}{dN} = C(U\Delta K)^m = U^m C(\Delta K)^m \tag{22}$$

U is the crack closure parameter, and its expression is

$$U = \frac{\Delta K_{eff}}{\Delta K} = \frac{\Delta \sigma_{eff}}{\Delta \sigma} = \frac{\left(\sigma_{\max} - \sigma_{op}\right)}{\Delta \sigma} < 1 \tag{23}$$

where efficient stress amplitude $\Delta\sigma_{eff}$ is the difference between maximum stress $\sigma_{\max}$ and crack opening stress σ_{op}.

3.2.3. Model considering crack retardation caused by high load

In Weeler's opinion [31], when structure bears cyclic load with constant amplitude; an occasional overload enlarges the size of plastic zone on crack tip, which would prevent crack from growing to some degree. On the basis of Weeler's research, Willenberg [32] assumed that crack retardation is due to residual compression stress σ_{res}, which is related to plastic deformation

caused by high load. Combining the expression of Forman formula, crack growth rate in retardation period is acquired:

$$\frac{da}{dN} = \frac{C\left(\Delta K_{eff}\right)^m}{\left(1 - R_{eff}\right)K_c - \Delta K_{eff}} \tag{24}$$

The effective stress intensity factor range is

$$\Delta K_{eff} = f\left[\left(\sigma_{\max}\right)_{eff} - \left(\sigma_{\min}\right)_{eff}\right]\sqrt{\pi a} \tag{25}$$

and the effective stress ratio is

$$R_{eff} = \left(\sigma_{\min}\right)_{eff} / \left(\sigma_{\max}\right)_{eff} \tag{26}$$

The maximum and minimum values of effective cyclic stress are

$$\left(\sigma_{\max}\right)_{eff} = \sigma_{\max} - \sigma_{res} \tag{27}$$

$$\left(\sigma_{\min}\right)_{eff} = \sigma_{\min} - \sigma_{res} \tag{28}$$

Then, crack growth rate in retardation period can be estimated as the residual stress σ_{res} is known. However, the residual stress σ_{res} can only be obtained via experimental method.

3.2.4. Model considering crack propagation threshold

In 1972, Donahue [33] took threshold of stress intensity factor range ΔK_{th} into consideration and proposed a generalized Paris law. The modified expression is

$$\frac{da}{dN} = C(\Delta K - \Delta K_{th})^m \tag{29}$$

The following expression was proposed by McEvily and Greoeger [34] in their research about fatigue crack propagation threshold in 1977:

$$\frac{da}{dN} = C(\Delta K - \Delta K_{th})^2\left(1 + \frac{\Delta K}{K_c - K_{\max}}\right) \tag{30}$$

in which material constant m equals 2.

Furthermore, if considering stress ratio at the same time, Paris law can be modified into the following expression:

$$\frac{da}{dN} = \frac{C[(\Delta K)^m - (\Delta K_{th})^m]}{(1 - R)K_c - \Delta K} \tag{31}$$

It can be figured out that the above equation is further modified on the basis of Forman formula.

In 1999, McEvily found it out that the following modification is suitable for many alloys' fatigue crack propagation:

$$\frac{da}{dN} = C\left(\Delta K_{eff} - \Delta K_{effth}\right)^2 \tag{32}$$

where ΔK_{effth} stands for the effective stress intensity factor range near crack propagation threshold. This modifying method considers the influences created by crack closure and small crack's elastic-plastic behavior, and it is useful to predict the long crack propagation under cyclic positive stress.

3.2.5. Model based on perturbation series expansion method

Perturbation series expansion method, which is a common method to deal with nonlinear problems, has been widely used in fluid mechanics, structure dynamics, and damage identification. In this method, the parameter in ideal model is regarded to have a small perturbation in order to study the properties of system. This parameter can be expanded into series form:

$$a = \sum_{i=0}^{\infty} a_i \varepsilon^i \tag{33}$$

where ε is a positive small constant.

Qiu and Zheng [35] proposed a novel numerical calculation method to investigate the fatigue crack growth evolution in aluminum alloy sheets accounting for the measurement error. The initial crack length is considered as a modified parameter with a small correction term due to the measurement error; the solution to the crack growth equation is expressed in the form of a perturbation series, and a series of modified equations for predicting the crack length history

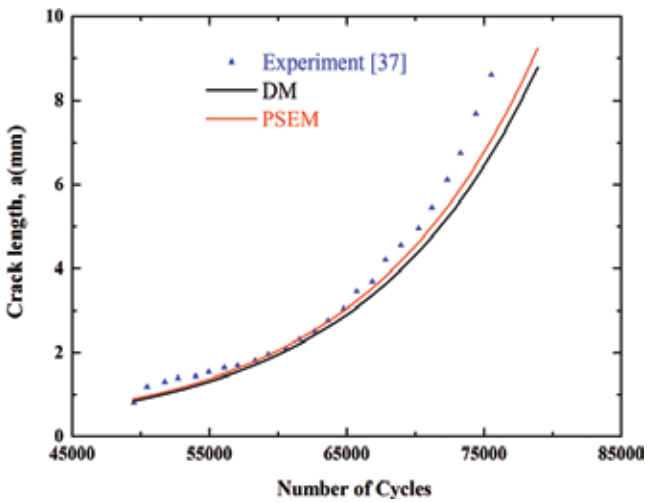

Figure 6. Comparison of the measured and predicted crack length history in Ref. [35].

are derived. The proposed method is verified to be indeed feasible and effective for predicting fatigue crack growth evolution by comparing numerical results with experimental data, as shown in **Figure 6**.

4. Finite element method

There are many kinds of numerical method to obtain stress intensity factor or crack growth route after continuous study of many researchers. Finite difference method (FDM), boundary element method (BEM), mesh-less method, and finite element method (FEM) are four common methods. Many studies have been carried out based on these numerical methods: Christen applied FEM to two-dimensional crack problem and obtained the displacement field and stress field; Nayroles [36] combined the moving least square method (MLSM) with mesh-less method to solve boundary problem. FEM is the most widely used method in above four methods at present [37, 38]. Considering singularity on crack tip, element's density is increased in order to obtain the precious results. Therefore, FEM's rate of convergence is low, and precision is unsatisfactory. People developed precious numerical solution methods based on several kinds of theories, in which semi-analytic numerical solution and new type elements are hot issues.

4.1. Extended finite element method

Collapsed singular isoparametric elements, which can reflect the singularity on crack tip correctly, were introduced by Barsoum [39]. This method is popular because of its high precision and executing simplicity. In this method, planar eight-node isoparametric element is degenerated into singular isoparametric element, as shown in **Figure 7**. Stress intensity factor is calculated based on the displacements of nodes A and B; the expression is.

$$K_{\mathrm{I}} = \frac{E'}{4}\sqrt{\frac{2\pi}{L}}(4v_A - v_B) \tag{34}$$

In plane stress problem, $E' = E$; in plane strain problem, $E' = \frac{E}{1-\mu^2}$. E, μ, and v are, respectively, elasticity modulus, Poisson ratio, and displacement perpendicular to crack surface. Chen and

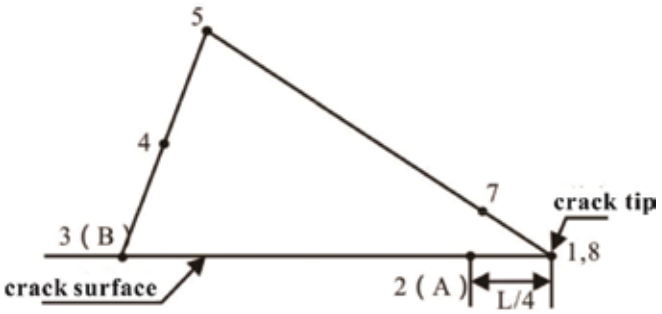

Figure 7. Eight-node singular isoparametric element.

Kuang [40] use interpolation method to acquire the displacements of nodes A and B on the basis of Barsoum's research and obtain the following expression of stress intensity factor:

$$K_{\mathrm{I}} = \frac{E'}{12}\sqrt{\frac{2\pi}{L}}(8v_A - v_B) \tag{35}$$

Lin [41] proposed the 1/4 node displacement method, as shown in **Figure 8**; the corresponding calculation equation of stress intensity factor is

$$K_{\mathrm{I}} = \frac{E'}{2}\sqrt{\frac{2\pi}{L}}v_A \tag{36}$$

Belytschko [42] applied extended finite element method (XFEM) to calculating stress intensity factor and neglected the high-order terms of asymptotic displacement function. The calculation results were not satisfying enough. Karihaloo and Xiao [43] took high-order terms of asymptotic displacement function and outer elements of crack tip into consideration, thus obtaining results of high accuracy. However, calculation efficiency of this method is relatively low. Although researchers have obtained precious results with the help of new type elements, there are still many factors that influence calculation results that need to be studied.

4.2. Fractal finite element method

In the aspect of semi-analytic numerical method, weighted function method and boundary collocation method develop fast. These methods are able to acquire results of high accuracy when dealing with particular models; however, calculation accuracy cannot be guaranteed when dealing with general models.

Fractal finite element method is also a semi-analytic method. Fractal geometry is introduced into ordinary FEM, which not only improves calculation accuracy but also shortens calculation time and saves storage capacity of a computer. In fractal finite element method, an artificial boundary Γ_0 is introduced to divide the structure with crack into two parts: singular field D

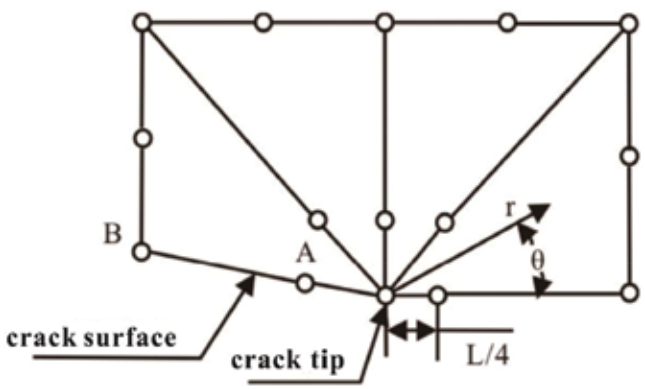

Figure 8. Mesh of 1/4 node element displacement method.

near crack tip and normal field Ω far away from crack tip, as shown in **Figure 9**. Ordinary finite element mesh is constructed in normal field; self-similar mesh needs to be constructed based on fractal theory in singular field.

Self-similar mesh is shown in **Figure 10**. In singular field, infinite curves $\{\Gamma_1, \Gamma_2, \Gamma_3, \cdots\}$ similar to Γ_0 are generated based on the proportionally coefficient $\xi(0 < \xi < 1)$ regarding crack tip as centre. The density of fractal mesh is controlled by ξ. Based on appropriate global interpolation function and fractal transforming technique, plenty of unknown degrees on slave nodes are

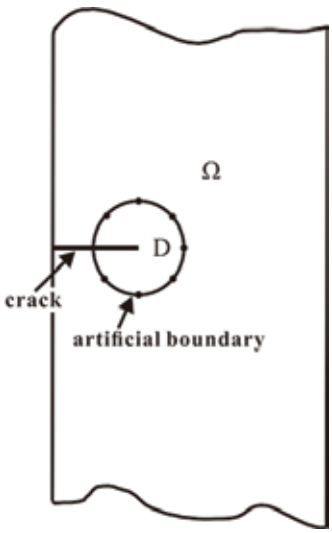

Figure 9. Illustration of division of structure with crack.

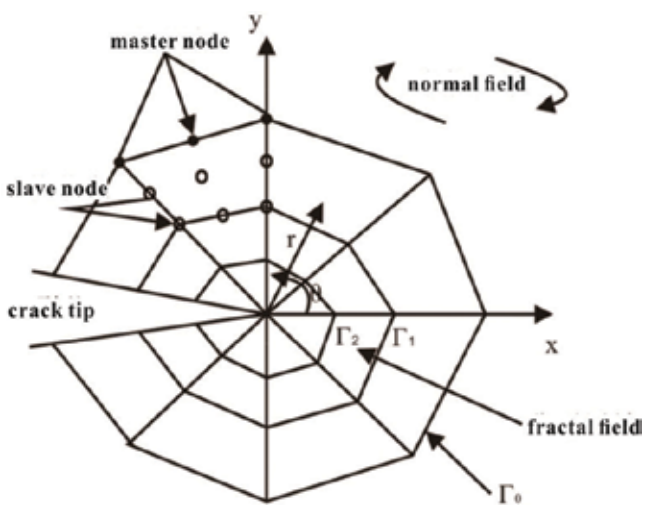

Figure 10. Self-similar mesh in singular field.

transformed into a series of generalized coordinates. Stress intensity factor on crack tip can be calculated via solving generalized coordinates, thus saving calculation time and storage capacity obviously.

5. Conclusion

This chapter reviews the most common empirical models and numerical methods of structural fatigue lifetime prediction. The main advantages and disadvantages of these methods are discussed.

Numerical method based on empirical models, as one of significant ways to analyze structural fatigue life, becomes popular in structural life prediction nowadays because of less cost and higher efficiency.

$S-N$ curve and $\varepsilon-N$ are applied to high-cycle and low-cycle fatigue problems, respectively. And there are many modified models considering mean stress or stress ratio. However, this chapter further shows that part of these models are too complicated to apply to engineering, and other models are only valid in some specific cases.

Paris law is the most significant model of crack propagation problem. But it only considers the stress intensity factor as the factors make influences on crack propagation. Many improved models considering stress ratio, crack closure, crack retardation, and crack propagation threshold have been put forward.

FEM is the most popular numerical method to obtain stress intensity factor or crack growth route. Extended finite element method and fractal finite element method are two mainly developing trends of FEM. However, it is still difficult to achieve high efficiency and accuracy of numerical method at the same time.

Author details

Qiu Zhiping, Zhang Zesheng and Wang Lei*

*Address all correspondence to: leiwang_beijing@buaa.edu.cn

Institute of Solid Mechanics, School of Aeronautic Science and Engineering, Beihang University, Beijing, China

References

[1] Jiang Y, Ding F, Feng M. An approach for fatigue lifetime prediction. Journal of Engineering Materials and Technology. 2007;**129**:182-189

[2] Schijve J. Fatigue of aircraft materials and structures. International Journal of Fatigue. 1994;**16**(1):21-32

[3] Starke P, Eifler D, Boller C. Fatigue assessment of metallic materials beyond strain measurement. International Journal of Fatigue. 2016;**82**:274-279

[4] Gugno N, Ciavarella M, Cornett P, Carpinteri A. A generalized Paris' law for fatigue growth. Journal of the Mechanics and Physics of Solids. 2006;**54**:1333-1349

[5] Zhao T, Jiang Y. Fatigue of 7075-T651 aluminum alloy. International Journal of Fatigue. 2008;**30**:834-849

[6] Jiang Y, Feng M. Modeling of fatigue crack propagation. Journal of Engineering Materials and Technology. 2004;**126**(1):77-86

[7] Vergani L, Guagliano M. From microstructure to design: Advances in fatigue of metals. International Journal of Fatigue. 2016;**83**:1

[8] Karolczuk A, Kluger K, Lagoda T. A correction in the algorithm of fatigue lifetime calculation based on the critical plane approach. International Journal of Fatigue. 2016; **83**:174-183

[9] Schijve J. Fatigue of structures and materials in the 20th century and the state of air. International Journal of Fatigue. 2003;**25**:679-702

[10] Basquin OH. The experimental law of endurance tests. Proceedings of ASTM. 1910;**10**(II): 625-630

[11] Coffin Jr LF. A study of the effects of cyclic thermal stresses on a ductile metal. Transactions of ASME. 1954;**76**:931-950

[12] Manson SS. Fatigue: A complex subject-some simple approximations. Experimental Mechanics. 1965;**5**(4):193-226

[13] Dowling NE, Calhoun CA, Arcari A. Mean stress effects in stress-life fatigue and the Walker formula. Fatigue & Fracture of Engineering Materials & Structures. 2009;**32**(3): 163-179

[14] Duran JAR, Hernandez CT. Evaluation of three current methods for including the mean stress effect in fatigue crack growth rate prediction. Fatigue & Fracture of Engineering Materials & Structures. 2015;**38**(4):410-419

[15] Jaske CE, Feddersen CE, Davis KB, Rice RC. Analysis of fatigue, fatigue crack propagation and fracture data. In: NASA CR-132332. United States. 1973. pp. 49-54

[16] Morrow J. Fatigue design handbook. Advances in Engineering. 1968;**4**(3,2):21-29

[17] Smith KN, Watson P, Topper TH. A stress-strain function for the fatigue of materials. Journal of Materials. 1970;**5**:767-778

[18] Sutherland HJ, Mandell JF. Optimized Goodman diagram for the analysis of fiberglass composites used in wind turbine blades. Journal of Solar Energy Engineering. 2005;**127**(4): 563-569

[19] Paris PC, Gomez RE, Anderson WE. A rational analytic theory of fatigue. The Trend in Engineering. 1961;**13**(1):9-14

[20] Liu HW. Crack propagation in thin metal sheet under repeated loading. Journal of Fluids Engineering. 1961;**83**(1):23-31

[21] Paris PC, Erdogan F. Critical analysis of crack growth propagation laws. ASNW Transactions, Journal of Basic Engineering. 1963;**85D**(4):528-534

[22] Jones R, Molent L, Pitt S. Similitude and the Paris crack growth law. International Journal of Fatigue. 2008;**30**(10):1873-1880

[23] Pugno N, Ciavarella M, Cometti P, Carpinteri A. A generalized Paris' law for fatigue crack growth. Journal of the Mechanics and Physics of Solids. 2006;**54**:1333-1349

[24] Mcclintock FA. On the plasticity of the fatigue cracks. Fracture of Solids. 1963;**20**(01):65-102

[25] Branco R, Antunes FV, Costa JD, Feng PY, Zhen BK. Determination of the Paris law constants in round bars from beach marks on fracture surfaces. Engineering Fracture Mechanics. 2012;**96**:96-106

[26] Rajabipour A, Melchers RE. Application of Paris' law for estimation of hydrogen-assisted fatigue crack growth. International Journal of Fatigue. 2015;**80**:357-363

[27] Carrascal I, Casado JA, Diego S, Lacalle R, Cicero S, Alvarez JA. Determination of the Paris' law constants by means of infrared thermographic techniques. Polymer Testing. 2014;**40**:39-45

[28] Forman RG. Numerical analysis of crack propagation in cyclic loaded structures. Journal of Basic Engineering, Transaction ASTM (Series D). 1967;**89**:459-465

[29] Walker EK. The effect of stress ratio during crack propagation and fatigue for 2024-T3 and 7075-T6 aluminum. In: Effects of Environment and Complex Load History on Fatigue. ASTM STP462, West Conshohocken; 1970. pp. 1-14

[30] Elber W. The significance of fatigue crack closure. Damage Tolerance in Aircraft Structure. 1971:230-242

[31] Weeler OE. Spectrum loading and crack growth. Journal of Fluids Engineering. 1972;**94**(1): 181-186

[32] Willenberg J, Engle RM, Wood HA. A crack growth retardation model using an effctive stress concept. AFFDL-TM-71-1-FBR:A715659

[33] Donahue RJ et al. Crack opening displacement and the rate of fatigue crack growth. International Journal of Fracture Mechanics. 1972;**8**:209-219

[34] McEvily AJ, Greoeger J. On the threshold for fatigue crack growth. Advances in Research on the Strength & Fracture of Materials. 1978: 1293-1298

[35] Qiu Z, Zheng Y. Predicting fatigue crack growth evolution via perturbation series expansion method based on the generalized multinomial theorem. Theoretical and Applied Fracture Mechanics. 2016;**86**:361-369

[36] Nayroles B, Touzoel G, Villon P. Generalizing the finite element method: Diffuse approximation and diffuse elements. Computational Mechanics. 1992;**10**(5):307-318

[37] Zheng X, Cui H, Su X, Engler-Pinto Jr CC, Wen W. Numerical modeling of fatigue crack propagation based on the theory of critical distances. Engineering Fracture Mechanics. 2013;**114**:151-165

[38] Proudhon H, Li J, Wang F, Roos A, Chiaruttine V, Forest S. 3D simulation of short fatigue crack propagation by finite element crystal plasticity and remeshing. International Journal of Fatigue. 2016;**82**:238-246

[39] Roshdy SB. Triangular quarter-point elements as elastic and perfectly-plastic crack tip elements. International Journal for Numerical Methods in Engineering. 1977;**11**(11):85-98

[40] Chen LS, Kuang JH. A modified linear extrapolation formula for determination of stress intensity factors. International Journal of Fracture. 1992;**54**(1):3-8

[41] Lin XB, Smith RA. An improved numerical technique for simulating the growth of planar fatigue cracks. Fatigue and Fracture of Engineering Materials and Structures. 1997;**20**(10): 1363-1373

[42] He WJ, Lin Y, Ding HJ. A three-dimensional formula for determining stress intensity factors in finite element analysis of cracked bodies. Engineering Fracture Mechanics. 1997;**57**(4):409-415

[43] Xiao QZ, Karihaloo BL. Direct evaluation of accurate coefficients of the linear elastic crack tip asymptotic field. Fatigue & Fracture of Engineering Materials & Structures. 2003;**26**(8): 719-729

Chapter 13

Accelerated Fatigue Test in Mechanical Components

Moises Jimenez

Additional information is available at the end of the chapter

http://dx.doi.org/10.5772/intechopen.72640

Abstract

The reduced time available for product development has forced original equipment manufacturers and their suppliers to develop new components and subsystems efficiently, to release it to the market with lightweight and innovate designs, guaranteeing non-failure on the service life. In order to reach these goals, accelerated tests are developed to evaluate its durability with different design proposals. Although durability is nowadays improved through virtual testing, it is mandatory to perform experimental tests before the final release of the product. The tests are done not only to reproduce the same loads; it has to be modified to reproduce the failures that are found on the roads under normal use conditions. The component can be evaluated as itself, in subassembly or in the assembly; the result among these possibilities have to be the same. To reach this aim, devices are designed to reproduce a specific stiffness, combining its mechanical behavior with the modified loads also known as spectrum. Accelerated test can be developed to increase its severity, reducing test time. The spectrum to perform the durability test was built with service loads and different profiles or users and different roads including weather conditions.

Keywords: accelerated tests, durability, spectrum, extrapolated tests, statistical analysis

1. Introduction

To release new or optimized component, it is mandatory to evaluate it under fatigue load conditions to prevent any kind of unexpected failure on the product life. To reduce the time of the development process, accelerated tests can be performed to obtain the mechanical strength feedback to improve its fatigue performance, thereby reducing the excessive material or reinforcing critical areas as stress concentrators. Nowadays, this information directly influences the component with physical optimization or analyzes it in a virtual way, in order to reduce the number of physical prototypes. The importance of implementing accelerated tests in the

early stages of design is to evaluate components developed in the concept stage or to modify it, for changes in design during its production life act as facelift. **Figure 1** shows the time development reduction when accelerated tests are implemented. Most improvements have to be made prior to mass production and in the early manufacturing process of the tooling [1].

To perform this kind of test, it is necessary to evaluate the critical failures on the component related with the major probability of occurrence. All the load cases are evaluated; however, the target of this kind of a test is to evaluate the component in an easier way, with uniaxial test, where it is possible.

In other cases, the test is developed depending on the part or the process that has to be evaluated, for example, a new stamped part, or the weld cordon or the sequence of the welding. In those cases, a localized damage is developed with a correlation to its use in normal load conditions, but the important thing is to find the direction and load amplitude generated by use conditions, to get a correlation between the number of load repetitions and how many kilometers or time of use represent it.

The way to develop this kind of test starts with the instrumentation of a car with displacement transducers, accelerometers, force-moment transducers and strain gauges where it is necessary. The instrumented car is measured on different roads, used by different drivers in all the markets and under different weather conditions to acquire loads to measure the changes on the responses of the wheels.

These responses are acquired as signals, which are analyzed to synthetize it in one signal representing all of these driving and use conditions. The new signal used for the durability test is known as spectrum. The reproduction of this spectrum in labs reaches the same damage on the component as in the roads, but the target of this kind of test is to reduce the time of evaluation in a controlled manner to detect the location of failure, the moment of occurrence and its propagation. To accelerate the test, the spectrum is extrapolated and proving grounds are developed. These are faster than duration cars on the roads, but it is possible to reduce the evaluation time developing accelerated test on test benches through extrapolating the loads; to perform this, the component can be mounted as assembly, subassembly or component as itself. Test reduction is reached due to the loads that represent more damage by their amplitude and severity, than that applied on the component in normal-use conditions.

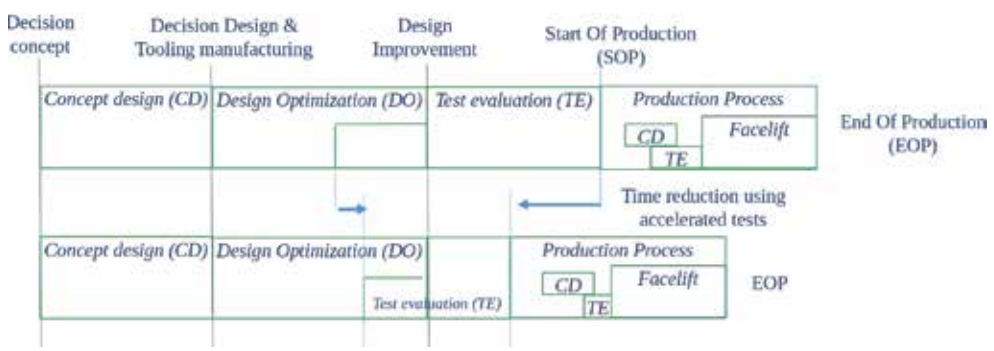

Figure 1. Development time reduction using accelerated tests.

Test responses and desired signals have to be evaluated through statistical analysis. The correlation of results in lab and on roads is essential as the main target of accelerated tests is to reproduce the same failures as on the road so as to take steps to prevent them. The component´s load spectrum is made more aggressive by including all the variables in load conditions as in the case of drivers on roads, and the spectrum is also modified to build test requirements to include the safety factor.

In this chapter, a review of durability test has been performed, describing the process to develop a fatigue test and also the development of accelerated test. A general overview is done on the product evolution process (PEP) to define where the evaluation of the component is applied and how it affects the development process, the general process of the fatigue life evaluation of the component, a description of the finite element analysis and its application on fatigue life prediction to evaluate an automotive component and develop stiffness devices necessary for the test that are used with the modified loads to reproduce the failures.

2. Fatigue tests

It is important to evaluate components in experimental tests because fatigue strength has its inherent scatter due to four main factors: the loading, design, manufacturing and material (**Figure 2**). Experimental results under variable loads differ from analytical predictions owing to the effect of sequence loads [2, 3], Jimenez et al. [4] proposed a modification in Linear Damage Rule to include the effect of sequence in fatigue life prediction.

While manufacturing generally determines the strength and scatter, the geometry can modify the effect of mechanical properties [5, 6] due to the material that has variations on its properties. Loads have the major variability due to the diversity of drivers and factors such as number of passengers, weight on the car and its distribution, weather and its effects on the interchange of the loads between the non-suspended mass and the pave and the loads generated by bumpy ways and maneuvers.

Fatigue strength at the endurance limit is affected by the type of load and the size, reliability and surface roughness of the component [7]. The surface roughness can be improved with

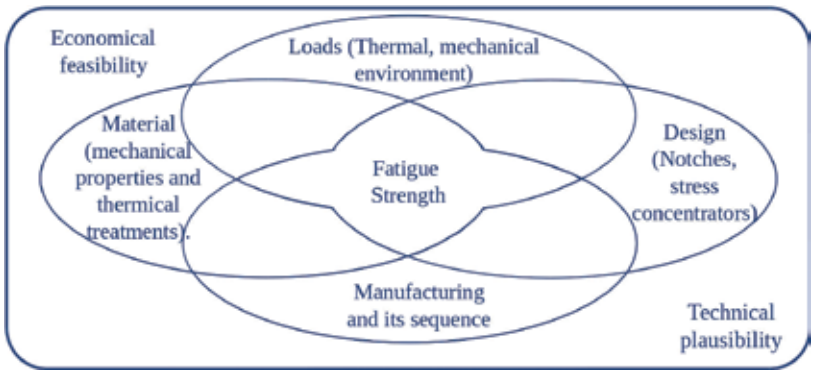

Figure 2. Parameters influencing the structural durability of components.

processes such as shot peening, which is important because fatigue cracks usually initiate at the surface in homogeneous materials [8, 9].

In durability tests, the aim is to minimize the likelihood of failure applied for the more aggressive driver using the weakest component. **Figure 3** shows a strength-load interference model [10], which helps to manage the likelihood of failure of a component. As described in **Figure 2**, the component has different sources of scatter and its structural strength is determined on a bell-shaped curve. On the other side is evaluated the scatter for the loads applied to the component. The safety factor is defined by the difference between the central value of applied loads and its difference with the central value of the component's structural strength.

Jimenez et al. [7] reported that the advantage of component testing is that the effects of the material, manufacturing process and geometry are inherently accounted for. Although with controlled process as in test laboratory, fatigue test results have scatter, the main sources of scatter are summarized in **Table 1** [11].

Fatigue evaluation is not simple to predict by analytical methods, and to perform durability assessment and to predict the component´s life, it is necessary to measure the most precise information, and to do this, the loads in service are acquired and analyzed, to reproduce them as shown in **Figure 4**.

To build a track to perform a durability test, it is necessary to get information from the customers through a data acquisition with strain gauges, accelerometers and displacement transducers; then this information is analyzed. The output of this analysis is to get the desired signal that is known as spectrum. The importance of getting the spectrum is to compare the loads with the S-N curve in order to predict the component life through damage accumulated rule. Every step of the development process is evaluated to improve its mechanical response, and after the design is released, tests are performed to monitor the quality of the product to prevent failures in its service life.

To reduce the time required for testing on public roads, accelerated tests are performed on proving grounds. This simulates road damage for different maneuvers, different vertical loads of frames and different longitudinal dynamics for accelerating and braking, lateral dynamics and vibrations [12], combining all the events (normal roads, rough roads, emergency braking, high speed, city and country roads). In addition, the tests can be performed in the laboratory [5]. It is possible to increase the number of repetitions at high or medium loads, avoiding inadmissible stresses that satisfy the test results. Although some proposals [13] have included

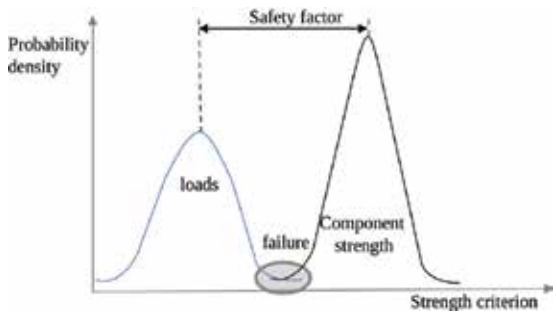

Figure 3. Failure likelihood in components subjected to cyclic loads.

the omission of low loads, they depend on the type of material and the application (**Figure 5**). The main objective is to develop an accelerated spectrum to get a test track.

Variable	Fatigue in components	
	In laboratory	**In service**
Production and materials.	Production samples and different lots	Material from different lots and suppliers processed in different facilities.
	Quality on the specimen Surface.	Quality on Surface in critical areas as in notches.
Loads including environment	Type of load (CA, VA)*	Loads in service from different users
	Accuracy of test equipment	Residual fatigue life
Environment	Temperature, humidity in laboratory	Temperature, snow, rain.
Human	Skills and expertise of lab staff to perform and evaluate the test.	Different users and styles of use, overloads not expected, abuse loads. Responses changed for the environment.

*CA-Constant amplitude; VA-Variable Amplitude.

Table 1. Main sources of scatter in mechanical fatigue.

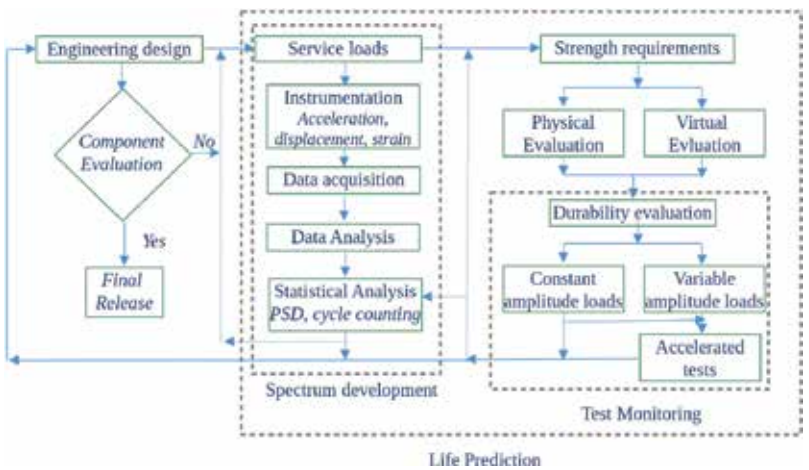

Figure 4. Parameters influencing the structural durability of components.

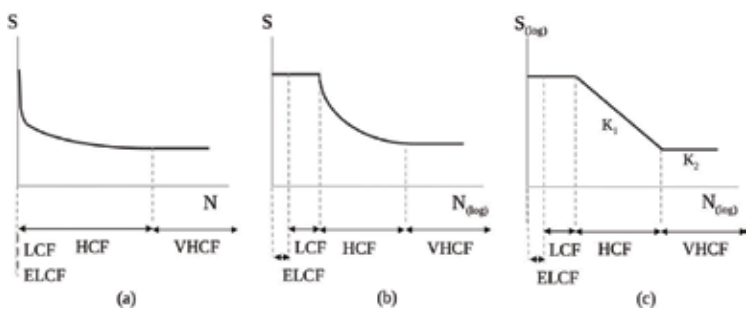

Figure 5. Schematic S-N curve: (a) linear-linear, (b) semi-log, and (c) log–log.

3. Statistical analysis

The loads acquired are compared with S-N curves. The S-N curves are often expressed on semi-log, normal and log–log coordinates. **Figure 5** shows a schematic curve on different coordinates, linear, semi-log and log–log. The most common representation is log-log since it becomes linear (**Figure 5c**).

The S-N curve represents the material or component fatigue strength, and is split into regions depending on its cycles. Extremely low cycle fatigue (ELCF) is defined from 0 until 100 cycles, between this limit and until 1000 cycles is low cycle fatigue (LCF), and between 1000 cycles and until 1 × 106 for steel and 5 × 107 for nodular cast iron is defined as high cycle fatigue (HCF). Anything beyond this point is defined as very high cycle fatigue (VHCF) [7].

To compare the S-N curve with loads, the time history is analyzed. **Figure 6** shows a schematic waveform. The main characteristic is the stress amplitude S_a. If it has constant amplitude, the stress range S_R is constant and is defined by the difference of the maximum stress (S_{max}) and minimum (S_{min}) in a cycle (Eqs. (1)–(3)).

$$S_R = S_{max} - S_{min} \tag{1}$$

$$S_a = \frac{S_R}{2} = \frac{S_{max} - S_{min}}{2} \tag{2}$$

The mean stress S_m is defined as

$$S_m = \frac{S_{max} - S_{min}}{2} \tag{3}$$

A fully alternating stress $S_m = S_a$.

The stress ratio *(R)* is defined as the ratio of minimum to maximum stress as is shown in Eq. (4).

$$R = \frac{S_{min}}{S_{max}} \tag{4}$$

The fatigue damage of a component is influenced in high cycle region by the mean stress expressed by its stress ratio. In normal $R \geq 0$, open microcracks accelerate the propagation of stress, while $R = \infty$ or >1 closes the microcrack that is beneficial for fatigue strength. In low cycle fatigue region, the plastic deformation eliminates the effect of mean stress to improve or detriment the fatigue strength. The schematic stress ratio is shown in **Figure 7**.

The amplitude ratio is the ratio of the stress amplitude to mean stress as show in Eq. (5).

$$A = \frac{S_a}{S_m} = \frac{1 - R}{1 + R} \tag{5}$$

The loads are monitored with cycle counting that is used to summarize variable amplitude time histories, providing the repetitions of the load during the time history. There are different

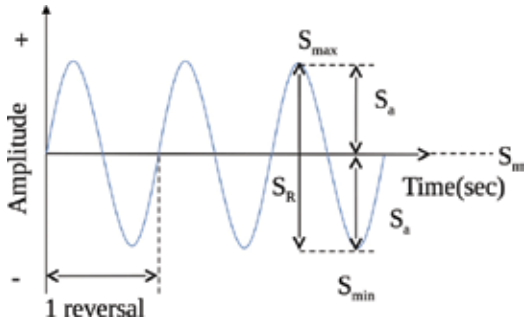

Figure 6. Signal characteristics.

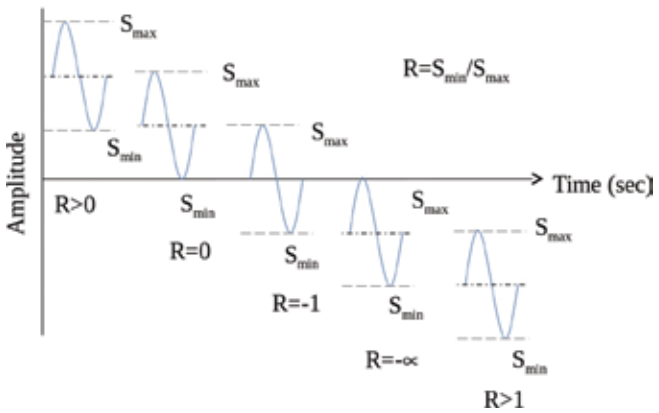

Figure 7. Stress ratio.

cycle counting methods such as the Rainflow used to extract cycles from random histories in the time domain [13, 14], based on the analogy of raindrops falling on a roof. **Figure 8** shows Rainflow counting process.

The cycle counting is represented in a matrix based on **Figure 5**. The signal has 2 cycles from 5 to 3, 1 cycle from 6 to 3, 1 cycle from 1 to 5, 1 cycle from 2 to 4 (**Figure 5a**), 2 cycles from 1 to 6 (**Figure 5b**), and it has residue. In **Figure 5c**, these cycles are tabulated on a matrix, which depending on its counting can be represented by colors.

It is possible to evaluate time histories with other types of cycle counting methods, such as the level crossing method [15] where the amplitudes of the loads are split into a number of levels based on ranges, and the load is counted when it has peak at a different level, changing its slope from positive to negative or negative to positive; the cycle counting is shown in **Figure 9**.

In the range pair counting method, the magnitude of loads is split into a number of levels. The result of the extracted number of reversals is shown tabulated in **Figure 10b**. **Table 2** summarizes the events counted in **Figure 10**.

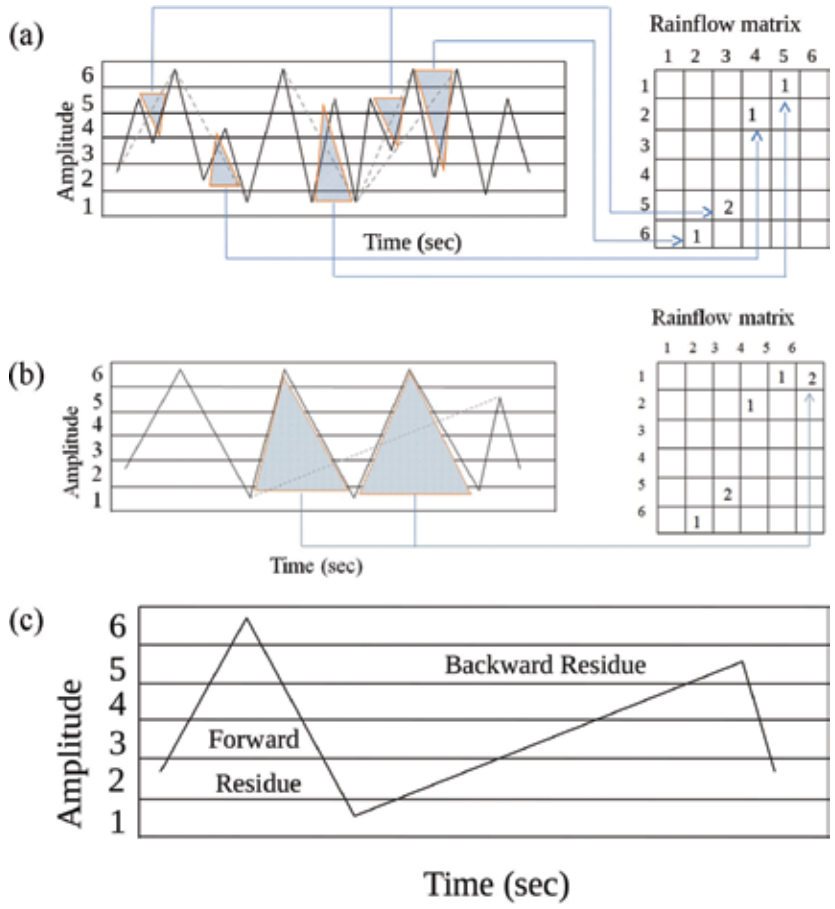

Figure 8. Rainflow counting process: (a) initial counting, (b) continue counting, and (c) residue.

The signals can be seen in time domain and frequency domain. A transfer function can be used in the frequency domain to relate the power spectral density (PSD) of the input desired load to the PSD of the output stress (Eq. (6)) [16]:

$$\sigma_{PSD}(w) = |h(w)|^2 F_{PSD}(w) \tag{6}$$

here the squaring process is required to get the transfer function in the correct units of PSD stress [17]. In this equation, σ_{PSD} (w) is the PSD of the stress at frequency w (N^2/Hz); h (W) is the linear transfer function at frequency w; and F_{PSD} (w) is the PSD of the input amplitude at frequency w (N^2/Hz). The advantage of analyzing the responses with PSD is that it helps us represent the energy of the time signal at each frequency.

The time histories for constant amplitude test spectrum is linear (**Figure 11a**), and for variable amplitude, it is a curve (**Figure 11b**) generated by the cycle counting. Although a theoretical fatigue limit has been proposed, with the introduction of new test equipment for high frequency, the prediction has been improved at low load levels. Although this stress couldn't

damage the components by itself, the accumulated damage induced by high loads can be propagated by such small loads. The correction factors for the slope depend on the material [18].

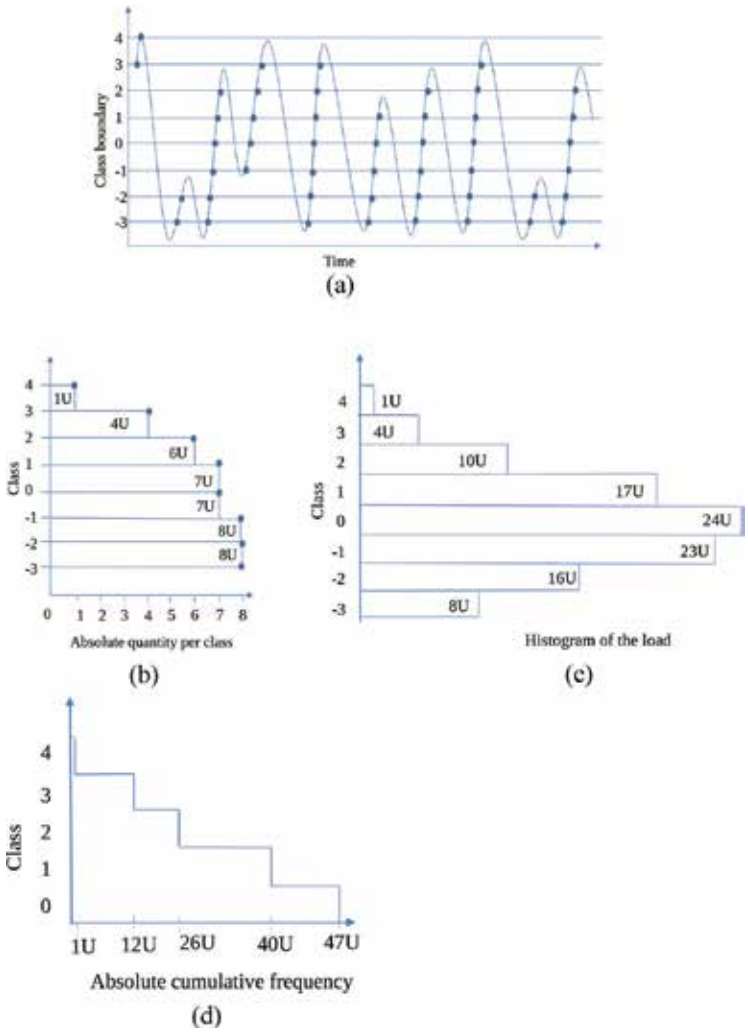

Figure 9. Level crossing counting process: (a) time history, (b) quantity per class, (c) histogram, and (d) absolute cumulative frequency.

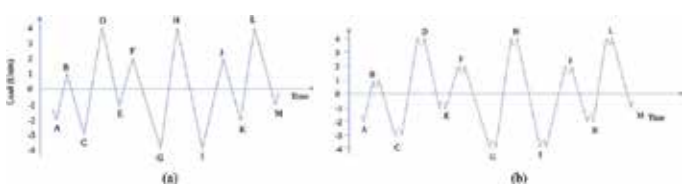

Figure 10. Range pair counting process, (a) time signal and (b) events.

Range (Units)	Cycle counts	Events
8	1.0	G-H,H-I
7	0.5	C-D
6	1.5	F-G, I-J,K-L
5	1.0	D-E,L-M
4	1.0	B-C,J-K
3	1.0	A-B,E-F
2	0	
1	0	

Table 2. Range pair counting.

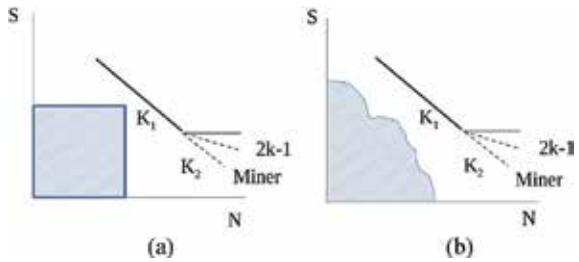

Figure 11. Schematic spectrums versus components S-N curves: (a) constant amplitude, (b) variable amplitude.

4. Accelerated tests

Component life testing is commonly designed to validate fatigue strength of a component based on a target customer usage and is based on loads acting on components. The measurement period is usually not long enough to be used directly in a test. The main target for extrapolated signals is based on time measurement restrictions and problems such as synchronicity, spikes, drifts observed on measurement devices. For this reason, the most representative road or proving ground is determined and that is extrapolated to reach the kilometers of the total life.

The advantages of finite element simulation are mainly in the early stages of design where the prototypes are not yet available, and also to improve its design without physical components. But also in this case, the loads for variable or spectrum as well as constant amplitude are developed to correlate with the accelerated tests. All the factors are evaluated in physical tests, and the results are analyzed through statistical results.

The load measures are extrapolated to the requirement. These spectrums are evaluated to include all the behaviors, as is shown in **Figure 12**. Spectrum test is developed using different

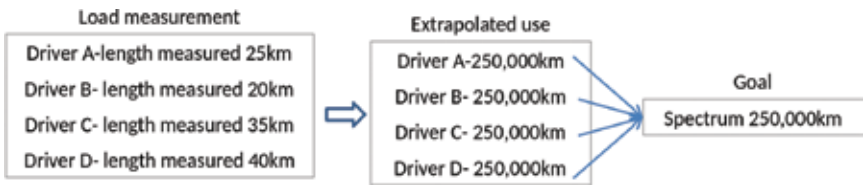

Figure 12. Spectrum development target.

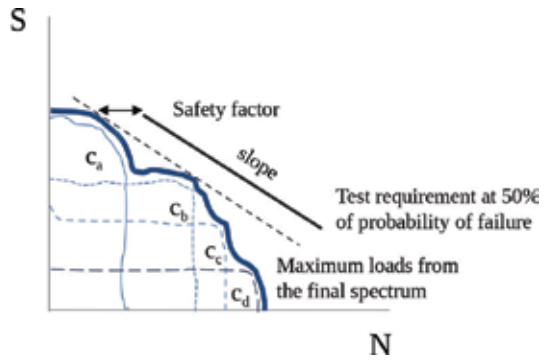

Figure 13. Schematic spectrum development.

loads from the users and different responses are taken into account. C_a is the driver A, the most aggressive driver, C_b is the average driver, and C_c and C_d are the drivers that use less aggressive components but for more time. After having extrapolated the goal use, the spectrum is built considering all these measurements. **Figure 13** shows a schematic spectrum development. For variable amplitude test, the spectrum is reproduced and monitored with statistical analysis.

The repetitions of the cycles are found using the linear damage rule of Miner (Eq. (7)), and damage is evaluated using the ratio of the loads *(n)* with the number of repetitions *(N)* tolerated at *i* load level.

$$D = \sum \frac{n_i}{N_i} \tag{7}$$

The damage could be reached when the summation is 1 and there is an effect of sequence load. Depending on sequence effect loads, the damage can be reached too with values above or below 1 [4]. The failure is observed when there is a physical crack.

5. Instrumentation

Figure 2 shows that the first point to acquire information is to install measurement devices on the component or in its vicinity, to obtain the responses of the components that induce

stress. To obtain the most important information we install the measurement devices at the main stress points. To do this, it is necessary to perform a finite element simulation in order to get the point and the direction of the stresses. **Figure 14** shows the typical process used to perform this kind of simulation.

The components evaluated can be from different materials and built with different manufacturing process. In the next figure are shown instrumented components with a point selection from finite element evaluation [7]. Then to find the point and direction of the main stresses, components are instrumented with strain gauges. Its nominal resistance is 120 or 350 ohms. Higher resistance can be used for base material with low heat conductivity and higher voltage excitation than 10 Volts can be mainly used in environments with high electrical noise [18]. **Figure 15** shows chassis components instrumented, **Figure 15a** the rear subframe for a rigid axle, **Figure 15b** a front axle steering knuckle and **Figure 15c** a frontal axle track control arm.

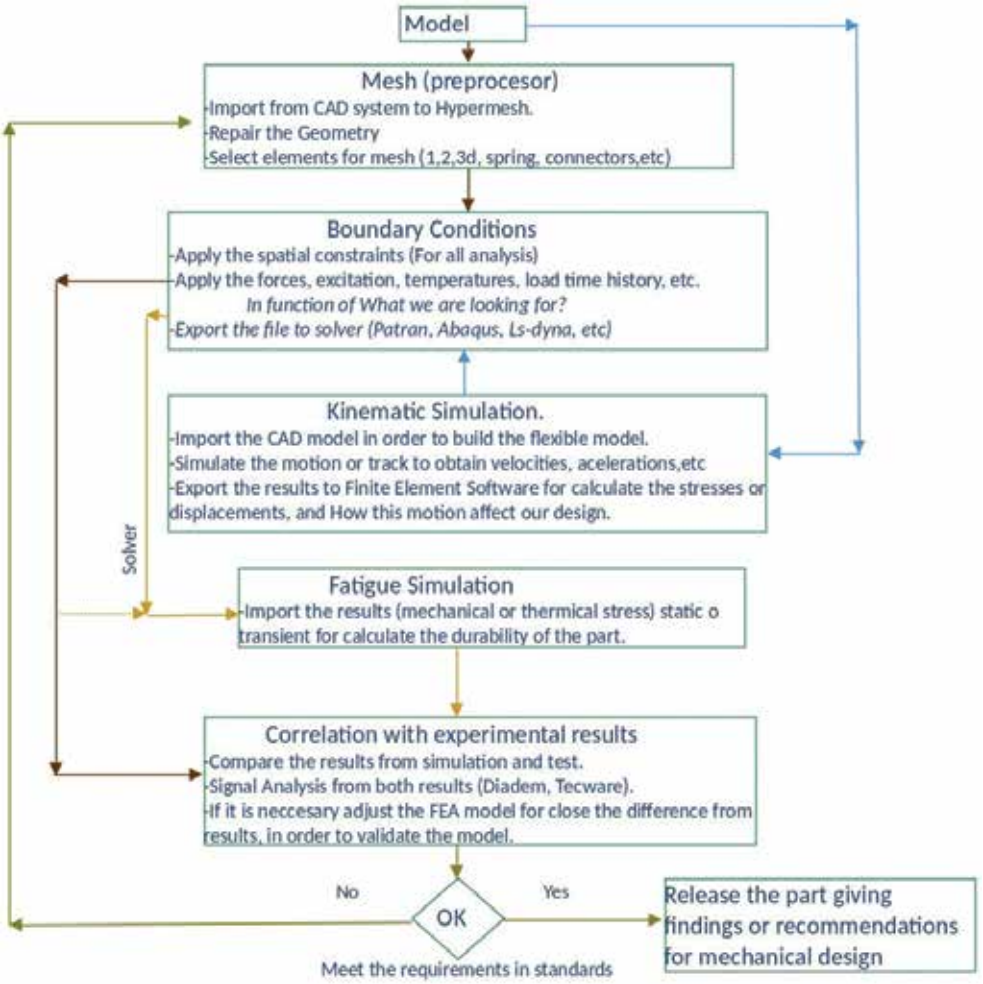

Figure 14. General procedure for simulation.

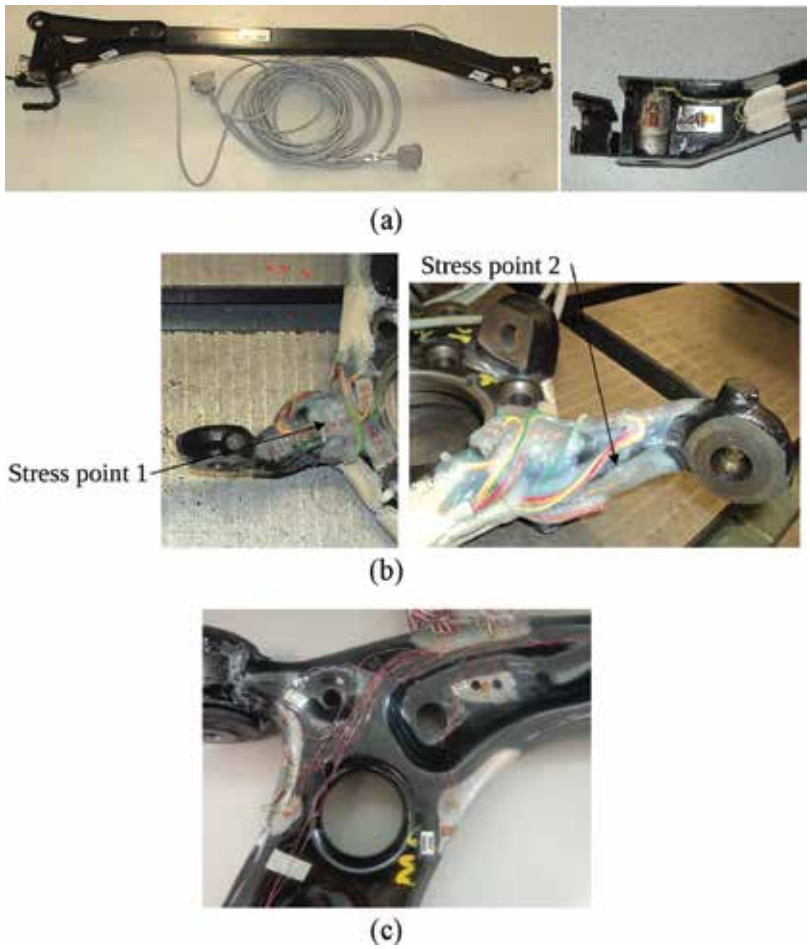

Figure 15. Instrumented components with strain gauges, (a) rear rigid axle subframe, (b) steering knuckle, and (c) track control arm.

6. Case study

The accelerated tests are developed to reduce the time and complexity of the test in order to have faster results. **Figure 16** shows a test stand to evaluate a frontal axle track control arm.

The information collected from the strain gauges can be used to evaluate the component, perform a correlation with virtual or analytical tools and build a spectrum. In not all the cases, can we directly measure the microstrain to validate the virtual simulation. The acceleration can be used to validate the finite element model with experimental acceleration results. With this validation, the stresses are found in a virtual way and can be used to perform the real-life prediction [4].

In the next part, the process to develop an accelerated test is shown. The time history in **Figure 17** shows the raw data time history to evaluate a track control arm, its main characteristics is a range of 42,354 N, maximum value of 21,473.6 N and minimum value of −20,880.8 N and the time length is 249.9 s.

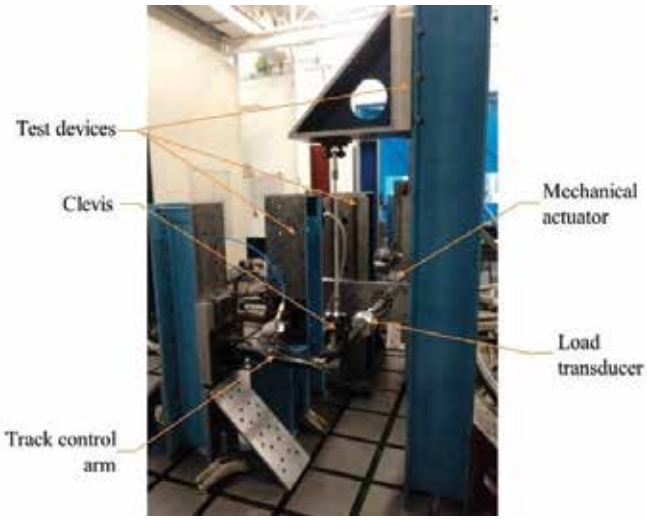

Figure 16. Durability test stand for frontal track control arm.

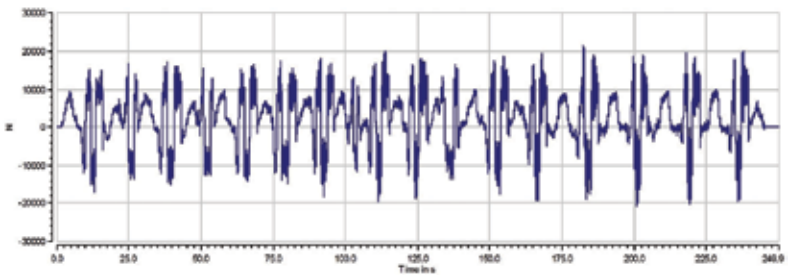

Figure 17. Raw data time history for uniaxial test of track control arm.

The information acquired is then analyzed to eliminate unnecessary information such a noise. To do this, we apply filters, and perform statistical analyses. For a structural analysis it is necessary to have a low pass filter of 100 Hz [19]. To evaluate the changes after applying the filter, it is necessary to perform the statistical analysis using cycle counting tools and evaluate the pseudodamage using the linear damage rule [4]. The results of this evaluation are shown in **Figure 18**.

After applying the filter, the time history obtained has the next characteristics: range of 41,715.3 N, maximum value of 21,283.5 N and minimum of −20,433.6 N; the time length keeps its length of 249.9 s. The pseudodamage was reduced from 4.55 to 4.41, it means a reduction of 3.07% of damage, taking as a reference the raw signal.

There are many ways to accelerate the test. One of them is to eliminate the loads amplitude that do not apply a high amount of damage. To do this, in the time history, we eliminate the amplitude below 5000 N. **Figure 19** shows the process to show the selected areas and the final time history.

The cut signal and the raw data and the filtered raw data were compared using statistical analysis as it is shown in **Figure 20**.

After eliminating the amplitudes below 5kN, the new time history has the next characteristics: range of 41,717 N, maximum value of 21,283.5 N and minimum value of −20,433.6 N and the time length is 208.4 s. The pseudodamage has not been modified, while the time has been compressed from 249.9 to 208.4 s (16.6%). This is our target signal to generate the test spectrum, in order to develop the durability test.

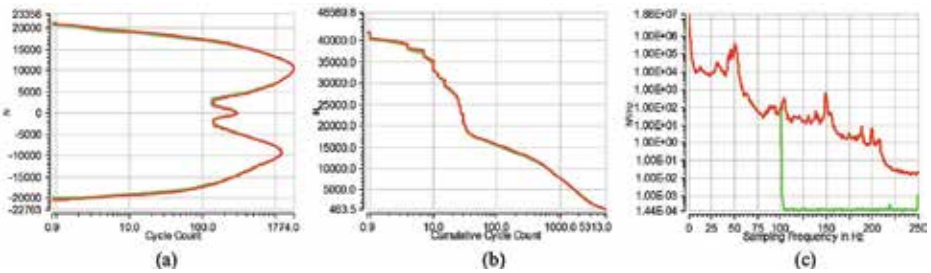

Figure 18. Statistical analysis of the raw data compared with the filtered signal (a) cycle counting, (b) cumulative cycle count, and (c)PSD.

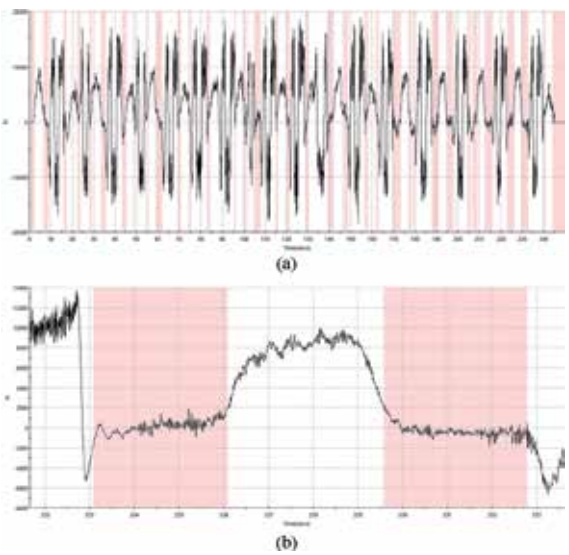

Figure 19. Cutting load damage areas from the raw data time history filtered, (a) 0–249.9 s, (b) zoom between 221.7 and 233.6 s.

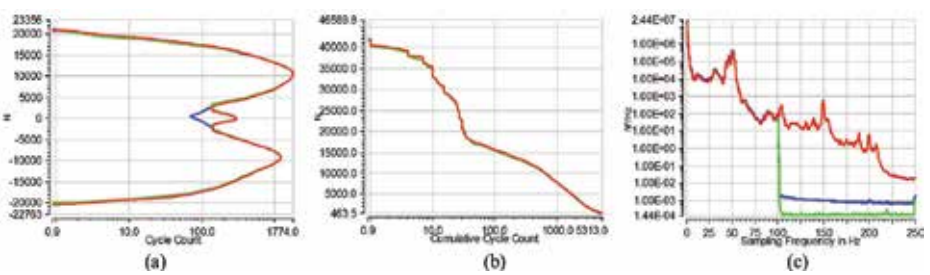

Figure 20. Statistical analysis after cutting loads below 5000 N, (a) cycle counting, (b) cumulative cycle count, and (c) PSD.

To accelerate the test, we can increase the number of repetitions of loads with amplitude high and medium. **Figure 21** shows the statistical analysis increasing the medium loads. The time history obtained has the next characteristics: range of 42,340.9 N, maximum value of 21,906.9 N and minimum value of −20,433.9 N; time length of 135.1 s. The damage was increased from 4.55 to 8.52, which means that it was increased by a factor of 1.87, reducing the time by 45.93% with respect to the raw data.

Figure 22 shows the statistical analysis increasing the amplitude of high loads and the number of repetitions of high and medium loads. The time history obtained has the next characteristics: range of 59,124.4 N, maximum amplitude of 30,670.6 N and minimum of −28,543.8 N; time length of 167.7 s. The damage was increased from 4.55 to 39.6. This means that it was increased by a factor of 8.7, reducing the time by 32.89% with respect to the raw data.

Figure 23a summarizes the spectrums of the all strategies extrapolated to the time histories, the raw filtered data could be cut at below load levels to reduce the time; the medium and high loads in the signal can be increased, reducing the original time and increasing the damage. **Figure 23b** shows the schematic techniques to accelerate the test.

An alternative option to represent the spectrum instead of time history is with Matrix Rainflow. **Figure 24** shows the four analyzed signals: original (**Figure 24a**), filtered (**Figure 24b**), increasing the medium loads (**Figure 24c**), and increasing the number of reversals in high loads inclusive of above the maximum loads of the raw data (**Figure 24d**). The major differences are shown in **Figure 24c** and **d** for medium and high loads, respectively, and the ranges for medium-to-high loads and its number of repetitions have been increased.

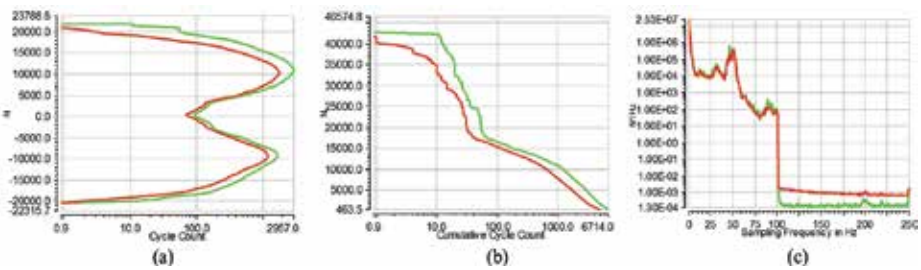

Figure 21. Statistical analysis increasing medium loads, (a) cycle counting, (b) cumulative cycle count, and (c) PSD.

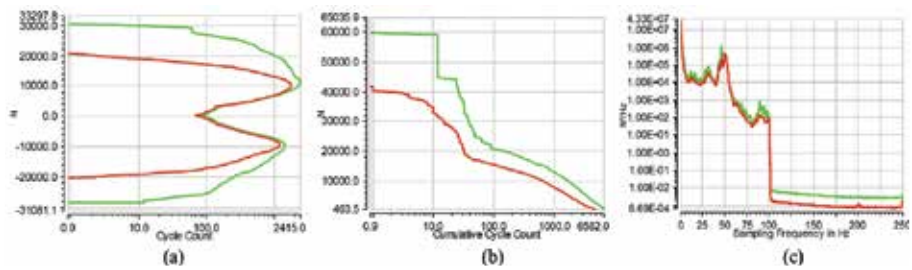

Figure 22. Statistical analysis increasing high loads: (a) cycle counting, (b) cumulative cycle count, and (c) PSD.

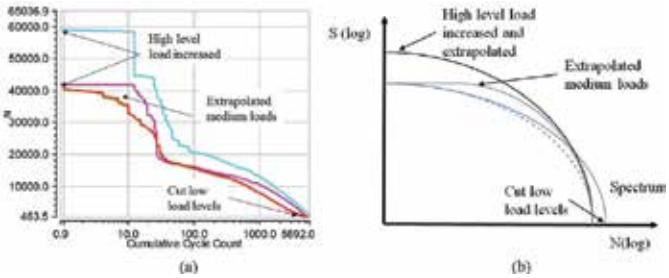

Figure 23. Spectrum of the time histories, (a) summary of time test reduction and (b) schematic accelerated test.

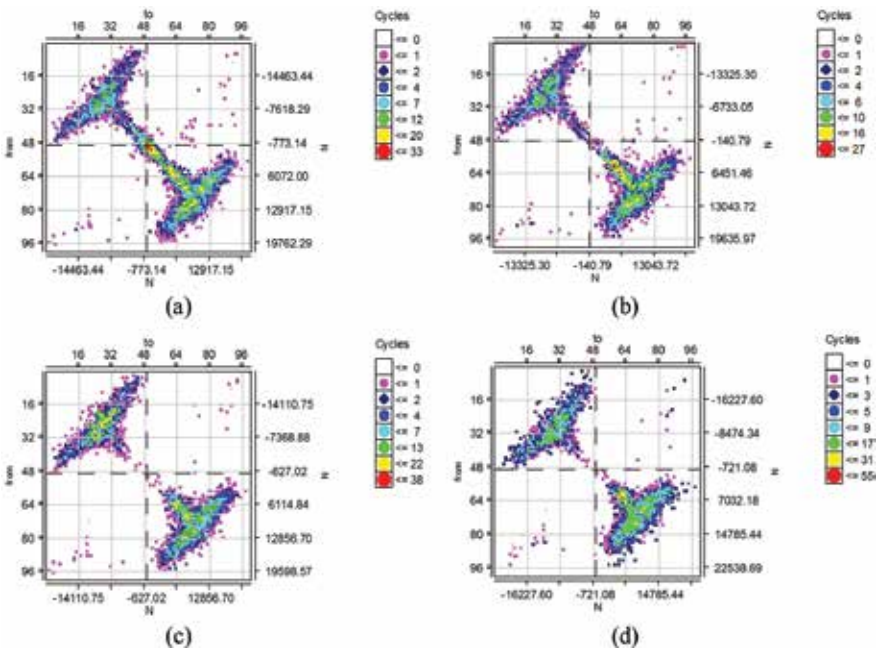

Figure 24. Rainflow matrix (a) raw data, (b) cut filtered signal, (c) medium loads increased, and (d) high loads increased.

For variable amplitude loads, this statistical analysis is used to monitor and guarantee that the loads have been applied correctly. Because it is necessary to build a drive used for the actuators to test the applied loads, the feedback through loads are measured and compared with the desired spectrum, and the drive to control the test actuators is developed through an iteration process [20]. Another way to perform an accelerated test based on the spectrum is using two load levels with a constant amplitude load for each load level. Then these results are plotted in an S-N component curve, and the specimen results are evaluated to predict the fatigue strength and different load levels [21]. **Figure 25** shows the experimental results of uniaxial constant amplitude loads of steering knuckle.

In an S-N curve, the percent replication *(PR)* is found by using the number of stress levels *(L)* and a sample size (n_s) as is shown in Eq. (8).

$$P_R = 100\left(1 - \frac{L}{n_s}\right) \tag{8}$$

This value represents the portion of specimens that may be used in the variability to replicate the tests. The recommended values by Lee et al. [18] are as follows:

17–33 for preliminary and exploratory tests,

33–50 for research and development tests,

50–75 for design allowable data tests and

75–88 for reliability tests.

Steering knuckle results shown in **Figure 25** have 7 level of loads, and 90 Specimens using Eq. (4) get a percent replication of 92.2. These high values obtained from these results are evaluated to analyze a proposal to estimate an S-N curve. For a component test, recommended samples used depend on the target, for research and development tests 6–12, and for reliability tests 12–24 samples. The minimum samples for two load levels are three specimens for each load level.

The median is the central value of results at each load level, and the tendency is considered at 50% of reliability and is necessary to evaluate it to know the scatter of the factors described in **Figure 1** (Eq. (8)).

$$\mu = \frac{1}{n}\sum_{i=1}^{n} x_i \tag{9}$$

To evaluate the scatter of the components based on its fatigue results, the standard deviation is evaluated using Eq. (10). To take into consideration, its results have to be between 0.05 and 0.15; for samples without notches, the range is between 0.1 and 0.2, for uniaxial tests the range is between 0.2 and 0.3, while in complex tests, it can reach values between 0.3 and 0.6 [22].

$$s^2 = \frac{1}{n-1}\sum_{i=1}^{n} (x_i - \mu)^2 \tag{10}$$

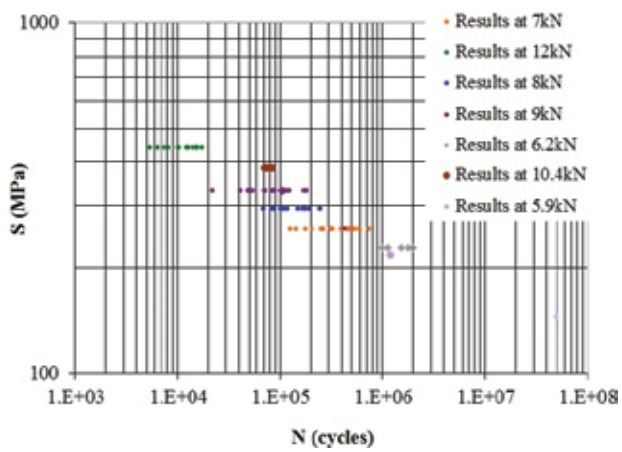

Figure 25. Test results in steering knuckle analysis.

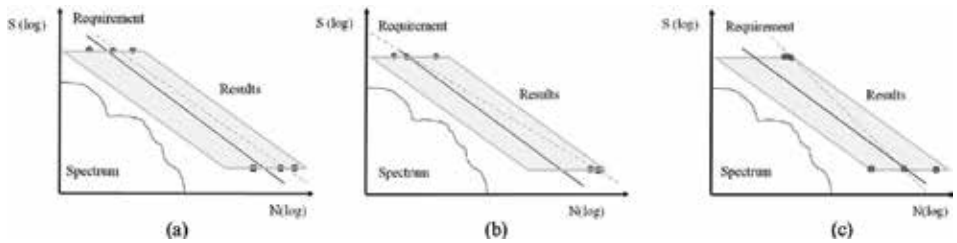

Figure 26. Evaluation results (a) slope test k_{test} = slope requirement k_{req}, (b) $k_{test} < k_{req}$, (c) $k_{test} > k_{req}$.

Results of the slope found in tests are compared with the requirement, and changes on the slope affect the behavior at low or high load levels. **Figure 26** shows the evaluation of the results with constant amplitude loads.

7. Conclusions

Accelerated tests are used to reduce cost and time in the development process. It can also be used to monitor the quality of the components during its manufacturing life. Experimental evaluation is mandatory prior to final release and start of production to analyze the scatter of the manufacturing process and prevent failures in service life. The importance of performing variable amplitude loads tests is because the prediction of fatigue life under the complex spectrum loads is not possible by any damage hypothesis. The spectrum to evaluate the components in the tests is developed with the loads from different customers and markets and use conditions. Experimental results show discrepancies even within the same batch of production, and the statistical value to evaluate the reliability of the lot under test is the standard deviation that shows the influence of the factors described in **Figure 1**. Although the tests are performed under controlled conditions in a laboratory, in specimens with notches, the batch of production is released if the standard deviation of its fatigue results has a maximum value of 0.2. For samples without notches in uniaxial tests, the maximum scatter allowed is 0.3 and 0.6 for complex test [22]. To evaluate the fatigue strength as well as the scatter, it is necessary to perform durability tests, to prevent failures on the service life.

Author details

Moises Jimenez[1,2]*

*Address all correspondence to: moisesjimenezmartinez@gmail.com

1 Technical Development, Volkswagen de Mexico, Puebla, México

2 Tecnologico de Monterrey, Escuela de Ingeniería y Ciencias, Monterrey, Mexico

References

[1] Nam JS, Shin HW, Choi GJ. Durability prediction for automobile aluminum front subframe using nonlinear models in virtual test simulations. International Journal of Automotive Technology. 2014;**15**(4):593-601. DOI: 10.1007/s12239-014-0062-2

[2] Kadhim NA, Abdullah S, Ariffin AK. Effective strain damage model associated with finite element modeling and experimental validation. International Journal of Fatigue. 2012;**36**(1):194-205. DOI: 10.1016/j.ijfatigue.2011.07.012

[3] Rejovitzky E, Altus E. Non-commutative fatigue damage evolution by material heterogeneity. International Journal of Fatigue. 2012;**37**(4):54-59. DOI: 0.1016/j.ijfatigue.2011.10.004

[4] Jimenez M, Martinez J, Figueroa U. Load sequence analysis in fatigue life prediction. Transactions of the Canadian Society for Mechanical Engineering. 2015;**39**(4):819-828. Available from: http://www.tcsme.org/Papers/Vol39/Vol39No4Paper6.pdf [Accessed 30 June 2017]

[5] Berger C, Eulitz K-G, Heuler P, Kotte K-L, Naundorf H, Schuetz W, Sonsino CM, Wimmer A, Zenner H. Betriebsfestigkeit in Germany – An overview. International Journal of Fatigue. 2002;**24**(6):603-625. DOI: 10.1016/S0142-1123(01)00180-3

[6] Lee KT, Park CS, Kim HY. Fatigue and buckling analysis of automotive components considering forming and welding effects. International Journal of Automotive Technology. 2017;**18**(1):97-102. DOI: 10.1007/s12239-017-0010-z

[7] Jimenez M, Martinez J, Figueroa U, Altamirano L. Estimated S-N curve for nodular cast iron: A steering knuckle case study. International Journal of Automotive Technology. 2014;**15**(7):1197-1204. DOI: 10.1007/s12239-014-0125-4

[8] Dalaei K, Karlsson B. Influence of shot peening on fatigue durability of normalized steel subjected to variable amplitude loading. International Journal of Fatigue. 2012;**38**(5): 75-83. DOI: 10.1016/j.ijfatigue.2011.11.011

[9] Ås SK, Skallervd B, Tveiten BW. Surface roughness characterization for fatigue life predictions using finite element analysis. International Journal of Fatigue. 2008;**30**(12): 2200-2209. DOI: 10.1016/j.ijfatigue.2008.05.020

[10] Xiong JJ, Shenol RA. Fatigue and Fracture Reliability Engineering. 2nd ed. London: Springer-Verlag; 2011. 156 p

[11] Schijve J. Fatigue of Structures and Materials. 2nd ed. New York: Springer; 2009. 613 p

[12] Ozmen B, Altiok B, Guzel A, Kocyigit I, Atamer S. A novel methodology with testing and simulation for the durability of leaf springs based on measured load collectives. Procedia Engineering. 2015;**101**:363-371. DOI: 10.1016/j.proeng.2015.02.044

[13] Kadhim NA, Abdullah S, Ariffin AK. Effect of the fatigue data editing technique associated with finite element analysis on the component fatigue design period. Materials and Design. 2011;**32**(2):1020-1030. DOI: 10.1016/j.matdes.2010.07.029

[14] Banvillet A, Lagoda T, Macha E, Nieslony A, Palin-Luc T, Vittori JF. Fatigue life under non-Gaussian random loading from various models. International Journal of Fatigue. 2004;**26**(4):349-363. DOI: 10.1016/j.ijfatigue.2003.08.017

[15] Shaumann P, Steppelers S. Fatigue tests of axially loaded butt welds up to very high cycles. Procedia Engineering. 2013;**66**:88-97. DOI: 10.1016/j.proeng.2013.12.065

[16] Haiba M, Barton DC, Brooks PC, Levesley MC. Review of life assessment techniques applied to dynamically loaded automotive components. Computers and Structures. 2002;**80**(5-6):481-494. DOI: 10.1016/S0045-7949(02)00022-6

[17] Wang X, Xu W, Huang Y, Zhong M, Fan H. Simulation of the vertical bending fatigue test of a five-link rear axle housing. International Journal of Automotive Technology. 2012;**13**(6):923-932. DOI: 10.1007/s12239-012-0093-5

[18] Lee T-L, Pan J, Hathaway R, Barkey M. Fatigue Testing and Analysis. 1st ed. Burlington, MA 01803, USA: Elsevier ButterWorth-Heinemann; 2005. 402 p

[19] Jimenez M, Martinez J, Figueroa U, Guevara A. Finite element simulation of mechanical bump shock absorber for sled tests. International Journal of Automotive Technology. 2015;**16**(1):167-172. DOI: 10.1007/s12239-015-0018-1

[20] Jimenez M, Martinez J. Durability tests. In: SOMIM, editor. Proceedings 13th World Congress in Mechanism and Machine Science; 19-25 June; Guanajuato, México. SOMIM; 2011. p. 1-6

[21] Sonsino C. Fatigue testing under variable amplitude loading. International Journal of Fatigue. 2007;**29**(6):1080-1089. DOI: 10.1016/j.ijfatigue.2006.10.011

[22] Kotte KL. Betriebsfestigkeit Studenbrief. Dresden: Technischen Universität Dresden; 2008

Edited by Pranav H. Darji and Veera P. Darji

This book contains two sections: Chapters 1–7 deal with contact mechanics, and Chapters 8–13 deal with fracture mechanics. The different contributions of this book will cover the various advanced topics of research. It provides some needed background with respect to contact mechanics, fracture mechanics and the use of finite element methods in both. All the covered chapters of this book are of a theoretical and applied nature, suitable for the researchers of engineering, physics, applied mathematics and mechanics with an interest in computer simulation of contact and fracture problems.

Published in London, UK

IntechOpen

ISBN 978-1-83881-353-6